Study and implementation of an Eulerian-Lagrangian method on 2D/3D unstructured meshes for the numerical simulation of fluid flow models

Moussa Ziggaf

UNIVERSITÉ PARIS XIII - SORBONNE PARIS NORD

École Doctorale Sciences, Technologies, Santé Galilée

UNIVERSITÉ MOHAMMED PREMIER

Centre d'Etudes Doctorales Sciences et Techniques

Étude et mise en œuvre d'une méthode Eulérienne-Lagrangienne sur des maillages non structurés 2D/3D pour la simulation numérique de modèles d'écoulements fluides

THÈSE DE DOCTORAT

Présentée par

Moussa ZIGGAF

Laboratoire Analyse, Géométrie et Applications

Laboratoire de Modélisation et Calcul Scientifique

Pour l'obtention du grade de

DOCTEUR EN MATHÉMATIQUES APPLIQUÉES

Soutenue le 10 Juillet 2023 devant le jury d'examen composé de :

Mme. Marion DARBAS	Professeure à l'Université Sorbonne Paris Nord	Présidente du jury
M. Christophe BERTHON	Professeur à l'Université de Nantes	Rapporteur
M. Manuel J. CASTRO DÍAZ	Professeur à l'Université de Malaga	Rapporteur
Mme. Linda El ALAOUI	MCF à l'Université Sorbonne Paris Nord	Examinatrice
M. Emmanuel AUDUSSE	MCF HDR à l'Université Sorbonne Paris Nord	Examinateur
M. Fayssal BENKHALDOUN	Professeur à l'Université Sorbonne Paris Nord	Directeur de thèse
M. Imad EL MAHI	Professeur à l'Université Mohammed Premier	Directeur de thèse
M. Imad KISSAMI	MCF à l'Université Mohammed VI Polytechnique	Co-encadrant de thèse
M. Driss OUAZAR	Professeur à l'Ecole Mohammadia d'Ingénieurs	Invité
Mme. Laurence HALPERN	Professeure émérite à l'Université Sorbonne Paris Nord	Invitée
Mme. Bérangère DELOURME	MCF à l'Université Sorbonne Paris Nord	Invitée
M. Mohammed BOUBEKEUR	Ingénieur de recherche à l'Université Sorbonne Paris Nord	Invité

Le livre de la nature est écrit en langage mathématique
Galileo Galilei

Les pages du livre de la vie sont formées de patience, son encre est constituée d'expérience, et sa couverture est un sourire
M. Ziggaf

À tous ceux qui ont repoussé les frontières du savoir mathématique,

À mes enseignants et mentors, qui ont nourri ma passion pour les nombres et les formules,

À ma famille et mes amis, qui ont toujours cru en moi et m'ont soutenu dans cette aventure,

À tous les chercheurs passés, présents et futurs, qui continuent d'explorer les mystères des mathématiques,

À moi-même, pour avoir persévéré et surmonté les défis qui se sont dressés sur mon chemin.

Remerciements

Ce travail a été réalisé au sein de trois établissements de recherche : le Laboratoire Analyse, Géométrie et Applications (LAGA) de l'Université Sorbonne Paris Nord (USPN), le Laboratoire de Modélisation et Calcul Scientifique (LMCS) de l'Université Mohammed Premier (UMP), et l'équipe de Modélisation, Simulation et Analyse de Données (MSDA) de l'Université Mohammed VI Polytechnique (UM6P).

Cette thèse n'aurait pas pu aboutir sans la présence de nombreuses personnes que je tiens à remercier ici.

En tout premier lieu j'exprime toute ma reconnaissance envers **M. Fayssal BENKHALDOUN**, professeur à l'Université Sorbonne Paris Nord, qui a assuré la direction scientifique de cette thèse avec beaucoup de patience et de gentillesse. Je le remercie tout particulièrement pour la confiance qu'il m'a accordée dès mon arrivée au LAGA en tant que stagiaire en Master 2 et pour l'opportunité qu'il m'a offerte en me proposant ce sujet de recherche très motivant.

J'adresse mes sincères remerciements à **M. Imad EL MAHI**, professeur à l'Université Mohammed Premier, pour la confiance qu'il m'a témoignée en acceptant la responsabilité de la cotutelle entre l'Université Mohammed Premier et l'Université Sorbonne Paris Nord.

Je leur suis reconnaissant pour leur intérêt constant pour le sujet, ainsi que pour la totale liberté de réflexion qu'ils m'ont accordée, leurs conseils et leur disponibilité. Malgré leurs emplois du temps très chargés, ils ont toujours trouvé du temps à m'accorder. Ils ont su me faire profiter de leur grande culture mathématique, de leur expérience et de leur compétence. Je les remercie également pour leur sympathie et leurs qualités humaines, sachant toujours me remotiver lorsque cela était indispensable. Je leur adresse mes remerciements les plus sincères et j'espère que nous aurons l'occasion de travailler à nouveau ensemble.

J'exprime toute ma reconnaissance envers **M. Mohammed BOUBEKEUR**, ingénieur de recherche au CNRS attaché au LAGA, ainsi que **M. Imad KISSAMI**, enseignant-chercheur à l'Université Mohammed VI Polytechnique, qui ont encadré ce travail. Je les remercie pour leur confiance constante et renouvelée, pour tout ce qu'ils m'ont appris concernant l'implémentation des schémas numériques, ainsi que pour leur aide scientifique et informatique. Je tiens également à les remercier pour leurs encouragements, leur motivation et leur soutien tout au long de ma thèse.

Je tiens à exprimer ma profonde gratitude envers **M. Christophe BERTHON**, pofesseur à l'Université de Nantes et **M. Manuel J. CASTRO DÍAZ**, professeur à l'Université de Malaga, de m'avoir fait l'honneur de bien vouloir se pencher sur la lourde tâche de relire attentivement ce mémoire. Vos commentaires critiques et éclairés seront d'une grande valeur et m'encourageront à poursuivre mes recherches avec encore plus de perspicacité et d'engagement. Une fois de plus, je vous suis reconnaissant pour votre précieuse contribution à mon travail.

Je remercie chaleureusement **Mme. Laurence HALPERN** professeure émérite à l'USPN, **Mme. Marion DARBAS** professeure à l'USPN, **Mme. Linda El ALAOUI** MCF à l'USPN, **Mme. Bérangère DELOURME** MCF à l'USPN, **M. Driss OUAZAR** professeur à l'École Mohammadia d'Ingénieurs et **M. Emmanuel AUDUSSE** MCF HDR à l'USPN qui m'ont fait l'honneur de faire partie de mon jury de soutenance.

Je tiens à remercier les différentes institutions qui ont contribué à la réalisation de ma thèse. Je remercie chaleureusement l'Université Mohammed Premier, l'Université Sorbonne Paris Nord et l'Université Mohammed VI Polytechnique de m'avoir octroyé une bourse de thèse et offert des conditions de travail des plus agréables au cours de ces années de thèse.

L'essentiel de mon travail de thèse s'est déroulé entre le LAGA de l'USPN et le MSDA de l'UM6P. Je tiens à exprimer mes sincères remerciements à tous les membres du LAGA et du MSDA qui ont contribué, par leur sympathie et leur bonne humeur, à rendre mon séjour au LAGA et à l'UM6P plus qu'agréable. J'ai vécu des années de thèse très enrichissantes, tant sur le plan humain que scientifique. Ces deux laboratoires offrent à un jeune doctorant de nombreuses occasions d'échanger, que ce soit officiellement ou autour d'une tasse de café, sur une grande variété de sujets scientifiques qui peuvent être abordés au cours de sa thèse.

Je tiens encore à remercier **M. Driss OUAZAR** pour sa confiance et ses encouragements depuis ma présence à l'UM6P. Je tiens également à remercier une fois de plus mon tuteur, **M. Emmanuel AUDUSSE**, pour ses précieux conseils et ses discussions scientifiques de très haute qualité. Je suis également reconnaissant envers **M. Mohammed SEAÏD** et **M. Mofdi EL AMRANI** pour leurs conseils, leur aide scientifique, leurs encouragements et leurs recommandations depuis mon année de licence en mathématiques appliquées à la FST de Tanger. Je leur exprime ma profonde gratitude pour tout ce qu'ils ont fait pour moi. Un grand merci à **M. Abdelhafid SERGHINI** pour l'accueil chaleureux lors de ma présence à la conférence NT2A à Oujda. Je tiens également à exprimer ma reconnaissance envers **M. Abdallah BRADJI**, **M. Abdellah CHKIFA**, **Mme. Ikram CHAIRI**, **M. Ahmed RATNANI**, **M. Abdelaziz BELJADID**, **M. Nabil El Moçayd**, **M. Saad BENJELLOUN**, **M. Maher ZERZERI** et **M. Nicolas VAUCHELET**.

Je voudrais aussi adresser mes remerciements à toute l'équipe administrative du LAGA, en particulier à Monsieur **Julien BARRAL** le directeur du LAGA, **M. Jean-Philippe Domergue**, **M. Gilles DESERT**, **Mme. Yolande JIMENEZ**, **Mme. Liala SEGAREL** et **Mme. Nathalie TAVARES** pour leur accueil chaleureux lors de mes séjours au LAGA, ainsi que pour leur serviabilité et efficacité dans toutes les procédures administratives, notamment pour les missions.

Ici, je tiens à exprimer ma gratitude en ayant une pensée pour ma famille et mon entourage proche qui ont toujours fait preuve d'un soutien infaillible à mon égard. Un grand merci à ma **mère**, mon **père**, ma sœur **Mariam** et son époux **Abdellatif**, ainsi qu'à leurs enfants **Adam** et **Amani**, ainsi qu'à mon frère **Otmane**.

Enfin, je termine ces remerciements en remerciant mes amis et collègues doctorants du LAGA, de l'UMP et du MSDA, qui ont rendu cette période de thèse inoubliable. Je souhaiterais exprimer ma gratitude aussi à : **Ilias El Alami** pour son amitié, son soutien et ses remarques judicieuses sur le manuscrit de thèse du point de vue physique et linguistique; **Samar Allouch** pour son aide durant la difficile phase finale de la thèse. Elle a courageusement participé à la relecture de ce manuscrit en fournissant des commentaires pertinents du point de vue linguistique et formel; **Safae Filali** pour ses encouragements et parce qu'elle m'a donné plus qu'elle ne le pense (courage, toi aussi tu vas finir bientôt); **Ismail OUBARKA** pour son aide précieuse dans les calculs sur le cluster et son accueil chaleureux lors de mon séjour à Oujda. Je tiens à citer ici chacun de mes collègues et à les remercier : **Guilhem B.**, **Gastón Vergara. H**, **Wassim A.**, **Marwane EL K.**, **Abdelouahed O.**, **Khouya B.**, **Hasnae Z.**, **Fatima Ezzahra EL H.**, **Ilyas B.**, **Ilham A.**, **Souhail M.**, **Sanae et Safae EL M.**, **Mustapha B.**, **Amine H.**, **Hassan K.**, **Mohamed B.**, **Mohamed H.**, **Asmaa H.**, **Jihane M.**, **Mohamed M.**, **Ali B.**, **Amine K.**, **Liala B.**, **Mouna B.**, **Hugo P.**, **Élie S.**, **Arthur A.**, **Tien Tai N.**, **Elyes B.**, **Neige P.**, **Mohamed Z.**, **René P.**, **Rebecca Z.**, **Victor S.**, **Maissâ B.**, **Safae EL A.**, **Ghina N.**. Un merci particulier à **Yakin M.**, **Mohamed F.A.**, **Ali B.**, **Sefiani Y.**, **Omar Z.**, **Mehdi M.**, **Abdeslam E.**, **Soufiane S. Younes C.**, **Nabil B.**, **Anas J.** et **Anis J.** .... Cette liste n'est pas exhaustive! Toutes mes excuses à ceux que je n'ai pas cités ici.

Résumé

Cette thèse présente une étude portant sur le développement et l'efficacité du schéma des Volumes Finis Caractéristiques (FVC) sur des maillages non structurés en 2D et 3D, pour la simulation de deux types d'écoulements : les écoulements d'eau peu profonde, décrits par les équations de Saint-Venant (également connues sous le nom d'équations de l'eau peu profonde), avec des configurations monocouche et multicouches, ainsi que les écoulements de gaz, modélisés par les équations d'Euler. Le schéma FVC se révèle prometteur en offrant une précision accrue au premier ordre et une meilleure représentation des phénomènes physiques. Un code de calcul basé sur ce schéma a été développé pour résoudre les équations correspondantes, et une discrétisation bien équilibrée du schéma FVC a été proposée pour le modèle d'eau peu profonde, permettant de prédire l'application du code à des problèmes avec des termes sources importants et une irrégularité du fond.

Différents cas test ont été exécutés pour évaluer la simulation numérique des écoulements à surface libre ainsi que les écoulements de gaz. Ces évaluations ont consisté en des comparaisons entre les résultats numériques et des solutions analytiques ou des données expérimentales. Les comparaisons effectuées confirment la fiabilité, la précision, la stabilité et la robustesse du code et du schéma proposés, ainsi que l'efficacité des techniques utilisées pour traiter les conditions aux limites. Les résultats obtenus lors des différents cas test sont satisfaisants, ce qui permet d'envisager avec confiance l'application à grande échelle, notamment dans des domaines tels que le transport de polluants dans le détroit de Gibraltar.

En résumé, cette étude démontre la fiabilité du schéma FVC sur des maillages non structurés pour la résolution des équations de conservation, telles que les équations d'Euler et les équations d'eau peu profonde. Ce schéma offre une solution robuste et précise pour une large gamme d'écoulements et de configurations de fond.

Mots clés Équations de Saint-Venant; Méthode des caractéristiques; Schéma FVC bidimensionnelle; Méthode des volumes finis; Équations multicouches d'eau peu profonde; Schéma bien équilibré; Équations d'Euler; Schéma FVC en 3D; Schéma diamond; Maillages non structurés; Lois de conservation; Problème de Riemann.

Abstract

This thesis presents a study on the development and effectiveness of the Characteristic Finite Volume (FVC) scheme on unstructured 2D and 3D meshes for simulating two types of flows: shallow water flows described by the Saint-Venant equations (also known as shallow water equations) with single-layer and multilayer configurations, and gas flows modeled by the Euler equations. The FVC scheme shows promise by offering first-order accuracy and improved representation of physical phenomena. A computational code based on this scheme was developed to solve the corresponding equations, and a well-balanced discretization of the FVC scheme was proposed for the shallow water model, allowing for the prediction of the code's application to problems with significant source terms and irregular bottom topography.

Various test cases were conducted to evaluate the numerical simulation of free-surface flows and gas flows. These evaluations involved comparisons between numerical results and analytical solutions or experimental data. The performed comparisons confirm the reliability, accuracy, stability, and robustness of the proposed code and scheme, as well as the effectiveness of the techniques used to handle boundary conditions. The results obtained from the various test cases are satisfactory, providing confidence in the large-scale application of the scheme, particularly in domains such as pollutant transport in the Strait of Gibraltar.

In summary, this study demonstrates the reliability of the FVC scheme on unstructured meshes for solving conservation equations, such as the Euler equations and shallow water equations. This scheme offers a robust and accurate solution for a wide range of flows and bottom topography configurations.

Keywords Shallow water model; Method of characteristics; 2D FVC scheme; Finite volume method; Multilayer shallow water equations; Well-balanced scheme; Euler equations, 3D FVC scheme; Diamond scheme; unstructured meshes; Conversations laws; Riemann problem.

Contents

First Part
General Introduction

Chapter 1

General Introduction

Short summary

1.1 General context

Computational Fluid Dynamics (CFD) has become an essential tool in numerous technical and scientific fields. It provides a cost-effective method for modeling and simulating complex flow phenomena. This approach is particularly useful for studying intricate flows, such as those around an aircraft wing, within a pipe, or surrounding a submerged object. It is also employed to analyze gravitational and hazardous flows, including floods, landslides, and rogue waves.

CFD also plays a crucial role in the advancement of sustainable energy, notably through hydrodynamic-biological coupling, biofuel production, and applications in marine energy. It further contributes to risk management and land development by analyzing morphodynamic changes and implementing early warning systems. Thus, it has become indispensable in all branches of fluid dynamics, from aerospace propulsion to weather forecasting. For instance, water resource management is a critical issue for poverty reduction, sustainable development, and the achievement of sustainable development goals. However, approximately 2.1 billion people, or 30 % of the global population, still lack access to safe drinking water (source: https://www.who.int/news/item/18-06-2019-1-in-3-people-globally). Climate change and uncontrollable human activities have led to an increase in the frequency of floods in recent decades, making flood-related incidents more frequent. Therefore, integrated water resource management is necessary, even essential, to prevent floods and droughts, preserve the environment, and mitigate and control the impact of natural hazards, which lie at the heart of major socio-economic challenges.

Within the scientific community, computational fluid dynamics (CFD) is highly valued for its ability to provide instantaneous information about key factors such as velocity, pressure, and concentration at every point in the computational domain, often at a lower cost compared to traditional experiments. Therefore, understanding and predicting the behavior of fluids in different environments and systems have become essential for scientists and engineers. A fundamental aspect of CFD lies in the numerical scheme used to solve the governing equations of the phenomena. Thus, numerical modeling remains an indispensable tool, with numerous applications in fluid flow modeling, as mentioned before, including aerodynamics, turbomachinery

design, and combustion. For more information, we invite you to consult the following references: [1, 2, 3] . Additionally, numerical modeling of fluid flows also finds applications in water resource management, environmental protection, and ecosystems. For example, it enables the simulation of flows resulting from dam breaks, diversion of river floods to water retention areas, simulation of riverbed changes, as well as the transport of sediments or pollutants in estuarine and coastal environments. To delve deeper into these topics, you can refer to the following references: [4, 5, 6, 7, 8, 9]. Currents in water bodies such as rivers, estuaries, and coastal regions exhibit significant topographic and morphological diversity. These areas can experience significant influences, including purely advective currents, especially when a dam breaks on a smooth and frictionless surface. The phenomena observed at these spatial scales can vary from tens to thousands of meters, while the temporal scales can range from minutes to several days. Therefore, when developing a computational method aimed at handling free-surface flows or the associated models, significant challenges arise due to the intricate nature of the mathematical model and the complexity of the computational domains.

Developing accurate numerical methods for hyperbolic systems poses a significant challenge due to their inherent non-linear nature, the underlying mathematical framework, and the resulting physical phenomena they present. In particular, the existence of a shock front leads to issues such as numerical fluctuations and artificial dispersion, which arise from the standard approximation techniques used to handle the advection terms in the equations governing the transport of water masses. Moreover, it is crucial to develop methods that maintain stable states, such as the equilibrium of calm water in the shallow water system. Various strategies have been suggested to ensure that the equilibrium property is satisfied (see, for example, [10, 11, 12, 13, 14, 15, 16, 17]), and recent extensions to other types of homogeneous solvers can be found in [18, 19, 20, 21].

The existence of non-trivial steady states, where the unknowns are not constant over the domain, is one of the specificities of the shallow water system, linked to the presence of source terms. This issue has been a significant research topic since the mid-1990s, and numerous publications have been dedicated to it up to the present day, see for example, the references cited in [22, 23, 24]. In addition to the C property, there are two other categories of steady states. The first, studied by hydraulic engineers [25] because it is crucial for river flows, but less explored by numerical engineers as it involves the balance between two constant source terms, which is relatively easy to satisfy at the discrete level, corresponds to an equilibrium. The second category of steady states results from an equilibrium, in a linearized version of the system, between the pressure term and the Coriolis term. This equilibrium is known as the geostrophic balance. At large scales, atmospheric and oceanic flows are primarily perturbations of this equilibrium [26]. The extension of the ENO and WENO schemes to the shallow water equations has been studied in [27]. Unfortunately, most ENO and WENO schemes that correctly solve real flows are still computationally expensive. On the other hand, numerical methods based on kinetic reconstructions have been studied in [28], but these methods are highly complex. However, most of the aforementioned works, even though they are two-dimensional unstructured methods, lead to rather complex and computationally intensive algorithms. Other approaches are more efficient, but to our knowledge, they are limited to one-dimensional problems or two-dimensional Cartesian grids.

Our main objective in this study is to develop a class of Eulerian-Lagrangian methods that accurately solve the shallow water equations on unstructured two- and three-dimensional spatial meshes, without relying on exact or approximate Riemann solvers. The proposed scheme, Finite Volume Characteristic (FVC), belongs to the class of methods that use only the physical fluxes and averaged states in their formulations. It can be interpreted as a predictor-corrector scheme. In the corrector step, the considered equations are integrated over a spatio-temporal Eulerian control volume, while in the predictor step, the variables of the equation system are rewritten in

an advective form and integrated along the characteristics defined by the advection velocity field. This approach has demonstrated its effectiveness through several test cases and benchmarks presented in the works [29, 30, 31, 32]. However, the authors of these three articles limited themselves to the formalism of Cartesian meshes, whereas, as mentioned earlier, real-world problems are characterized by significant topographic and geometric complexity, thereby limiting the applicability of this formalism. A more in-depth study of the accuracy of this finite volume discretization method on unstructured meshes has always been the objective of these works (see the conclusions of [29] and [30]). Consequently, the unstructured finite volume method not only guarantees mass conservation, which is an important property in fluid flow calculations, but also enables the accurate representation of the complex geometry of the computational domain. For these reasons, we propose an extension of this scheme to an unstructured mesh. It is worth noting that a convergence analysis of the method for a scalar equation was conducted in this work [31], and the results of this analysis will be presented in the following sections of this manuscript.

Another strength of the scheme is that the Jacobian matrix of the system, which is the cause of the sluggishness in many approximation schemes, does not play a role in the computation. Additionally, numerous approximation schemes in the context of conservation laws require a solver for the Riemann problem at each time step in order to reconstruct the numerical flux, which is completely avoided in our FVC scheme, as mentioned earlier. In simple terms, this approach combines the method of characteristics with the finite volume method. Unlike traditional finite volume methods, this technique integrates our equations along the characteristic curves, which facilitates the computation of numerical fluxes.

We have observed several advantages of this approach compared to other solutions for conservation laws. Firstly, a key characteristic of such an Eulerian-Lagrangian finite volume scheme is its ability to satisfy the conservation property, resulting in numerical solutions free from spurious oscillations. Secondly, it achieves robust stability and high accuracy for numerical solutions containing shocks or discontinuities, along with efficient CPU performance.

1.2 Motivation and purpose of this thesis

In the context of the growing demand for accurate and efficient numerical simulation techniques for studying fluid dynamics, fluid flows play a central role in various industrial applications and natural systems. For example, this includes the transport of sediment in rivers and dams, as well as the transportation of industrial materials (such as phosphates, phosphogypsum, etc.) through pipelines, the operation of turbines and pumps, large-scale atmospheric movements, etc.

The main objective of this thesis is therefore to study and implement the FVC scheme on unstructured grids, in order to improve the applicability of the scheme to real simulations and problems. The FVC scheme is recognized for its ability to accurately and efficiently handle flows with discontinuities, shocks, and complex boundary phenomena.

By focusing on fluid flow models, this thesis aims to develop the FVC scheme in its general version and demonstrate its robustness and efficiency in simulating complex phenomena and solving complicated equations, such as the multilayer system. The goal is to contribute to a better understanding of the underlying physical phenomena while providing accurate results for performance prediction and optimization of industrial systems.

Within the framework of this study, several key objectives have been defined to deepen the research. The main objective of this work is to study and develop the FVC scheme by combining the advantages of Eulerian-Lagrangian approaches to achieve accurate and robust results, even

in complex situations.

Another major objective of this thesis is to implement this method on unstructured grids. This approach will allow for the treatment of complex geometries with great flexibility, which is a significant advantage. However, adapting the FVC scheme to unstructured grids will require a thorough study of appropriate algorithms and discretization techniques. This represents a key objective of this research as it will enhance the accuracy and efficiency of real-world simulations.

To move towards three-dimensional modeling, it is necessary to overcome the limitations of the Saint-Venant equations, which are specifically designed for two-dimensional flows. In this context, we have opted for the use of three-dimensional Euler equations to account for phenomena occurring in three-dimensional flow.

Finally, this study aims to evaluate the performance and efficiency of the developed scheme in the numerical simulation of fluid flow models. To achieve this, case studies will be utilized, and comparisons will be made with other existing methods. The obtained results will provide valuable insights into the applicability and potential advantages of the FVC scheme in solving complex problems related to fluid flows.

To accomplish these objectives, several steps will be undertaken. Firstly, a comprehensive review of the scientific literature will be conducted to understand the theoretical foundations of the FVC scheme and Eulerian-Lagrangian approaches. This literature review will also identify different existing methods for simulating fluid flows and compare them to the FVC scheme.

Next, special attention will be given to adapting the FVC scheme to unstructured grids. This will require an in-depth study of discretization techniques suitable for these grids. Advanced numerical methods will be explored to ensure accurate and efficient resolution of flow equations on these grids.

Once the FVC scheme has been successfully implemented on unstructured grids, representative test cases will be selected to evaluate the model's performance. Numerical simulations will be conducted, and the results will be analyzed in terms of accuracy, efficiency, and robustness. Comparisons with other existing methods will also be made to demonstrate the potential advantages of the FVC scheme as well as its limitations.

1.3 Contents of this work

This manuscript consists of six chapters organized into five parts. Below, we present a chapter-wise summary of the conducted research.

1st Part: General Introduction

Chapter 1: General Introduction

In this chapter, we have addressed the general context of the limitations in the use of numerical schemes in the fields of modeling and scientific computing, as well as in the field of CFD. We have highlighted the current difficulties and limitations encountered in the development of these schemes, particularly regarding the accuracy, stability, and efficiency of the obtained results. Furthermore, we have discussed the motivations that have driven us to undertake this thesis, which mainly involve overcoming these issues and proposing new approaches to enhance the performance of numerical schemes. We have also outlined the specific objectives we have set for ourselves, such as developing more accurate, robust, and faster methods and applying them to practical problems in modeling and scientific computing, with the ultimate goal of enhancing the understanding and prediction of physical phenomena.

2^{nd} Part: Mathematical and Numerical Formulation of the Treated Models

Chapter 2: General presentation of the treated models

In this chapter, we have discussed hyperbolic systems from a theoretical perspective in a general manner. We have explored the fundamental concepts of these systems and their implications. Next, we have presented several examples of PDEs that have been treated and numerically solved. Among the studied models, we have examined the shallow water equations, which allow for the analysis of solute dispersion carried by a fluid flow. We have also studied two-dimensional multi-layer equations used to model flows with vertical density variations. Finally, we have addressed the three-dimensional Euler equations, which describe the motion of an incompressible and non-viscous fluid. These examples illustrate the diversity and relevance of the hyperbolic systems studied in this chapter.

Chapter 3: Generalities on Numerical Methods

In this chapter, we began by addressing general aspects of finite volume numerical methods. We then provided an overview of the context of the proposed method in its 1D version, presenting the associated stability and convergence results. This preliminary analysis lays the necessary foundations for a thorough understanding of the two-dimensional and three-dimensional numerical schemes presented in subsequent chapters. By exploring the results obtained in this initial context, we will be able to better grasp the more complex aspects of the method in higher dimensions, enabling us to deepen our understanding and delve further into our study.

3^{rd} Part: FVC Scheme on Unstructured Meshes in Multiple Spatial Dimensions

Chapter 4: 2D FVC scheme on unstructured meshes: application to free surface flows in shallow water

This chapter provides a detailed exposition of the techniques used to construct the 2D version of the FVC scheme adapted to unstructured meshes, along with three specific applications. Firstly, we explore the application of the scheme to shallow water equations. Secondly, we address the solute transport model through fluid flow, focusing on the propagation and dispersion of dissolved substances in fluids. Finally, we examine the two-dimensional multilayer shallow water equations, which investigate the complex interactions between different fluid levels in shallow depth systems. Concurrently, we present key numerical results obtained for solving the problems, phenomena, and challenges associated with these equations.

Chapter 5: 3D FVC scheme on unstructured meshes: application to compressible Euler equations

This chapter explores a three-dimensional extension of the FVC approach, which maintains a formulation suitable for unstructured meshes. It also presents a specific application to the Euler equations, along with crucial numerical results for solving the problems, phenomena, and challenges associated with these equations.

4^{th} Part: Conclusions and Perspectives

Chapter 6: Conclusions and Perspectives

In conclusion, this section will consolidate the knowledge gained during the study and provide prospects for future research. It will thus serve as a clear recapitulation of the obtained results and act as a guide to steer forthcoming investigations.

Appendix

In this section, I have compiled all the supplementary formulas and calculations that lead to the formulas used in chapters 3, 4, and 5. This provides a centralized reference for readers and facilitates the understanding and application of the concepts discussed in these crucial chapters.

5^{th} Part: Bibliographical References

The final section of this study encompasses all the bibliographic references utilized in this research. Additionally, an exhaustive list of publications produced during my doctoral period is also included, attesting to the dedication and expertise gained throughout this investigation.

Second Part

Mathematical and Numerical Formulation of the Considered Models

Chapter 2

General presentation of the considered models

Short summary

2.1 Generalities of hyperbolic systems

The theory of numerical methods for nonlinear hyperbolic partial differential equations (PDEs), or conservation laws, remains one of the great successes of numerical analysis. Constructing schemes for nonlinear hyperbolic equations requires a good understanding of numerical analysis and the theory of nonlinear hyperbolic equations. Accurate solution methods have been developed using the solutions of these equations.

The development of hyperbolic PDE theory in recent years has been driven by its growth in applications such as supersonic aerodynamics, wave propagation in elastic solids, thermonuclear explosions, gravitational flows, morphodynamic evolution, and pollutant transport. For example, in pollutant transport in water, the shallow water equations (2.20) are coupled with the convection-diffusion equation (2.35), which can also represent a challenging model to handle, especially as these terms can affect the numerical methods for hyperbolic equations.

The fundamental difficulty of nonlinear hyperbolic PDEs lies in the fact that their solutions develop singularities, commonly called shocks or shock waves. With the development of these discontinuities, the uniqueness of the solution is no longer guaranteed. The mathematical problem is therefore to introduce some restrictions on the class of solutions to ensure the existence of a unique solution that corresponds well to the physical problem being studied. In this section, we introduce some definitions and theorems related to hyperbolic equations. For more detailed presentation, we recommend the reader to consult the following bibliographies [33, 34, 35, 36].

2.1.1 Hyperbolic conservation laws

Conservation law systems are partial differential equations that depend on time and are typically nonlinear. In d-dimensional space, these equations have the following general form:

$$\frac{\partial \mathbf{u}(x,t)}{\partial t} + \sum_{j=1}^{d} \frac{\partial \mathbf{f}_j(\mathbf{u}(x,t))}{\partial x_j} = 0, \quad x = (x_1, x_2, \cdots, x_d) \in \mathcal{D} \subset \mathbb{R}^d, t > 0, \tag{2.1}$$

where, $\mathbf{u} : \mathcal{D} \times \mathbb{R}^+ \longrightarrow \Omega$ is a p-dimensional vector of conserved quantities or state variables, such as mass, momentum, and energy in the case of fluid dynamics problems. Ω is a bounded open subset of $\mathbb{R}^p$. The functions $\mathbf{f}_j$ $(1 \leq j \leq d)$, called flux functions, are "sufficiently smooth" and are defined from Ω to $\mathbb{R}^p$. The system (2.1) must be supplemented with initial conditions

$$\mathbf{u}(x,0) = \mathbf{u}_0(x), \tag{2.2}$$

and possibly with boundary conditions on a bounded spatial domain.

2.1.1.1 Hyperbolicity

Let $A_j(\mathbf{u})$ the Jacobian matrix of the function $\mathbf{f}_j(\mathbf{u})$:

$$A_j(\mathbf{u}) = \left(\frac{\partial \mathbf{f}_{ij}}{\partial \mathbf{u}_k}(\mathbf{u})\right)_{1 \leqslant i,k \leqslant p}, \quad j = 1, \cdots, d. \tag{2.3}$$

The system (2.1) is said to be hyperbolic if for all $\mathbf{n} = (n_1, \cdots, n_d) \in \mathbb{R}^d$, the matrix $A(\mathbf{u}, \mathbf{n}) = \sum_{j=1}^{d} n_j A_j(\mathbf{u})$ is diagonalizable and all its eigenvalues are real. Furthermore, if these eigenvalues are distinct, the system is said to be strictly hyperbolic. We will order these eigenvalues in increasing order

$$\lambda_1(\mathbf{u}, \mathbf{n}) < \lambda_2(\mathbf{u}, \mathbf{n}) < \cdots < \lambda_p(\mathbf{u}, \mathbf{n}), \tag{2.4}$$

where $\lambda_j(\mathbf{u}, \mathbf{n})$ is the j^{th} eigenvalue of $A(\mathbf{u}, \mathbf{n})$.

2.1.1.2 Weak solutions and entropy condition

Let us consider the Cauchy problem, defined by the following conservation law

$$\begin{cases} \dfrac{\partial \mathbf{u}}{\partial t} + \dfrac{\partial \mathbf{f}(\mathbf{u})}{\partial x} = 0 & x \in \mathcal{D} \subset \mathbb{R}, t > 0, \\ \mathbf{u}(x,0) = \mathbf{u}_0(x) & x \in \mathcal{D}, \end{cases} \tag{2.5}$$

where $\mathbf{f} : \Omega \longrightarrow \mathbb{R}$ and $\mathbf{u} : \mathcal{D} \times \mathbb{R}^+ \longrightarrow \Omega$.

Definition 2.1.1. *Let $\boldsymbol{u}_0 \in \mathcal{L}^\infty_{loc}(\mathcal{D})$[1], a function $\boldsymbol{u} \in \mathcal{L}^\infty_{loc}(\mathcal{D} \times \mathbb{R}^+)$ is a weak solution of the Cauchy problem (2.5) if, for all $\phi \in \mathcal{C}^1_0(\mathcal{D} \times \mathbb{R}^+)$, we have*

$$\int_{\mathcal{D}} \int_{\mathbb{R}^+} \left(\boldsymbol{u} \frac{\partial \phi}{\partial t} + \boldsymbol{f}(\boldsymbol{u}) \frac{\partial \phi}{\partial x}\right) dt dx + \int_{\mathcal{D}} \boldsymbol{u}_0(x) \phi(x,0) dx = 0. \tag{2.6}$$

By construction, any classical solution of problem (2.5) is a weak solution. Moreover, it is shown by integration by parts of (2.6) that weak solutions satisfy (2.5) in the classical sense except along a finite number of parametric curves $(t, \xi(t))$ in the (x,t) plane. It can be shown that on each of these parametric curves (discontinuity curves), the following Rankine-Hugoniot

[1] $\mathcal{L}^\infty_{\text{loc}}(\mathcal{D})$ is the space of locally bounded functions.

condition must be satisfied:
Let

$$\begin{aligned} \mathbf{u}_l &= \lim_{\delta \to 0^+} \mathbf{u}(\xi - \delta t), \\ \mathbf{u}_r &= \lim_{\delta \to 0^+} \mathbf{u}(\xi + \delta t), \end{aligned} \tag{2.7}$$

the values immediately to the left and right of the discontinuity. Define the shock speed by $s = \frac{d\xi(t)}{dt}$, then s must satisfy the condition

$$s\left(\mathbf{u}_r - \mathbf{u}_l\right) = \mathbf{f}\left(\mathbf{u}_r\right) - \mathbf{f}\left(\mathbf{u}_l\right). \tag{2.8}$$

Instead of using the formulation (2.6) to decide whether a function $\mathbf{u}$ is a weak solution or not, we can use the Rankine-Hugoniot condition (2.8). We can then state the following theorem:

Theorem 2.1.1. *Let $\boldsymbol{u} : \mathcal{D} \times \mathbb{R}^+ \longrightarrow \mathbb{R}$, $\mathcal{C}^1$ be a piecewise function. $\boldsymbol{u}$ is a weak solution of (2.5) if and only if it satisfies the following conditions:*
i) $\boldsymbol{u}$ is a classical solution of (2.5) where it is $\mathcal{C}^1$.
ii) At a discontinuity, $\boldsymbol{u}$ satisfies the Rankine-Hugoniot condition (2.8).

2.1.1.3 Existence of a physical solution

As previously mentioned, there are situations where the weak solution is not unique. In this case, it becomes necessary to establish additional criteria to determine the "correct" weak solution (in the physical sense) to the problem. For specific nonlinear systems appearing in physics, there exist criteria, such as the second law of thermodynamics, that allow for the selection of a unique solution among the weak solutions.

▶ Viscous limit solutions

The entropic solution of (2.1) is the solution that is obtained from the limit as ϵ approaches zero of the solution $\mathbf{u}^\epsilon$ of the corresponding viscous parabolic problem

$$\begin{cases} \dfrac{\partial \mathbf{u}^\epsilon}{\partial t} + \displaystyle\sum_{j=1}^{d} \frac{\partial \mathbf{f}_j\left(\mathbf{u}^\epsilon\right)}{\partial x_j} = \epsilon \Delta \mathbf{u}^\epsilon & x \in \mathcal{D}, t > 0, \\ \mathbf{u}^\epsilon(x, 0) = \mathbf{u}_0(x) & x \in \mathcal{D}. \end{cases} \tag{2.9}$$

Except for the scalar case and some particular systems, it is not always possible to show the existence of this limit, see [37]. Nevertheless, this provides a good criterion for choosing a solution by introducing the notion of entropy due to Lax. The entropy condition is defined as the condition requiring that the solution of (2.1) is the limit solution of the problem (2.9). A weak solution satisfying the entropy condition will be called an entropy weak solution. In the scalar case, a theorem of uniqueness of the entropy weak solution was proved by Kružkov [38]. The entropy condition can be written in different ways. One way to approach this is to define an entropy function $\eta(\mathbf{u})$, which requires a new conservation law to be fulfilled for smooth solutions, while for discontinuous solutions, the law becomes an inequality.

Definition 2.1.2. *A regular convex function $\eta : \Omega \longrightarrow \mathbb{R}$ is said to be the entropy of the system (2.1) if there exist a d real and regular functions $G_j : \Omega \longrightarrow \mathbb{R}$ such that,*

$$\forall \boldsymbol{u} \in \Omega, \quad \eta'(\boldsymbol{u}) \boldsymbol{f}_j'(\boldsymbol{u}) = G_j'(\boldsymbol{u}), \quad j = 1, \cdots, d. \tag{2.10}$$

The functions $G_j(\boldsymbol{u})$ for $1 \leq j \leq d$ are called entropy fluxes.

Corollary 2.1.1. *The regular solutions of (2.1) satisfy*

$$\frac{\partial \eta(\boldsymbol{u})}{\partial t} + \sum_{j=1}^{d} \frac{\partial G_j(\boldsymbol{u})}{\partial x_j} = 0. \tag{2.11}$$

Definition 2.1.3. *We say that $\boldsymbol{u}$, a weak solution of system (2.1), is an entropic solution of this system if for every convex entropy η of this system, we have*

$$\frac{\partial \eta(\boldsymbol{u})}{\partial t} + \sum_{j=1}^{d} \frac{\partial G_j(\boldsymbol{u})}{\partial x_j} \leq 0, \tag{2.12}$$

in the sense of distributions.

Theorem 2.1.2. *Suppose that system (2.1) has a convex entropy η with entropy fluxes G_j. Let $(\boldsymbol{u}^\epsilon)$ be a sequence of regular solutions of (2.9) such that*
i) $\exists C > 0$ independent of ϵ such that $||\boldsymbol{u}^\epsilon||_{\mathcal{L}^\infty(\mathcal{D}\times\mathbb{R}^+)} \leq C$.
ii) $\boldsymbol{u}^\epsilon \longrightarrow \boldsymbol{u}$ almost everywhere in $\mathcal{D}\times\mathbb{R}^+$ as $\epsilon \longrightarrow 0$.
Then $\boldsymbol{u}$ is a solution of (2.1) satisfying the entropy inequality (2.12) in the sense of distributions on $\mathcal{D}\times\mathbb{R}^+$.

Let's examine the scalar case ($p = 1, d \geq 1$) of the multidimensional conservation law (2.1). We have seen that a function $\mathbf{u}$ is the unique solution of (2.1) if it satisfies
i) the definition of a weak solution,
ii) the entropy condition.
In some situations, it is preferable to have only one condition instead of the two mentioned above. Here we give the definition of Kružkov [38], which combines *i*) and *ii*) and represents a mechanism for identifying the unique physical solution of (2.1).

Definition 2.1.4. *$\boldsymbol{u}$ is a weak entropy solution of (2.1) if for any constant a and for any $\phi \in \mathcal{C}_0^1(\mathcal{D}\times\mathbb{R}^+), \phi \geq 0$, the following inequality holds*

$$\begin{aligned} &\int_{\mathcal{D}}\int_{\mathbb{R}^+} \left(|\boldsymbol{u}-a| \frac{\partial \phi}{\partial t} + \operatorname{sign}(\boldsymbol{u}-a) \sum_{j=1}^{d} \left(\boldsymbol{f}_j(\boldsymbol{u}) - \boldsymbol{f}_j(a) \right) \frac{\partial \phi}{\partial x_j} \right) dt dx_1 \cdots dx_d \\ &+ \int_{\mathcal{D}} |\boldsymbol{u}_0 - a|\, \phi(x_1, \cdots, x_d, 0)\, dx_1 \cdots dx_d \geq 0. \end{aligned} \tag{2.13}$$

2.1.1.4 1D Riemann problem

The Riemann problem involves studying the following equation

$$\begin{cases} \dfrac{\partial \mathbf{u}}{\partial t} + \dfrac{\partial \mathbf{f}(\mathbf{u})}{\partial x} = 0 \quad \text{for } x \in \mathcal{D} \subset \mathbb{R}, t > 0, \\ \mathbf{u}(x,0) = \mathbf{u}_0(x) = \begin{cases} \mathbf{u}_l & \text{if } x \leq 0, \\ \mathbf{u}_r & \text{if } x > 0. \end{cases} \end{cases} \tag{2.14}$$

This problem was first studied by Riemann in gas dynamics (the "shock tube problem"): a tube filled with gas is separated into two sections by a membrane. The gas has a higher density and pressure in the first half of the tube than in the second, and zero velocity everywhere. The question is: happens if the membrane is removed or broken at $t = 0$. This situation is modeled

by the one-dimensional Euler equations, and the solution is obtained by solving the Riemann problem for this system of conservation laws.

For scalar conservation laws, the Riemann problem is relatively simple to construct. The solution is self-similar $\mathbf{u} = \mathbf{u}(\xi)$ where $\left(\xi = \frac{x}{t}\right)$ satisfies $\mathbf{u}(-\infty) = \mathbf{u}_l$ and $\mathbf{u}(+\infty) = \mathbf{u}_r$. Between the states $\mathbf{u}_l$ and $\mathbf{u}_r$, $\mathbf{u}$ decomposes into two types of waves: shock waves and rarefaction waves.

► **Shock waves:** A shock wave is an elementary wave consisting of a simple discontinuity that satisfies the Rankine-Hugoniot condition and the entropy condition, i.e., a wave of the form.

$$\mathbf{u}(x,t) = \begin{cases} \mathbf{u}_l & \text{if } x \leq st, \\ \mathbf{u}_r & \text{if } x > st, \end{cases} \tag{2.15}$$

where s is given by

$$s = \frac{f(\mathbf{u}_r) - f(\mathbf{u}_l)}{\mathbf{u}_r - \mathbf{u}_l}.$$

To determine if the shock wave (2.15) is an entropic solution to the Riemann problem, two cases must be considered

$$\begin{cases} \textit{Case 1: } \mathbf{u}_l < \mathbf{u}_r, \\ \text{in this case, } \mathbf{u}(\text{x, t}) \text{ is a solution if } \mathbf{f}(\mathbf{u}) \geq \mathbf{f}(\mathbf{u}_l) + s(\mathbf{u} - \mathbf{u}_l) \\ \text{for all } \mathbf{u} \in (\mathbf{u}_l, \mathbf{u}_r), \\ \\ \textit{Case 2: } \mathbf{u}_l > \mathbf{u}_r, \\ \text{in this case, } \mathbf{u}(\text{x, t}) \text{ is a solution if } \mathbf{f}(\mathbf{u}) \leq \mathbf{f}(\mathbf{u}_l) + s(\mathbf{u} - \mathbf{u}_l) \\ \text{for all } \mathbf{u} \in (\mathbf{u}_r, \mathbf{u}_l), \end{cases} \tag{2.16}$$

► **Rarefaction wave:** it is a continuous solution of (2.14). It takes the form

$$\mathbf{u}(x,t) = \begin{cases} \mathbf{u}_l & \text{if } \xi \leq \mathbf{f}'(\mathbf{u}_l), \\ v(\xi) & \text{if } \mathbf{f}'(\mathbf{u}_l) < \xi \leq \mathbf{f}'(\mathbf{u}_r), \\ \mathbf{u}_r & \text{if } \xi > f'(\mathbf{u}_r), \end{cases} \tag{2.17}$$

where $v(\xi)$ is given by the equation

$$\mathbf{f}'(v(\xi)) = \xi. \tag{2.18}$$

The speed of the rarefaction wave is given by $\mathbf{f}'(v(\xi))$, which must be an increasing function. If we derive (2.18), we find that

$$\mathbf{f}''(v(\xi))v'(\xi) = 1.$$

In a rarefaction wave, $\mathbf{f}'$ and v' must have the same sign. As for the shock wave solution, two cases must be considered

$$\begin{cases} \textit{Case 1: } \mathbf{u}_l < \mathbf{u}_r, \\ \text{the rarefaction wave (2.17) is a solution of (2.14) if } \mathbf{f}''(v) > 0 \\ \text{for all } v \in (\mathbf{u}_l, \mathbf{u}_r), \\ \\ \textit{Case 2: } \mathbf{u}_l > \mathbf{u}_r, \\ \text{the rarefaction wave (2.17) is a solution of (2.14) if } \mathbf{f}''(v) < 0 \\ \text{for all } v \in (\mathbf{u}_r, \mathbf{u}_l), \end{cases} \tag{2.19}$$

2.2 The physical models considered

In this section, we will describe some models (PDEs) that will be used to validate our two-dimensional and three-dimensional FVC scheme. The first model consists on the Saint-Venant equations [39], also known as shallow water equations, will be used to describe free surface flows in shallow water. Despite their age, the Saint-Venant equations remain relevant in the field of maritime or river hydraulics. They are derived by vertically integrating the Navier-Stokes equations under several assumptions [40, section 2.2]. By coupling these equations with convection-diffusion equations for one or more tracers released in the water, we obtain equations that can be used to model the transport and dispersion of a passive tracer (e.g., nutrients, pollutants, temperature, etc.) using a fluid flow. For the three-dimensional case, we will focus on the three-dimensional Euler equations, which can simulate the dynamics of non-viscous gases. Using these equations, we aim to demonstrate the effectiveness of the FVC scheme in capturing fluid dynamics in 3D.

2.2.1 Shallow water equations

The 2D shallow water system for the free-surface flow with the Coriolis effect and bottom friction stress is formulated as

$$\begin{cases} \partial_t h + \nabla \cdot (h\mathbf{u}) = 0, \\ \partial_t h\mathbf{u} + \nabla \cdot (h\mathbf{u} \otimes \mathbf{u}) + \dfrac{1}{2}\boldsymbol{\nabla}(gh^2) = -gh\boldsymbol{\nabla}Z - f_c \times h\mathbf{u}^{\perp} - r(h,\mathbf{u}), \end{cases} \tag{2.20}$$

where the unknowns are always the water height $h(t,x,y) \geqslant 0$ and the horizontal velocity mean $\mathbf{u}(t,x,y) := (u,v)^T(t,x,y) \in \mathbb{R}^2$. The parameter f_c is linked to the angular speed of the earth's rotation, g is the gravitational acceleration, $r(h,\mathbf{u})$ has various expressions, for example, the asymptotic derivation mentioned in [41] leads the authors to consider, at first order, a linear friction term. The quadratic form in the Manning-Strickler velocity is nevertheless the most widely used in river flow applications [42, 43], so in this study we use the latter approximation such that the bottom's friction term $r(h,\mathbf{u})$ is given by, $r(h,\mathbf{u}) = (r_{f_x}, r_{f_y}) := \eta^2 g h^{-1/3}|\mathbf{u}|\mathbf{u}$, η being the Manning roughness. The function $Z(x,y)$ represents the bottom profile, see Fig 2.1 below.

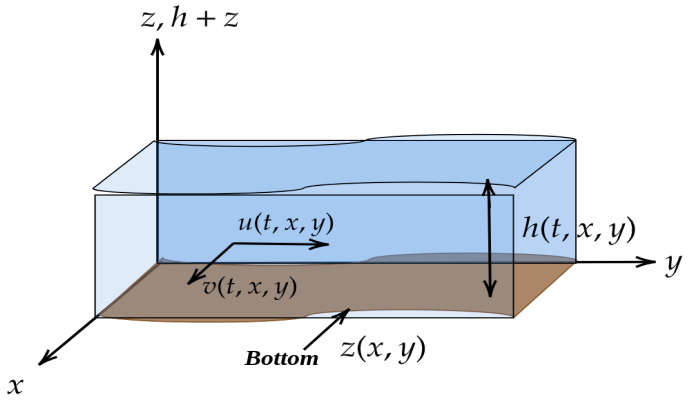

Fig 2.1. Illustration of shallow water model variables.

In order to give the reader a global view of the shallow water system we propose to add other aspects the the right-hand side of the second equation of system (2.20). For example, we can

add the wind's effect on the free surface, i.e., in the case where the wind is moving with high velocity there is the friction term $\tau(h, \breve{\mathbf{u}})$ which is not negligible. The viscosity or diffusion term can also be added if we want to solve turbulence problems in free surface flow. In this case, the second equation of the system (2.20) becomes

$$\partial_t h\mathbf{u} + \nabla \cdot (h\mathbf{u} \otimes \mathbf{u}) + \frac{1}{2}\boldsymbol{\nabla}(gh^2) = -gh\boldsymbol{\nabla}Z - f_c \times h\mathbf{u}^{\perp} - r(h, \mathbf{u}) + \tau(h, \breve{\mathbf{u}}) + \nu\overrightarrow{\triangle}h\mathbf{u}, \quad (2.21)$$

where $\tau(h, \breve{\mathbf{u}}) = (\tau_{s_x}, \tau_{s_y}) := \frac{1}{2}\breve{C}_f|\breve{\mathbf{u}}|\breve{\mathbf{u}}$, in which $\breve{\mathbf{u}} = (\breve{u}, \breve{v})^T$ represents the wind speed and $\breve{C}_f$ is the coefficient of wind friction with water. ν is the diffusion coefficient associated with the term, $\overrightarrow{\triangle}h\mathbf{u} := (\triangle(hu),\ \triangle(hv))^T$.
In this study we will not deal with these two terms ($\tau(h, \breve{\mathbf{u}})$ and $\nu\overrightarrow{\triangle}h\mathbf{u}$), otherwise the implementation of these terms is simple.
For simplicity, we rewrite system (2.20) in a vector form

$$\partial_t W + \nabla \cdot \mathbb{F}(W) = S(W) + R(W), \quad (2.22)$$

where $\mathbb{F}(W) = (F(W),\ G(W))^T$. Such that, we note A^T is the transpose of a matrix A,

$$W = \begin{pmatrix} h \\ hu \\ hv \end{pmatrix}, \quad F(W) = \begin{pmatrix} hu \\ hu^2 + \frac{1}{2}gh^2 \\ huv \end{pmatrix}, \quad G(W) = \begin{pmatrix} hv \\ huv \\ hv^2 + \frac{1}{2}gh^2 \end{pmatrix},$$

$$S(W) = \begin{pmatrix} 0 \\ -gh\partial_x Z \\ -gh\partial_y Z \end{pmatrix} \text{ and } R(W) = \begin{pmatrix} 0 \\ f_c hv - r_{f_x} \\ -f_c hu - r_{f_y} \end{pmatrix}.$$

Note that system (2.22) has to be solved in a bounded spatial domain Ω, with given boundary and initial conditions. In practice, these conditions depend on the phenomenon studied (see Chapter 4 where numerical examples are discussed).

2.2.1.1 Properties of the system

Here we present some important properties of the shallow water equation (2.20). The present numerical approach will ensure that the approximate solutions satisfy, when possible, all these properties.

2.2.1.1.1 Eigenstructure The shallow water system (2.20) can be written in a quasi-linear form

$$\partial_t W + \mathbf{J}_F \partial_x W + \mathbf{J}_G \partial_y W = S(W) + R(W), \quad (2.23)$$

where $\mathbf{J}_F$ and $\mathbf{J}_G$ are the Jacobian matrices of the fluxes

$$\mathbf{J}_F = \begin{pmatrix} 0 & 1 & 0 \\ gh - u^2 & 2u & 0 \\ -uv & v & u \end{pmatrix} \quad \text{and} \quad \mathbf{J}_G = \begin{pmatrix} 0 & 0 & 1 \\ -uv & v & u \\ gh - v^2 & 0 & 2v \end{pmatrix}. \quad (2.24)$$

Using conventional techniques [33], we establish the definition $\mathbf{J}_{\mathbb{F}}((\alpha_1, \alpha_2)) := \alpha_1\mathbf{J}_F + \alpha_2\mathbf{J}_G$. For any $(\alpha_1, \alpha_2) \in \mathbb{R}^2$, the matrix $\mathbf{J}_{\mathbb{F}}((\alpha_1, \alpha_2))$ exhibits three eigenvalues given by: $\lambda_1 = \alpha_1 u + \alpha_2 v$, $\lambda_2 = \alpha_1 u + \alpha_2 v + \|(\alpha_1, \alpha_2)\|\sqrt{gh}$, and $\lambda_3 = \alpha_1 u + \alpha_2 v - \|(\alpha_1, \alpha_2)\|\sqrt{gh}$.

The shallow water system is a first-order hyperbolic system of balance laws, and it is also strictly hyperbolic for $h > 0$. The Jacobian matrix associated with the normal flow is defined as

$$\mathbf{J}_{\mathbb{F}_\mathbf{n}} = \mathbf{J}_F n_x + \mathbf{J}_G n_y = \begin{pmatrix} 0 & n_x & n_y \\ ghn_x - uu_\eta & u_\eta + un_x & un_y \\ ghn_y - vu_\eta & vn_x & u_\eta + vn_y \end{pmatrix}, \tag{2.25}$$

where $\mathbf{n} = (n_x, n_y)^t$ is the normal vector and $u_\eta = un_x + vn_y$, The matrix $\mathbf{J}_{\mathbb{F}_\mathbf{n}}$ is diagonalizable such that

$$\mathbf{J}_{\mathbb{F}_\mathbf{n}} = \mathbf{P}_\mathbf{n} \mathbf{\Lambda}_\mathbf{n} \mathbf{P}_\mathbf{n}^{-1} \tag{2.26}$$

where

$$\mathbf{\Lambda}_\mathbf{n} = \begin{pmatrix} u_\eta - \sqrt{gh} & 0 & 0 \\ 0 & u_\eta & 0 \\ 0 & 0 & u_\eta + \sqrt{gh} \end{pmatrix} \text{ and } \mathbf{P}_\mathbf{n} = \begin{pmatrix} 1 & 0 & 1 \\ u - \sqrt{gh}n_x & -n_y & u + \sqrt{gh}n_x \\ v - \sqrt{gh}n_y & n_x & v + \sqrt{gh}n_y \end{pmatrix}, \tag{2.27}$$

2.2.1.1.2 Rotational invariance The two dimensional homogeneous shallow water equations (2.22) satisfy

$$\mathbf{H} \equiv \mathbf{n} \cdot [F(W), G(W)] = \mathbf{T}^{-1} F(\mathbf{T}(W)), \tag{2.28}$$

for all vectors W and for all real angles θ, or equivalently, normal directions of the surface Ω. Here $\mathbf{T} = \mathbf{T}(\theta)$ is a rotation matrix and $\mathbf{T}^{-1}(\theta)$ is its inverse, given respectively as

$$\mathbf{T} = \begin{pmatrix} 1 & 0 & 0 \\ 0 & \cos\theta & \sin\theta \\ 0 & -\sin\theta & \cos\theta \end{pmatrix} \quad \text{and} \quad \mathbf{T}^{-1} = \begin{pmatrix} 1 & 0 & 0 \\ 0 & \cos\theta & -\sin\theta \\ 0 & \sin\theta & \cos\theta \end{pmatrix}. \tag{2.29}$$

Proof. We invite the reader to consult [44, proposition 3.10.1 p 66]. □

2.2.1.1.3 Equilibrium An important property is related to the source terms, and the most studied balance family is related to the presence of topography's source term: the shallow water system admits non-trivial steady-states. They are characterized by

$$\nabla \cdot \mathbf{hu} = 0, \quad \mathbf{\nabla}\left(\frac{|\mathbf{u}|^2}{2} + g(h + Z)\right) - \begin{pmatrix} v \\ -u \end{pmatrix} \mathbf{\nabla} \times \mathbf{u} = 0, \tag{2.30}$$

where the operator $\mathbf{\nabla}\times$ is defined from $\mathbb{R}^2$ into $\mathbb{R}$, it is the scalar rotational defined by $\mathbf{\nabla} \times \mathbf{u} = \partial_x v - \partial_y u$. For flows in complex geometry, it seems very difficult to numerically preserve all two-dimensional balances, except those that correspond to an area at rest and whose characterization is independent of the dimension considered.

$$h + Z = constant, \qquad \mathbf{u} = 0. \tag{2.31}$$

This particular stationary state, known as the resting lake state, is important because many flows in lakes or coastal bays are perturbations around this balance. Therefore it is essential to prevent numerical anomalies from disrupting the approached solution. However, the preservation of the stationary states at the numerical level is not obvious to be achieved, and even the simplest one is not an exception. In fact, (2.31) corresponds to a balance between flow terms and source

terms, whose discretizations are not correlated. There are other categories of stationary states resulting from an equilibrium between the pressure term and the Coriolis term, i.e.,

$$g\boldsymbol{\nabla} h + f_c \times \mathbf{u} = 0. \tag{2.32}$$

For example, at large scales, the atmospheric and oceanic flows bear most of the time the perturbations of this stationary state [26], therefore it is also very important to be represented in the approached solution. This balance adds a complexity to the balance of the lake at rest because it involves non-zero speeds.

2.2.1.1.4 Entropy inequality The physical system we are dealing with here is a system of conservation laws, so the energy aspect is very important in this type of system. Thus we propose to say a few words on this point in order to provide insight into the treatment of this notion when constructing approximate solutions under the constraint of preserving certain properties, for example, the decay of energy in the presence of friction source terms. We call the entropy solution to the shallow water system (see e.g. [45]), a weak solution that satisfies the following entropy inequality

$$\partial_t E + \boldsymbol{\nabla} \cdot \left[(E + \frac{gh^2}{2})\mathbf{u} \right] \leqslant 0, \tag{2.33}$$

where E is a mathematical entropy (which is the mechanical energy see [46]), defined as $E(h, \mathbf{u}, Z) = h\frac{|\mathbf{u}|^2}{2} + \frac{gh^2}{2} + ghZ$. This inequality becomes equality for regular solutions, in the absence of energy loss terms, notably friction, and remains inequality, for admissible discontinuous solutions, resulting from classical calculations; we invite the reader to refer to [47, subsection 1.1]. The mechanical energy, which is easily verified as convex with respect to the conservative variables, acts here as a mathematical entropy. In the case of the system without source terms and in the 1D problem, the mechanical energy is only one of the entropies that must be associated with the system for the problem to be properly posed. In 2D, or when the system contains the source terms, there is no longer a complete family of mathematical entropies. Therefore, even if the inequality (2.33) alone is not sufficient for a rigorous mathematical study, it nevertheless ensures the presence of an additional bound on a certain positive function of the system unknowns and can provide information on the choice of a physical solution. The finite volume scheme will be presented in the Chapter 3 verifies innately the conservation properties. The energy decay property remains more difficult to satisfy.

2.2.2 Model of solute transport by fluid flow

Simulations that calculate the movement and dispersion of passive substances in natural water bodies (e.g. a pollutants concentration) are essential for evaluating water pollution, developing strategies to enhance water quality, and assessing potential impacts on ecosystems [48, 49, 50]. The shallow water equations are typically used to model flows in settings where horizontal dimensions greatly exceed vertical ones. If a passive substance is thoroughly mixed vertically, its behavior can be depicted by a depth-averaged movement-dispersion equation. Combining the shallow water equations with the movement-dispersion equation results in a parabolic partial differential equation. These equations govern distinct physical phenomena at different scales: in the movement process, small waves travel at a finite speed, while in the dispersion process, minor disturbances in flow fields or passive substance concentration spread at an infinite speed. This aspect, along with the intricate morphologies of natural water bodies that may include wet and dry zones, makes the problem especially challenging from a numerical

standpoint. In the past ten years, numerical methods for scalar transport issues have gained significant interest, particularly for scalar movement, a more intricate problem involving both movement and dispersion. Notable examples include the works [7, 51], as well as the movement-dispersion of a reactive tracer, such as in [52, 53]. Numerous other relevant studies can be found in the existing literature. The mathematical model used to describe the transport of a tracer with free-surface flow is based on the two-dimensional equations of shallow water. These equations, now fairly established in the literature, do not account for turbulence and viscosity-related terms in this research. The system can be expressed in the following form

$$\begin{cases} \partial_t h + \nabla \cdot (h\mathbf{u}) = 0, \\ \partial_t h\mathbf{u} + \nabla \cdot (h\mathbf{u} \otimes \mathbf{u}) + \dfrac{1}{2}\boldsymbol{\nabla}(gh^2) = -gh\boldsymbol{\nabla} Z - f_c \times h\mathbf{u}^{\perp} - r(h,\mathbf{u}) + \tau(h,\breve{\mathbf{u}}), \end{cases} \tag{2.34}$$

when a pollutant is released into a flow, the following pollutant transport and diffusion equation must be linked to the system of equations (2.34)

$$\partial_t hC + \nabla \cdot (h\mathbf{u}C) - \nabla \cdot (hD\nabla C) = hQ, \tag{2.35}$$

where C denotes the pollutant's average concentration, while $D = (D_x, D_y)^T$ signifies the diffusion coefficients in both spatial directions. The term Q stands for the pollutant's source, and $r(h,\mathbf{u})$ and $\tau(h,\breve{\mathbf{u}})$ represent the friction terms related to the bottom and the wind at the free surface, respectively. These terms' expressions can be found in Section 2.2.1. Additionally, the Coriolis term is indicated by $f_c \times h\mathbf{u}^{\perp}$.

It is important to note that the water body's geometry within our computational domain shows that the horizontal length scale is significantly larger than the vertical length scale by several orders of magnitude. Moreover, the pollutant is assumed to be released at the free surface and stays on the water surface throughout the entire simulation period. The employment of the two-dimensional hydrodynamic model combined with the advection-diffusion equation (2.35) is well-founded. The systems (2.34) and (2.35) can be expressed in the following vector form in terms of the flow variables $W(h, hu, hv, hC)^T$

$$\frac{\partial W}{\partial t} + \nabla \cdot (\mathbb{F}(W) - \tilde{\mathbb{F}}(W)) = S(W) + R(W), \tag{2.36}$$

where

$$\mathbb{F}(W) = \left(\begin{pmatrix} hu \\ hu^2 + \frac{1}{2}gh^2 \\ huv \\ huC \end{pmatrix}, \begin{pmatrix} hv \\ huv \\ hv^2 + \frac{1}{2}gh^2 \\ hvC \end{pmatrix} \right)^T, \quad \tilde{\mathbb{F}}(W) = \left(\begin{pmatrix} 0 \\ 0 \\ 0 \\ hD_x\partial_x C \end{pmatrix}, \begin{pmatrix} 0 \\ 0 \\ 0 \\ hD_y\partial_y C \end{pmatrix} \right)^T,$$

$$S(W) = \begin{pmatrix} 0 \\ -gh\partial_x Z \\ -gh\partial_y Z \\ 0 \end{pmatrix} \text{ and } R(W) = \begin{pmatrix} 0 \\ f_c hv - r_{f_x} + \tau_{s_x} \\ -f_c hu - r_{f_y} + \tau_{s_y} \\ hQ \end{pmatrix}.$$

2.2.2.1 Properties of the system

The properties of system (2.36) are comparable to those of system (2.22), except for a slight difference in the eigenstructure. In the pollutant transport-diffusion equation model, the velocity field is generated by the dynamics of shallow water flow, resulting in primarily horizontal dispersion of the pollutant along the surface, while vertical variations can be neglected.

2.2.2.1.1 Eigenstructure We establish the definition of the normal flux associated with the convective part of (2.36) in the following manner

$$\mathbb{F}_{\mathbf{n}} = (\mathtt{F}, \mathtt{G}) \cdot \mathbf{n}, \tag{2.37}$$

where $\mathbf{n} = (n_x, n_y)^T$ is the normal vector,

$$\mathtt{F} = \begin{pmatrix} hu \\ hu^2 + \frac{1}{2}gh^2 \\ huv \\ huC \end{pmatrix} \quad \text{and} \quad \mathtt{G} = \begin{pmatrix} hv \\ huv \\ hv^2 + \frac{1}{2}gh^2 \\ hvC \end{pmatrix}. \tag{2.38}$$

The Jacobian matrices associated with the fluxes $\mathtt{F}$ and $\mathtt{G}$ are provided as follows

$$\mathbf{J}_{\mathtt{F}} = \begin{pmatrix} 0 & 1 & 0 & 0 \\ gh - u^2 & 2u & 0 & 0 \\ -uv & v & u & 0 \\ -uC & C & 0 & u \end{pmatrix} \quad \text{and} \quad \mathbf{J}_{\mathtt{G}} = \begin{pmatrix} 0 & 0 & 1 & 0 \\ -uv & v & u & 0 \\ gh - v^2 & 0 & 2v & 0 \\ -vC & 0 & C & v \end{pmatrix}. \tag{2.39}$$

The Jacobian matrix $\mathbf{J}_{\mathbb{F}\mathbf{n}}$, which corresponds to the normal flux presented in equation (2.37), can be expressed as follows

$$\mathbf{J}_{\mathbb{F}\mathbf{n}} = \begin{pmatrix} 0 & n_x & n_y & 0 \\ (gh - u^2)\, n_x - uvn_y & 2un_x + vn_y & un_y & 0 \\ -uvn_x + (gh - v^2)\, n_y & n_x v & un_x + 2vn_y & 0 \\ -C\,(un_x + vn_y) & Cn_x & Cn_y & un_x + vn_y \end{pmatrix}. \tag{2.40}$$

The matrix (2.40) has eigenvalues that can be expressed as follows

$$\lambda_1 = u_\eta - c,\ \lambda_2 = \lambda_3 = u_\eta \quad \text{and} \quad \lambda_4 = u_\eta + c, \tag{2.41}$$

where $c = \sqrt{gh}$ and $u_\eta = un_x + vn_y$.

2.2.3 Two-dimensional multilayer shallow water equations

The classical shallow water systems have some limitations. In fact, the formulation of the system in terms of height and depth-averaged velocity leads to a loss of information on the vertical profile of fluid velocity. In order to overcome this lack of information on the velocity inside the fluid while preserving the shallow water formulation known for its numerical efficiency, semi-discrete versions in z of the hydrostatic Navier-Stokes equations have been introduced, known as shallow water-type multilayer models.

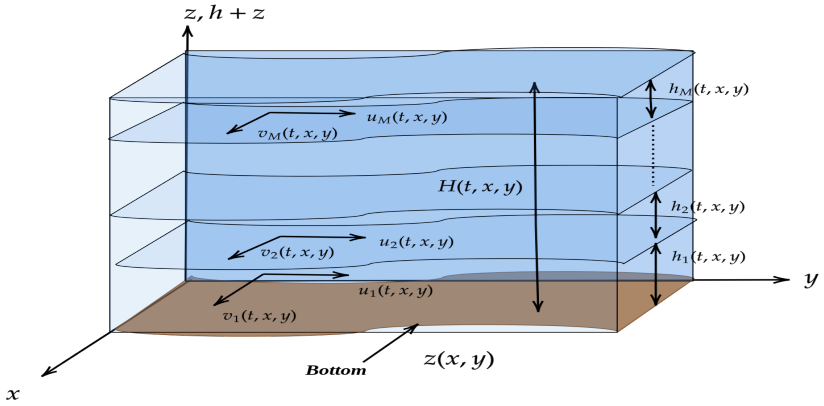

Fig 2.2. Illustration of a two-dimensional multilayer shallow water system.

The general principle of multilayer models is to partition the total height of the fluid, denoted by H, as illustrated in Fig 2.2. In other words, the total height of the fluid H is divided into M layers

$$H(t,x,y) = \sum_{\theta=1}^{M} h_\theta.$$

This division is used in the integration of the Navier-Stokes conservation equation for momentum, which is carried out after a vertical discretization of the fluid volume in each of the defined domains.

A multilayer model can be seen as a partial discretization (with respect to the variable) of the Navier-Stokes equations. The nature of this discretization leads to different multilayer models. Three examples of multilayer models introduced in recent years are the Rambaud model [54], the Audusse et al. model [55], and the Audusse model [56]. In this work, we will focus on the multilayer model introduced by Audusse et al. [55]. Finally, we note that the multilayer models mentioned here are very different in nature from the multifluid models studied in [57, 58], where the layers correspond to physical distinctions between miscible fluids. Here, the notion of layer is purely numerical.

In this study, we consider the two-dimensional version of a model expressed in a conservative form which was presented in [59] as

$$\begin{cases} \partial_t H + \sum_{\theta=1}^{M} \partial_x \left(l_\theta H u_\theta\right) + \sum_{\theta=1}^{M} \partial_y \left(l_\theta H v_\theta\right) = 0, \\ \partial_t \left(l_\theta H u_\theta\right) + \partial_x \left(l_\theta H u_\theta^2 + \frac{1}{2} g l_\theta H^2\right) + \partial_y \left(H u_\theta v_\theta\right) = -g l_\theta H \partial_x Z + f_c l_\theta H v_\theta + F_\theta, \\ \partial_t \left(l_\theta H v_\theta\right) + \partial_x \left(H u_\theta v_\theta\right) + \partial_y \left(l_\theta H v_\theta^2 + \frac{1}{2} g l_\theta H^2\right) = -g l_\theta H \partial_y Z - f_c l_\theta H u_\theta + G_\theta. \end{cases} \tag{2.42}$$

The model is described by a set of partial differential equations that relate the water height and velocity for each layer. The equations include terms that represent advection, gravity, the Coriolis force, and external forces. The water velocity vector for the θ^{th} layer is represented by $\mathbf{u}_\theta = (u_\theta, v_\theta)^T$, while $Z(x,y)$ represents the topography of the basin. The Coriolis parameter f_c is a function of the rotation of the Earth, and $H(t,x,y)$ represents the water height for the entire system. Moreover, l_θ denotes the relative size of the θ^{th} layer with, $l_\theta > 0$, and $\sum_{\theta=1}^{M} l_\theta = 1$, and

$h_\theta(t,x,y)$ is defined as $h_\theta = l_\theta H, \quad \theta = 1,2,\ldots,M$, where M is the total number of layers in the flow domain, see Fig 2.2. The source term F_θ represents the external force in the x-direction acting on the θ^{th} layer, the force F_θ takes into account the effects of friction and momentum exchange. Therefore, we can write

$$F_\theta = \mathcal{F}_\theta^{(u)} + \mathcal{F}_\theta^{(\nu)} + \mathcal{F}_\theta^{(b)} + \mathcal{F}_\theta^{(w)} + \mathcal{F}_\theta^{(\mu)}, \quad \theta = 1,2,\ldots,M. \tag{2.43}$$

The first term $\mathcal{F}_\theta^{(u)}$ is associated with the exchange of x-momentum between layers defined by the vertical discretization P_0 of the flow domain. The forcing term $\mathcal{F}_\theta^{(\nu)}$ arises from horizontal diffusion, while the last three terms $\mathcal{F}_\theta^{(b)}, \mathcal{F}_\theta^{(w)}$ and $\mathcal{F}_\theta^{(\mu)}$ are related to frictional effects. To compute the advection term $\mathcal{F}_\theta^{(u)}$, we use the techniques presented in [55]

$$\mathcal{F}_\theta^{(u)} = u_{\theta+1/2}\mathcal{E}^x_{\theta+1/2} - u_{\theta-1/2}\mathcal{E}^x_{\theta-1/2}, \tag{2.44}$$

where the computing of the mass exchange terms $\mathcal{E}^x_{\theta+1/2}$ is performed as follows

$$\mathcal{E}^x_{\zeta+1/2} = \begin{cases} 0, & \text{if} \quad \zeta = 0, \\ \displaystyle\sum_{\beta=1}^{\zeta}\left(\partial_x\left(h_\beta u_\beta\right) - l_\beta \sum_{\gamma=1}^{M}\partial_x\left(h_\gamma u_\gamma\right)\right), & \text{if} \quad \zeta = 1,2,\ldots,M-1, \\ 0, & \text{if} \quad \zeta = M, \end{cases} \tag{2.45}$$

and the computation of the interface velocity $u_{\theta+1/2}$ in equation (2.44) employs a straightforward upwind technique that incorporates the polarity of the mass exchange term.

$$u_{\theta+1/2} = \begin{cases} u_\theta, & \text{if} \quad \mathcal{E}^x_{\theta+1/2} \geq 0, \\ u_{\theta+1}, & \text{if} \quad \mathcal{E}^x_{\theta+1/2} < 0. \end{cases} \tag{2.46}$$

The vertical kinematic eddy viscosity term denoted by $\mathcal{F}_\theta^{(\mu)}$ incorporates the effects of inter-layer friction and is formulated as follows

$$\mathcal{F}_\theta^{(\mu)} = \begin{cases} 2\nu\frac{u_2-u_1}{(l_2+l_1)H}, & \text{if} \quad \theta = 1, \\ 2\nu\frac{u_{\theta+1}-u_\theta}{(l_{\theta+1}+l_\theta)H} - 2\nu\frac{u_\alpha-u_{\theta-1}}{(l_\theta+l_{\theta-1})H}, & \text{if} \quad \theta = 2,3,\ldots,M-1, \\ -2\nu\frac{u_M-u_{M-1}}{(l_M+l_{M-1})H}, & \text{if} \quad \theta = M. \end{cases} \tag{2.47}$$

It should be noted that the eddy viscosity ν is utilized in this context. Additionally, a comprehensive formulation of the viscous tensor in multilayer shallow water equations has been presented in [60]. Moreover, the interface velocity in equation (2.46) has been estimated using the mean of the two velocities $u_{\theta+1}$ and u_θ, as described in [60]. The expressions for the external friction terms in equation (2.43) are also provided.

$$\mathcal{F}_\theta^{(b)} = \begin{cases} -\frac{\tau_b^x}{\rho}, & \text{if} \quad \theta = 1, \\ 0, & \text{if} \quad \theta = 2,\ldots,M, \end{cases} \quad \text{and} \quad \mathcal{F}_\theta^{(w)} = \begin{cases} 0, & \text{if} \quad \theta = 1,\ldots,M-1, \\ \frac{\tau_w^x}{\rho}, & \text{if} \quad \theta = M, \end{cases} \tag{2.48}$$

where, ρ represents the water density, while τ_b^x and τ_w^x denote the bed shear stress and the shear of the blowing wind, respectively. These variables are defined based on the water velocity, given by (u_1, v_1), and the wind velocity, denoted as $w = (w_x, w_y)^T$.

$$\tau_b^x = \rho C_b u_1\sqrt{u_1^2+v_1^2} \quad \text{and} \quad \tau_w^x = \rho C_w w_x\sqrt{w_x^2+w_y^2}, \tag{2.49}$$

where C_b is the bed friction coefficient, which may be either constant or estimated using the Manning equation as $C_b = \frac{gn_b^2}{H^{1/3}}$, where the Manning roughness coefficient of the bed is denoted by n_b, while the wind friction coefficient C_w is expressed as [61].

$$C_w = \frac{\sigma^2 \rho_a}{H}, \tag{2.50}$$

where σ represents the wind stress coefficient, and ρ_a represents the density of air. In equation (2.43), the horizontal diffusion terms $\mathcal{F}_\theta^{(\nu)}$ are defined as follows for $\theta = 1, 2, \ldots, M$

$$\mathcal{F}_\theta^{(\nu)} = \nu_H \partial_x \left(l_\theta H \partial_x u_\theta \right) + \nu_H \partial_y \left(l_\theta H \partial_y u_\theta \right), \quad \theta = 1, 2, \ldots, M, \tag{2.51}$$

where ν_H is the horizontal viscosity coefficient.

Similarly, the same expressions for all forces (G_θ), mass exchange terms, and horizontal diffusion term are used in the y-direction acting on the θ layer, with only the substitution of u_θ by v_θ in the aforementioned formulas (i.e., from (2.44) to (2.51)).

It should be noted that the bed friction forcing terms $\mathcal{F}_\theta^{(b)}$ and $\mathcal{G}_\theta^{(b)}$ act exclusively on the lower layer, while the wind-driven forcing terms $\mathcal{F}_\theta^{(w)}$ and $\mathcal{G}_\theta^{(w)}$ act solely on the upper layer. Additionally, it is important to emphasize that the internal friction terms $\mathcal{F}_\theta^{(\mu)}$ and $\mathcal{G}_\theta^{(\mu)}$ represent the friction between adjacent layers, as explained in [56]. Equation (2.42) can also be expressed concisely in vector form

$$\partial_t W + \partial_x \mathbf{F}(W) + \partial_y \mathbf{G}(W) = \mathbf{S}(W) + \mathbf{R}(W), \tag{2.52}$$

where is the vector W, which contains the conserved variables. The vectors of flux functions, denoted as $\mathbf{F}$ and $\mathbf{G}$, are also involved in this equation. Additionally, the vector of source terms is defined by $\mathbf{S}$ and $\mathbf{R}$.

$$W = \begin{pmatrix} H \\ l_1 H u_1 \\ l_2 H u_2 \\ \vdots \\ l_M H u_M \\ l_1 H v_1 \\ l_2 H v_2 \\ \vdots \\ l_M H v_M \end{pmatrix}, \quad \mathbf{F}(W) = \begin{pmatrix} \sum_{\theta=1}^{M} l_\theta H u_\theta \\ l_1 H u_1^2 + \frac{1}{2} g l_1 H^2 \\ l_2 H u_2^2 + \frac{1}{2} g l_2 H^2 \\ \vdots \\ l_M H u_M^2 + \frac{1}{2} g l_M H^2 \\ l_1 H u_1 v_1 \\ l_2 H u_2 v_2 \\ \vdots \\ l_M H u_M v_M \end{pmatrix}, \quad \mathbf{G}(W) = \begin{pmatrix} \sum_{\theta=1}^{M} l_\theta H v_\theta \\ l_1 H u_1 v_1 \\ l_2 H u_2 v_2 \\ \vdots \\ l_M H u_M v_M \\ l_1 H v_1^2 + \frac{1}{2} g l_1 H^2 \\ l_2 H v_2^2 + \frac{1}{2} g l_2 H^2 \\ \vdots \\ l_M H v_M^2 + \frac{1}{2} g l_M H^2 \end{pmatrix},$$

$$\mathbf{S}(W) = \begin{pmatrix} 0 \\ -gl_1H\partial_x Z + f_c l_1 H v_1 \\ -gl_2H\partial_x Z + f_c l_2 H v_2 \\ \vdots \\ -gl_M H\partial_x Z + f_c l_M H v_M \\ -gl_1H\partial_y Z - f_c l_1 H u_1 \\ -gl_2H\partial_y Z - f_c l_2 H u_2 \\ \vdots \\ -gl_M H\partial_y Z - f_c l_M H u_M \end{pmatrix}, \quad \mathbf{R}(W) = \begin{pmatrix} \mathcal{F}_1^{(u)} + \mathcal{F}_1^{(b)} + \mathcal{F}_1^{(w)} + \mathcal{F}_1^{(\mu)} + \mathcal{F}_1^{(\nu)} \\ \mathcal{F}_2^{(u)} + \mathcal{F}_2^{(b)} + \mathcal{F}_2^{(w)} + \mathcal{F}_2^{(\mu)} + \mathcal{F}_2^{(\nu)} \\ \vdots \\ \mathcal{F}_M^{(u)} + \mathcal{F}_M^{(b)} + \mathcal{F}_M^{(w)} + \mathcal{F}_M^{(\mu)} + \mathcal{F}_M^{(\nu)} \\ \mathcal{G}_1^{(u)} + \mathcal{G}_1^{(b)} + \mathcal{G}_1^{(w)} + \mathcal{G}_1^{(\mu)} + \mathcal{G}_1^{(\nu)} \\ \mathcal{G}_2^{(u)} + \mathcal{G}_2^{(b)} + \mathcal{G}_2^{(w)} + \mathcal{G}_2^{(\mu)} + \mathcal{G}_2^{(\nu)} \\ \vdots \\ \mathcal{G}_M^{(u)} + \mathcal{G}_M^{(b)} + \mathcal{G}_M^{(w)} + \mathcal{G}_M^{(\mu)} + \mathcal{G}_M^{(\nu)} \end{pmatrix}.$$

It is important to note that for a problem to be well-posed, the system (2.52) must be solved over a time interval of $[0, T]$ in a two-dimensional spatial domain Ω, bounded by Γ, and subject to specified initial and boundary conditions.

2.2.4 Three–Dimensional Euler equations

We consider the two-dimensional Euler equations for modeling the dynamics of non-viscous gases. In the following presentation, the chosen variables to describe the laws of conservation include density, ρ, the velocity vector $\mathbf{u} := (u, v, w)$, total energy, E, and pressure, p. Generally, the flow is three-dimensional, time-dependent, and compressible, with the fluid being viscous and consisting of a single phase (gas). This study excludes volumetric forces (such as gravity, etc.) and volumetric heat fluxes (radiation, etc.). The equations presented here will be formulated in differential form, using Einstein's notation to simplify their expression.

$$\begin{cases} \partial_t \rho + \nabla \cdot (\rho \mathbf{u}) = 0, \\ \partial_t \rho \mathbf{u} + \nabla \cdot (\rho \mathbf{u} \otimes \mathbf{u}) = -\boldsymbol{\nabla} p, \\ \partial_t \rho E + \nabla \cdot (\mathbf{u} \rho E) = -\nabla \cdot (\mathbf{u} p). \end{cases} \tag{2.53}$$

The law established by the state connects E, ρ, p, and $\mathbf{u}$ and can be represented in the following manner

$$E = \rho(\frac{1}{2}|\mathbf{u}|^2 + e(\rho, p)), \tag{2.54}$$

where e is the specific internal energy; for ideal gases, it can be described using the subsequent formula

$$e(\rho, p) = \frac{p}{(\gamma - 1)\rho}, \tag{2.55}$$

with γ is the ratio of specific heats, it is a constant that depends on the particular gas, e.g $\gamma = 1.4$ for air. Another quantity that expresses the ratio of the local velocity of the fluid to the sound speed in this same fluid is called Mach number, which is a dimensionless number defined as

$$M = \frac{|\mathbf{u}|}{c}, \tag{2.56}$$

where c is the sound speed in a gas. For ideal gas, we can express c by:

$$c = \sqrt{\frac{\gamma p}{\rho}}. \tag{2.57}$$

c varies with the nature and temperature of the fluid. So, the Mach number does not correspond to a fixed speed, it depends on local conditions. Generally, velocity is categorized according to

its corresponding regimes [62], for example, the subsonic ($M < 0.8$), transsonic ($0.8 \leqslant M < 1.2$), supersonic ($1.2 \leqslant M < 5$) and hypersonic ($M \geqslant 5$) regimes.

To enhance the clarity of the expression, we have rephrased the system (2.53) by employing the subsequent conservative vector representation, which will be utilized for the numerical reformulation

$$\frac{\partial \mathbf{W}}{\partial t} + \nabla \cdot \mathbf{F}(\mathbf{W}) = 0, \tag{2.58}$$

with

$$\mathbf{W} = \begin{pmatrix} \rho \\ \rho u \\ \rho v \\ \rho w \\ \rho E \end{pmatrix}, \quad \mathbf{F}(\mathbf{W}) = \left(\begin{pmatrix} \rho u \\ \rho u^2 + p \\ \rho uv \\ \rho uw \\ u(\rho E + p) \end{pmatrix}, \begin{pmatrix} \rho v \\ \rho uv \\ \rho v^2 + p \\ \rho vw \\ v(\rho E + p) \end{pmatrix}, \begin{pmatrix} \rho w \\ \rho uw \\ \rho vw \\ \rho w^2 + p \\ w(\rho E + p) \end{pmatrix} \right)^T, \tag{2.59}$$

where $\mathbf{F}$ is the flux tensor and $\mathbf{W}$ is the vector of unknowns. We also define the normal flux as follows

$$\mathbf{F_n} = (\mathtt{F}, \mathtt{G}, \mathtt{H}) \cdot \mathbf{n}, \tag{2.60}$$

where $\mathbf{n} = (n_x, n_y, n_z)^t$ is the normal vector, and

$$\mathtt{F} = \begin{pmatrix} \rho u \\ \rho u^2 + p \\ \rho uv \\ \rho uw \\ u(\rho E + p) \end{pmatrix}, \ \mathtt{G} = \begin{pmatrix} \rho v \\ \rho uv \\ \rho v^2 + p \\ \rho vw \\ v(\rho E + p) \end{pmatrix}, \ \mathtt{H} = \begin{pmatrix} \rho w \\ \rho uw \\ \rho vw \\ \rho w^2 + p \\ w(\rho E + p) \end{pmatrix}. \tag{2.61}$$

2.2.4.1 Properties of the system

Here we use the results stated and proved in Toro's book [63] for three-dimensional time-dependent Euler equations. The proofs are omitted, as they involve elementary but tedious algebra.

2.2.4.1.1 Eigenstructure The Jacobians matrices corresponding to the fluxes `F`, `G` and `H` in (2.61) are given by

$$\mathbf{J}_{\mathtt{F}} = \begin{pmatrix} 0 & 1 & 0 & 0 & 0 \\ \frac{\gamma-1}{2}|\mathbf{u}|^2 - u^2 & (3-\gamma)u & (1-\gamma)v & (1-\gamma)w & \gamma - 1 \\ -uv & v & u & 0 & 0 \\ -uw & w & 0 & u & 0 \\ \left(\frac{\gamma-1}{2}|\mathbf{u}|^2 - H\right)u & H + (1-\gamma)u^2 & (1-\gamma)uv & (1-\gamma)uw & \gamma u \end{pmatrix}, \tag{2.62}$$

$$\mathbf{J}_{\mathtt{G}} = \begin{pmatrix} 0 & 0 & 1 & 0 & 0 \\ -vu & v & u & 0 & 0 \\ \frac{\gamma-1}{2}|\mathbf{u}|^2 - v^2 & (1-\gamma)v & (3-\gamma)u & (1-\gamma)w & \gamma - 1 \\ -vw & 0 & w & v & 0 \\ \left(\frac{\gamma-1}{2}|\mathbf{u}|^2 - H\right)v & (1-\gamma)uv & H + (1-\gamma)v^2 & (1-\gamma)vw & \gamma v \end{pmatrix}, \tag{2.63}$$

$$\mathbf{J}_{\mathtt{H}} = \begin{pmatrix} 0 & 0 & 0 & 1 & 0 \\ -uw & w & 0 & u & 0 \\ -vw & 0 & w & v & 0 \\ \frac{\gamma-1}{2}|\mathbf{u}|^2 - w^2 & (1-\gamma)u & (1-\gamma)v & (3-\gamma)w & \gamma-1 \\ \left(\frac{\gamma-1}{2}|\mathbf{u}|^2 - H\right)w & (1-\gamma)uw & (1-\gamma)vw & H+(1-\gamma)w^2 & \gamma w \end{pmatrix}, \tag{2.64}$$

in these matrices, H represents the total specific enthalpy defined by

$$H = E + \frac{p}{\rho}. \tag{2.65}$$

The Jacobian matrix $\mathbf{J}_{\mathbf{F_n}}$ corresponding to the normal flux (2.60) is given by

$$\mathbf{J}_{\mathbf{F_n}} = \mathbf{J}_{\mathtt{F}} n_x + \mathbf{J}_{\mathtt{G}} n_y + \mathbf{J}_{\mathtt{H}} n_z$$

$$= \begin{pmatrix} 0 & n_x & n_y & n_z & 0 \\ \frac{\breve{\gamma}}{2}|\mathbf{u}|^2 n_x - u u_\eta & u n_x - \breve{\gamma} u n_x + u_\eta & u n_y - \breve{\gamma} v n_x & u n_z - \breve{\gamma} w n_x & \breve{\gamma} n_x \\ \frac{\breve{\gamma}}{2}|\mathbf{u}|^2 n_y - v u_\eta & v n_x - \breve{\gamma} u n_y & v n_y - \breve{\gamma} v n_y + u_\eta & v n_z - \breve{\gamma} w n_y & \breve{\gamma} n_y \\ \frac{\breve{\gamma}}{2}|\mathbf{u}|^2 n_z - w u_\eta & w n_x - \breve{\gamma} u n_z & w n_y - \breve{\gamma} v n_z & w n_z - \breve{\gamma} w n_z + u_\eta & \breve{\gamma} n_z \\ \left(\frac{\breve{\gamma}}{2}|\mathbf{u}|^2 - H\right) u_\eta & H n_x - \breve{\gamma} u u_\eta & H n_y - \breve{\gamma} v u_\eta & H n_z - \breve{\gamma} w u_\eta & \gamma u_\eta \end{pmatrix},$$

where $\breve{\gamma} = \gamma - 1$ and $u_\eta := \mathbf{u} \cdot \mathbf{n} = u n_x + v n_y + w n_z$. The three-dimensional system (2.58) is hyperbolic with eigenvalues given by

$$\lambda_1 = u_\eta - c,\ \lambda_2 = u_\eta,\ \lambda_3 = u_\eta + c \quad \text{and} \quad \lambda_4 = \lambda_5 = u_\eta, \tag{2.66}$$

the matrix $\mathbf{J}_{\mathbf{F_n}}$ is diagonalizable and we write

$$\mathbf{J}_{\mathbf{F_n}} = \mathbf{P_n} \mathbf{\Lambda_n} \mathbf{P_n}^{-1}, \tag{2.67}$$

where

$$\mathbf{\Lambda_n} = \begin{pmatrix} u_\eta - c & 0 & 0 & 0 & 0 \\ 0 & u_\eta & 0 & 0 & 0 \\ 0 & 0 & u_\eta + c & 0 & 0 \\ 0 & 0 & 0 & u_\eta & 0 \\ 0 & 0 & 0 & 0 & u_\eta \end{pmatrix}, \tag{2.68}$$

and

$$\mathbf{P_n} = \begin{pmatrix} 1 & 1 & 1 & 0 & 0 \\ u - c n_x & u & u + c n_x & b_x & \tau_x \\ v - c n_y & v & v + c n_y & b_y & \tau_y \\ w - c n_z & w & w + c n_z & b_z & \tau_z \\ H - u_\eta c & |\mathbf{u}|^2/2 & H + u_\eta c & u_b & u_\tau \end{pmatrix}, \tag{2.69}$$

where $\mathbf{n} := (n_x, n_y, n_z)^T$, $\tau := (\tau_x, \tau_y, \tau_z)^T$ and $\mathbf{b} = (b_x, b_y, b_z)^T$ are the three orthogonal unit vectors such as, $\mathbf{b} := \tau \wedge \mathbf{n}$, $\tau := \mathbf{n} \wedge \mathbf{b}$ and $\mathbf{n} := \mathbf{b} \wedge \tau$. The corresponding velocities are defined as $u_\tau := \mathbf{u} \cdot \tau$ and $u_b := \mathbf{u} \cdot \mathbf{b}$.

2.2.4.1.2 Rotational invariance As for the shallow water equation, the important property of rotational invariance is also verified by the Euler equations. This property allows in fact prove the hyperbolicity in time of the Euler equations and it can also be used for computational purposes to deal with domains that are not aligned with the Cartesian directions.

Definition 2.2.1. *Define two component rotation matrices as:*

$$\mathbf{R}_Y(\phi) = \begin{pmatrix} 1 & 0 & 0 & 0 & 0 \\ 0 & \cos\phi & 0 & \sin\phi & 0 \\ 0 & 0 & 1 & 0 & 0 \\ 0 & -\sin\phi & 0 & \cos\phi & 0 \\ 0 & 0 & 0 & 0 & 1 \end{pmatrix},$$

which rotates the momentum components of $\mathbf{W}$ *through an angle* ψ *about the* y *axis, and*

$$\mathbf{R}_Z(\theta) = \begin{pmatrix} 1 & 0 & 0 & 0 & 0 \\ 0 & \cos\theta & \sin\theta & 0 & 0 \\ 0 & -\sin\theta & \cos\theta & 0 & 0 \\ 0 & 0 & 0 & 1 & 0 \\ 0 & 0 & 0 & 0 & 1 \end{pmatrix},$$

which rotates the momentum components of $\mathbf{W}$ *through an angle* θ *about the* z *axis.*

Definition 2.2.2. *Define the compound rotation matrix as*

$$\mathbf{R}(\theta,\phi) = \mathbf{R}_Y(\phi)\mathbf{R}_Z(\theta) = \begin{pmatrix} 1 & 0 & 0 & 0 & 0 \\ 0 & \cos\phi\cos\theta & \cos\phi\sin\theta & \sin\phi & 0 \\ 0 & -\sin\theta & \cos\theta & 0 & 0 \\ 0 & -\sin\phi\cos\theta & -\sin\phi\sin\theta & \cos\phi & 0 \\ 0 & 0 & 0 & 0 & 1 \end{pmatrix},$$

which rotates first about the z *axis, then about the* y *axis.*

Proposition 2.2.1. *The time-dependent three dimensional Euler equations are rotationally invariant, that is they satisfy*

$$\cos\phi\cos\theta\ \mathtt{F} + \cos\theta\sin\phi\ \mathtt{G} + \sin\phi\ \mathtt{H} = \mathbf{R}^{-1}\mathtt{F}(\mathbf{R}\,\boldsymbol{W})$$

for all angles ϕ, θ *and vectors* $\mathbf{W}$*.*

For more details on rotational invariance and related properties of Euler equations. See [63, section 3.2].

2.2.4.1.3 Primitive Variable Formulation Another form of Euler equations using the primitive variables $\breve{\mathbf{W}} = (\rho, u, v, w, p)^T$ can be formulated as

$$\partial_t \breve{\mathbf{W}} + \mathbf{A}_{\breve{\mathbf{W}}}\partial_x \breve{\mathbf{W}} + \mathbf{B}_{\breve{\mathbf{W}}}\partial_x \breve{\mathbf{W}} + \mathbf{C}_{\breve{\mathbf{W}}}\partial_x \breve{\mathbf{W}} = 0, \tag{2.70}$$

where the coefficient matrices $\mathbf{A}_{\breve{\mathbf{W}}}$, $\mathbf{B}_{\breve{\mathbf{W}}}$ and $\mathbf{C}_{\breve{\mathbf{W}}}$ are given by

$$\mathbf{A}_{\breve{\mathbf{W}}} = \begin{pmatrix} u & \rho & 0 & 0 & 0 \\ 0 & u & 0 & 0 & 1/\rho \\ 0 & 0 & u & 0 & 0 \\ 0 & 0 & 0 & u & 0 \\ 0 & \rho c^2 & 0 & 0 & u \end{pmatrix}, \quad \mathbf{B}_{\breve{\mathbf{W}}} = \begin{pmatrix} v & \rho & 0 & 0 & 0 \\ 0 & v & 0 & 0 & 0 \\ 0 & 0 & v & 0 & 1/\rho \\ 0 & 0 & 0 & v & 0 \\ 0 & 0 & \rho c^2 & 0 & v \end{pmatrix}, \tag{2.71}$$

and

$$\mathbf{C}_{\breve{\mathbf{W}}} = \begin{pmatrix} w & \rho & 0 & 0 & 0 \\ 0 & w & 0 & 0 & 0 \\ 0 & 0 & w & 0 & 0 \\ 0 & 0 & 0 & w & 1/\rho \\ 0 & 0 & 0 & \rho c^2 & w \end{pmatrix}. \tag{2.72}$$

We also define the matrix $J_{\mathbf{n}}$ as follows

$$J_{\mathbf{n}} = \mathbf{A}_{\breve{\mathbf{W}}} n_x + \mathbf{B}_{\breve{\mathbf{W}}} n_y + \mathbf{C}_{\breve{\mathbf{W}}} n_z. \tag{2.73}$$

This matrix is diagonalizable and has the same eigenvectors as the matrix $\mathbf{J}_{\mathbf{F_n}}$ (2.67).

Remark 2.2.1. *According to Toro [63], for regular solutions, this formulation yields the same results as the conservative formulation. However, the same behavior is not observed for other solutions, as this form generates incorrect shocks.*

This remark is addressed through the shallow water equations and the isothermal equations in [63, section 3.3]. However, non-conservative formulations offer certain advantages over their conservative counterparts when analyzing the equations, for instance. Moreover, from a numerical standpoint, there has been a recent resurgence of interest in using schemes for non-conservative formulations of the equations. The FVC scheme, which we will describe in detail in the following chapter, has the advantage of being reformulated for both conservative and non-conservative variables without any notable concerns.

Chapter 3

Generalities on Numerical Methods

Short summary

3.1 Discretization techniques in the framework of the finite volume method

The finite volume method is a widely used numerical technique for discretizing equations or systems of conservation laws. As the name suggests, a conservation law preserves a specific physical quantity $\mathbf{Q}(t, X)$, for instance, conserved entities may include mass, momentum, or energy. Assuming that the local conservation equation takes the following form

$$\partial_t \mathbf{Q}(t, X) + \nabla \cdot \mathbf{F}(\mathbf{Q}(t, X)) = \mathbf{S}(t, X), \tag{3.1}$$

where $\mathbf{F}$ represents the flux responsible for transporting $\mathbf{Q}$, while $\mathbf{S}$ denotes the source term, which may account for factors such as gravity, the emergence or disappearance of chemical species, bottom friction, and so on. If necessary, state laws are introduced to close the problem. The spatial domain is partitioned into a finite number of elements, which can form either structured or unstructured meshes. Next, control volumes must be defined, potentially consisting of one or more mesh elements. Control volumes and elements may not always correspond. Control volumes are employed during spatial discretization, with the solution computed at a point

within the control volume known as the collocation point. Various options exist for defining control volumes: cell-centered, cell-vertex, and node-vertex. Fig 3.1 illustrates the finite volume method using the "cell-vertex" formulation as seen in [33]. In this example, the control volume is determined by considering all triangles sharing a common vertex p_i and connecting their mid-points from p_i to the triangle's barycenter. **It is important to note that in the manapy code[2], elements and control volumes are conflated and the solution is computed at the center of gravity, following the "cell-centered" formulation, see Fig 3.3**.

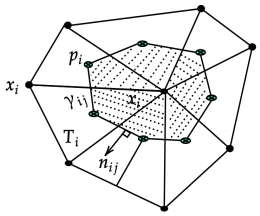

Fig 3.1. Finite volume "cell-vertex" formulation.

Before presenting the finite volume method, we will establish the concept of a "good" mesh. This definition is introduced because it is often overlooked in the context of the problem, as seen in [64]. However, it is crucial to remember that it plays a role in achieving convergence results in numerical methods, whether in finite element or finite volume formulations, as discussed in Section 3.1.3. Since the majority of examples we will examine feature simple geometry, we assume the finite volume mesh is admissible. The definition we will provide is derived from reference [65].

Definition 3.1.1. *Let Ω be a polygonal bounded open of $\mathbb{R}^d$ with $d = 1, 2, 3$ and let $\partial\Omega = \bar{\Omega}\backslash\Omega$ be its boundary. An admissible discretization by finite volumes of Ω is given by a triplet $\mathcal{T} = (\mathcal{O}, \mathcal{E}, \mathcal{P})$ with $\mathcal{O}$ is a non-empty finite family of disjoint convex polygonal open sets of Ω, this is what we call "control volumes" such that $\bar{\Omega} = \bigcup_{T\in\mathcal{O}} \bar{T}$. $\mathcal{E}$ is a finite family of disjoint sets of $\bar{\Omega}$ that is the "edges" such that for any $\gamma \in \mathcal{E}$, there exists a hyperplane H of $\mathbb{R}^d$ and $T \in \mathcal{O}$ with $\bar{\gamma} = \partial T \bigcap H$ and γ a non-empty open subset of H. We also assume that for any $T \in \mathcal{O}$, there exists a subset $\mathcal{E}_T$ of $\mathcal{E}$ such that $\partial T = \bigcup_{\gamma\in\mathcal{E}_T} \bar{\gamma}$. $\mathcal{P}$ is a family of points of Ω indexed by $\mathcal{O}$, $\mathcal{P} = (x_T)_{T\in\mathcal{O}}$, such that for all $T \in \mathcal{O}, x_T \in T$.*

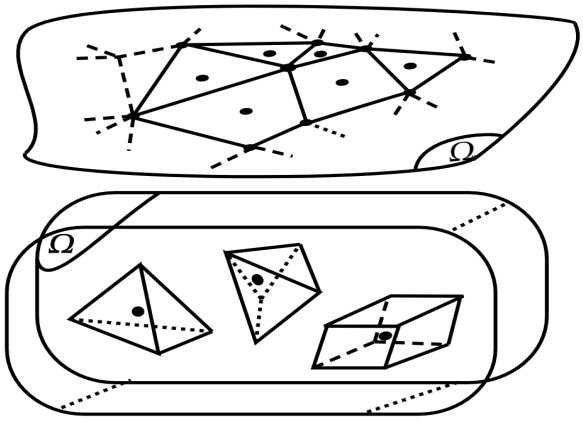

Fig 3.2. Types of 2D and 3D finite volume elements used and implemented.

[2]https://github.com/imadki/manapy

As an illustration, Fig 3.2 shows the elements used to construct the scheme and which are also implemented in manapy.

The finite volume method possesses several notable characteristics. Firstly, it is conservative, enabling the effective treatment of discontinuities such as shocks. In fluid-structure interaction problems, the fluid acts as a load on the structure (e.g., shock wave, rarefaction, explosion, etc.), which must be accurately modeled. Other benefits of the finite volume method include its simplicity and adaptability.

Unlike the finite element method, there is no need to define a reference element for coordinate systems. Moreover, it is especially well-suited for problems involving complex geometry. This is the reason finite volumes are the most prevalent numerical method employed in commercial CFD codes today. Nonetheless, the finite volume method has its limitations, while it produces satisfactory results, it could be more precise and less diffusive. To address these shortcomings, two options are available: dynamic mesh refinement or improving the accuracy of the scheme. In the following sections, we will discuss the development of accurate schemes.

3.1.1 Spatial discretization

We have previously stated that the equations of interest can be expressed in the following form.

$$\partial_t \mathbf{Q} + \nabla \cdot \mathbf{F}(\mathbf{Q}) = \mathbf{S}. \tag{3.2}$$

Suppose that the domain Ω is partitioned into a finite collection of control volumes $\Omega = (T_i)_{i\in I}$, where I represents a finite set of indices. Additionally, we will assume that the mesh is admissible according to the definition previously provided. To obtain a weak solution to the problem, we need to establish a variational approximation. For a first-order solution, we will consider the following function space

$$V_h = \left\{ v \in L^2(\Omega) \ : \ v_{|T_i} = constant; \ i \in I \right\}. \tag{3.3}$$

The functions $\psi_i(X) = \mathbb{1}_{T_i}(X)$ form a basis of V_h. We are looking for $\mathbf{Q}$ solution of the equation

$$\int_\Omega (\partial_t \mathbf{Q} + \nabla \cdot \mathbf{F}(\mathbf{Q}))\psi_j d\mu = \int_\Omega \mathbf{S}\psi_j d\mu, \tag{3.4}$$

that gives

$$\sum_{i\in I} \int_{T_i} (\partial_t \mathbf{Q} + \nabla \cdot \mathbf{F}(\mathbf{Q}))\psi_j d\mu = \sum_{i\in I} \int_{T_i} \mathbf{S}\psi_j d\mu. \tag{3.5}$$

Let us choose $\psi_j(X) = \mathbb{1}_{T_j}(X)$; consequently, formula (3.5) thus becomes

$$\int_{T_j} (\partial_t \mathbf{Q} + \nabla \cdot \mathbf{F}(\mathbf{Q}))d\mu = \int_{T_j} \mathbf{S} d\mu. \tag{3.6}$$

Then, applying the divergence theorem, we have

$$\int_{T_j} \nabla \cdot \mathbf{F}(\mathbf{Q}) d\mu = \int_{\partial T_j} \mathbf{F}(\mathbf{Q}) \cdot \mathbf{n} d\sigma_j. \tag{3.7}$$

In this context, ∂T_j represents the boundary of the control volume T_j, $\mathbf{F}$ refers to the convective flux tensor, and $\mathbf{n}$ is the outward normal of T_j. $\mathbf{F} \cdot \mathbf{n}$ signifies the normal flux. We will adopt

the Eulerian frame to streamline the explanation and assume that the control volume remains constant over time. Consequently,

$$\partial_t \int_{T_j} \mathbf{Q} d\mu = |T_j| \partial_t \bar{\mathbf{Q}}_j, \tag{3.8}$$

where, $\bar{\mathbf{Q}}_j$ represents the average value of the solution over the control volume T_j, and $|T_j|$ is the measure of the control volume T_j. By following a similar approach for $\mathbf{S}$, we only need to approximate the surface integral.

In summary, we can state that defining a finite volume scheme involves deciding how to compute the surface integral through the flux. For instance, we assume that the flux remains constant on each face and is estimated at its center. The semi-discrete equation associated with (3.2) is defined as follows

$$\frac{\partial \bar{\mathbf{Q}}_j}{\partial t} = -\frac{1}{|T_j|} \sum_{k=1}^{N_{edges}} |\gamma_{jk}| \Phi_{jk} + \bar{\mathbf{S}}_j, \tag{3.9}$$

where Φ_{jk} is the computed numerical flux at the surface of the k^{th} face of the control volume T_j. For more clarity in the notations used, we will use as an example in 2D, a mesh represented in Fig 3.3, T_i, T_j refer to the control volumes, γ_{ij} is the edge between T_i and its neighbour T_j and $\mathbf{n}_{ij}$ is the normal vector to γ_{ij}.

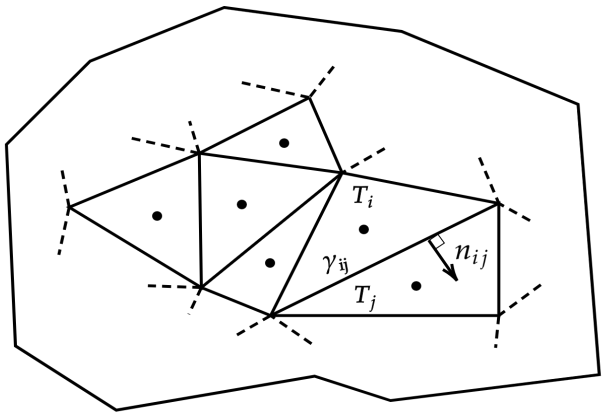

Fig 3.3. "Cell-centered" formulation.

A flux function, Φ_{ij}, can then be employed to determine the flux value from two states (Left state $\bar{\mathbf{Q}}_L$ and right state $\bar{\mathbf{Q}}_R$). For instance, in structured or unstructured meshes, the flux can be defined as the average of the convective fluxes located to the left and right of the shared face. This can also be achieved by solving the Riemann problem associated with these two evaluated states through interpolation using multiple collocation points. Alternatively, the intermediate state at the face can be approximated by solving local linearized Riemann problems and then applying the physical flux to this state to find the numerical flux. Among these numerical fluxes, we can mention [66, 67, 68, 69, 70, 71, 72, 73, 31, 74]. This list is not exhaustive, there are other numerical schemes that we have omitted here to avoid making the document overly lengthy.

The FVC scheme approximates the intermediate state at each interface (referred to as $\bar{\mathbf{Q}}_{i+1/2}$) using the method of characteristics and then evaluates the physical flux at these intermediate states $\mathbf{F}(\bar{\mathbf{Q}}_{i+1/2})$, without employing the Jacobian matrix or solving the Riemann problem.

From a physical standpoint, the existence of non-trivial stationary states, which are those where the unknowns are not constant within the domain, is a characteristic of some equation systems of type (3.2) related to the presence of source terms. This issue has been a significant research topic since the mid-1990s, with numerous publications addressing it up to the present day; see the references cited in the books [11, 22, 23, 18]. The most extensively studied family of equilibrium is associated with the presence of the topography source term (Shallow water equation) and the gravity term (Euler equations). A numerical scheme that does not preserve equilibrium is not useful.

3.1.2 Temporal discretization

An explicit first-order scheme is typically used for time discretization of the semi-discrete equation (3.9). The time step is denoted as $\Delta t \in \mathbb{R}_+^*$, and the initial time is set as $t_0 = 0$, with $t_n = n\Delta t$ representing subsequent times. Let's note $\bar{\mathbf{Q}}_j^n$ the approximate solution in the cell T_j at time t_n, then

$$\frac{\partial \bar{\mathbf{Q}}_j^n}{\partial t} \simeq \frac{\bar{\mathbf{Q}}_j^{n+1} - \bar{\mathbf{Q}}_j^n}{\Delta t}, \tag{3.10}$$

finally we get

$$\bar{\mathbf{Q}}_j^{n+1} = \bar{\mathbf{Q}}_j^n - \frac{\Delta t}{|T_j|} \sum_{k=1}^{N_{edges}} |\gamma_{jk}| \Phi_{jk}^n + \Delta t \bar{\mathbf{S}}_j^n. \tag{3.11}$$

The discretization's explicit aspect enforces a stability condition on the time step known as the CFL (Courant-Friedrichs-Lewy). To circumvent stability issues, an implicit time scheme is also a viable option. Nonetheless, the flux term's non-linear nature presents another challenge that requires a system of equations and a root-finding algorithm to complete the computational process. Please note that in the subsequent text, we will eliminate the bar above the variables to simplify notation. However, it is essential to keep in mind that we are solely computing the solution's average value over the control volume.

3.1.3 Convergence

There are convergence results for the case of hyperbolic equations in one or more space dimensions. In general, if the flux verifies specific properties such as consistency, there is convergence to a weak solution, but this solution is usually not unique. Some of these solutions need to be corrected from a physical point of view. In order to find a physically acceptable solution, additional conditions have to be verified, such as the Lax entropy condition [75]. In this case, the solution is unique and verifies the Rankine-Hugoniot conditions. For systems of hyperbolic equations, there are few theoretical results on convergence. However, for further information, refer to [33].

3.1.4 Godunov's theorem

In order to explain the necessity of the transition to 2^{nd} order in space and time, we will talk in this paragraph about Godunov's theorem. Before starting it, we need to give some definitions. These notions describe the various properties that numerical schemes can verify.

Consider a discrete function $u = (u_i)_{i\in\mathbb{Z}}$ defined on $\mathbb{R}$ i.e., u is given by its values on a discrete set of points, we define its total variation by

$$TV(u) = \sum_{-\infty}^{+\infty} |u_{j+1} - u_j|, \tag{3.12}$$

A numerical scheme is said to be Total Variation Diminishing (TVD) if it satisfies the following condition

$$TV(W^{n+1}) \leqslant TV(W^n). \tag{3.13}$$

In this context, W^n represents the numerical solution at time t_n, and W^0 signifies the initial condition. As a result, the solution's maximum (or minimum) cannot increase (or decrease) correspondingly. A scheme preserves monotonicity if, for any monotonic sequence $(W_i^n)_{i\in\mathbb{Z}}$, the sequence $(W_i^{n+1})_{i\in\mathbb{Z}}$ continues to be monotonic. This characteristic is crucial as it ensures the absence of oscillations in the solution. There are relations between the monotonicity and the TVD properties. In the scalar case, it is possible to demonstrate that these two concepts are equivalent and represent a convergence criterion for a conservative scheme. Nevertheless, Godunov's theorem asserts that these two properties cannot be extended beyond the first order: "*Numerical linear schemes that preserve monotonicity can only have a maximum order of one*" [67].

3.1.5 Second-order extension

For the second order in space, it is not assumed that the solution remains constant within each control volume; rather, it is considered linear. However, according to Godunov's theorem, elevating a scheme's order will result in oscillations within the solution. To address this inconsistency, the notion of limiters will be introduced in this section.

3.1.5.1 TVD Scheme

The concept of a TVD scheme has been discussed earlier. When fluid variables are portrayed as piecewise linear within each control volume, oscillations can occur. This happens if the slope linked to a variable in a single volume exceeds the disparity between the average values of the neighboring volumes. As a result, implementing a TVD scheme is crucial to prevent the solution's non-monotonic behavior. In [76], Van Leer established the subsequent criterion: "*The interpolation in a given element must not be outside the values defined by the neighboring values of the interpolated variable*".
This condition is mathematically described by the relation

$$\min_{|l-i|\leqslant 1} W_l \leqslant \pi_i(x) \leqslant \max_{|l-i|\leqslant 1} W_l, \tag{3.14}$$

where $\pi_i(x)$ is the interpolation polynomial in the cell i, see Fig 3.4. In order to develop highly accurate methods, the TVD scheme is commonly employed. Although this primarily holds significance in scalar cases, the TVD scheme concept is also utilized for systems of conservation laws. The justification for this lies in its simplicity and the satisfactory numerical results it yields. There are other methods to increase the order in space, such as the Piecewise Parabolic Method (PPM) [77] or Essentially Non-Oscillatory (ENO) schemes [78].

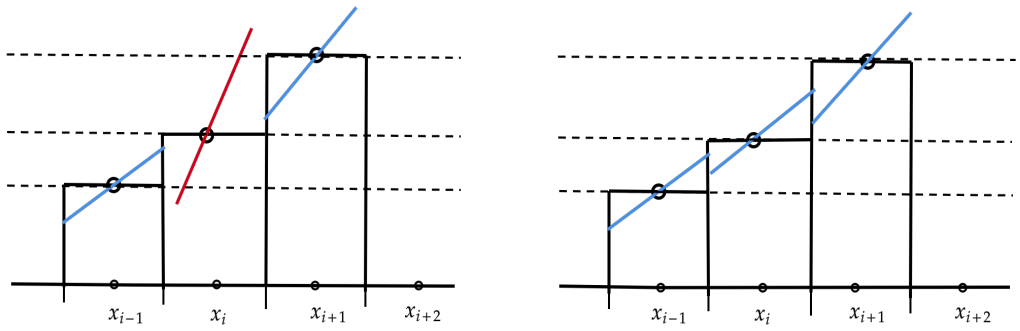

Fig 3.4. Monotonicity - Van Leer criterion. Right: monotone. Left: not monotone.

3.1.5.2 Second order in space

We will now explain how to increase the accuracy of a finite volume scheme via a monotone Upwind-centered Schemes for Conservation Laws (MUSCL) approach.

To move to a second-order approximation, we will apply a first-order Taylor approximation to the solutions at the center of gravity of each control volume. This will give us an evaluation of the solution to the left and right of the common face

$$\begin{aligned} W_{ij}^L &= W_i + (\vec{r}_{ij} - \vec{r}_i)\,\nabla W_i, \\ W_{ij}^R &= W_j + (\vec{r}_{ij} - \vec{r}_j)\,\nabla W_j, \end{aligned} \tag{3.15}$$

where ∇W_i and ∇W_j are the gradients calculated at the centers of the control volumes T_i and T_j respectively. Finding the gradient in a Cartesian mesh is straightforward, but for triangular or unstructured meshes, special techniques are often necessary to estimate the gradient at the center. There are two main methods of calculation. One is based on the Green-Ostrogradski theorem, and the other is based on the least squares method, see [79, section 3.2.4].
$\vec{r}_{ij} - \vec{r}_i$ and $\vec{r}_{ij} - \vec{r}_j$ are the vectors originating at the center of the two control volumes and pointing to the center of the face.

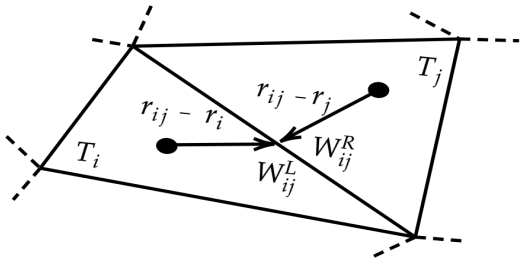

Fig 3.5. Reconstruction for Cell-centered formulation.

The reconstruction was done component by component using the conservative variables of the system of equations to be solved. The method based on the least squares method explained in detail in [79] has been implemented in the manapy code and validated on numerous examples.

3.1.5.3 Concept of limiters

As we have seen, to improve the accuracy of the scheme, we have chosen to approximate the solution linearly for each control volume. However, the calculation of the gradient can lead to the

appearance of oscillations and thus degrade the approximation of the solution. For this, we want to build a TVD scheme, as explained above. To solve this problem, Sweby [80] introduced the notion of a limiter. In [80], Sweby proves that the flux limiter ψ must check certain conditions. A TVD region can then be associated with the limiter for a second-order scheme Fig 3.6.

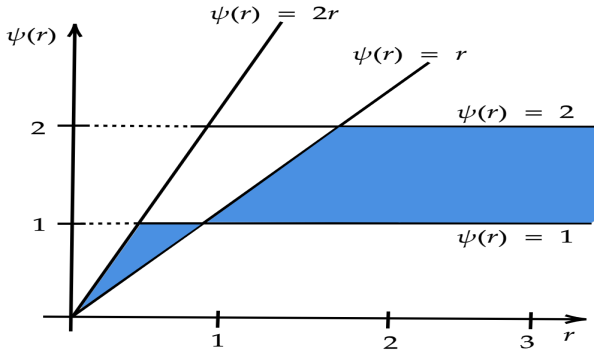

Fig 3.6. Limiter region associated with a second-order TVD scheme.

Note that flux limiters are also called slope limiters because they both have the same mathematical form and both have the effect of limiting the solution gradient near shocks or discontinuities. Some of the limiters that are frequently used in general meshes include [81, 82, 83, 84], but this is not an exhaustive list of all the limiters available.

3.1.5.4 Second order in time

To extend the scheme to second order in time, there are methods such as the Runge-Kutta scheme, the MUSCL-Hancock type scheme, and other methods that are described in [85, 86]. Originally, the MUSCL-type scheme was introduced by Van Leer to allow for an extension to order two in space, as discussed above. Hancock proposes a MUSCL-type scheme that also allows for a second-order extension in time. This shift to the second order in time will increase the robustness of the calculations and limit the oscillations when approaching the CFL condition.

3.1.6 Godunov's scheme

The Godunov scheme [87] is the most natural finite volume scheme. It is based on the exact resolution of the Riemann problem, which is a Cauchy problem where the initial data is composed of only two constant states separated by a discontinuity

$$\begin{cases} \partial_t W + \partial_x \mathbf{F}(W) = 0, \\ W(0,x) = \begin{cases} W_L, & \text{if } x < 0, \\ W_R, & \text{if } x > 0. \end{cases} \end{cases} \tag{3.16}$$

We assume that the weak entropic self-similar solution of this problem, denoted by $W_{\mathcal{R}}\left(\frac{x}{t}, W_L, W_R\right)$, is known. It is well known that in a hyperbolic system, information propagates at a finite speed. Thus, $\lambda^-\left(W_L, W_R\right)$ and $\lambda^+\left(W_L, W_R\right)$ denote respectively the smallest and largest wave speeds developed by the Riemann problem $W_{\mathcal{R}}\left(\frac{x}{t}, W_L, W_R\right)$. Before introducing the Godunov scheme, we present the following result, which will be useful later.

Lemma 3.1.1. *Let Δt and Δx satisfy the following condition*

$$\frac{\Delta t}{\Delta x} \max \left|\lambda^{\pm}\left(W_L, W_R\right)\right| \leq \frac{1}{2}, \tag{3.17}$$

then, the mean of the exact solution of the Riemann problem (3.16) is given by

$$\frac{1}{\Delta x}\int_{-\Delta x/2}^{\Delta x/2} W_{\mathcal{R}}\left(\frac{x}{\Delta t}, W_L, W_R\right) dx = \frac{W_L + W_R}{2} - \frac{\Delta t}{\Delta x}\left(\boldsymbol{F}(W_R) - \boldsymbol{F}(W_L)\right). \tag{3.18}$$

Proof. We integrate equation (3.16) over the rectangle $[-\Delta x/2, \Delta x/2] \times [0, \Delta t]$ to obtain

$$\begin{aligned}\int_{-\Delta x/2}^{\Delta x/2} W_{\mathcal{R}}\left(\frac{x}{\Delta t}, W_L, W_R\right) dx - \int_{-\Delta x/2}^{\Delta x/2} W(0,x)dx + \int_0^{\Delta t} \mathbf{F}\left(W_{\mathcal{R}}\left(\frac{\Delta x}{2t}, W_L, W_R\right)\right) dt \\ - \int_0^{\Delta t} \mathbf{F}\left(W_{\mathcal{R}}\left(-\frac{\Delta x}{2t}, W_L, W_R\right)\right) dt = 0.\end{aligned} \tag{3.19}$$

The condition (3.17) implies that

$$W_{\mathcal{R}}\left(-\frac{\Delta x}{2t}, W_L, W_R\right) = W_L \quad \text{and} \quad W_{\mathcal{R}}\left(\frac{\Delta x}{2t}, W_L, W_R\right) = W_R, \quad \forall t \in [0, \Delta t], \tag{3.20}$$

we immediately obtain equation (3.18). We now consider an approximation of the solution at time t^n, which is piecewise constant

$$W_{\Delta x}^n(x) = W_i^n, \quad \text{if } x \in T_i. \tag{3.21}$$

Note that at each interface $x_{i+1/2}$, we have a local Riemann problem. Therefore, we can exactly solve the Cauchy problem

$$\begin{cases} \partial_t W + \partial_x \mathbf{F}(W) = 0, \\ W\left(x, t^n\right) = W_{\Delta x}^n(x), \end{cases} \tag{3.22}$$

at least for small time intervals $t^n + t$, the exact solution of this Cauchy problem is composed of the juxtaposition of local Riemann problems $W_{\mathcal{R}}\left(\frac{x - x_{i+1/2}}{t}, W_i^n, W_{i+1}^n\right)$ as long as they do not interact. A sufficient condition for the non-interaction of the local Riemann problems is the CFL condition introduced in [88]

$$\frac{\Delta t}{\Delta x}\max_{i\in\mathbb{Z}}\left|\lambda^{\pm}\left(W_i^n, W_{i+1}^n\right)\right| \leq \frac{1}{2}, \tag{3.23}$$

where, $W_{\Delta x}\left(x, t^n + t\right)$ denotes the solution of the Cauchy problem (3.22) if $x \in [x_i, x_{i+1}[$, where $W_{\mathcal{R}}\left(\frac{x - x_{i+1/2}}{t}, W_i^n, W_{i+1}^n\right)$ is the local Riemann problem. At time t^{n+1}, the solution $W_{\Delta x}$ is not constant on each cell T_i. Therefore, we perform an L^2 projection onto the space of constant functions on each cell T_i to define

$$W_i^{n+1} = \frac{1}{\Delta x}\int_{T_i} W_{\Delta x}\left(x, t^n + \Delta t\right) dx. \tag{3.24}$$

This provides an approximation of the solution at time t^{n+1}, constant on each cell T_i, defined by

$$W_{\Delta x}^{n+1}(x) = W_i^{n+1}, \quad \text{if } x \in T_i. \tag{3.25}$$

□

In summary, the Godunov scheme consists of two stages: an exact time evolution step followed by a spatial projection step. It is now demonstrated that the Godunov scheme can be expressed in a conservative form.

Lemma 3.1.2. *Let us assume that the CFL condition (3.23) is satisfied. Then, the Godunov scheme (3.24) is reformulated as a following conservative scheme*

$$W_i^{n+1} = W_i^n - \frac{\Delta t}{\Delta x}\left[\Phi\left(W_i^n, W_{i+1}^n\right) - \Phi\left(W_{i-1}^n, W_i^n\right)\right], \tag{3.26}$$

where a numerical flux given by

$$\Phi\left(W_L, W_R\right) = \boldsymbol{F}\left(W_{\mathcal{R}}\left(0, W_L, W_R\right)\right). \tag{3.27}$$

Furthermore, the numerical flux Φ is consistent with $\boldsymbol{F}$.

Proof. By definition, we have

$$\begin{aligned} W_i^{n+1} &= \frac{1}{\Delta x}\int_{T_i} W_{\Delta x}\left(x, t^n + \Delta t\right) dx \\ &= \frac{1}{\Delta x}\int_0^{\Delta x/2} W_{\mathcal{R}}\left(\frac{x}{\Delta t}, W_{i-1}^n, W_i^n\right) dx + \frac{1}{\Delta x}\int_{-\Delta x/2}^0 W_{\mathcal{R}}\left(\frac{x}{\Delta t}, W_i^n, W_{i+1}^n\right) dx, \end{aligned} \tag{3.28}$$

Integrating equation (3.16) over the rectangle $[0, \Delta x/2] \times [0, \Delta t]$, we obtain:

$$\frac{1}{\Delta x}\int_0^{\Delta x/2} W_{\mathcal{R}}\left(\frac{x}{\Delta t}, W_L, W_R\right) dx = \frac{1}{2}W_R - \frac{\Delta t}{\Delta x}\left(\mathbf{F}\left(W_R\right) - \mathbf{F}\left(W_{\mathcal{R}}\left(0, W_L, W_R\right)\right)\right), \tag{3.29}$$

and integrating equation (3.16) over the rectangle $[\Delta x/2, 0] \times [0, \Delta t]$, we obtain

$$\frac{1}{\Delta x}\int_{-\Delta x/2}^0 W_{\mathcal{R}}\left(\frac{x}{\Delta t}, W_L, W_R\right) dx = \frac{1}{2}W_L - \frac{\Delta t}{\Delta x}\left(\mathbf{F}\left(W_{\mathcal{R}}\left(0, W_L, W_R\right)\right) - \mathbf{F}\left(W_L\right)\right). \tag{3.30}$$

Therefore, we can write

$$W_i^{n+1} = W_i^n - \frac{\Delta t}{\Delta x}\left(\mathbf{F}\left(W_{\mathcal{R}}\left(0, W_i^n, W_{i+1}^n\right)\right) - \mathbf{F}\left(W_{\mathcal{R}}\left(0, W_{i-1}^n, W_i^n\right)\right)\right). \tag{3.31}$$

This represents the conservative form of the Godunov scheme, where the numerical flux F is defined by equation (3.27). The consistency of the numerical flux Φ with $\mathbf{F}$ is demonstrated by

$$\begin{aligned} \Phi(W, W) &= \mathbf{F}\left(W_{\mathcal{R}}(0, W, W)\right) \\ &= \mathbf{F}(W). \end{aligned} \tag{3.32}$$

□

Moreover, we demonstrate that the Godunov scheme is entropic.

Lemma 3.1.3. *States that assuming the CFL condition (3.23) is satisfied, the Godunov scheme (3.24) is entropic. This means that for any pair of entropy $(\eta, \mathcal{G})$, the scheme satisfies the discrete entropy inequality (2.12), where the entropy flux G is defined by the expression*

$$G\left(W_L, W_R\right) = \mathcal{G}\left(W_{\mathcal{R}}\left(0, W_L, W_R\right)\right).$$

Proof. Since η is a convex function, Jensen's inequality gives us

$$\begin{aligned}\eta\left(W_i^{n+1}\right) &\leq \frac{1}{\Delta x}\int_{T_i}\eta\left(W_{\Delta x}\left(x,t^n+\Delta t\right)\right)dx \\ &\leq \frac{1}{\Delta x}\int_0^{\Delta x/2}\eta\left(W_{\mathcal{R}}\left(\frac{x}{\Delta t},W_{i-1}^n,W_i^n\right)\right)dx \\ &+\frac{1}{\Delta x}\int_{-\Delta x/2}^0\eta\left(W_{\mathcal{R}}\left(\frac{x}{\Delta t},W_i^n,W_{i+1}^n\right)\right)dx.\end{aligned} \tag{3.33}$$

By integrating the entropy inequality (2.12) on the rectangle $[0,\Delta x/2]\times[0,\Delta t]$, we obtain

$$\frac{1}{\Delta x}\int_0^{\Delta x/2}\eta\left(W_{\mathcal{R}}\left(\frac{x}{\Delta t},W_L,W_R\right)\right)dx \leq \frac{1}{2}\eta\left(W_R\right)-\frac{\Delta t}{\Delta x}\left(\mathcal{G}\left(W_R\right)-\mathcal{G}\left(W_{\mathcal{R}}\left(0,W_L,W_R\right)\right)\right),$$

and integrating (2.12) over the rectangle $[-\Delta x/2,0]\times[0,\Delta t]$, we obtain

$$\frac{1}{\Delta x}\int_{-\Delta x/2}^0\eta\left(W_{\mathcal{R}}\left(\frac{x}{\Delta t},W_L,W_R\right)\right)dx \leq \frac{1}{2}\eta\left(W_L\right)-\frac{\Delta t}{\Delta x}\left(\mathcal{G}\left(W_{\mathcal{R}}\left(0,W_L,W_R\right)\right)-\mathcal{G}\left(W_L\right)\right).$$

The discrete entropy inequality is deduced

$$\eta\left(W_i^{n+1}\right)\leq\eta\left(W_i^n\right)-\frac{\Delta t}{\Delta x}\left(\mathcal{G}\left(W_{\mathcal{R}}\left(0,W_i^n,W_{i+1}^n\right)\right)-\mathcal{G}\left(W_{\mathcal{R}}\left(0,W_{i-1}^n,W_i^n\right)\right)\right).$$

It remains to be shown that the numerical flux of entropy

$$G\left(W_L,W_R\right)=\mathcal{G}\left(W_{\mathcal{R}}\left(0,W_L,W_R\right)\right),$$

□

is consistent with $\mathcal{G}$, which is the case because $W_{\mathcal{R}}(0,W,W)=W$. Although accurate due to its reliance on the exact resolution of Riemann problems, the Godunov scheme has several drawbacks and is often superseded by other schemes. In fact, the exact resolution of Riemann problems can be very difficult or even impossible for some systems and it is often computationally expensive. Additionally, the accuracy achieved by the exact evolution step is erased by the projection step. An alternative emerged in the 1980*s* with the work of Roe [69] and Harten, Lax, and Van Leer [89], which involves using an approximate solution of the Riemann problem instead of the exact solution. This approach leads to Godunov-type schemes, whose formalism was introduced by Harten et al. [89]. The basic idea is to use an approximation $\widetilde{W}\left(\frac{x}{t},W_L,W_R\right)$ of the solution of the Riemann problem (3.16). To ensure that all the necessary information is retained, it is necessary to include the domain of dependence of the exact solution within the domain of dependence of the approximate solution. Furthermore, it is required that the average of the exact solution over a cell be preserved by the approximate solver, see [89] for more details.

3.2 Boundary conditions

The process of modeling and providing a theoretical framework for boundary conditions in hyperbolic problems presents intricate challenges that have been extensively explored in numerous studies, such as those by [33, 64, 90]. Nevertheless, it is possible to effectively address relatively simple scenarios, including those involving stationary or mobile walls.

3.2.1 Shallow water flow

In a free surface flow problem, boundaries are classified into two types: solid and open boundaries.

► ***Wall boundary condition***

On this boundary, no flow must cross. The normal component of the velocity vector as well as the gradient of the free surface, must be zero ("mirror" effect of the wall)

$$\partial_\eta h = 0 \quad \text{and} \quad u_\eta = 0. \tag{3.34}$$

The tangential component of the velocity vector can be zero, i.e., the wall can slip or not. In the case of non-slip walls, we impose that the tangential component of the velocity vector u_τ at the boundary is zero, i.e.,

$$u_\tau = 0. \tag{3.35}$$

For slip walls, the condition implies that the normal velocity and the gradient normal to the wall of the tangential velocity are zero.

$$u_\eta = 0 \quad \text{and} \quad \partial_\eta u_\tau = 0. \tag{3.36}$$

► ***Open boundary condition***

The open boundary conditions are the most difficult to deal with because they involve the existence of a fluid domain that does not belong to the computational domain but that can influence it and may influence it [91]. In practice, the different types of boundary conditions adapted to the four types of boundaries are composed in a modular way:

- Flow rate and free surface are prescribed variables, specifically in the context of supercritical flow at the inlet
- Uniform flow or a free surface condition imposed, in the case of subcritical flow at the inlet
- Free boundary, no conditions imposed (supercritical flow at the outlet)
- Imposed free surface (subcritical flow at the inlet)

A unit flow rate or normal velocity is typically prescribed at the boundary as an inlet condition for the computational domain. Consequently, an additional requirement for the height of the free surface is necessary to ensure the well-posedness of the 2D flow problem.
In a free surface flow problem, a condition on the free surface elevations is often imposed at the end of the computational domain. This information is sufficient for the outgoing flow. However, an additional condition on the flow rate or velocity at the outlet may be necessary when the flow is incoming [90].

In this context of shallow water flow, other types of boundary conditions have been proposed. Among them are conditions based on the method of characteristics, where the prescribed beginning or elevation is calculated from Riemann invariants that are constant along characteristic lines [40, section 4.2]. The radiation method, proposed by [92], is also widely utilized in ocean modeling. [93, 94, 95, 96, 97].

3.2.2 Euler equations

Similar to free surface flow, handling boundary conditions continues to be a unique challenge in solving the system of Euler equations. When calculating the gradient, it is essential to differentiate the scenario where the control volume surface corresponds to a domain edge. In such instances, it is necessary to distinguish between two situations, depending on whether the surface represents a wall (either fixed or moving) or a fluid interface.

In the case of a fluid interface, such as an absorbing boundary condition or a prescribed flow rate, a straightforward approach is to extrapolate the values of conservative or primitive variables from the control volume to the fluid boundary.

$$\mathbf{W}_{edge} = \mathbf{W}_i. \tag{3.37}$$

In the case of a wall, the field $\mathbf{W}$ of the conservative variables at the center of gravity of the face is estimated simply as the arithmetic mean between the field $\mathbf{W}_i$ at the center of the element and its mirror state $\mathbf{W}_i^M$ expressed in the global frame. For the mirror state, the associated normal velocity is the opposite sign of the normal velocity, while the tangent velocities are equal. The fluid velocity can be decomposed into a normal component $\mathbf{u}_n$ at the surface and a tangential component $\mathbf{u}_\tau$ as

$$\mathbf{u} = \mathbf{u}_n + \mathbf{u}_\tau, \tag{3.38}$$

where $\mathbf{u}_n = (\mathbf{u} \cdot n) \cdot n \quad$ and $\mathbf{u}_\tau = \mathbf{u} - \mathbf{u}_n = \mathbf{u} - (\mathbf{u} \cdot n) \cdot n$.

For the mirror state, the normal velocities are of opposite sign and the tangential velocities are equal to that of the fluid of the element adjacent to the face, that is

$$\begin{cases} \mathbf{u}^M = \mathbf{u}_n^M + \mathbf{u}_\tau^M, \\ \quad\quad = -\mathbf{u}_n + \mathbf{u}_{\tau^{\text{`}}}, \\ \quad\quad = -(\mathbf{u} \cdot n) \cdot n + \mathbf{u} - (\mathbf{u} \cdot n) \cdot n, \\ \quad\quad = \mathbf{u} - 2(\mathbf{u} \cdot n) \cdot n. \end{cases} \tag{3.39}$$

The mirror state $\mathbf{W}_i^M$ is defined in the case of a fixed wall by

$$\begin{cases} \rho_i^M = \rho_i, \\ p_i^M = p_i, \\ \rho u_i^M = \rho_i (u_i - 2(\mathbf{u}_i \cdot n_{ij}) \cdot n_{x_{ij}}), \\ \rho v_i^M = \rho_i (v_i - 2(\mathbf{u}_i \cdot n_{ij}) \cdot n_{y_{ij}}), \\ \rho w_i^M = \rho_i (w_i - 2(\mathbf{u}_i \cdot n_{ij}) \cdot n_{z_{ij}}), \\ \rho E_i^M = \rho E_i. \end{cases} \tag{3.40}$$

In the case of a moving wall, the $\mathbf{W}$ field of conservative variables at the center of gravity of the face is estimated simply as the arithmetic mean between the $\mathbf{W}_i$ field at the center of the

element and its mirror state expressed in the local reference frame.

$$\begin{cases} \rho_i^M = \rho_i, \\ p_i^M = p_i, \\ (\mathbf{u}_{\tau^1}^M)_i = (\mathbf{u}_{\tau^1})_i, \\ (\mathbf{u}_{\tau^2}^M)_i = (\mathbf{u}_{\tau^2})_i, \\ (\mathbf{u}_n^M)_i = -(\mathbf{u}_n)_i + 2\mathbf{V}\cdot n, \\ \rho E_i^M = \rho E_i^M + \dfrac{1}{2}\Big(\rho_i^M(\mathbf{u}_n)_i^2 - \rho_i(\mathbf{u}_n)_i^2\Big), \end{cases} \tag{3.41}$$

where

- $(\mathbf{u}_n)_i$, $(\mathbf{u}_{\tau^1})_i$, $(\mathbf{u}_{\tau^2})_i$ are respectively the fluid velocities of the control volume i expressed in the local reference frame of the face.
- $(\mathbf{u}_n^M)_i$, $(\mathbf{u}_{\tau^1}^M)_i$, $(\mathbf{u}_{\tau^2}^M)_i$ are the velocities associated with the mirror state in the local reference frame of the face.
- $\mathbf{V}$ is the grid speed (in the case of a mobile mesh) such that $\mathbf{V} = \frac{X(t_{n+1})-X(t_n)}{\Delta t}$.

3.3 Background on FVC Scheme

In this thesis, we develop a Characteristic Finite Volume (FVC) scheme based on the one proposed by Benkhaldoun and Seaïd [31], expanding it to be applicable to unstructured 2D and 3D meshes. The FVC scheme was initially introduced in a one-dimensional version for simulating the 1D shallow water equations. An aspect of the FVC scheme is its independence from the Jacobian matrix of the equation system for constructing the numerical flux. Additionally, it circumvents the need to solve the Riemann problem at each interface, making it an efficient method in terms of CPU time.

The FVC scheme exhibits well-balanced, conservative, and non-oscillatory characteristics, making it suitable for hyperbolic equations where Riemann problems are difficult to solve. According to [31, Lemma 3.1], this scheme is stable and Total Variation Diminishing (TVD). Moreover, the second-order transition occurs automatically, bypassing the MUSCL reconstruction procedure, as shown in Lemma 3.2 in [31]. Benkhaldoun and Sari [30] also presented a two-dimensional extension of this scheme, albeit in a formulation exclusive to Cartesian grids.

In this subsection, we begin by briefly reviewing the one-dimensional FVC scheme, and then we present in the following chapters the FVC approach in unstructured grids for two and three spatial dimensions.

3.3.1 One-dimensional FVC scheme

The scalar conservation law (3.42) is considered to formulate the 1D FVC scheme, which combines the method of characteristics and the finite volumes method

$$\partial_t W(t,x) + \partial_x \mathbf{F}(W(t,x)) = \mathbf{S}(W(t,x)), \tag{3.42}$$

where W is a scalar function from $\Omega \subset \mathbb{R}\times[0,T)$ to $\mathbb{R}$. Its finite volume formulation in a one-dimensional grid is given by

$$W_i^{n+1} = W_i^n - \frac{\Delta t}{\Delta x}\left[\Phi\left(W_{i+1/2}^n\right) - \Phi\left(W_{i-1/2}^n\right)\right] + \Delta t \mathbf{S}_i^n. \tag{3.43}$$

The process of spatially discretizing the equation (3.43) is accomplished when a numerical representation of the fluxes, $\Phi\left(W^n_{i\pm1/2}\right)$, is determined. Generally, this involves solving Riemann problems at the $x_{i\pm1/2}$ boundaries. However, this can be computationally challenging and may restrict the technique's applicability when solutions to Riemann problems are intricate or unattainable. That is why we have chosen to construct intermediate states, $W^n_{i\pm1/2}$, using the method of characteristics. The numerical flux is subsequently computed with the physical flux as $\Phi\left(W_{i\pm1/2}\right) := \mathbf{F}\left(W_{i\pm1/2}\right)$. This approach's fundamental concept involves implementing a uniform grid at the updated time step and tracing the flow's trajectories back to the previous time step.

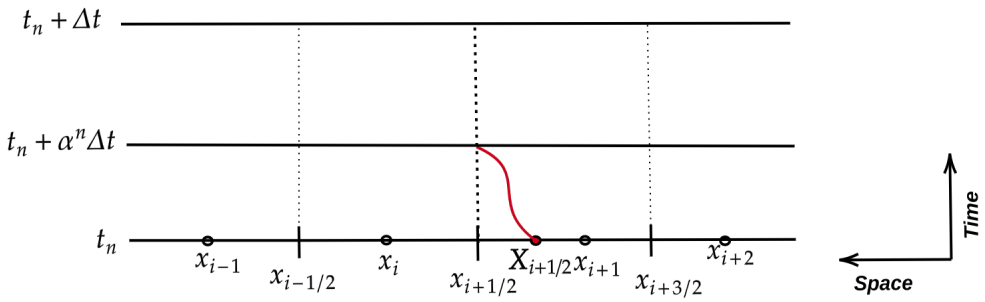

Fig 3.7. Space-time control volumes used by the FVC scheme.

Quantities required for the calculation are assessed at the previous time step by interpolating the known values on a consistent time-based grid. Consequently, the characteristic curves related to equation (3.42), excluding the source term, effectively serve as solutions to the given problem

$$\begin{cases} \dfrac{\mathrm{d}\mathbf{X}_{i+1/2}(s)}{\mathrm{d}s} = V_{i+1/2}\left(s, \mathbf{X}_{i+1/2}(s)\right), \quad s \in [t_n, t_n + \alpha^n \Delta t], \\ \mathbf{X}_{i+1/2}\left(t_n + \alpha^n \Delta t\right) = x_{i+1/2}, \end{cases} \tag{3.44}$$

where $V_{i+1/2} = \mathbf{F}'\left(W_{i+1/2}\right)$ et $\alpha^n \in]\,0, 1]$ is a parameter to be chosen later. Note that $\mathbf{X}_{i+1/2}(s)$ is the departure point at time s of the particle that will reach the interface $x_{i+1/2}$ of the grid at time $t_n + \alpha^n \Delta t$. The solutions of (3.44) can be expressed as

$$\begin{aligned} \mathbf{X}_{i+1/2}\left(t_n\right) &= x_{i+1/2} - \int_{t_n}^{t_n + \alpha^n \Delta t} V_{i+1/2}\left(s, \mathbf{X}_{i+1/2}(s)\right) ds, \\ &= x_{i+1/2} - \mathbf{I}_{i+1/2}. \end{aligned} \tag{3.45}$$

In the case where the velocity field is explicitly provided and does not depend on the solution W, the integral in (3.45) can be computed analytically. Alternatively, for other situations, this integral can be evaluated using a second-order extrapolation, which is based on the mid-point rule. This approach typically results in a non-linear equation involving $\mathbf{X}_{i+1/2}(t_n)$. To resolve this equation, it becomes necessary to employ a root-finding algorithm. For comprehensive understanding, the algorithm's reformulation for determining the initial points is elaborated upon in the appendix of [31]. After determining the characteristic curves $\mathbf{X}_{i+1/2}\left(t_n\right)$, the numerical fluxes in (3.43) can be reconstructed by employing the subsequent equation, as referenced in [98, section 2.1.2]

$$W^n_{i+1/2} = W\left(t_n + \alpha \Delta t, x_{i+1/2}\right) = \tilde{W}\left(t_n, \mathbf{X}_{i+1/2}\left(t_n\right)\right) + \int_{t_n}^{t_n + \alpha^n \Delta t} \mathbf{S}\left(W\left(s, x(s)\right)\right) ds, \tag{3.46}$$

where $\tilde{W}\left(t_n, \mathbf{X}_{i+1/2}(t_n)\right)$ is the solution at the foot of the characteristic calculated by interpolation from the solutions on the neighboring control volumes of the interface

$$\tilde{W}\left(t_n, \mathbf{X}_{i+1/2}(t_n)\right) = \mathcal{P}\left(W\left(t_n, \mathbf{X}_{i+1/2}(t_n)\right)\right), \tag{3.47}$$

where $\mathcal{P}$ represents a Lagrange interpolation polynomial calculated from the evolved solution at the center of each control volume.

Therefore, the proposed FVC scheme can be interpreted as a predictor step (3.46) where the intermediate state $W_{i\pm1/2}$ is computed and the corrector step $\left(\Phi\left(W_{i\pm1/2}\right) := \mathbf{F}\left(W_{i\pm1/2}\right)\right)$ where the conservation property is preserved. Note that interpolation procedures other than (3.47) can also be applied.

3.3.2 Analysis of FVC scheme

To analyze the FVC scheme, we consider a nonlinear conservation law's scalar homogeneous equation, which can be expressed as follows

$$\partial_t u + \partial_x(\mathbf{F}(u)) = 0, \tag{3.48}$$

In this part, we make the assumption that a linear interpolating polynomial $\mathcal{P}$ is used in the predictor stage (3.47). Thus, we have the following results [31]

Lemma 3.3.1. *Suppose $u_0 \in L^\infty(\mathbb{R})$ with $u_{\min} = \min(u_0)$ and $u_{\max} = \max(u_0)$. Define $\lambda = \sup_{u\in[u_{\min},u_{\max}]} |\boldsymbol{F}'(u)|$, and let Δt satisfy the condition*

$$\frac{1}{2\alpha^n} \leq \lambda\frac{\Delta t}{\Delta x} \leq \frac{1}{\sqrt{2\alpha^n}}. \tag{3.49}$$

Then the FVC scheme (3.46) and (3.43) is stable and TVD.

Proof. Applied to the problem (3.48), the corrector stage (3.43) (here $\mathbf{S}_i = 0$) gives

$$U_i^{n+1} = U_i^n - v\left(\mathbf{F}\left(U_{i+1/2}^n\right) - \mathbf{F}\left(U_{i-1/2}^n\right)\right), \tag{3.50}$$

with $v = \frac{\Delta t}{\Delta x}$ and the averaged states are given by

$$U_{i+1/2}^n = u\left(t_n + \alpha^n\Delta t, x_{i+1/2}\right) = u\left(t_n, \mathbf{X}_{i+1/2}\right), \tag{3.51}$$

where the characteristic curves are given by

$$\mathbf{X}_{i+1/2} = x_{i+1/2} - \alpha^n\Delta t\mathbf{F}'\left(U_{i+1/2}^n\right). \tag{3.52}$$

Using the linear interpolating polynomial, the solution at the departure points in (3.51) is calculated as

$$\begin{aligned} U_{i+1/2}^n &= U_i^n + \left(\mathbf{X}_{i+1/2} - x_i\right)\frac{U_{i+1}^n - U_i^n}{x_{i+1} - x_i}, \\ &= U_i^n + \frac{\frac{\Delta x}{2} - \alpha^n\Delta t\mathbf{F}'\left(U_{i+1/2}^n\right)}{\Delta x}\left(U_{i+1}^n - U_i^n\right). \end{aligned} \tag{3.53}$$

Hence, the predictor stage (3.46) becomes

$$U_{i+1/2}^n = \frac{U_i^n + U_{i+1}^n}{2} - \alpha^n v\mathbf{F}'\left(U_{i+1/2}^n\right)\left(U_{i+1}^n - U_i^n\right). \tag{3.54}$$

Note that we have assumed by construction that the problem (3.54) has a unique solution. There exists $\gamma_i^n \in \left[U_{i-1/2}^n, U_{i+1/2}^n\right]$ such that

$$\mathbf{F}\left(U_{i+1/2}^n\right) - \mathbf{F}\left(U_{i-1/2}^n\right) = \mathbf{F}'\left(\gamma_i^n\right)\left(U_{i+1/2}^n - U_{i-1/2}^n\right). \tag{3.55}$$

Thus, substituting (3.54) in the corrector stage (3.50) we obtain

$$\begin{aligned} U_i^{n+1} = U_i^n - v\mathbf{F}'\left(\gamma_i^n\right)\left[\left(\frac{1}{2} - \alpha^n v\mathbf{F}'\left(U_{i+1/2}^n\right)\right)\left(U_{i+1}^n - U_i^n\right)\right] \\ - v\mathbf{F}'\left(\gamma_i^n\right)\left[\left(\frac{1}{2} + \alpha^n v\mathbf{F}'\left(U_{i-1/2}^n\right)\right)\left(U_i^n - U_{i-1}^n\right)\right], \end{aligned} \tag{3.56}$$

which can be reformulated in a compact form as

$$U_i^{n+1} = U_i^n + C_{i+1/2}^n \Delta U_{i+1/2}^n - D_{i-1/2}^n \Delta U_{i-1/2}^n, \tag{3.57}$$

where $\Delta U_{i+1/2}^n = U_{i+1}^n - U_i^n$,
$C_{i+1/2}^n = v\mathbf{F}'\left(\gamma_i^n\right)\left(\alpha^n v\mathbf{F}'\left(U_{i+1/2}^n\right) - \frac{1}{2}\right)$ and $D_{i-1/2}^n = \mathbf{F}'\left(\gamma_i^n\right) v\left(\alpha^n v\mathbf{F}'\left(U_{i-1/2}^n\right) + \frac{1}{2}\right)$. Under the condition (3.49), it is clear that

$$C_{i+1/2}^n \geq 0, \quad D_{i-1/2}^n \geq 0, \quad C_{i+1/2}^n + D_{i-1/2}^n \leq 1. \tag{3.58}$$

Therefore, the characteristic finite volume scheme is L^∞-stable, see [99, section 3.2 p 133] □

Lemma 3.3.2. *Assume a linear interpolating polynomial $\mathcal{P}$ is used in the predictor stage (3.47). The FVC method is second-order accurate scheme if $\alpha^n = 1/2$.*

Proof. By using a linear interpolating polynomial $\mathcal{P}$, the FVC method yields

$$\begin{aligned} U_{i+1/2}^n &= \frac{U_i^n + U_{i+1}^n}{2} - \alpha^n \frac{\Delta t}{\Delta x}\mathbf{F}'\left(U_{i+1/2}^n\right)\left(U_{i+1}^n - U_i^n\right), \\ U_i^{n+1} &= U_i^n - \frac{\Delta t}{\Delta x}\left(\mathbf{F}\left(U_{i+1/2}^n\right) - \mathbf{F}\left(U_{i-1/2}^n\right)\right). \end{aligned} \tag{3.59}$$

The FVC method (3.59) can be easily formulated in a compact form as

$$U_i^{n+1} = H\left(U_{i-1}^n, U_i^n, U_{i+1}^n\right). \tag{3.60}$$

Hence, the truncation error associated with (3.60) is defined by

$$u(x, t+\Delta t) - H(u(x-\Delta x, t), u(x,t), u(x+\Delta x, t)) = -\Delta t^2 \frac{\partial}{\partial x}\left(\beta\left(u, \frac{\Delta t}{\Delta x}\right)\frac{\partial u}{\partial x}\right) + \mathcal{O}\left(\Delta t^3\right), \tag{3.61}$$

where

$$\beta(u, v) = \frac{1}{2v^2}\sum_{j=-1}^{+1} j^2 \frac{\partial H}{\partial v_j}(u, u, u) - \frac{1}{2}\left(\mathbf{F}'(u)\right)^2. \tag{3.62}$$

The proof of the Lemma 3.3.2 follows from the [99, proposition 1.2 p 103] which states that if β vanishes in (3.61), then the scheme (3.60) is second-order accurate. Indeed,

$$\begin{aligned} \frac{\partial H}{\partial U_{i+1}} &= -v\mathbf{F}'\left(U_{i+1/2}^n\right)\frac{\partial U_{i+1/2}^n}{\partial U_{i+1}}, \\ \frac{\partial H}{\partial U_{i-1}} &= v\mathbf{F}'\left(U_{i-1/2}^n\right)\frac{\partial U_{i-1/2}^n}{\partial U_{i-1}}. \end{aligned} \tag{3.63}$$

Hence,

$$\begin{aligned}\frac{\partial H}{\partial U_{i+1}}(u,u,u) &= -v\mathbf{F}'(u)\left(\frac{1}{2}-\alpha^n v f'(u)\right),\\ \frac{\partial H}{\partial U_{i-1}}(u,u,u) &= v\mathbf{F}'(u)\left(\frac{1}{2}+\alpha^n v f'(u)\right).\end{aligned} \tag{3.64}$$

Thus,

$$\beta = \left(\alpha^n - \frac{1}{2}\right)\left(\mathbf{F}'(u)\right)^2. \tag{3.65}$$

It is clear that for $\alpha^n = 1/2$, the parameter $\beta = 0$ and this resumes the proof. □

3.3.2.1 Application of FVC scheme to transport equation

In order to simplify the formulation of the FVC scheme, we propose to use the transport equation with a constant velocity, and a linear interpolation polynomial in the predictor step (3.46). Let the following transport equation

$$\partial_t u + \partial_x(\mathbf{f}(u)) = 0, \tag{3.66}$$

where $\mathbf{f}$ is the physical flux given by $\mathbf{f}(u) = \mathbf{c}u$, and $\mathbf{c}$ is a real constant representing the transport velocity of the quantity u.
The backward characteristic curves (formula (3.45)) are given by

$$\mathbf{X}_{i+1/2}(t_n) = x_{i+1/2} - \alpha^n \Delta t \mathbf{c}. \tag{3.67}$$

Using linear interpolation, the solution at the departure points in (3.47) is calculated by

$$\begin{aligned}u^n_{i+1/2} &= u^n_i + \Big(\mathbf{X}_{i+1/2} - x_i\Big)\frac{u^n_{i+1}-u^n_i}{\Delta x},\\ &= u^n_i + \Big(\frac{\Delta x}{2} - \alpha^n \Delta t \mathbf{c}\Big)\frac{u^n_{i+1}-u^n_i}{\Delta x}.\end{aligned} \tag{3.68}$$

Thus the predictor stage (3.46) becomes

$$u^n_{i+1/2} = \frac{u^n_i - u^n_{i+1}}{2} - \alpha^n \frac{\Delta t}{\Delta x}\mathbf{c}\Big(u^n_{i+1} - u^n_i\Big). \tag{3.69}$$

Therefore, the FVC scheme is written using linear interpolation as

$$u^n_{i+1/2} = \frac{u^n_i - u^n_{i+1}}{2} - \alpha^n \frac{\Delta t}{\Delta x}\mathbf{c}\Big(u^n_{i+1} - u^n_i\Big), \tag{3.70a}$$

$$u^{n+1}_i = u^n_i - \frac{\Delta t}{\Delta x}\Big(\mathbf{f}(u^n_{i+1/2}) - \mathbf{f}(u^n_{i-1/2})\Big). \tag{3.70b}$$

We propose performing a numerical calculation to solve the transport equation using the FVC scheme. Our objective is to compare the solution obtained with this scheme to the exact solution, as well as two other schemes known in the literature. To begin, we define the initial condition as a step function, where the function $u(x,0)$ is equal to 1 in the interval $[0.5, 1.5]$ and zero elsewhere. The scalar transport velocity used is $\mathbf{c} = 2m/s$. Regarding the numerical parameters, we choose a CFL condition equal to 0.8, $\alpha^n = 0.7$ and a grid with 100 cells. In summary, this approach involves numerically solving the transport equation using the FVC scheme.

The results obtained are illustrated in Fig 3.8, which clearly highlights that this simplified version of the FVC scheme exhibits lower diffusion compared to the other schemes.

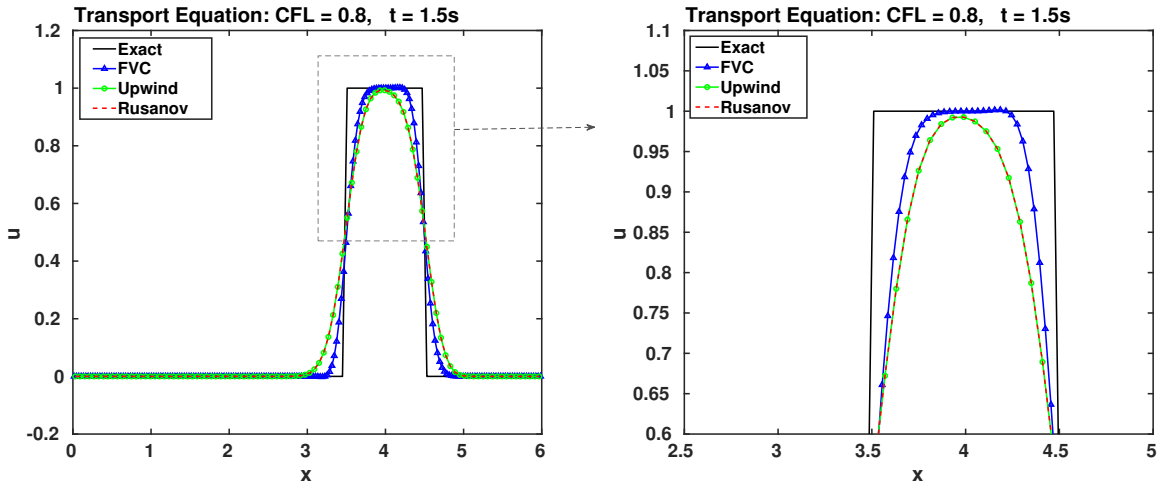

Fig 3.8. Comparison of results for the transport equation: the scalar quantity $u(x,t)$ (left) and a closer look at $u(x,t)$ (right) at a time $t = 1.5s$ using a grid with 100 regular cells.

The adaptation of the FVC scheme for hyperbolic systems in the context of conservation laws can be carried out by examining each component individually, provided that the conservative equations can be restructured into an advective form. Generally, the investigated system's advective representation is expressed in such a way that both non-conservative and conservative variables are transported using an identical velocity field. This concept for one-dimensional hyperbolic systems of conservation laws is discussed in [31, section 4].
In this context of the equation systems, we present a comparison between the solutions obtained using the FVC scheme for the one-dimensional shallow water system and those obtained using the SRNH scheme (Non-Homogeneous Riemann Solver) proposed and studied in [100], Roe and Rusanov. The computed water heights are shown in Fig 3.9 at time $t = 50s$ using a spatial discretization of $\Delta x = 10m$.

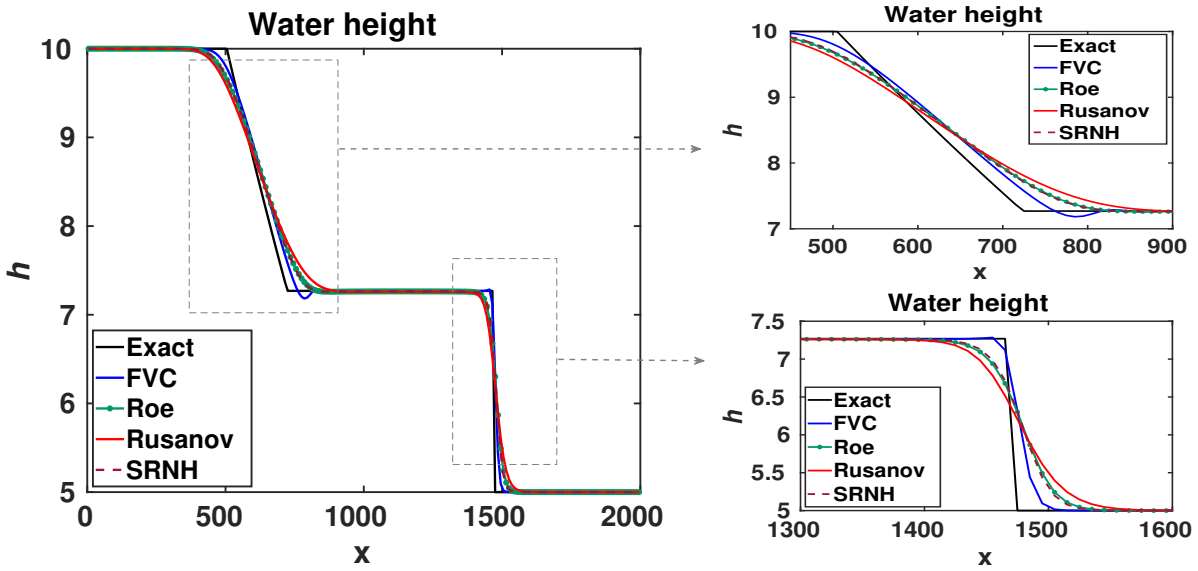

Fig 3.9. Comparative results for dam break problem [31] in 1D shallow water equations: water height (left) and a zoom on water height around the rarefaction and shock regions (right) at time $t = 50s$ with 200 regular cells.

For the considered dam break conditions, the FVC scheme produces numerical results that are as accurate as those obtained using the SRNH and Roe schemes, with low computational costs. A detailed study has been conducted in [31]. A similar study was conducted in [101] on the Euler equations, and a portion of the results are displayed in Fig 3.10. The same observation was made regarding the accuracy of the FVC scheme, especially in capturing contact discontinuities. Additionally, the computational speed of the FVC scheme, as measured by CPU performance, remains considerable see [101, table 2].

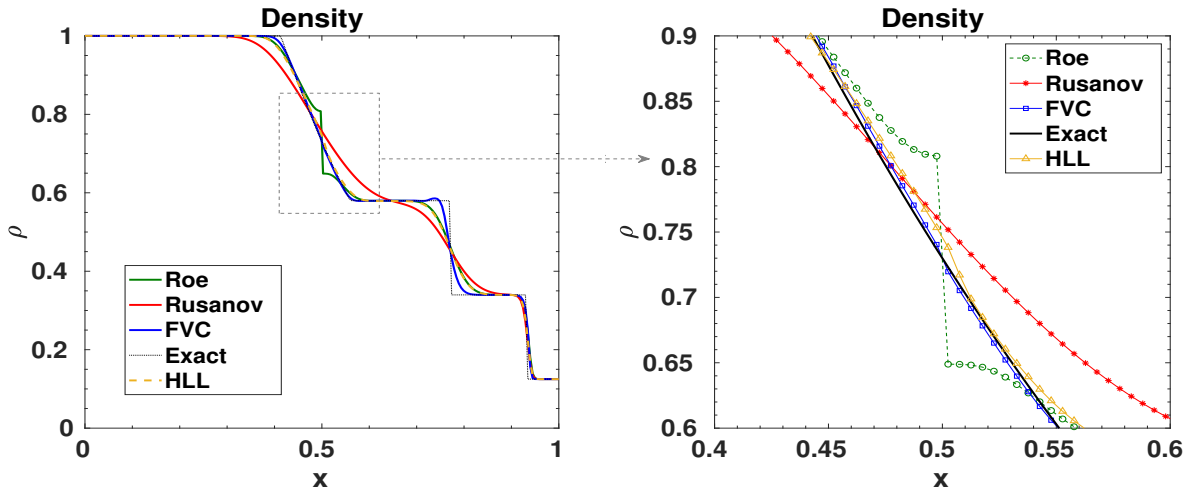

Fig 3.10. Comparative results for shock tube problem [102] in 1D Euler equations: density (left) and a zoom on density around the sonic point (right) at time $t = 0.2s$ with 200 regular cells.

3.3.3 Two-dimensional FVC scheme in Cartesian mesh

This section aims to construct the FVC scheme for two-dimensional conservation law systems in a Cartesian mesh

$$\partial_t W + \partial_x \mathbf{F}(W) + \partial_y \mathbf{G}(W) = 0, \tag{3.71}$$

where W is the unknown solution, $\mathbf{F}(W)$ and $\mathbf{G}(W)$ are non-linear flux functions and can depend on space as well as on time.

To explain the FVC scheme on a structured mesh, we start by discretizing the spatial domain into rectangular cells $\mathcal{C}_{i,j} = \left[x_{i-\frac{1}{2}}, x_{i+\frac{1}{2}}\right] \times \left[y_{j-\frac{1}{2}}, y_{j+\frac{1}{2}}\right]$. Then, we integrate equation (3.71) in time on each control volume $\mathcal{C}_{i,j}$. The idea of finite volumes is to construct a numerical sequence of the form

$$W_{i,j}^{n+1} = W_{i,j}^{n} - \frac{\Delta t}{\Delta x}\left(\mathcal{F}_{i+1/2,j}^{n} - \mathcal{F}_{i-1/2,j}^{n}\right) - \frac{\Delta t}{\Delta y}\left(\mathcal{G}_{i,j+1/2}^{n} - \mathcal{G}_{i,j-1/2}^{n}\right), \tag{3.72}$$

where

$$W_{i,j}^{n} \approx \frac{1}{\Delta x}\frac{1}{\Delta y}\int_{x_{i-\frac{1}{2}}}^{x_{i+\frac{1}{2}}}\int_{y_{j-\frac{1}{2}}}^{y_{i+\frac{1}{2}}} W\left(t_n, x, y\right) dxdy, \tag{3.73}$$

$$\mathcal{F}_{i\pm1/2,j}^{n} \approx \frac{1}{\Delta t}\int_{t_n}^{t_{n+1}} \mathbf{F}\left(W\left(t, x_{i\pm1/2}, y_j\right)\right) dt,$$

and

$$\mathcal{G}^n_{i,j\pm1/2} \approx \frac{1}{\Delta t}\int_{t_n}^{t_{n+1}} \mathbf{G}\left(W\left(t_n, x_i, y_{j\pm1/2}\right)\right) dt.$$

As already mentioned, the main idea of this method is to impose a regular grid at time t_n and to look for an approximation of the quantities $W^n_{i\pm1/2,j}$ and $W^n_{i,j\pm1/2}$ by going backwards along the flow trajectories between time $t_n + \alpha^n\Delta t$ and t_n. The necessary quantities are evaluated at the former time level by interpolating their known values on the regular grid. Thereafter, the numerical flux $\mathcal{F}^n_{i\pm1/2,j}$ (respectively $\mathcal{G}^n_{i\pm1/2,j}$) will be evaluated using the physical flux as $\mathcal{F}^n_{i\pm1/2,j} := \mathbf{F}(W^n_{i\pm1/2,j})$ (respectively $\mathcal{G}^n_{i\pm1/2,j} := \mathbf{G}(W^n_{i\pm1/2,j})$).
Since, the conservation law (3.71) can be rewritten in an advective form as

$$\partial_t W + \mathbf{F}'(W)\partial_x(W) + \mathbf{G}'(W)\partial_y(W) = 0, \tag{3.74}$$

then the characteristic curves associated with equation (3.74) are solutions of the flowing ordinary differential equation

$$\begin{cases} \dfrac{\mathrm{d}\mathbf{X}_{i+1/2,j}(s)}{\mathrm{d}s} = \mathcal{U}\left(s, \mathbf{X}_{i+1/2,j}(s), y_j(s)\right), \quad s \in [t_n, t_n + \alpha^n\Delta t], \\ \mathbf{X}_{i+1/2,j}\left(t_n + \alpha^n\Delta t\right) = x_{i+1/2}, \end{cases} \tag{3.75}$$

with a similar system of the characteristic curves $\mathbf{Y}_{i,j+1/2}(s)$ in the y-direction, and instead of $\mathcal{U}$ we have, $\mathcal{V}\left(x_i, \mathbf{Y}_{j+1/2}(s), s\right)$.

$\mathcal{U}$ and $\mathcal{V}$ being the advection velocities defined by

$$\mathcal{U}(t,x,y) = \mathbf{F}'(W(t,x,y)), \quad \text{and} \quad \mathcal{V} = \mathbf{G}'(W(t,x,y)). \tag{3.76}$$

The solution of (3.75) can be expressed as

$$\mathbf{X}_{i+1/2,j}\left(t_n\right) = x_{i+1/2,j} - \int_{t_n}^{t_n+\alpha^n\Delta t} \mathcal{U}\left(s, \mathbf{X}_{i+1/2,j}(s), y_j(s)\right) ds \tag{3.77}$$

The same formula applies to $\mathbf{Y}_{i+1/2,j}$. Moreover, the numerical fluxes in (3.72) are calculated using

$$\begin{aligned} W^n_{i+1/2,j} &= \tilde{W}\left(t_n, \mathbf{X}_{i+1/2}\left(t_n\right), y_j\right) = \mathcal{P}\left(W\left(t_n, \mathbf{X}_{i+1/2}\left(t_n\right), y_j\right)\right), \\ W^n_{i,j+1/2} &= \tilde{W}\left(t_n, x_i, \mathbf{Y}_{j+1/2}\left(t_n\right)\right) = \mathcal{P}\left(W\left(t_n, x_i, \mathbf{Y}_{j+1/2}\left(t_n\right)\right)\right), \end{aligned} \tag{3.78}$$

where $\widetilde{W}\left(t_n, \mathbf{X}_{i+1/2}\left(t_n\right), y_j\right)$ and $\widetilde{W}\left(t_n, x_i, \mathbf{Y}_{j+1/2}\left(t_n\right)\right)$ are the solutions to the characteristics foot calculated by interpolation and $\mathcal{P}$ is a polynomial interpolation to be defined.
So far, the FVC scheme has been presented in the formalism of Cartesian mesh, however, real-world problems are characterized by high topographical and geometrical complexity, which limits the applicability of this formalism. A more in-depth study of the accuracy of this finite volume discretization method on unstructured meshes has always been the goal of this work (see the conclusions of [29] and [30]). Therefore, the unstructured finite volume method not only ensures mass conservation, which is an important property in fluid flow calculations, but also allows for the accurate representation of the complex geometry of the computational domain. For these reasons, in the following chapters, we propose an extension of this scheme to unstructured meshes in two and three dimensions of space.

Third Part

FVC Scheme on Unstructured Meshes in Multiple Spatial Dimensions

Chapter 4

2D FVC scheme on unstructured meshes: application to free surface flows in shallow water

Short summary

In this particular chapter, we introduce an expanded and generalized version of the FVC scheme, specifically tailored to the context of finite volume discretization on non-uniform triangular meshes, utilizing a cell-centered formulation.

4.1 Shallow water equations

In the present study, we propose the shallow water system (2.22) as a means of presenting 2D formulations of the FVC scheme. However, the approach we adopt in this case is applicable to any equation system that shares a similar structure. As previously emphasized, this strategy comprises two fundamental stages. The first stage involves the utilization of the method of characteristics to determine the intermediate state, while the second stage relies on the conventional finite volume discretization.

4.1.1 Discretization

The integral form of system (2.22) can be written as

$$\frac{\partial}{\partial t}\int_{\Omega} W \mathrm{d}\mu + \int_{\partial\Omega} \mathbb{F}(W)\cdot \mathbf{n}\mathrm{d}\sigma = \int_{\Omega}(S(W)+R(W))\mathrm{d}\mu, \tag{4.1}$$

Where Ω is the domain of interest, $\partial\Omega$ is the surrounding boundary, $\mathbf{n}$ is the outward normal vector to $\partial\Omega$, and $\mathrm{d}\mu$ and $d\sigma$ are the surface element and the length element, respectively. The problem domain is initially discretized into a collection of triangular cells that form an unstructured computational mesh, as depicted in Figure 4.1. The average of conserved variables is stored at the center of each cell, and the edges of each cell define the faces of a cell control, which is called "control volume".

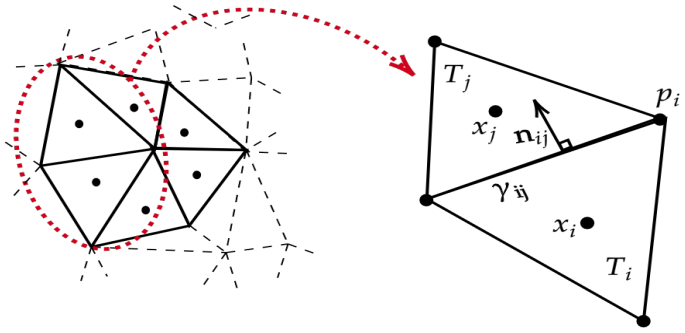

Fig 4.1. Generic definition of the Ω domain and the control cells of the mesh.

Notations:

- x_i, centroid of the cell T_i,
- p_i, vertex of T_i,
- γ_{ij}, boundary edge between T_i and T_j,
- ∂T_i, boundary of the cell T_i,
- $|\gamma_{ij}|$, length of γ_{ij},
- $|T_i|$, area of the cell T_i,
- $\mathbf{n}_{ij}$, unit normal to γ_{ij}, outward to T_i such as, $\mathbf{n}_{ji} = -\mathbf{n}_{ij}$,
- $\mathcal{P}_i$, the perimeter of the cell T_i.

For each triangular control volume, the finite volume formulation of system (2.22) is written as

$$|T_i|\frac{dW_i}{dt} + \int_{\partial T_i} \mathbb{F}(W)\cdot \mathbf{n}\mathrm{d}\sigma = \int_{T_i}(S(W)+R(W))\mathrm{d}\mu, \tag{4.2}$$

where W_i is the average quantity on cell T_i stored at the cell center. The flux vector over each edge of the triangular cell and the discrete form of the integral is

$$\int_{\partial T_i} \mathbb{F}(W)\cdot\mathbf{n}\mathrm{d}\sigma \simeq \sum_{j\in N(i)} |\gamma_{ij}|\Phi(W_{ij},\mathbf{n}_{ij}),$$

where $\Phi(W_{ij},\mathbf{n}_{ij}) \simeq \dfrac{1}{|\gamma_{ij}|}\displaystyle\int_{\gamma_{ij}} \mathbb{F}(W)\cdot\mathbf{n}_{ij}d\sigma$, is the numerical flux computed at the interface γ_{ij} between the cells T_i and T_j and $N(i)$ is the set of neighboring triangles of the cell T_i. The intermediate solution W_{ij} is reconstructed using the FVC scheme (see subsection 4.1.3). The time discretization of (4.2) is performed by a first-order time stepping scheme, in which the fully-discrete formulation of system (2.22). The time domain is divided into N sub-intervals $[t_n, t_{n+1}]$ with time step $\Delta t = t_{n+1} - t_n$ for $n = 0, 1, ..., N-1$. W^n is the value of a generic function W at time t_n. The fully-discrete formulation of system (2.22) is given by

$$W_i^{n+1} = W_i^n - \frac{\Delta t}{|T_i|}\sum_{j\in N(i)} |\gamma_{ij}|\Phi(W_{ij}^n,\mathbf{n}_{ij}) + \Delta t S_i^n + \Delta t R_i^n. \tag{4.3}$$

The finite volume characteristic method has been introduced in [31] for the 1D shallow water equation. In [103], the method has been used for the simulation of 2D shallow water flows on flat topography. In this work, we present a generalization of this scheme, taking into account the bottom source term, leading to a well-balanced scheme preserving the steady state. For the corrector stage, we will use the 2D finite volume formalism described in Section 4.1.1. Finally, the predictor stage and the final reformulation of the FVC scheme will be presented in this subsection.

4.1.2 Construction of the projected speed model

This projection aims to write the system of type (3.1) in an advective form in which the unknown vector will be transported with the same speed, which will be taken into account in the calculation of the characteristic curves.

Let discretize the spatial domain Ω with cells T_i as $\overline{\Omega} = \bigcup_{i=1}^{N_{ele}} T_i$ and $\partial T_i = \bigcup_{j\in N(i)} \gamma_{ij}$, with ∂T_i is the border of the cell T_i and N_{ele} is the total number of element.
Integrating the system (2.20) over the cell T_i, the basic equations of the finite volume method obtained using the divergence theorem are given by

$$\frac{\partial}{\partial t}\int_{T_i} h\ \mathrm{d}V + \int_{\partial T_i} hu_\eta\ \mathrm{d}\sigma = 0, \tag{4.4a}$$

$$\frac{\partial}{\partial t}\int_{T_i} hu\ \mathrm{d}\mu + \int_{\partial T_i}\Big(huu_\eta + \frac{1}{2}gh^2 n_x\Big)\mathrm{d}\sigma = \int_{T_i}\Big(-gh\partial_x Z + f_c hv - \eta^2 ghu\frac{|\mathbf{u}|}{h^{4/3}}\Big)\ \mathrm{d}\mu, \tag{4.4b}$$

$$\frac{\partial}{\partial t}\int_{T_i} hv\ \mathrm{d}\mu + \int_{\partial T_i}\Big(hvu_\eta + \frac{1}{2}gh^2 n_y\Big)\mathrm{d}\sigma = \int_{T_i}\Big(-gh\partial_y Z - f_c hu - \eta^2 ghv\frac{|\mathbf{u}|}{h^{4/3}}\Big)\ \mathrm{d}\mu, \tag{4.4c}$$

where $\eta = (n_x, n_y)^T$ represents the unit outward normal to cell T_i, and $\tau = (-n_y, n_x)^T$ represents the tangential direction. The normal velocity, u_η, is defined as $un_x + vn_y$, and the tangential velocity, u_τ, is given by $vn_x - un_y$. It should be noted that $\eta\cdot\tau = 0$, as illustrated in Figure 4.2. In order to simplify the system (4.4), we do the following operations: $(4.5b) \leftarrow n_x(4.4b) + n_y(4.4c)$, $(4.5c) \leftarrow n_x(4.4c) - n_y(4.4b)$.

It is a procedure which is done on all the edges of the triangle T_i. The outcome of these operations is

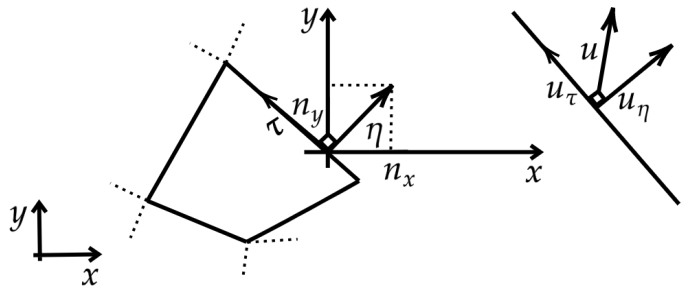

Fig 4.2. The projected velocity on the control volume.

$$\frac{\partial}{\partial t}\int_{T_i} h \,\mathrm{d}\mu + \int_{\partial T_i} hu_\eta \,\mathrm{d}\sigma = 0, \tag{4.5a}$$

$$\frac{\partial}{\partial t}\int_{T_i} hu_\eta \,\mathrm{d}\mu + \int_{\partial T_i} \left(hu_\eta{}^2 + \frac{1}{2}gh^2\right)\mathrm{d}\sigma = \int_{T_i} \Big(- gh\boldsymbol{\nabla} Z\cdot\mathbf{n} + f_c hu_\tau - \eta^2 ghu_\eta \frac{|\mathbf{u}|}{h^{4/3}}\Big)\mathrm{d}\mu, \tag{4.5b}$$

$$\frac{\partial}{\partial t}\int_{T_i} hu_\tau \,\mathrm{d}\mu + \int_{\partial T_i} hu_\tau u_\eta \,\mathrm{d}\sigma = \int_{T_i} \Big(- gh\boldsymbol{\nabla} Z\cdot\tau - f_c hu_\eta - \eta^2 ghu_\tau \frac{|\mathbf{u}|}{h^{4/3}}\Big)\mathrm{d}\mu, \tag{4.5c}$$

which can be rewritten the system (4.5) in a differential form as

$$\begin{cases} \dfrac{\partial h}{\partial t} + \dfrac{\partial hu_\eta}{\partial \eta} = 0, \\ \dfrac{\partial hu_\eta}{\partial t} + \dfrac{\partial}{\partial \eta}\left(hu_\eta{}^2 + \dfrac{1}{2}gh^2\right) = -gh\partial_\eta Z + f_c hu_\tau - \eta^2 ghu_\eta \dfrac{|\mathbf{u}|}{h^{4/3}}, \\ \dfrac{\partial hu_\tau}{\partial t} + \dfrac{\partial}{\partial \eta}\left(hu_\eta u_\tau\right) = -f_c hu_\eta - \eta^2 ghu_\tau \dfrac{|\mathbf{u}|}{h^{4/3}}. \end{cases} \tag{4.6}$$

The system (4.6) can also be reformulated in the transport equation form as

$$\frac{\partial \mathbf{U}}{\partial t}(t,X) + u_\eta(t,X)\frac{\partial \mathbf{U}}{\partial \eta}(t,X) = \mathbf{F}(\mathbf{U}), \quad \forall \;\; X=(x,y)\in\Omega\subset\mathbb{R}^2, \;\; t>t_0, \tag{4.7}$$

where

$$\mathbf{U} = \begin{pmatrix} h \\ hu_\eta \\ hu_\tau \end{pmatrix}, \quad \mathbf{F}(\mathbf{U}) = \begin{pmatrix} -h\partial_\eta(u_\eta) \\ -gh\partial_\eta(h+Z) + f_c hu_\tau - hu_\eta\partial_\eta(u_\eta) - \eta^2 ghu_\eta \frac{|\mathbf{u}|}{h^{4/3}} \\ -f_c hu_\eta - hu_\tau\partial_\eta(u_\eta) - \eta^2 ghu_\tau \frac{|\mathbf{u}|}{h^{4/3}} \end{pmatrix}.$$

The purpose of using this technique on the local coordinates of the two-dimensional shallow water system (2.20) in the control volume T_i, is to reduce the dynamics of our starting system as an advection equation (4.7) which transports the projected conservative variables through the normal velocity on the edge of each control volume T_i.

4.1.3 Flux construction

We reconstruct the numerical flux $\Phi(W_{ij}^n, \mathbf{n}_{ij})$ using the method of characteristics. The fundamental idea of this method is to impose a regular grid at the new time level and to backtrack the flow trajectories to the previous time level, for more details see [103]. At the previous time level, the quantities that are needed are evaluated by interpolation from their known values on a irregular grid.

▶ **Method of characteristics**

The characteristic curves associated with the equation (4.6) are solutions of the following Cauchy problem

$$\begin{cases} \dfrac{dX^c(t)}{dt} = u_\eta(t, X^c(t))\mathbf{n}, \quad t \in [t_n, t_n + \alpha^n \Delta t], \\ X^c(t_n + \alpha^n \Delta t) = X_\star. \end{cases} \tag{4.8}$$

Note that $X^c(t)$ is the departure point at time t of a particle that will arrive at the interface γ_{ij} in time $t_n + \alpha^n \Delta t$, see Fig 4.3. The method of characteristics does not follow the flow particles forward in time, as the Lagrangian schemes do, instead, it traces backwards the position at time t_n of particles that will reach the points of a fixed mesh at time $t_n + \alpha^n \Delta t$. By doing so, the method avoids the grid distortion difficulties that conventional Lagrangian schemes have. Hence, the solution of (4.8) can be expressed in an integral form as

$$X^c(t_n) = X_\star - \int_{t_n}^{t_n + \alpha^n \Delta t} u_\eta(s, X^c(s))\mathbf{n} \, \mathrm{d}s. \tag{4.9}$$

This integral can be calculated using an integral approximation method, which generally leads to a non-linear equation in $X^c(t_n)$. A root-finding algorithm is subsequently required to solve this equation. In our simulations, we used a rectangular rule to approximate the integral in (4.9). In order to complete the reformulation of the algorithm used, the departure points must be calculated once the characteristic curves are known. Therefore, the solution of the transport equation (4.7) is given by

$$\mathbf{U}(t_n + \alpha^n \Delta t, X_\star) = \mathbf{U}(t_n, X^c(t_n)) + \int_{t_n}^{t_n + \alpha^n \Delta t} \mathbf{F}(\mathbf{U}(s, X^c(s))) \, \mathrm{d}s, \tag{4.10}$$

where $\mathbf{U}(t_n, X^c(t_n))$ is the solutions at the characteristic feet computed by the local least squares interpolation method.
In other cases, the integral of the equation (4.10) is calculated using a first-order approximation based on the rectangle method, which enough to maintain a particle on its curved trajectory. The solution $\hat{\mathbf{U}}_{ij}^n$ is reconstructed at the interfaces using the same methodology presented by the authors in [104] except that here we used a local least square plane in each cell. We have:

$$\hat{\mathbf{U}}_{ij}^n = \mathbf{U}(t_n, X^c(t_n)) = \sum_{k \in V(c)} \beta_k(c) \mathbf{U}(X^k), \tag{4.11}$$

with $V(c)$ is the set of neighbours by face and vertices to the cell of X^c, see Fig 4.4 and $\beta_k(c)$ is weights coming from the least squares method (LSM). It can be written

$$\beta_k(c) = \frac{1 + \lambda \cdot (X^k - X^c)}{\#V(c) + \lambda \cdot R}, \tag{4.12}$$

The choice of the two-dimensional least squares plane-based interpolation method, aimed at minimizing quadratic errors between data points, is motivated by two reasons. Firstly, the data being used is inconsistent due to the unstructured mesh. Additionally, this method enables straightforward linear interpolation.

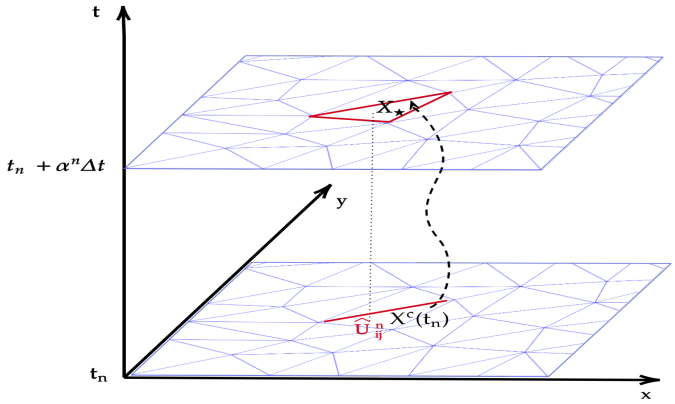

Fig 4.3. Illustration of the method of characteristics: an Eulerian mesh point $X^c(t_n)$ is traced back in time to $X_\star$ where the intermediate solution $\hat{\mathbf{U}}_{ij}^n$ is interpolated.

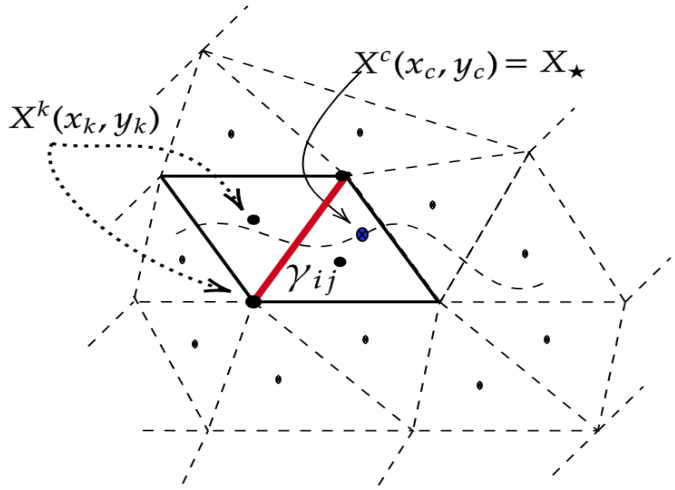

Fig 4.4. Point clouds used for interpolation using the least squares method-based plane.

such as, $\lambda = (\lambda_x, \lambda_y)$ and $R = (R_x, R_y)$. The weights parameters are given by the following formulas

$$R_x = \sum_{k \in V(c)} (x_k - x_c), \quad R_y = \sum_{k \in V(c)} (y_k - y_c),$$

$$\lambda_x = \frac{I_{xy} R_y - I_{yy} R_x}{I_{xx} I_{yy} - I_{xy}^2}, \quad \text{and} \quad \lambda_y = \frac{I_{xy} R_x - I_{xx} R_y}{I_{xx} I_{yy} - I_{xy}^2},$$

where

$$I_{xx} = \sum_{k \in V(c)} (x_k - x_c)^2, \quad I_{yy} = \sum_{k \in V(c)} (y_k - y_c)^2, \quad I_{xy} = \sum_{k \in V(c)} (x_k - x_c)(y_k - y_c).$$

To approximate the terms of $\mathbf{F}(\mathbf{U})$, (i.e., $\partial_\eta(u_\eta)$, $\partial_\eta(h+Z)$, etc.) we will need to calculate these derivatives in the interfaces, for that, we use the diamond cell Fig 4.5. This cell is constructed by the connection of gravity centers (L, R) of cells T_i, T_j which share the interface γ_{ij} and its endpoints S, N. We obtain the co-volume $\mathcal{V}_{SRNL}$ by this construction. One can assume that the gradient is constant on the co-volume $\mathcal{V}_{SRNL}$. According to Green-Gauss theorem the approximation leads to

$$\nabla u_{ij} = \frac{1}{2\mu\left(\mathcal{V}_{SRNL}\right)} \left\{ (u_{_S} - u_{_N}) n_{_{LR}} |\gamma_{_{LR}}| + (u_{_R} - u_{_L}) n_{ij} |\gamma_{ij}| \right\}, \tag{4.13}$$

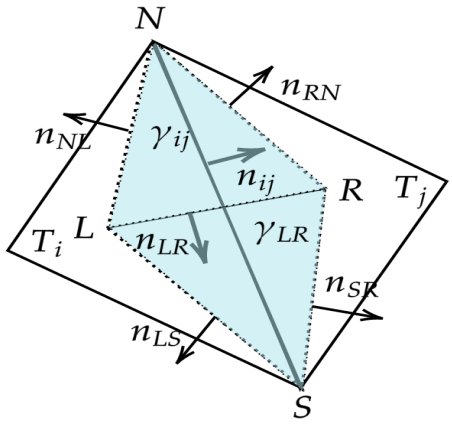

Fig 4.5. Diamond cell in 2D.

where $u_{_N}$, $u_{_S}$, $u_{_R}$, and $u_{_L}$ represent respectively the values of the quantity u in the point N, S, R and L. $n_{_{LR}}$ is a unit normal vector of the co-volume face $\gamma_{_{LR}}$ and $|\gamma_{_{LR}}|$ is its length. The other co-volume interfaces and their normal vectors are labeled analogically. $\mu_{_{SRNL}}$ is the area of the co-volume $SRNL$. The calculation that gives us the formula (4.13) is detailed in the appendix. After the discretization of the source terms (see subsection 4.1.4), the discrete equation system (4.10) leads to the following predictor step.

▶ **Predictor stage**

$$\left| \quad \mathbf{U}_{ij}^n = \hat{\mathbf{U}}_{ij}^n + \mathbf{I_F}(\hat{\mathbf{U}}_{ij}^n), \right. \tag{4.14}$$

where $\mathbf{I_F}$ is the approximation of the integral in (4.10). Once these projected states are calculated, the quantity W_{ij} will be calculated using the following transformations

$$hu_{ij}^n = (hu_\eta)_{ij}^n n_x - (hu_\tau)_{ij}^n n_y, \quad \text{and} \quad hv_{ij}^n = (hu_\tau)_{ij}^n n_x + (hu_\eta)_{ij}^n n_y. \tag{4.15}$$

▶ **Corrector stage**

$$\left| \quad \Phi(W_{ij}^n, \mathbf{n}_{ij}) = \mathbb{F}(W_{ij}^n) \cdot \mathbf{n}_{ij}. \right. \tag{4.16}$$

Note that in the FVC scheme, the corrector stage is used to evaluate the numerical flux at the edges by using the corrector step to construct the intermediate states W_{ij}. The final iteration process is based on the discrete equation (4.3). In order to develop a second-order FVC scheme, an appropriate choice of the α^n parameter which increases the accuracy of the spatial approximation. To preserve the TVD property of the FVC scheme, we use techniques based on the

limiter function in order to select a good time parameter α^n. This approach leads us to:

$$\alpha^n = \underline{\alpha}^n + \Psi_{ij}^n(\alpha_\star^n - \underline{\alpha}^n) \tag{4.17}$$

where $\alpha_\star^n$, and α_*^n defined as

$$\alpha_\star^n := \frac{2|\gamma_{ij}|\Delta t}{|T_i| + |T_j|} \max_q \Big(\max\Big(\big|\lambda_{q,i}^n\big|, \big|\lambda_{q,j}^n\big|\Big)\Big),\ \underline{\alpha}^n = \frac{\max_q \Big(\max\Big(\big|\lambda_{q,i}^n\big|, \big|\lambda_{q,j}^n\big|\Big)\Big)}{\min_q \Big(\max\Big(\big|\lambda_{q,i}^n\big|, \big|\lambda_{q,j}^n\big|\Big)\Big)}, \tag{4.18}$$

where $\lambda_{q,i}^n$ is the q^{th} eigenvalue of (2.23) evaluated in cell T_i. The choices of $\alpha_\star^n$ and $\underline{\alpha}^n$, were inspired by the work of M. Kamel et al [105, 106]. Proposition 4.3.1 in [105] proves that with this choice the scheme is L^∞ stable. Ψ_{ij}^n is an appropriate limiter that is defined using a flux limiter function acting on a quantity that measures the fluctuation rate. In the computational results presented in Section 4.4 and in Chapter 5, the value of α^n was assumed to be a fixed constant.

4.1.4 The discretization of the bottom source term (Well-balanced FVC scheme)

In order to be able to calculate realistic flows we now consider the case $\boldsymbol{\nabla} Z \neq 0_{\mathbb{R}^2}$ and introduce a numerical discretization of the source terms. As discussed in paragraph 2.2.1.1, the treatment of source terms related to bottom in the shallow water system poses a challenge in many numerical methods. In the FVC scheme, the approximation of the source term S_i^n is reconstructed in such a way that the C-property [11] is satisfied, i.e. to maintain a discrete local balance of the continuous stationary state in still water.

$$\left.\begin{array}{l} h_i^n + Z_i = h_j^n + Z_j = H := constant \\ \mathbf{u}_i^n + \mathbf{u}_j^n = 0_{\mathbb{R}^2},\ \ \forall\, T_i, T_j \in \overline{\Omega} \end{array}\right\} \Rightarrow h_i^{n+1} + Z_i = H, \quad \text{and} \quad \mathbf{u}_i^{n+1} = 0_{\mathbb{R}^2}. \tag{4.19}$$

▶ The hydrostatic balance

We prove from the hydrostatic balance $\left(\boldsymbol{\nabla}\left(\frac{1}{2}gh^2\right) = -gh\boldsymbol{\nabla} Z\right)$ that the model of the projected speed preserves the stationary state of the lake at rest

▶ The projected speed model

$$\partial_t \begin{pmatrix} h \\ 0 \\ 0 \end{pmatrix} + 0 \times \partial_\eta \begin{pmatrix} h \\ 0 \\ 0 \end{pmatrix} = \begin{pmatrix} 0 \\ -g\partial_\eta(h+Z) \\ 0 \end{pmatrix}, \tag{4.20}$$

$\partial_t h = 0, \quad \text{and} \quad \partial_\eta(h+Z) = 0 \Longrightarrow h(x,y,t) + Z(x,y) = constant\ \ \forall\ x,\ y,\ t$. This result ensures the equilibrium property corresponding to the lake at rest, and therefore it is consistent with the continuous form of the system's equilibrium with bottom source term.

$$\frac{\Delta t}{|T_i|} \sum_{j \in N(i)} |\gamma_{ij}| \Phi(W_{ij}^n, \mathbf{n}_{ij}) = \frac{\Delta t}{|T_i|} \int_{T_i} S d\mu, \tag{4.21}$$

which is equivalent to

$$\begin{pmatrix} 0 \\ \sum_{j\in N(i)} \frac{1}{2} g (h_{ij})^2 (n_{ij})_x |\gamma_{ij}| \\ \sum_{j\in N(i)} \frac{1}{2} g (h_{ij})^2 (n_{ij})_y |\gamma_{ij}| \end{pmatrix} = \begin{pmatrix} 0 \\ -g \int_{T_i} h \partial_x Z d\mu \\ -g \int_{T_i} h \partial_y Z d\mu \end{pmatrix}. \tag{4.22}$$

To approximate the source terms, we proceed as follows. First, we decompose the triangle T_i into three sub-triangles, as depicted in Fig 4.6. where $N_{xij} = (n_{ij})_x |\gamma_{ij}|$ and $N_{yij} = (n_{ij})_y |\gamma_{ij}|$. Then, the source term is approximated as

$$\int_{T_i} h \partial_x Z d\mu = h_1 \int_{T_1} \partial_x Z d\mu + h_2 \int_{T_2} \partial_x Z d\mu + h_3 \int_{T_3} \partial_x Z d\mu, \tag{4.23}$$

with h_1, h_2 and h_3 are the average values of h over T_1, T_2 and T_3 respectively, the following calculation is intended to determine them.

$$\begin{aligned} h_1 \int_{T_1} \partial_x Z d\mu &= h_1 \sum_{j\in N(1)} \int_{\gamma_{1j}} Z n_x d\mu = h_1 \sum_{j\in N(1)} \frac{Z_1 + Z_j}{2} N_{x1j} \\ &= \frac{h_1}{2} \left\{ (Z_1 + Z_l) N_{x1l} + (Z_1 + Z_2) N_{x12} + (Z_1 + Z_3) N_{x13} \right\}. \end{aligned} \tag{4.24}$$

The same is applies to the y-direction. Again the stationary flow condition $h_1 + Z_1 = h_j + Z_j = H = constant$, $\forall j \in N(1) \Rightarrow h_1 + h_j + Z_1 + Z_j = 2H$ and $H - \frac{h_1 + h_j}{2} = \frac{Z_1 + Z_j}{2}$. Thus, (4.24) gives

$$\int_{T_1} h \partial_x Z d\mu = h_1 \sum_{j\in N(1)} \left(H - \frac{h_1 + h_j}{2} \right) N_{x1j} \overbrace{=}^{\sum_{j\in N(1)} N_{x1j} = 0} -\frac{h_1}{2} \sum_{j\in N(1)} h_j N_{x1j}. \tag{4.25}$$

A similar procedure leads to the following approximations of the other terms in (4.23):

$$\int_{T_2} \partial_x Z d\mu = -\frac{h_2}{2} \sum_{j\in N(2)} h_j N_{x2j}, \quad \text{and} \quad \int_{T_3} \partial_x Z d\mu = -\frac{h_3}{2} \sum_{j\in N(3)} h_j N_{x3j}. \tag{4.26}$$

Notice that h_l, h_k and h_j are the average values of h, respectively, on the triangle T_l, T_k and T_j. Summing up, using the fact that $(N_{xij} = -N_{xji})$ so, the discretization (4.23) gives

$$\int_{T_i} h \partial_x Z d\mu = -\frac{1}{2} \left(h_1 h_l N_{x1l} + h_2 h_k N_{x2k} + h_3 h_j N_{x3j} \right). \tag{4.27}$$

For this reconstruction, the source terms in (4.22) result in

$$\begin{aligned} \sum_{j\in N(i)} (h_{ij}^n)^2 N_{xij} &= h_1 h_l N_{x1l} + h_2 h_k N_{x2k} + h_3 h_j N_{x3j}, \\ \sum_{j\in N(i)} (h_{ij}^n)^2 N_{yij} &= h_1 h_l N_{y1l} + h_2 h_k N_{y2k} + h_3 h_j N_{y3j}. \end{aligned} \tag{4.28}$$

If you have noticed, we will need h_1, h_2 and h_3 to be able to calculate the values of the integrals in equation (4.27) but the system. (4.28) has two equations for the three unknowns. To complete

the system, we add the natural conservation equation, $h_1 + h_2 + h_3 = 3h_i$. The following system gives us the values we need

$$\begin{pmatrix} h_1 \\ h_2 \\ h_3 \end{pmatrix} = \begin{pmatrix} 1 & 1 & 1 \\ h_l N_{x1l} & h_k N_{x2k} & h_j N_{x3j} \\ h_l N_{y1l} & h_k N_{y2k} & h_j N_{y3j} \end{pmatrix}^{-1} \cdot \begin{pmatrix} 3h_i \\ \sum_{j\in N(i)} (h_{ij}^n)^2 N_{xij} \\ \sum_{j\in N(i)} (h_{ij}^n)^2 N_{yij} \end{pmatrix}. \tag{4.29}$$

Analogously, the bottom values $Z_j,\ \ j = 1,..,3$ are reconstructed in each sub-triangle of T_i as $Z_j = Z_i + h_i^n - h_j^n \quad \forall j = 1,..,3$. Then the source terms in (4.27) are approximated as

$$\begin{aligned} \int_{T_i} h\partial_x Z d\mu = h_1 \sum_{m\in N(1)} \frac{Z_1 - Z_m}{2} N_{x1m} + h_2 \sum_{m\in N(2)} \frac{Z_2 - Z_m}{2} N_{x2m} \\ + h_3 \sum_{m\in N(3)} \frac{Z_3 - Z_m}{2} N_{x3m}, \end{aligned} \tag{4.30}$$

with a similar equation for the other source terms in the y-direction.

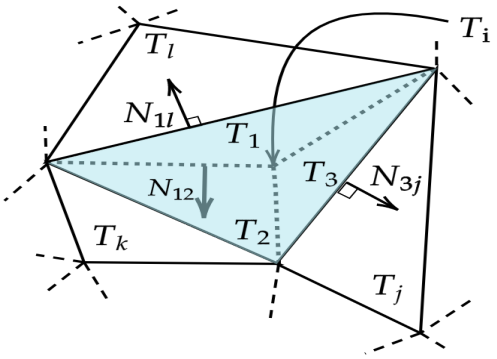

Fig 4.6. Sub-triangles used in the discretization of source terms.

▶ Computation of the solution

Finally, we write the formally well-balanced FVC scheme after calculation of the interface values (4.14) and the bottom source term approximation (4.30) as

$$W_i^{n+1} = W_i^n - \frac{\Delta t}{|T_i|} \sum_{j\in N(i)} |\gamma_{ij}| \Phi(W_{ij}^n, \mathbf{n}_{ij}) + \Delta t S_i^n. \tag{4.31}$$

For this writing, the forward Euler method is used for temporal discretization. In other cases. We can use the various temporal numerical approximations.

4.1.5 Semi implicit treatment of friction term source

To avoid stability problems related to the bottom friction source term, a fractional semi implicit treatment for this term is proposed. The idea is to evaluate the momentum in the system (2.22) by decomposing it into two equations

$$\begin{cases} \dfrac{\partial h\mathbf{u}}{\partial t} = -\eta^2 g h^{-1/3} |\mathbf{u}| \mathbf{u} \\ \dfrac{\partial h\mathbf{u}}{\partial t} + \Phi_{h\mathbf{u}}(W) = -gh\boldsymbol{\nabla} Z, \end{cases} \tag{4.32}$$

where $\Phi_{h\mathbf{u}}(W)$ represents the convection terms corresponding to the equations of the momentum. In a first step, a linearized semi implied method is used to integrate the first equation of the system (4.32)

$$\frac{(\tilde{h\mathbf{u}})_i - (h\mathbf{u})_i^n}{\Delta t} = -\eta^2 g(\tilde{h\mathbf{u}})_i |\mathbf{u}_i^n| (h_i^n)^{-4/3}. \tag{4.33}$$

In the second step, the value $(\tilde{h\mathbf{u}})_i$ is taken as the initial condition for solving the second equation of (4.32). Such a methodology was introduced in particular in this publication [107].

4.2 Model of solute transport by fluid flow

We propose to rewrite and apply the FVC finite volume solver described previously in 4 to consider the pollutant transport-diffusion equation in the shallow water model. The modification on the discretization of the source terms describing the bottom variation will make it possible to obtain an equilibrium scheme while keeping the accuracy in space, see 4.1.4. It is recalled that the scheme's construction is done in two steps: calculating the intermediate states and calculating the numerical flux using the physical flux.

The FVC scheme is formulated by considering only the convective part of the system (2.36) and the source terms describing the bottom profile, the friction, and the Coriolis terms of the domain. The diffusion part will be treated using the diamond scheme, see Appendix.
Consider the following system, which is the model (2.36) without a diffusion term.

$$\frac{\partial W}{\partial t} + \nabla \cdot \mathbb{F}(W) = S(W) + R(W), \tag{4.34}$$

where

$$\mathbb{F}(W)) = \begin{pmatrix} hu & hv \\ hu^2 + \frac{1}{2}gh^2 & huv \\ huv & hv^2 + \frac{1}{2}gh^2 \\ huC & hvC \end{pmatrix}, \; S(W) = \begin{pmatrix} 0 \\ -gh\partial_x Z \\ -gh\partial_y Z \\ 0 \end{pmatrix}, \; R(W) = \begin{pmatrix} 0 \\ f_c hv - r_{f_x} + \tau_{s_x} \\ -f_c hu - r_{f_x} + \tau_{s_y} \\ hQ \end{pmatrix}.$$

Following the same calculation used in section 4.1.2, we return to the projected speed model associated with (4.34), which is written as

$$\begin{cases} \dfrac{\partial h}{\partial t} + \dfrac{\partial h u_\eta}{\partial \eta} = 0, \\ \dfrac{\partial h u_\eta}{\partial t} + \dfrac{\partial}{\partial \eta}\left({hu_\eta}^2 + \dfrac{1}{2}gh^2 \right) = -gh\partial_\eta Z + f_c h u_\tau - \eta^2 g h u_\eta \dfrac{|\mathbf{u}|}{h^{4/3}}, \\ \dfrac{\partial h u_\tau}{\partial t} + \dfrac{\partial}{\partial \eta}\left(h u_\eta u_\tau \right) = -f_c h u_\eta - \eta^2 g h u_\tau \dfrac{|\mathbf{u}|}{h^{4/3}}, \\ \dfrac{\partial hC}{\partial t} + \dfrac{\partial (h u_\eta C)}{\partial \eta} = hQ. \end{cases} \tag{4.35}$$

Can also be reformulated in the transport equation as

$$\frac{\partial \mathbf{U}}{\partial t}(t, X) + u_\eta(t, X)\frac{\partial \mathbf{U}}{\partial \eta}(t, X) = \mathbf{F}(\mathbf{U}), \quad \forall \;\; X = (x, y) \in \Omega \subset \mathbb{R}^2, \;\; t > t_0, \tag{4.36}$$

where

$$\mathbf{U} = \begin{pmatrix} h \\ hu_\eta \\ hu_\tau \\ hC \end{pmatrix}, \quad \mathbf{F}(\mathbf{U}) = \begin{pmatrix} -h\partial_\eta(u_\eta) \\ -gh\partial_\eta(h+Z) + f_c h u_\tau - hu_\eta \partial_\eta(u_\eta) - \eta^2 g h u_\eta \frac{|\mathbf{u}|}{h^{4/3}} \\ -f_c h u_\eta - hu_\tau \partial_\eta(u_\eta) - \eta^2 g h u_\tau \frac{|\mathbf{u}|}{h^{4/3}} \\ hQ - hC\partial_\eta(u_\eta) \end{pmatrix}.$$

The computation of the characteristic curves, the treatment of the background source term, and the friction terms are treated in the same way as the techniques explained in the section 4.
In order to complete the construction of the numerical scheme for the considered pollutant transport model, the part concerning the diffusion term has to be integrated. It is assumed here that the diffusion coefficients in the concentration equation are constant, so we have to evaluate the terms of the form

$$\int_{\gamma_{ij}} \left(hD_x \frac{\partial C}{\partial x} n_x + hD_y \frac{\partial C}{\partial y} n_y \right) d\sigma. \tag{4.37}$$

The discretization of these diffusion flows on unstructured meshes is still a complex problem. Many theoretical investigations and mathematical analyses have been directed in this direction see e.g. [108, 109, 110]. In this work, we present a finite volume scheme for this type of problem when unstructured meshes are used. The algorithm is based on a Green-Gauss-type interpolation to construct the gradients at the mesh interfaces. The weak consistency of this scheme has been proven under certain conditions regarding the interpolation points. We write

$$\int_{\gamma_{ij}} hD_x \frac{\partial C}{\partial x} n_x d\sigma = D_x h_{\gamma_{ij}} \left.\frac{\partial C}{\partial x}\right|_{\gamma_{ij}} \int_{\gamma_{ij}} n_x d\sigma. \tag{4.38}$$

The problem now depends on the way to evaluate $\frac{\partial C}{\partial x}$ on the interface γ_{ij}. Our choice falls on the diamond scheme described in detail in the appendix. Thanks to its robustness and accuracy, especially when the meshes do not have a great regularity on the triangles, contrary to the FV4 scheme adopted, studied, and analyzed by T. Gallouët and his colleagues in [110].

4.3 Two-dimensional multilayer shallow water equations

Due to the large size of the system and the difficulty, even impossibility, of computing eigenvalues, the use of classical Riemann solvers is challenging. In [56, 55], numerical methods based on kinetic interpretations were developed to solve the equations for shallow water in multiple layers. These methods possess interesting stability properties but are also known to introduce significant numerical diffusion, requiring higher-order methods for practical applications.

In this work, we propose the FVC numerical solution as an alternative. The method was first presented and analyzed in [31] for standard shallow water equations in a single layer. It should be noted that the proposed FVC scheme avoids the solution of Riemann problems and is a predictor-corrector type method. The prediction step uses the method of characteristics to reconstruct the numerical fluxes, while the correction step treats the initial equations in conservative form. The proposed method is simple, conservative, non-oscillatory, and adapted to shallow water equations in multiple layers, for which Riemann problems are difficult to solve.

For the numerical resolution of the model, we begin by rewriting the equations (2.42) as

$$\begin{cases} \dfrac{\partial H}{\partial t} + \displaystyle\sum_{\theta=1}^{M} \frac{\partial}{\partial x}\left(l_\theta H u_\theta\right) + \sum_{\theta=1}^{M} \frac{\partial}{\partial y}\left(l_\theta H v_\theta\right) = 0, \\ \dfrac{\partial}{\partial t}\left(l_\theta H u_\theta\right) + \dfrac{\partial}{\partial x}\left(l_\theta H u_\theta^2 + \dfrac{1}{2} g l_\theta H^2\right) + \dfrac{\partial}{\partial y}\left(H u_\theta v_\theta\right) = -g l_\theta H \dfrac{\partial Z}{\partial x} + f_c l_\theta H v_\theta + F_\theta, \\ \dfrac{\partial}{\partial t}\left(l_\theta H v_\theta\right) + \dfrac{\partial}{\partial x}\left(H u_\theta v_\theta\right) + \dfrac{\partial}{\partial y}\left(l_\theta H v_\theta^2 + \dfrac{1}{2} g l_\theta H^2\right) = -g l_\theta H \dfrac{\partial Z}{\partial y} - f_c l_\theta H u_\theta + G_\theta. \end{cases} \tag{4.39}$$

The same projection techniques as those used in subsection 4.1.2 are employed, resulting in the following systems

$$\begin{cases} \dfrac{\partial H}{\partial t} + \displaystyle\sum_{\theta=1}^{M} \frac{\partial}{\partial \eta}\left(l_\theta H u_{\theta,\eta}\right) = 0, \\ \dfrac{\partial}{\partial t}\left(l_\theta H u_{\theta,\eta}\right) + \dfrac{\partial}{\partial \eta}\left(l_\theta H u_{\theta,\eta}^2 + \dfrac{1}{2} g l_\theta H^2\right) = -g l_\theta H \dfrac{\partial Z}{\partial \eta} - f_c l_\theta H u_{\theta,\tau}, \\ \dfrac{\partial}{\partial t}\left(l_\theta H u_{\theta,\tau}\right) + \dfrac{\partial}{\partial \eta}\left(l_\theta H u_{\theta,\eta} u_{\theta,\tau}\right) = f_c l_\theta H u_{\theta,\eta}. \end{cases} \tag{4.40}$$

where the normal projected velocity $u_{\theta,\eta} = u_\theta n_x + v_\theta n_y$ and the tangential projected velocity $u_{\theta,\tau} = v_\theta n_x - u_\theta n_y$.

The system (4.40) can be rearranged in a compact form as

$$\frac{\partial \mathbf{U}_\theta}{\partial t}(t,X) + V_{\xi,\eta}(t,X)\frac{\partial \mathbf{U}_\theta}{\partial \eta}(t,X) = \mathbf{Q}(\mathbf{U}_\theta), \quad \forall \;\; X=(x,y) \in \Omega \subset \mathbb{R}^2, \;\; t > t_0, \tag{4.41}$$

where

$$\mathbf{U}_\theta = \begin{pmatrix} H \\ l_1 H u_{1,\eta} \\ l_2 H u_{2,\eta} \\ \vdots \\ l_M H u_{M,\tau} \\ l_1 H u_{1,\tau} \\ l_2 H u_{2,\tau} \\ \vdots \\ l_M H u_{M,\tau} \end{pmatrix}, \quad \mathbf{Q}(\mathbf{U}_\theta) = \begin{pmatrix} -\displaystyle\sum_{\theta=1}^{M} l_\theta H \frac{\partial u_{\theta,\eta}}{\partial \eta} \\ -l_1 H u_{1,\eta}\frac{\partial u_{1,\eta}}{\partial \eta} - gH\frac{\partial}{\partial \eta}(H+Z) + f_c l_1 H u_{1,\eta} \\ -l_2 u_{2,\eta}\frac{\partial u_{2,\eta}}{\partial \eta} - gH\frac{\partial}{\partial \eta}(H+Z) + f_c l_2 H u_{2,\eta} \\ \vdots \\ -l_M u_{M,\eta}\frac{\partial u_{M,\eta}}{\partial x} - gH\frac{\partial}{\partial \eta}(H+Z) + f_c l_M H u_{M,\eta} \\ -l_1 H u_{1,\tau}\frac{\partial u_{1,\tau}}{\partial \eta} - f_c l_1 H u_{1,\eta} \\ -l_2 H u_{2,\tau}\frac{\partial u_{2,\tau}}{\partial \eta} - f_c l_2 H u_{2,\eta} \\ \vdots \\ -l_M H u_{M,\tau}\frac{\partial u_{M,\tau}}{\partial \eta} - f_c l_M H u_{M,\eta} \end{pmatrix},$$

and

$$V_{\xi,\eta} = \begin{cases} \sum_{\theta=1}^{M} l_\theta u_{\theta,\eta}, & \text{if} \quad \xi = 0, \\ u_{\xi,\eta}, & \text{if} \quad \xi = 1, 2, \ldots, M. \end{cases} \tag{4.42}$$

Following the procedure outlined in Section 4.1, we can write the characteristic curves for equation (4.41) and then use them to construct intermediate states. Concerning the time integration of system (2.52) can be achieved using splitting methods, as compared to [59, 111] for a first-order splitting method. In this study, we consider a second-order splitting method studied in [112]. We also use the notation W^n to denote the value of a generic function W at time t_n. The considered splitting operator method consists of three steps given by
Stage 1:

$$\partial_t W^* = \mathbf{R}\left(W^*\right), \quad \text{on} \quad \left(t_n, t_{n+1/2}\right], \quad W^*\left(t_n\right) = W\left(t_n\right). \tag{4.43}$$

Stage 2:

$$\partial_t W^{**} + \partial_x \mathbf{F}\left(W^{**}\right) + \partial_y \mathbf{G}\left(W^{**}\right) = \mathbf{S}\left(W^{**}\right), \quad \text{on} \quad \left(t_n, t_{n+1}\right], \quad W^{**}\left(t_n\right) = W^*\left(t_{n+1/2}\right). \tag{4.44}$$

Stage 3:

$$\partial_t W^{***} = \mathbf{R}\left(W^{***}\right), \quad \text{on} \quad \left(t_{n+1/2}, t_{n+1}\right], \quad W^{***}\left(t_{n+1/2}\right) = W^{**}\left(t_{n+1}\right). \tag{4.45}$$

The time integration process for the system is accomplished by applying a time-stepping technique to the three stages mentioned above. The first and third stages handle nonlinear terms and vertical diffusion, whereas only linear terms are addressed in the second stage of the splitting. To avoid solving linear systems of algebraic equations associated with implicit time stepping, we use explicit time integration methods for stages (4.43-4.45). This study used the explicit third-order Runge-Kutta method investigated in [113]. Therefore, advancing the solution of an ordinary differential equation with the structure (4.43) from time t_n to the subsequent time t_{n+1} can be accomplished through this procedure.

$$\begin{aligned} \mathcal{W}^{(1)} &= W^n + \Delta t \mathbf{R}\left(W^n\right) \\ \mathcal{W}^{(2)} &= \frac{3}{4} W^n + \frac{1}{4} \mathcal{W}^{(1)} + \frac{1}{4} \Delta t \mathbf{R}\left(\mathcal{W}^{(1)}\right) \\ W^{n+1} &= \frac{1}{3} W^n + \frac{2}{3} \mathcal{W}^{(2)} + \frac{2}{3} \Delta t \mathbf{R}\left(\mathcal{W}^{(2)}\right) \end{aligned} \tag{4.46}$$

where the asterisks of the variables have been removed for ease of notation. It should be noted that the Runge-Kutta (4.46) method has been widely used for the time integration of hyperbolic systems of conservation laws, mainly because it can be interpreted as a convex combination of first-order Euler steps that exhibit strong stability properties. Therefore, the Runge-Kutta (4.46) method is TVD, accurate to the third order in time, and stable under the usual CFL condition involving the eigenvalues of the system under study. However, calculating the eigenvalues of the system (2.52) is not trivial, and in many flow cases, these eigenvalues become complex. In the present work, the proposed FVC scheme does not require the calculation of the eigenvalues for the multilayer system, and the time step selection can be performed using the eigenvalues associated with the single-layer counterparts in shallow water, defined as follows

$$\lambda_\theta^{\pm} = \mathbf{u}_\theta \cdot \mathbf{n} \pm \sqrt{gH}, \quad \theta = 1, 2 \ldots, M. \tag{4.47}$$

It should be noted that the time increment can be modified by utilizing the maximum wave velocity for the multi-layered shallow water model. This approach ensures the stability of the technique, however, for a given simulation duration, it may necessitate a greater number of iterations compared to the alternative approach that relies on the eigenvalue-based selection (4.47).

4.4 Numerical results

It is clear from (4.16) that the scheme is conservative and can compute the numerical flux corresponding to the physical solutions of water flow without relying on Riemann problem solvers. With the same proof of theorem 2.3 in [114], the CFL condition for the explicit scheme (4.31) can be written

$$\Delta t \leqslant \min\left\{\frac{|T_i|}{\mathcal{P}_i(|\mathbf{u}\cdot\mathbf{n}|+\sqrt{gh})_i}, \frac{|T_i|}{\mathcal{P}_i(|\mathbf{u}\cdot\mathbf{n}|+\sqrt{gh})_i\sqrt{2\alpha^n}}, \frac{|T_i|}{2\max\left(D_{xx}, D_{yy}, \epsilon\right)}\right\}. \tag{4.48}$$

A fixed CFL = 0.9 is used, and in all of our simulations, we use $\alpha^n = 1$ in a first-order approximation, except in cases where we specify the value of α^n used. The used computer is an Intel Core i7-8565U CPU @ 1.80GHz × 8, with 15 GB RAM.

In order to validate the FVC scheme on unstructured meshes to simulate shallow water flows, we present some test cases that are proposed by several authors to validate their model and their numerical approach. The accuracy is demonstrated by comparing numerical solutions produced by the FVC scheme with analytical solutions, especially in the tests 4.4.1, 4.4.2 and 4.4.3. To reproduce the calculation results reported in the literature, the source term of the bed is always taken into account. The C-property produced by this term has also been treated in tests 4.4.4 and 4.4.5. The Coriolis effect was taken into account in test 4.4.6 and this test's results are in good agreement with those presented in the literature. The test 4.4.8 compares the experimental data of a dam break flow in a channel with a 90° bend. This experiment was carried out in the laboratory of the Civil Engineering Department of the UCLouvain University, Belgium. We took into account the friction source term for this last simulation.

4.4.1 Accuracy test example

We test the present approach on a problem where the exact solution is known [115]. It can be easily checked that.

$$h(t,x,y) = 1 - \frac{a^2}{4bg}\exp\Big(-2b(\bar{x}^2+\bar{y}^2)\Big),$$

$$u(t,x,y) = Mcos(\theta) + a\bar{y}\exp\Big(-b(\bar{x}^2+\bar{y}^2)\Big), \quad v(t,x,y) = Msin(\theta) - a\bar{x}\exp\Big(-b(\bar{x}^2+\bar{y}^2)\Big),$$

where $\bar{x} = x - x_0 - Mt\cos(\theta)$ and $\bar{y} = y - y_0 - Mt\sin(\theta)$,
give a smooth solution of the shallow water system (2.20) without the source terms (i.e. $\boldsymbol{\nabla} Z = 0$, and $f_c = 0$) for any choice of constants, M, a, b, x_0, y_0 and θ. Initial and boundary condition are set according to the exact solution. We let $M = \frac{1}{2}$, $g = 1$, $a = 0.04$, $b = 0.02$, and $(x_0, y_0) = (-20, -10)$. To test the ability of the scheme to resolve flows that are not aligned with the computational mesh, we let $\theta = \frac{\pi}{6}$. The computational domain is a square $\Omega = [-50, 50] \times [-50, 50]$, and the simulations performed up to time $t = 100\ s$.
The results obtained by FVC scheme are then compared with those of the well known Roe solver and the SRNH originally introduced in [73, 107] for hyperbolic systems with source terms. Note that, for homogeneous systems. We also propose to see the effect of different choices of the

parameter α^n. In [31] the authors showed that the parameter α^n controls the accuracy of the FVC scheme for its one-dimensional formulation. The reader can refer to the lemma 3.3.2 and its proof. Our study reaches almost the same conclusion on α^n, for this purpose, the Fig 4.11 shows the convergence order for three different choices of α^n.

Table 4.1: Relative L^1 errors obtained for the accuracy test example at time t = 100 s using the SRNH, Roe and FVC schemes.

Schemes	SRNH			Roe			$\text{FVC}_{\alpha^n=1}$		
	L^1 error in			L^1 error in			L^1 error in		
# Cells	h	hu	hv	h	hu	hv	h	hu	hv
2648	2.042E-04	5.344E-03	9.546E-04	2.107E-04	5.501E-03	9.867E-04	1.785E-04	4.379E-03	8.763E-04
10362	1.627E-04	7.626E-03	7.626E-03	1.673E-04	7.812E-03	7.931E-03	1.078E-04	1.534E-03	3.475E-03
40690	1.317E-04	2.716E-03	5.450E-03	1.359E-04	3.001E-03	5.656E-03	4.518E-05	5.430E-04	1.249E-03
161316	9.363E-05	1.628E-03	3.441E-03	9.930E-05	1.812E-03	3.666E-03	1.986E-05	2.083E-04	4.868E-04
640138	6.108E-05	4.911E-04	2.099E-03	6.619E-05	5.431E-04	2.565E-03	7.910E-06	6.798E-05	1.893E-04

Table 4.2: CPU time (s) obtained for the accuracy test example at time t = 100 s using the SRNH, Roe and FVC schemes.

Schemes	SRNH scheme	Roe scheme	$\text{FVC}_{\alpha^n=1}$ scheme
# Cells			
2648	16.71	14.31	11.91
10362	31.30	27.14	21.49
40690	184.81	163.55	101.46
161316	1887.89	1776.13	1003.26
640138	21031.82	17987.04	10524.03
$\simeq 10^6$	2.602E+05	2.082E+05	5.713E+04

A simple inspection of Table 4.2 reveals that for meshes with a low number of the cells, the measured computation time is comparable for the SRNH, Roe and FVC schemes, this performance was also observed in the 1D version of the FVC scheme (see Table 5.2 in [31]).

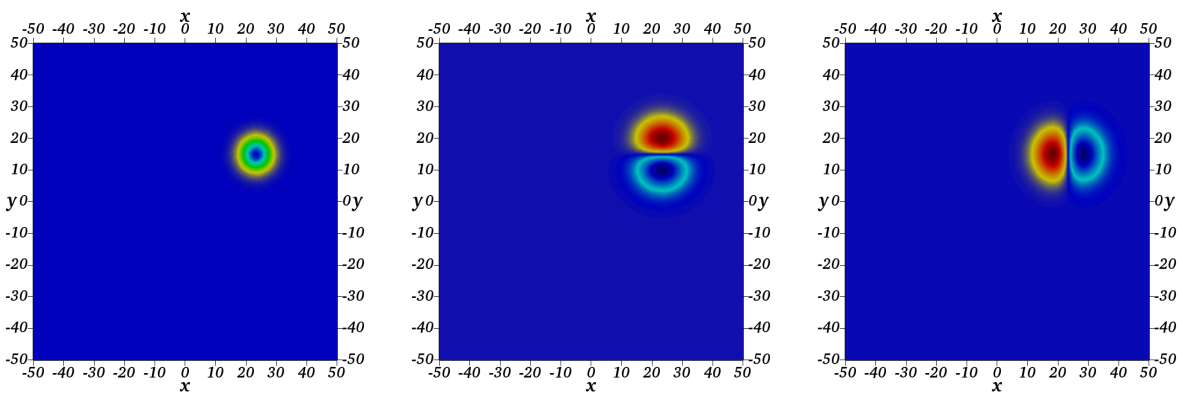

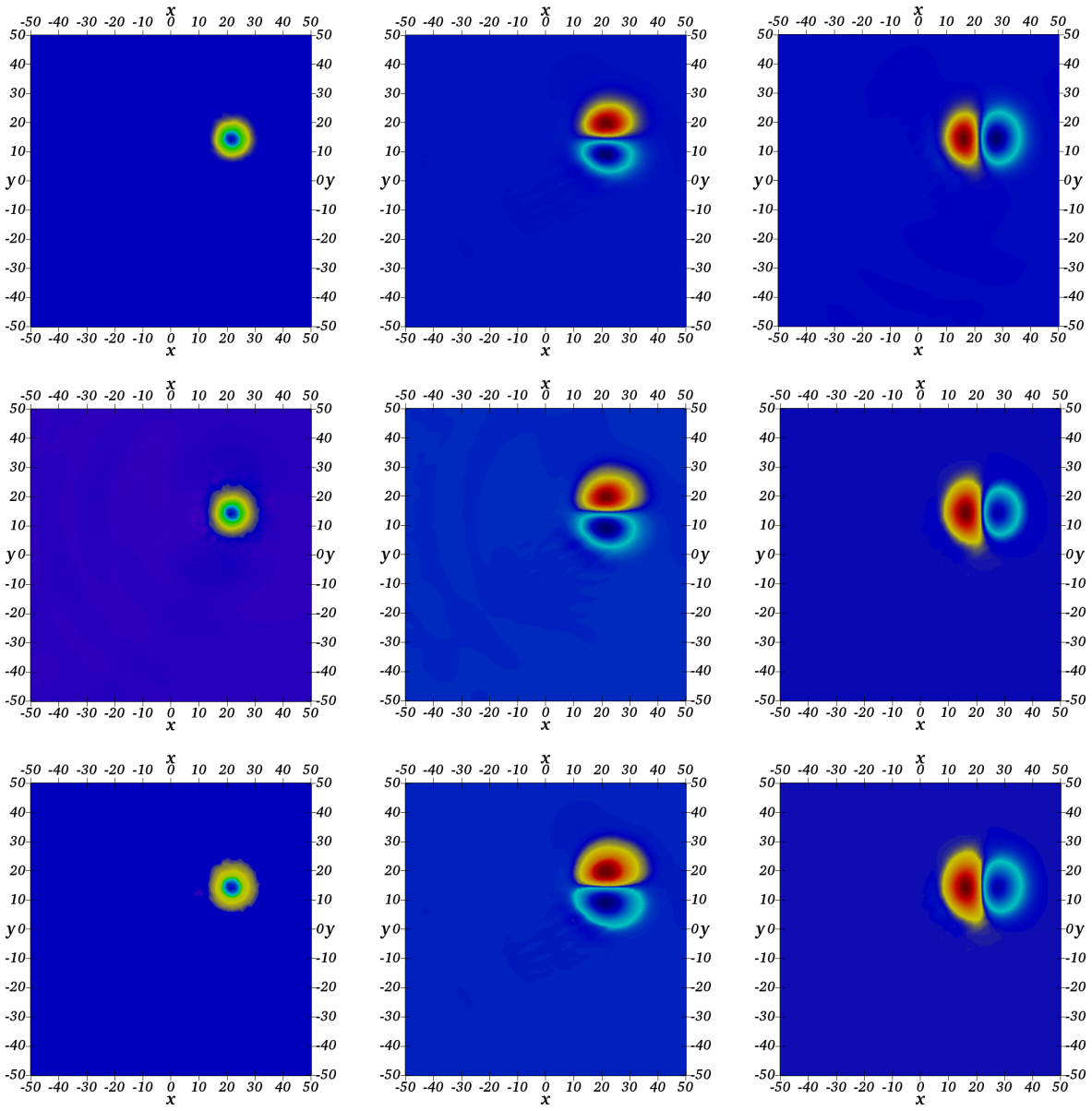

Fig 4.10. Water depth h and discharge hu and hv for the accuracy test example. First row: Exact solution. Second row: FVC scheme with $\alpha^n = 1$. Third row: Roe scheme. Fourth row SRNH scheme using a mesh with 10362 cells at t = 100 s.

The results in Table 4.1 show that increasing the number of cells in the computational domain leads to a decrease in the L^1 error for the water height h, and the discharges hu and hv in all schemes. A faster decay of the error is observed in the FVC scheme than in the SRNH and Roe schemes, which is expected. Moreover, for meshes with a somewhat large number of cells, the FVC method is the most efficient. For example, for a mesh of $\simeq 10^6$ cells, the Table 4.2 also shows the FVC scheme is about four times faster than the SRNH and Roe schemes. This is due to the fact that the FVC approach does note require the calculation of the Jacobian matrix of the system, this matrix occurs in many Q-scheme type approximation schemes, and is responsible for the slowness of this kind of scheme. Note that the Roe and SRNH schemes require a solver for the Riemann problem at each time step to reconstruct the numerical flux,

which is completely avoided in the FVC scheme. We can see that the three schemes could reach the designed order of accuracy. In Fig 4.11 we have plotted the log of L^1 error calculated in Table 4.1 and the other fixed values calculated for $\alpha^n = 0.5$ and then $\alpha^n = 2$ against the log of the maximum value of the mesh edges. We find that the L^1 errors of the FVC scheme lie on a slope line of 1.4, indicating that the accuracy order of the scheme is about 1.4 for $\alpha^n = 0.5$. These results are consistent with what the authors said in [31].

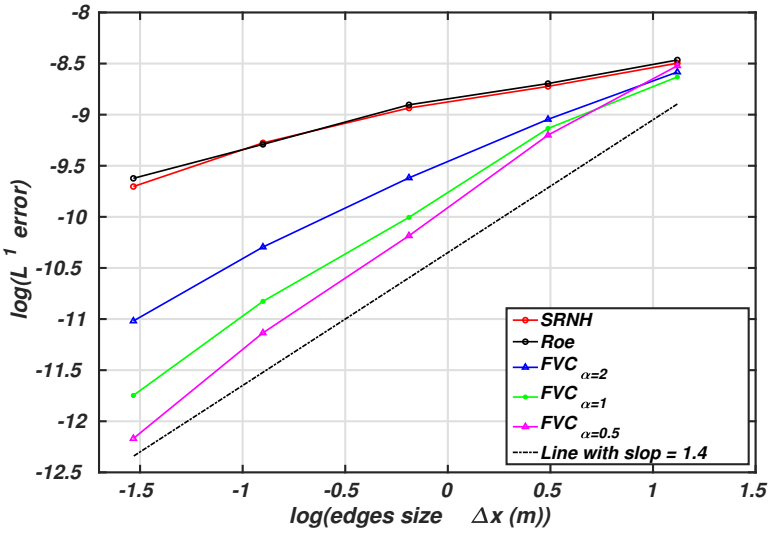

Fig 4.11. Convergence order in L^1 error of a water height.

4.4.2 Dam-break problem

Flood flows produced by the dam break, segments of dykes, or other structures are torrential in nature, with the presence of a discontinuous front propagating downstream and a rarefaction wave propagating upstream. The characteristics of these flows, such as velocity, water level, and time of arrival of floods must be determined in advance in order to manage floods and reduce their impact on the environment and economic infrastructure. In order to test the present approach for problems related to dam break, we carried out a series of test cases proposed in the literature (see, e.g. [31]).
The proposed approach is not based on a Riemann solver technique, which is very appropriate for a hyperbolic problem whose solution is often represented by a discontinuous front. Thus it will be interesting to examine the accuracy of the present approach by simulating torrential flows in the presence of a discontinuity in the velocity profile and the free surface.

4.4.2.1 Description of the problem

We consider a rectangular channel with a flat bottom, $Z(x, y) = 0$ and no friction, i.e., there is no source terms, the problem is purely hyperbolic. The channel is 1.6 m long and 0.1 m wide (we assume a nondimensionalization problem), and the initial conditions are given by

$$h(0, x, y) = \begin{cases} h_l & if\ x \leqslant x_m, \\ h_r & if\ x > x_m, \end{cases} \qquad 0 \leqslant y \leqslant 0.1 \tag{4.49}$$

$u(0, x, y) = v(0, x, y) = 0\ m/s$. A dam is placed in the middle of the channel i.e., $x_m = 0.8\ m$

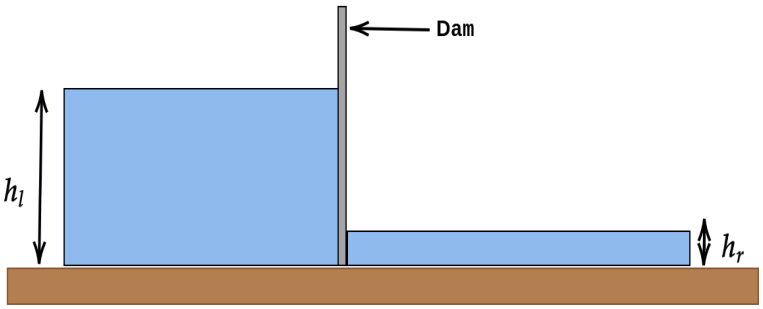

Fig 4.12. Initial condition of the problem.

This corresponds to a homogeneous Riemann problem. Initially, the water is at rest, and the height h_l remains 1.0 m for all simulations. The downstream height h_r takes on different values 0.5 m, 0.1 m, and 0.025 m. The nature of the torrential flow due to the dam break depends essentially on the ratio h_r/h_l.
A numerical instability is likely to occur for small values of the ratio h_r/h_l. At $t = 0\ s$, it is assumed that the dam is abruptly removed causing a shock wave with the presence of a discontinuous front of the water surface propagating downstream.
The channel is assumed to be closed on all four sides and the "slip" conditions are imposed on all walls. The computational domain is discretized by a mesh of 41776 triangles with an average size of 0.003 m^2. We will compare the water height and velocity obtained by the FVC scheme with the analytical solution, which is calculated using the Stoker method [116], its expression is written in the appendix section.

The evolution of the water surface profile is used to examine the behaviour of the FVC scheme in capturing the discontinuous shock front. Henderson [117] notes that when the ratio h_r/h_l is greater than 0.138, the flow is sub-critical in the whole of the channel. When the ratio h_r/h_l is smaller than 0.138, the flow is supercritical downstream and sub-critical upstream of the dam.
For very small values of h_r/h_l, the upstream flow regime becomes strongly supercritical, and it may be difficult to capture such a shock wave numerically.

4.4.2.2 Results and discussion

The first simulation concerns a river flow with $h_r/h_l = 0.5$. The Fig 4.13 shows the cross-section at $y = 0.05$ m of the evolution of the water depth and the longitudinal velocity. Excellent agreement is obtained between the numerical and analytical results, this is clear from Table 4.3 where the L^1 error and the accuracy order of h and hu are presented, respectively. The comparison shows that, under this condition, the FVC scheme can accurately predict the shock wave without creating oscillations.

In [118] the authors have proven that for a ratio h_r/h_l smaller than 0.05, most of the existing numerical models cannot give accurate results especially on the front. The last simulations, with $h_r/h_l = 0.025$ and ∞ (see Fig 4.14 and Fig 4.15), create supercritical flows downstream and sub-critical flows upstream. When $h_r/h_l \leqslant 0.025$, a slight, non-physical oscillation occurs at the shock front.

Table 4.3: Relative L^1 error and CPU times for dam break test at t = 0.1 s using FVC scheme on a different meshes.

# Cells	Maximum of edges size	Error in h	Error in hu	Order	CPU time (s)
5252	0.0127	2.612E-03	2.189E-02	-	7.91
10632	0.00913	1.650E-03	1.378E-02	1.402	10.66
21224	0.00666	1.045E-03	8.711E-03	1.453	19.96
41776	0.00479	6.255E-04	5.169E-03	1.583	30.21

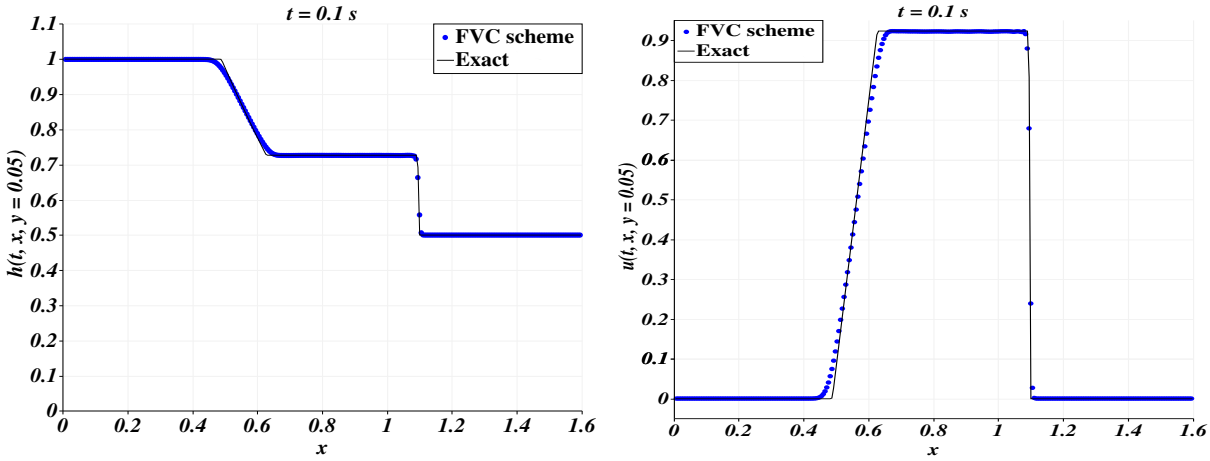

Fig 4.13. Comparison of results for $h_r/h_l = 0.5$ at t = 0.1 s. Left: water height h. Right: longitudinal velocity u.

The ratio h_r/h_l is largely responsible for the problem of numerical instabilities that occur in the simulation of torrential flow due to dam break. The difficulty of the problem increases as the ratio h_r/h_l decrease. We conclude that the proposed approach is well able to simulate torrential flows with a good capture of the shock front for the small ratio h_r/h_l.

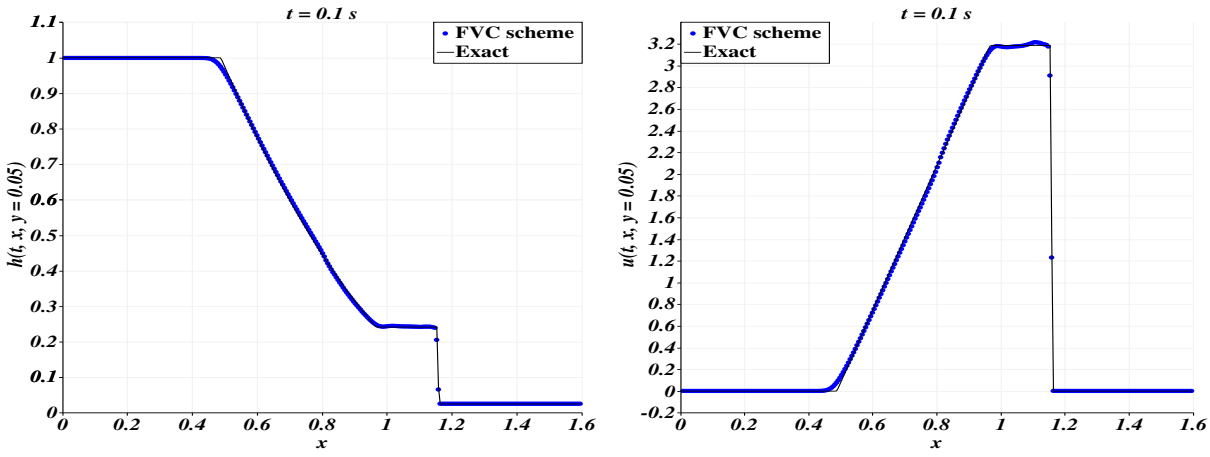

Fig 4.14. Comparison of results for $h_r/h_l = 0.025$ at t = 0.1 s. Left: water height h. Right: longitudinal velocity u.

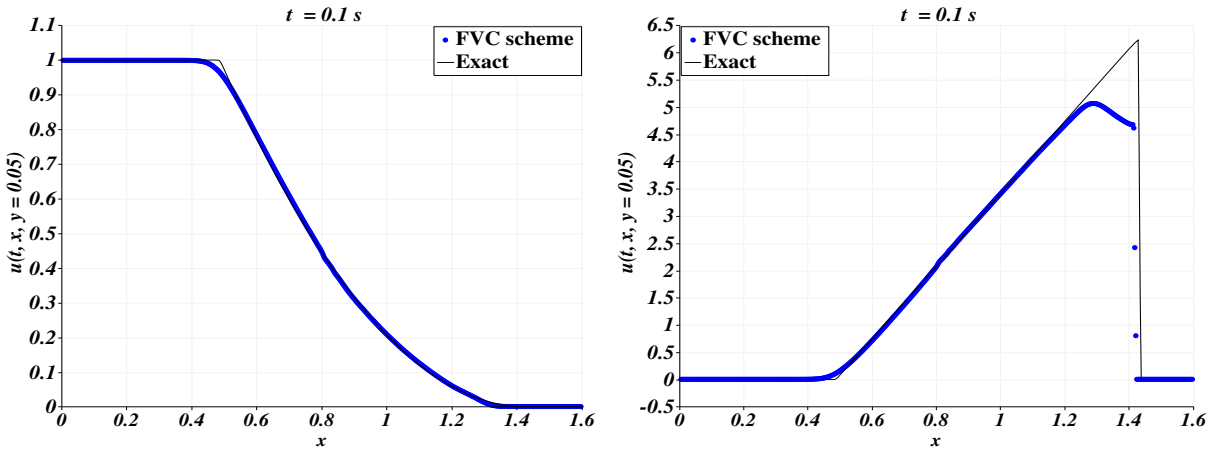

Fig 4.15. Comparison of results for $h_l = 0$ at t = 0.1 s. Left: water height h. Right: longitudinal velocity u.

Now let's consider a test with a non-flat bottom. We consider a two-dimensional dam break problem on a discontinuous bottom where the discontinuity is present at the dam location. The bottom of the bed is assumed to be without friction. This test is very interesting because it includes most flow structures such as shocks, rarefaction waves and contact discontinuities. The purpose of this test is to compare the scheme's performance with the results of the SRNH scheme presented in [7]. We used $Z_l = 0m$, $Z_r = 1m$, $h_l = 5m$, $h_r = 1m$. An unstructured grid with 13145 elements is used for this simulation. In Fig 4.16, we show cross-sections of the water free surface and the velocity at $y = 0.05m$ and at time $t = 0.5s$. We found that the obtained results are in good agreement with previous research, (for more details, we invite readers to consult 4.1 of [7]). We define the relative error in the L^1 norm defined as $\frac{\sum_{i=1}^{N_{ele}} |T_i||u_i^n - u(t_n, x_i, y_i)|}{\sum_{i=1}^{N_{ele}} |T_i||u(t_n, x_i, y_i)|}$, where u_i^n and $u(t_n, x_i, y_i)$ are respectively, the computed and exact solutions at the cell T_i, and N_{ele} denotes the total number of cells.

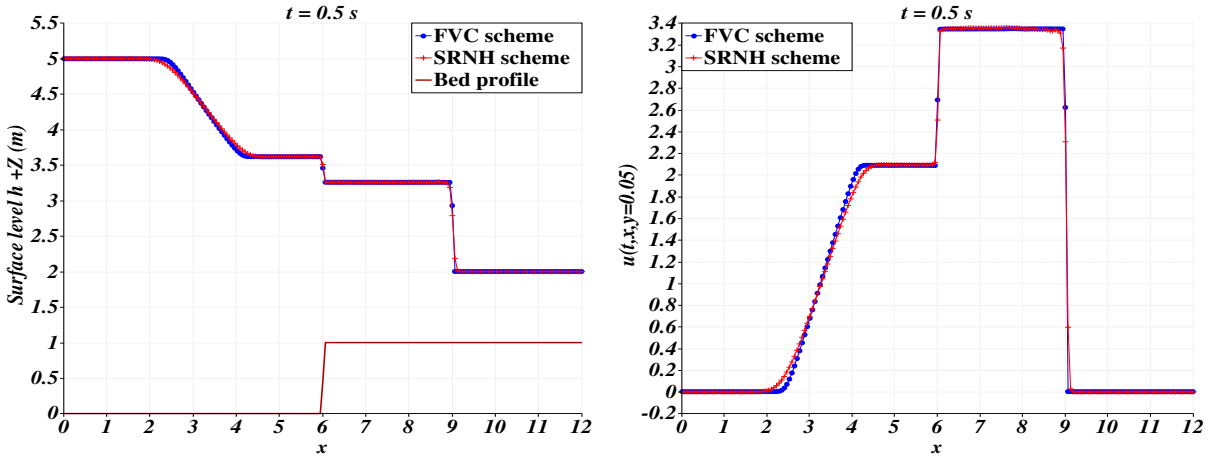

Fig 4.16. Shallow water flow over a forward facing step at t = 0.5 s. Left: surface level $h + Z$. Right: longitudinal velocity u.

The previous test case was one-dimensional in nature. In the real-world applications, torrential flows due to dam and dike segment failures are often two-dimensional. Therefore, the objec-

tive of the Fig 4.17 is to show the ability of the proposed scheme to reproduce two-dimensional flood propagation in the presence of a discontinuous front of water height and velocity over a wet bottom. This problem has been treated by many authors to validate their dam break models approximation schemes (see, e.g. [119, 120]). We suppose that at $t = 0$ s, abruptly reservoir dam is partially broken and unsymmetrical over a length of 75 m. Initially $h_r/h_l = 0.5$ is fixed with $h_l = 10$ m as the water depth in the reservoir and $h_r = 5$ m as the water level downstream of the dam. The water in the basin is at rest at $t = 0$ s, that is $u(0, x, y) = v(0, x, y) = 0m/s$. The gravitational acceleration is fixed to $g = 9.81m/s^2$ and the simulation is performed on a triangular unstructured mesh with 4066 elements up to physical time t=7.2s. Fig 4.17 and Fig 4.18 show respectively 3D view of the water height h, contours of h and the velocity field at physical time 7.2s.

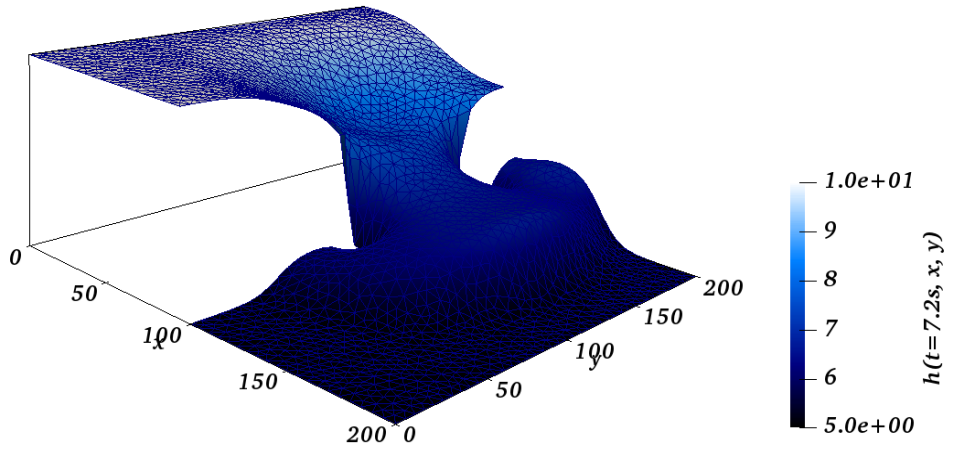

Fig 4.17. Water height at = 7.2 s.

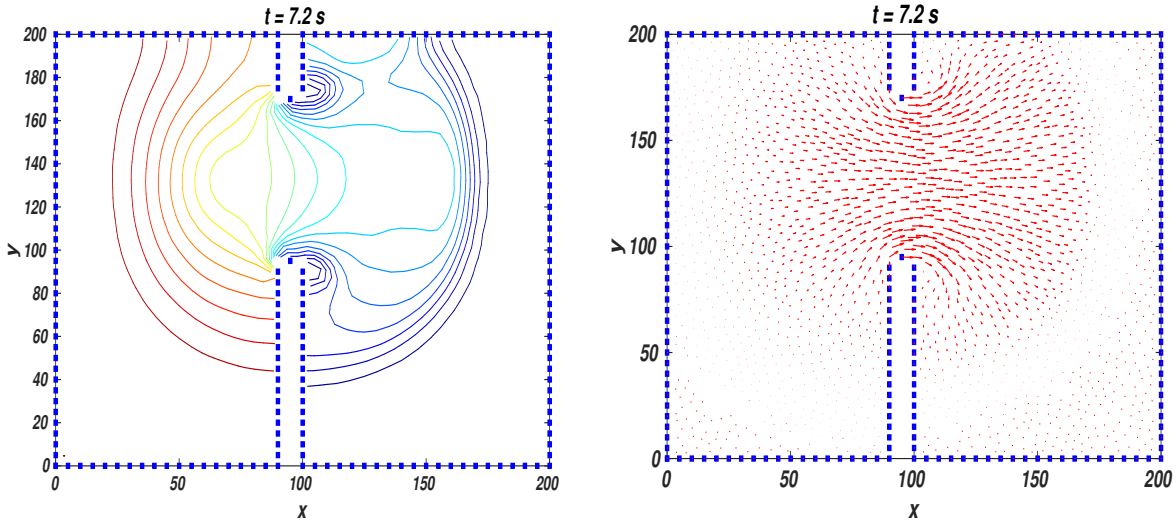

Fig 4.18. Left: contours of water depth h. Right: velocity vector field.

We can observe that the right-hand flow propagates downstream from top to bottom, the rarefaction wave propagates upstream and two asymmetric weak eddies develop on both sides of the rift. Good resolution is achieved in areas characterized by significant water level gradients,

such as moving fronts. Furthermore, the global flow is preserved without excess numerical diffusion. Our results seem to be very similar to those presented by the existing studies mentioned above.

In order to show the convergence accuracy of the FVC scheme the same simulations were performed on three types of meshes: mesh 1 is a coarse mesh with 2012 triangles, mesh 2 has twice the number of the mesh 1 triangles, 4066 triangles and a fine mesh with 10083 triangles. A reference solution is calculated by the FVC scheme on a mesh of 101005 triangles; this solution is used to quantify the numerical results obtained on the three meshes. In Fig 4.19, we present the cross-sections of the water height and the hu discharge in different meshes along the axes $y = 125\ m$ at time $t = 7.2\ s$.

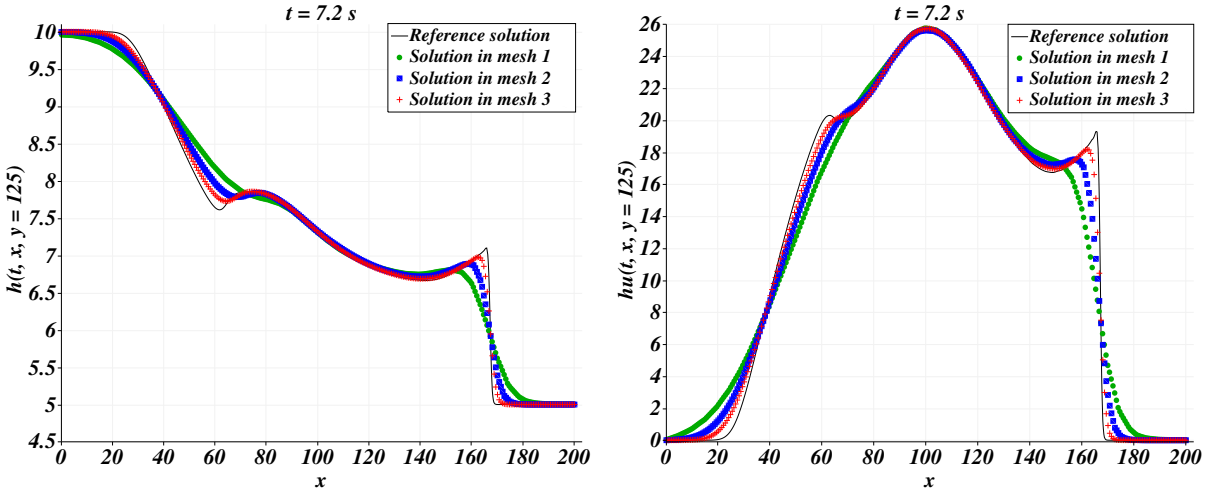

Fig 4.19. Horizontal cross-sections at $y = 125\ m$ of the water depth (left Fig) and the water velocity (right Fig) for the partial dam-break problem obtained by using different meshes at time 7.2 s.

This test case confirms the ability of the FVC scheme to reproduce two-dimensional flows in the presence of a discontinuous front. The uncovering and overlapping domains are well treated by the scheme. Furthermore, this test case allows us to perform the calculations using the present approach to determine both the water head and the velocity at the open boundary. It excludes numerical oscillations, therefore it is stable.

4.4.3 Tidal wave flow over an irregular bed

Here we propose to study a tidal flow on an irregular bed. This test case has been proposed in several works to validate and to test the C-property of their approximation method [10]. It is well known that in the shallow water equations describing a flow over an irregular background, the source terms become dominant and may cause undesirable numerical instabilities. Therefore this test case allows us to test the reliability and robustness of the proposed model when the bottom variation is irregular. The bottom profile is defined in the appendix (table of bed elevation $Z(x)$ and its illustration). The initial and boundary conditions are constructed from the asymptotic analytical solution given by

$$h(t,x) = h_0 + 4 - Z(x) - 4\sin\Big(\pi(\frac{4t}{86400} + \frac{1}{2})\Big),\quad u(t,x) = \frac{\pi(x-1500)}{5400\cdot h(t,x)}\cos\Big(\pi(\frac{4t}{86400} + \frac{1}{2})\Big)$$

with, $\quad h_0 = 16\ m, \quad h(0,x) = h_0 - Z(x).$

In Fig 4.20 we present a comparison between surface level and the analytical solution at $t = 10800\ s$ as well as the water height at the same time using a mesh of 200 grid points in the x-direction. We also include in Fig 4.21 a comparison between the water velocity generated by the FVC scheme and the analytical velocity at $t = 10800\ s$ then at $t = 32400\ s$. In Table 4.4 we present a comparison between the exact solution and the solution generated by the FVC scheme using the relative L^1 error. An excellent agreement is obtained between the numerical and analytical solutions. This confirms that the proposed scheme is also accurate for tidal flow over an irregular bed.

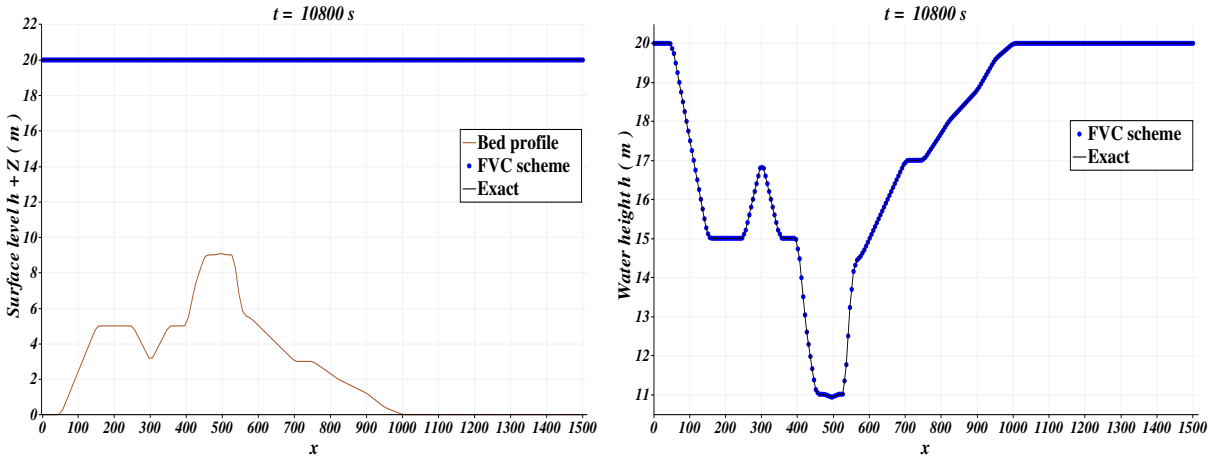

Fig 4.20. Tidal wave flow over an irregular bed. Left: comparison of surfaces level $h + Z$ at $t = 10800\ s$ and bed Z. Right: Comparison of water height h.

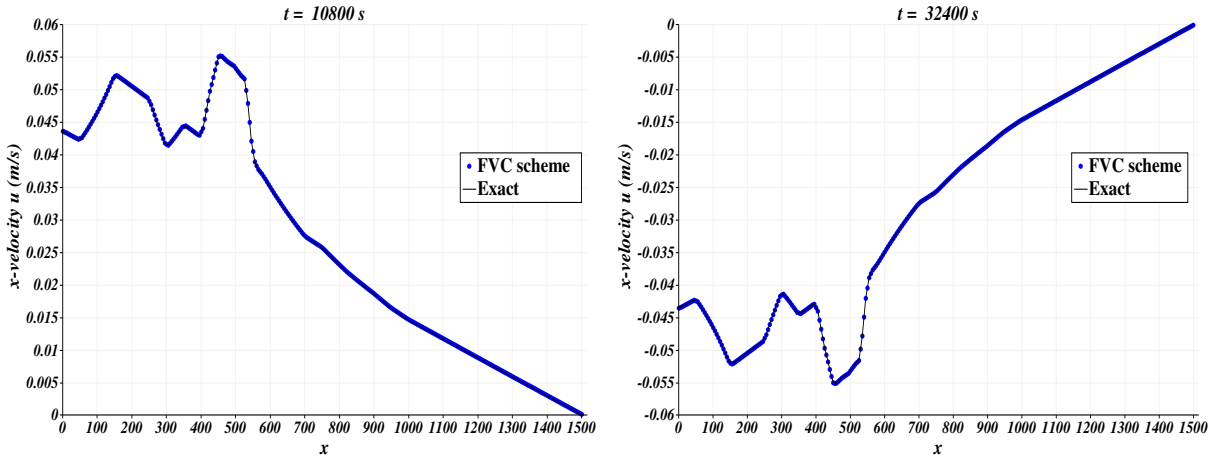

Fig 4.21. Comparison of water velocity u in tidal wave flow over an irregular bed. Left: at $t = 10800\ s$. Right: at 32400 s.

Table 4.4: Relative L^1 error and CPU times for the tidal wave flow over an irregular bed using FVC scheme over a mesh of 1510 cells.

t_{end}	Error in h	Error in hu	Error in $h+Z$	CPU time (s)
10800	1.254E-05	4.230E-03	1.012E-05	545.95
32400	7.719E-06	5.731E-03	1.241E-05	1583.41

The accuracy of the proposed scheme in the treatment of the source terms has been identified. The numerical errors produced by the model remain very low even though the mesh is coarse and the bed is very irregular, for comparison we can see Table 1 of Section 4 in [10]. The results of this test case confirm the good performance of FVC scheme in the treatment of the source terms while avoiding undesirable numerical errors due to the rapid variation of the bed.

4.4.4 Flow over a non-flat irregular bed

•) ***Case 1***

We consider the example of water flow in a two-dimensional channel including an irregular bed, a similar test has been proposed in [10]. The mathematical formulation consists of solving the shallow water system (2.20) without Coriolis force and subjected to Neumann boundary conditions. The initial conditions as follow

$h(0,x,y) = 1 - Z(x,y)\ m, \qquad u(0,x,y) = v(0,x,y) = 0\ m/s,$

where the bed profile is defined by: $Z(x,y) = \sum_{k=1}^{5} a_k \exp\left(-\dfrac{(x-x_k)^2+(y-y_k)^2}{\sigma_k^2}\right),$

with $(a_1,\sigma_1^2,x_1,y_1) = (0.75,2,-4,5)$, $(a_2,\sigma_2^2,x_2,y_2) = (0.7,2,-2.5,2.5)$, $(a_3,\sigma_3^2,x_3,y_3) = (0.65,3.3,0,0)$, $(a_4,\sigma_4^2,x_4,y_4) = (0.6,2.5,3,-2)$, and $(a_5,\sigma_5^2,x_5,y_5) = (0.55,1.48,5,-4)$.

The purpose of this test example is to verify the achievement of the C-property for the FVC scheme applied to shallow water flows over non-flat bed.

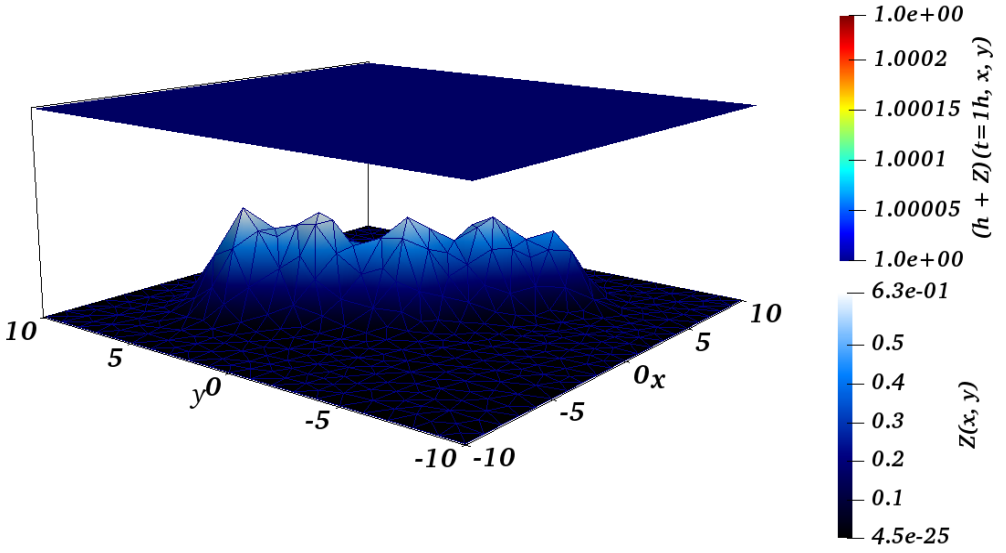

Fig 4.22. Water free-surface for the flow over a non-flat irregular bed at t = 1 hour.

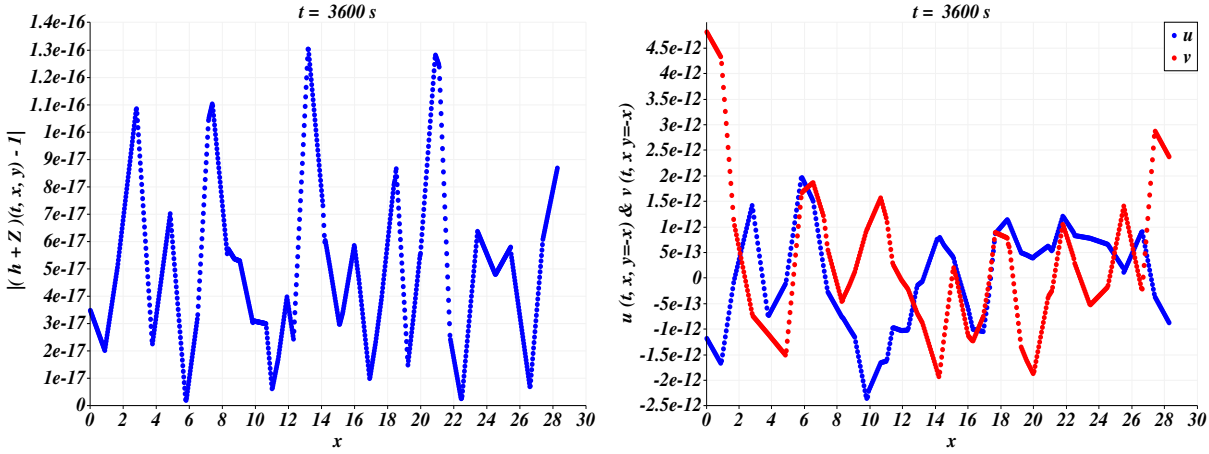

Fig 4.23. Cross-sections at $y = -x$. Left: the absolute error of the free-surface for the lake at rest. Right: velocities values after 1 hour.

The C-property of well-balanced FVC scheme on unstructured meshes is checked in this example. In Fig 4.22, we present 3D view of the water free-surface obtained at time $t = 3600\ s$ using an unstructured mesh of 1030 cells. As expected the water free-surface remains constant during the simulation time. The velocities and the error presented in Fig 4.23 also show that the equilibrium of the lake at rest is verified. These results shows that the proposed FVC scheme perfectly preserves the C-property.

•) ***Case 2***

We will treat the same problem as in case 1 but this time with a very large computational domain $\Omega = [0, 1500] \times [0, 500]$ and a non-smooth bed profile. As you have seen in case 1, the C-property is verified with a qualitatively admissible accuracy but the idea behind using this case is to compare the accuracy of the FVC scheme with the results of work that has been done using a Cartesian mesh [30, subsection 4.1]. The bed profile and the initial condition are defined as

$h(0, x, y) = 20 - Z(x, y)\ m, \qquad u(0, x, y) = v(0, x, y) = 0\ m/s,$

the bed profile $Z(x)$ is defined in the appendix. The results presented in Table 4.5 and in the figures, Fig 4.24 and Fig 4.25 are in good agreement and even better than those in [30]. They also demonstrate that the present approach accurately preserves the C-property, regardless of the complexity of the bed.

Table 4.5: Relative L^1 and L^∞ errors of the water free surface for flow over a non-flat irregular bed case 2 at 1h, 2h then 3hours.

		L^1 error			L^∞ error		
# Cells	Maximum of edges size	$t = 3600s$	$t = 7200s$	$t = 10800s$	$t = 3600s$	$t = 7200s$	$t = 10800s$
776	68.94	1.700E-15	3.109E-15	3.231E-14	2.664E-15	4.085E-15	3.428E-14
1664	50.96	1.401E-15	3.023E-15	6.332E-15	1.580E-15	8.881E-16	8.015E-16
3218	35.58	4.845E-16	4.813E-16	7.011E-16	1.010E-15	8.881E-16	8.015E-16

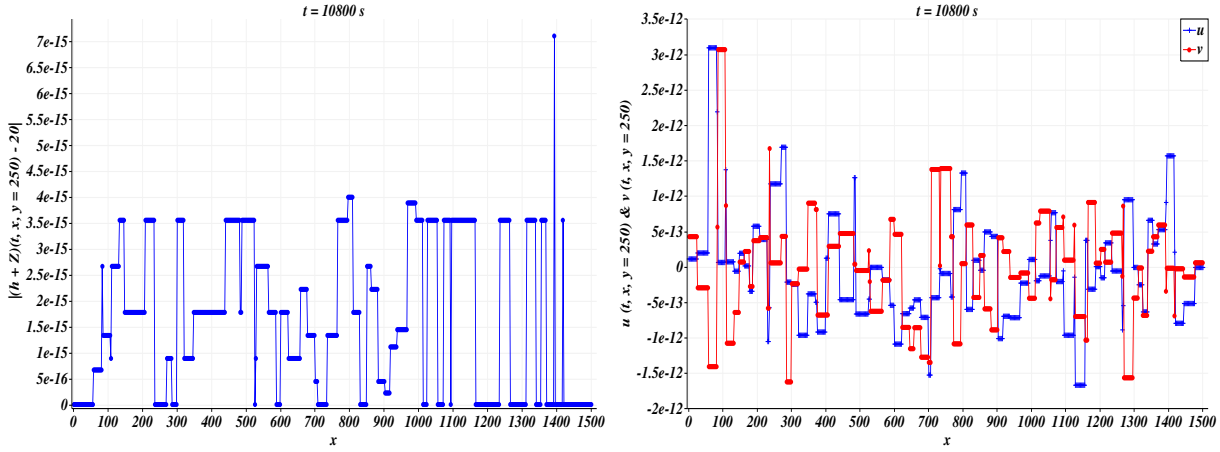

Fig 4.24. Cross-sections at $y = 250$. Left: the absolute error of the free-surface for the lake at rest. Right: velocities values at 10800 s.

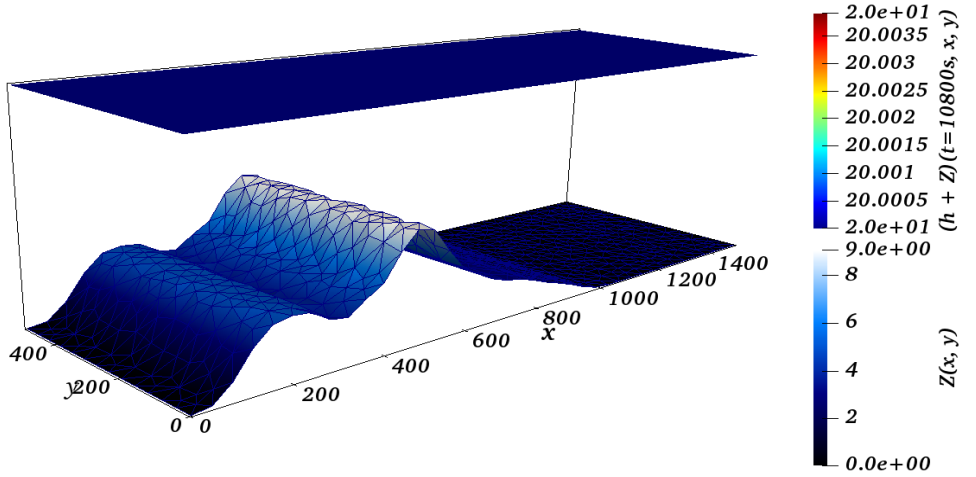

Fig 4.25. Water free-surface for the flow over a non-flat irregular bed case 2 using a mesh with 1664 cells at t = 10800 s.

4.4.5 A small perturbation of a steady-state over a smooth bed

This test was introduced by R.J. LeVeque in [121] and recently used in [122]. This is a classical example demonstrating the effectiveness of the proposed well-balanced FVC scheme in handling perturbations in the stationary state. We solve the two-dimensional shallow water equations in the rectangular domain $\Omega = [0, 2]\times[0, 1]$ subjected to Neumann boundary conditions and the following initial conditions

$$h(0,x,y) = \begin{cases} 1 - Z(x,y) + 0.01 & if \quad 0.05 \leqslant x \leqslant 0.15, \\ 1 - Z(x,y) & otherwise, \end{cases} \qquad 0 \leqslant y \leqslant 1, \tag{4.50}$$

$u(0,x,y) = v(0,x,y) = 0\ m/s$. It is assumed that the bottom has the following form:

$$Z(x,y) = 0.8\exp\Big(-5(x-0.9)^2 - 50(y-0.5)^2\Big).$$

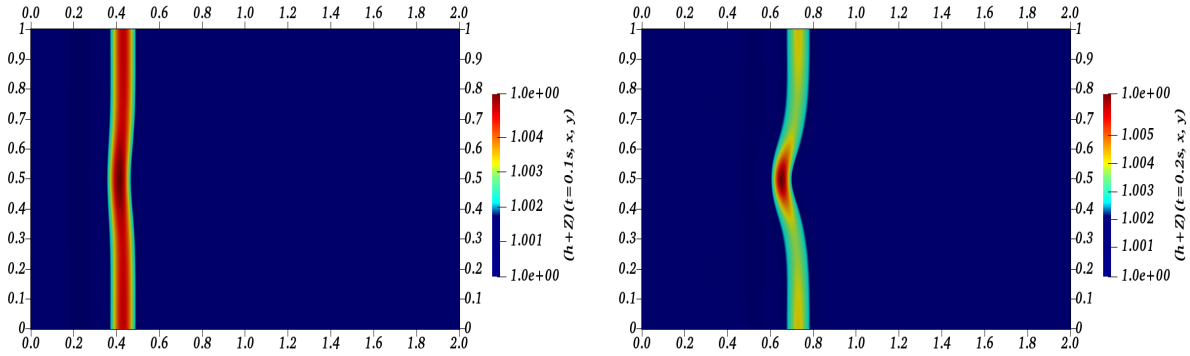

Fig 4.26. Illustration of the surface level $h + Z$ at times $t = 0.10\ s$ and $0.20\ s$ respectively.

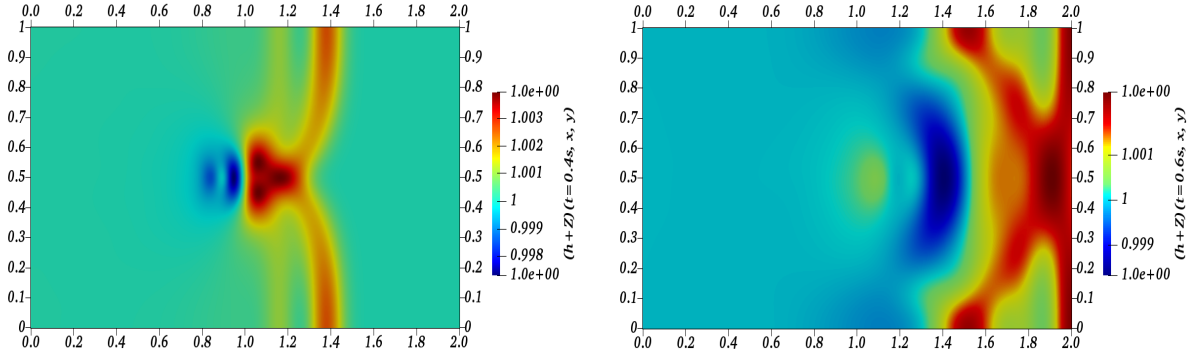

Fig 4.27. Illustration of the surface level $h + Z$ at times $t = 0.40\ s$, and $0.60\ s$, respectively.

Fig 4.26 and Fig 4.27 display the right going of the disturbance as it propagates over the hump on an unstructured triangular mesh of 165008 cells, the surface level $h + Z$ is shown at different times. From top to bottom: $t = 0.10\ s$ from $0.999906\ m$ to $1.003861\ m$; $t = 0.20\ s$ from $0.999733\ m$ to $1.004363\ m$; $t = 0.40\ s$ from $0.998553\ m$ to $1.001256\ m$; and $t = 0.60\ s$ from $0.999339\ m$ to $1.000898\ m$. No spurious oscillations are present in the solution. The results indicate that the FVC scheme can resolve the complex small details of the flow over a smooth bed very well.

4.4.6 Circular dam-break problem

We consider the benchmark problem proposed in [123] to study cyclone/anticyclone asymmetry in nonlinear geostrophic adjustment. We solve the shallow water system (2.20) with a Coriolis effect on a non-flat bottom in the spatial domain $\Omega = [-10, 10] \times [-10, 10]$ subjected to Neumann boundary conditions and the following initial conditions

$$h(0, x, y) = 1 + \frac{1}{4}\left(1 - \tanh\left(\frac{\sqrt{ax^2 + by^2} - 1}{c}\right)\right), \quad u(0, x, y) = v(0, x, y) = 0m/s,$$

where $a = \frac{5}{2}$, $b = \frac{2}{5}$, $c = 0.1$, $f_c = 1\ Kg.m/s^2$ and $g = 1\ m/s^2$.

The bottom profile has the following expression: $Z(x, y) = 0.3\left(1 + \tanh\left(\frac{3x}{2}\right)\right)$.

Let's start by looking at the behaviour of this phenomenon in a domain with a flat bottom. The Fig 4.28 shows the representation of the water level calculated at different times for this test case with $Z(x, y) = 0$. As can be seen, a hole has formed, and water is flowing out of the deepest

region as a rarefaction wave progresses outward. It is clear from the results presented that the initial elliptical mass imbalance evolves in a non-axisymmetric manner. The two expected shock waves are very well captured by the proposed FVC method. These results are qualitatively in good agreement with those published in [30, 123]. In Fig 4.29 we exhibit the results for the velocity field corresponding to the plots Fig 4.28. As can be seen the two shock waves that originated behind the water elevation are slowly spinning clockwise in the computational domain. The velocity field is well represented by the FVC scheme, and re-circulation regions within the flow domain are well captured.

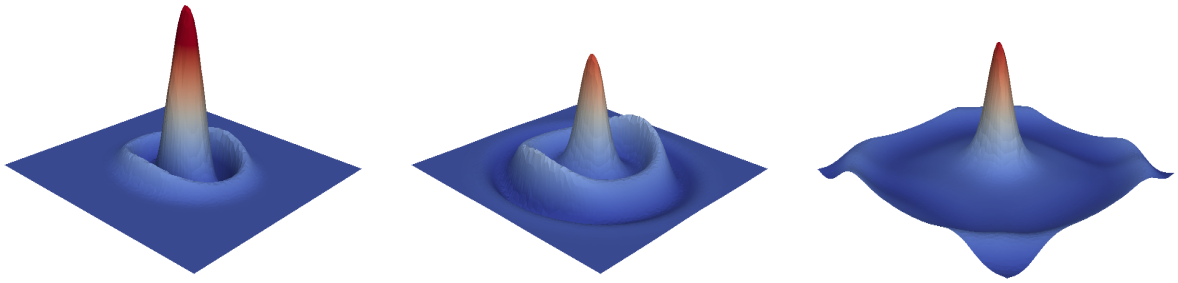

Fig 4.28. Water depth for the circular dam-break problem on flat bottom obtained at different times using a mesh with 10040 cells. From top to bottom $t = 4$ s, 8 s and 16 s.

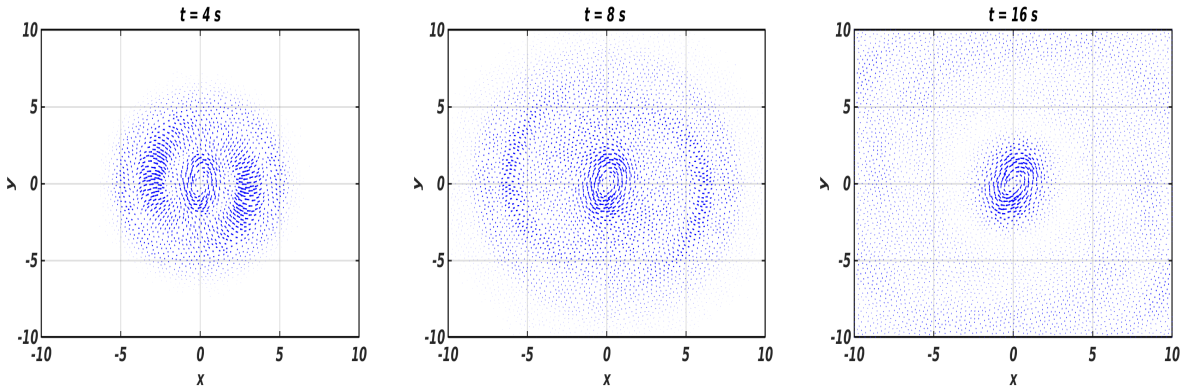

Fig 4.29. Velocity fields for the circular dam-break problem corresponding to the plots represented in Fig 4.28.

Let's move on to the case of the non-flat bottom to assess the performance of the FVC scheme on unstructured meshes to solve the circular dam-break problem on a non-flat bottom. The Fig 4.30 shows the calculated results for the water depth at $t = 2$ s, 8 s and 16 s using two meshes of 10040 and 40146 cells. The corresponding results for velocity field are presented in Fig 4.31. From a numerical point of view this test example is more difficult than the previous one as the flow is expected to exhibit complex features due to the interaction between the water surface and the bed. As in the previous test a hole has formed and the water drains from the deepest region as a rarefaction wave progresses outwards. However, a slower propagation is detected for the water free-surface in this test compared to the simulations on flat-bottom.

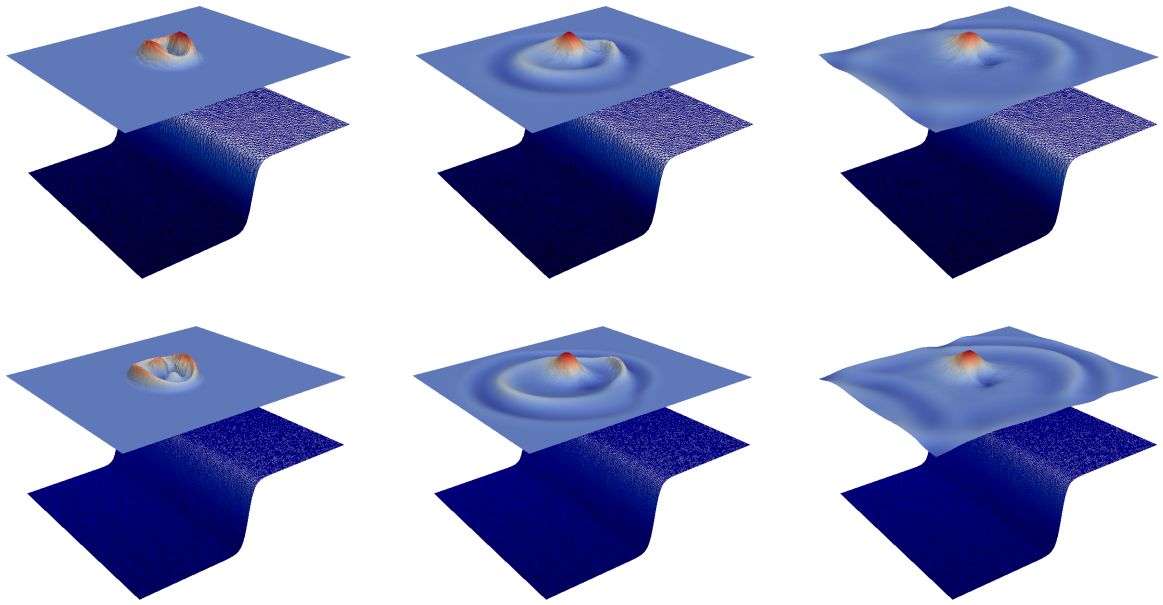

Fig 4.30. Water depth for the circular dam-break problem on non-flat bottom using a mesh with 10040 cells (first row) and 40146 cells (second row). From left to right $t = 2$s, 8s and 16s.

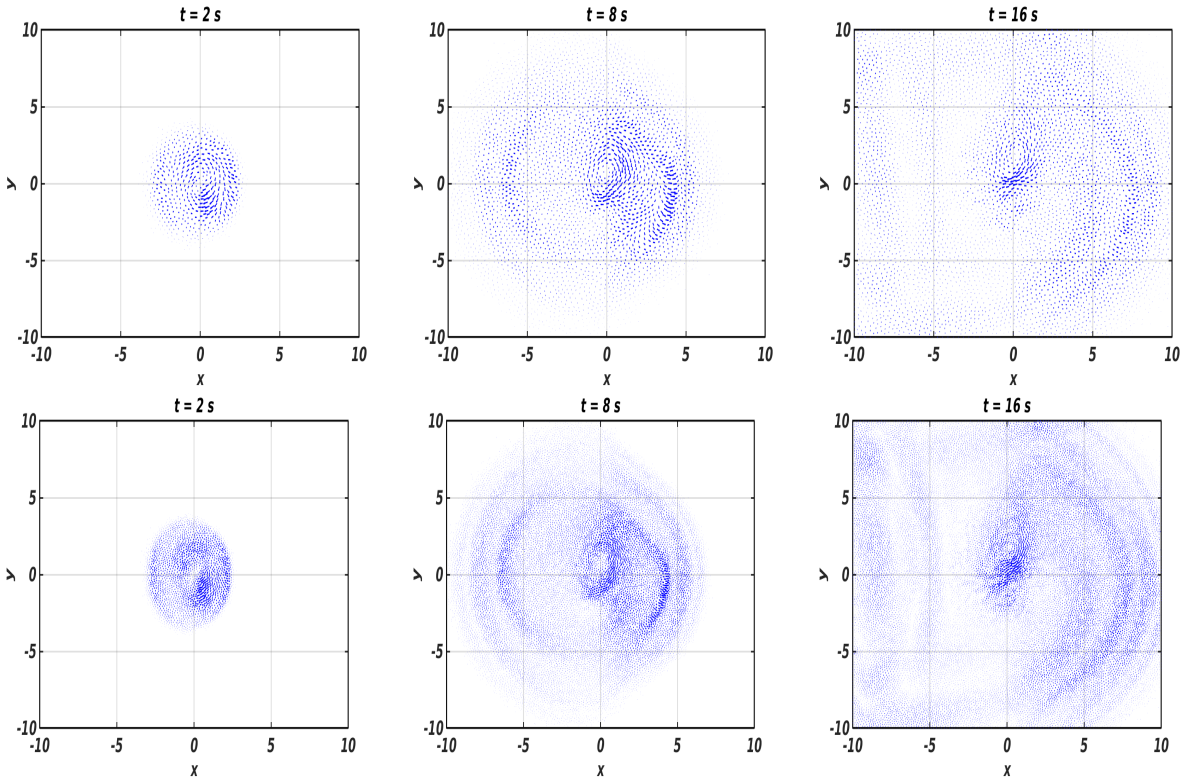

Fig 4.31. Velocity fields corresponding to the plots represented in Fig 4.30.

4.4.7 Oblique hydraulic jump

In this test, we examine an oblique hydraulic jump formed through the interaction of a supercritical flow on a flat surface and a converging wall tilted at an angle of $\theta = 8.95°$. The channel geometry's contraction, as depicted in Fig 4.32 generates the slanted hydraulic with an angle of $\beta = 30°$, resulting in a sudden rise in water depth. The parameters used in the simulation are the same as those referenced in [10, 124]. Consequently, the initial conditions are $h = 1m$, $u = 8.57m/s$, and $v = 0m/s$, yielding a Froude number of $Fr = 2.74$. The supercritical flow boundary conditions ($h = 1m$, $u = 8.57m/s$, and $v = 0m/s$) are specified at the upstream boundary, while transmissive boundary conditions are applied at the downstream boundary. The steady state solution stops the time integration process when the following inequality is satisfied

$$\frac{\left\|h^{n+1} - h^n\right\|_2}{\left\|h^n\right\|_2} \leqslant \epsilon.$$

In this case, the given tolerance ϵ is set to 10^{-6} for our computation. To demonstrate the effectiveness of the FVC scheme, we present the results obtained using a fixed grid of 29497 cells in Fig 4.33. It is noteworthy that the computed results exhibit good qualitative agreement with those reported in [10].

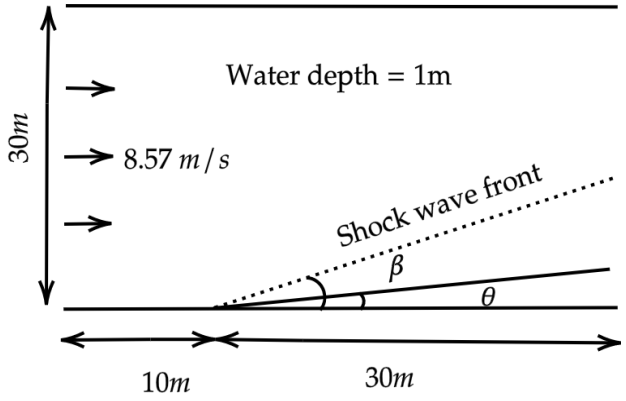

Fig 4.32. Oblique hydraulic jump.

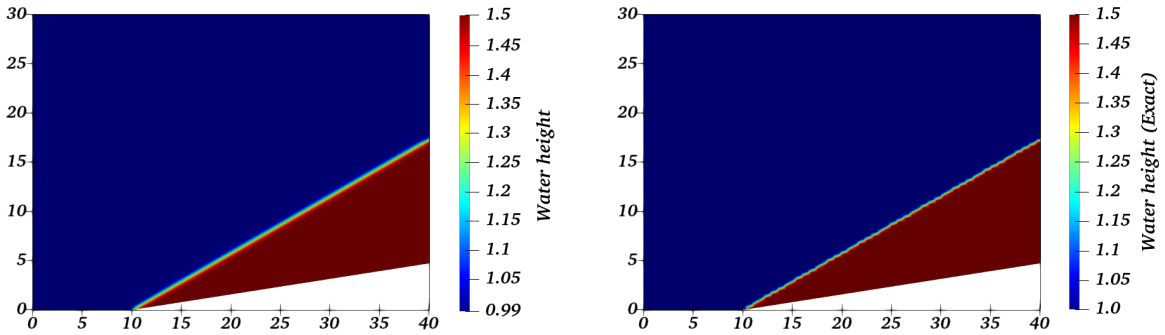

Fig 4.33. Water height using the FVC scheme (left figure) and exact solution (right figure).

In order to demonstrate the comparison between the FVC solution and the exact solution, we present a cross-sectional view at the downstream channel position $x = 40m$ in Fig 4.34 of the outcomes derived from the FVC scheme and the exact solution. It is important to mention that the FVC scheme generates accurate results in actual flow conditions compared to the exact solution.

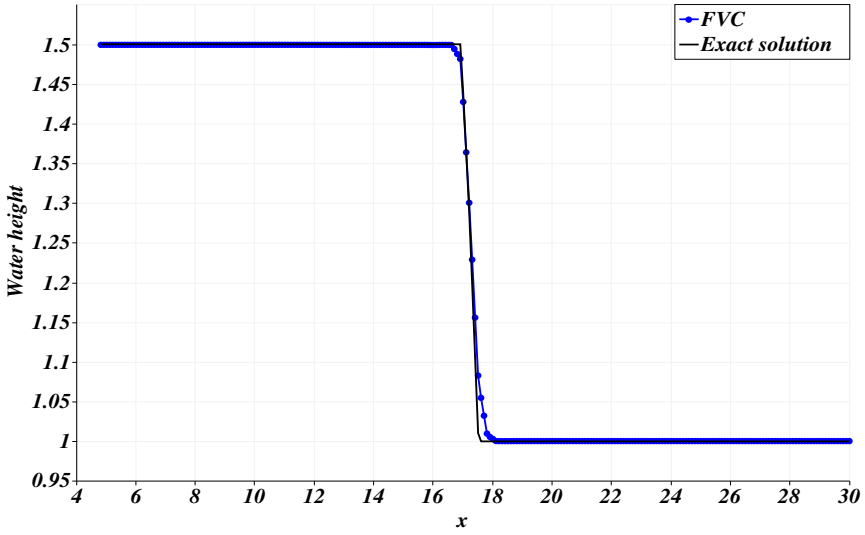

Fig 4.34. Water height for the oblique hydraulic jump: exact and FVC solutions.

4.4.8 Tidal wave of a dam burst: Experimental validation

The previous test cases pertain to simulating various types of flows in non-complex geometries without friction. Under these conditions, we do not generally encounter numerical problems due to the complexity of the computational domain. The present test case is used to evaluate the ability of the proposed model to calculate the flows due to a dam break through a 90° bend on a non-flat bottom with a large discontinuity in the bottom profile, as well as the assumption of friction terms. This is a physical experiment carried out in the framework of the European CADAM project in the laboratory of the Civil Engineering Department of the UCLouvain University, Belgium [125], for which a number of velocity and water level measurements are available in a laboratory channel.

4.4.8.1 Description of the problem

The geometry used in the experimental facilities consists of a rectangular reservoir of $2.44m$ $\times$ $2.39m$ and a $7.83m$ long channel with a 90° bend, as shown in Fig 4.35. The channel bed level is $0.33m$ above ground level. The bed is relatively smooth, with a Manning friction coefficient of 0.0095 $s.m^{-\frac{1}{3}}$. The initial water level in the reservoir is $0.25m$ and $0.01m$ in the whole channel. The authors of [126] used this test case to validate their numerical model, which is based on the solution of the shallow water equations over complex topography with wetting and drying. In order to compare the FVC scheme with the experimental results we propose six measurement points, which are located at $G_1(1.19m, 1.21m)$, $G_2(2.74m, 0.69m)$, $G_3(4.24m, 0.69m)$, $G_4(5.74m, 0.69m)$, $G_5(6.56m, 1.51m)$ and $G_6(6.56m, 3.01m)$, exactly like the study cited above. These measurements allow us to illustrate and compare the output of the code with the results of the experiment. The computational domain is discretized by an unstructured triangular mesh of 6165 cells see Fig 4.36.

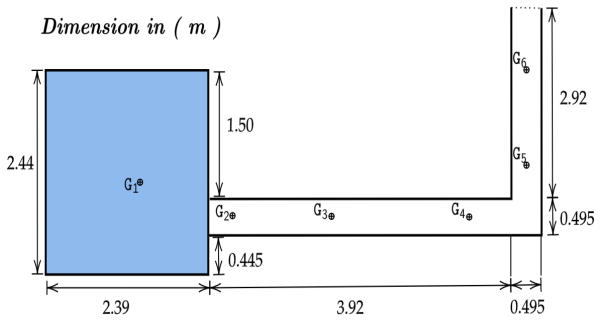

Fig 4.35. Plane view of the reservoir and the channel.

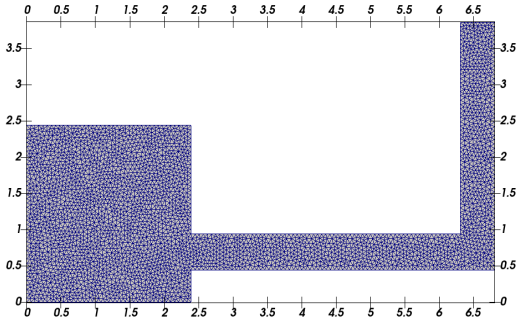

Fig 4.36. Unstructured mesh of the computational domain.

4.4.8.2 Results and discussion

Fig 4.37 presents the free surface and bottom profile obtained by the simulation at $t = 3\ s$, $5\ s$, $7\ s$ and $14\ s$, respectively. These figures show that the supercritical flow induced by the dam break is reflected in the bend, its speed becomes zero, and the water level rises. Then this column of water collapses, and a new waterfront propagates both downstream and upstream. Upstream, this results in a bore receding towards the reservoir. However, the flow rate at the bore head is now subcritical, therefore much slower than the initial supercritical flow. After this very transient phase, the flow approaches stable conditions where the inclination of the free surface is close to the description presented by [125]. Fig 4.39 allows us to compare the water height h obtained by FVC scheme with the experimental measurements and the results of the SRNH scheme. The FVC scheme gives values of h almost identical to the measured values, especially in the critical areas where there is an additional local pressure drop caused by a sudden change in the channel geometry [127, subsection 3.3]. In the flow process, it can be seen that the water arrives at the 90° bend at about 3 s after the dam break. Then the water is reflected by the wall to form a front that propagates back towards the reservoir, while the water flow after the 90° bend continues to flow downwards, and multiple reflections are observed. The water flow after the 90° bend continues to flow downwards and multiple reflections are observed on the channel walls with the appearance of complicated shapes on the part of the channel. Comparisons between the numerical results and the data collected for a wetted bottom of the measurement gauge points show that the flow arrival time is in good agreement on all gauge points. However, we notice that the FVC scheme captures the water level at gauge point 2 with good accuracy, while the SRNH scheme gives different results to the experimental data after 40 s. These results allow us to say that ou approach would predict dam break currents on a vertical step. It also confirms the ability of the FVC scheme to reproduce two-dimensional flows in the presence of a discontinuous front with friction.

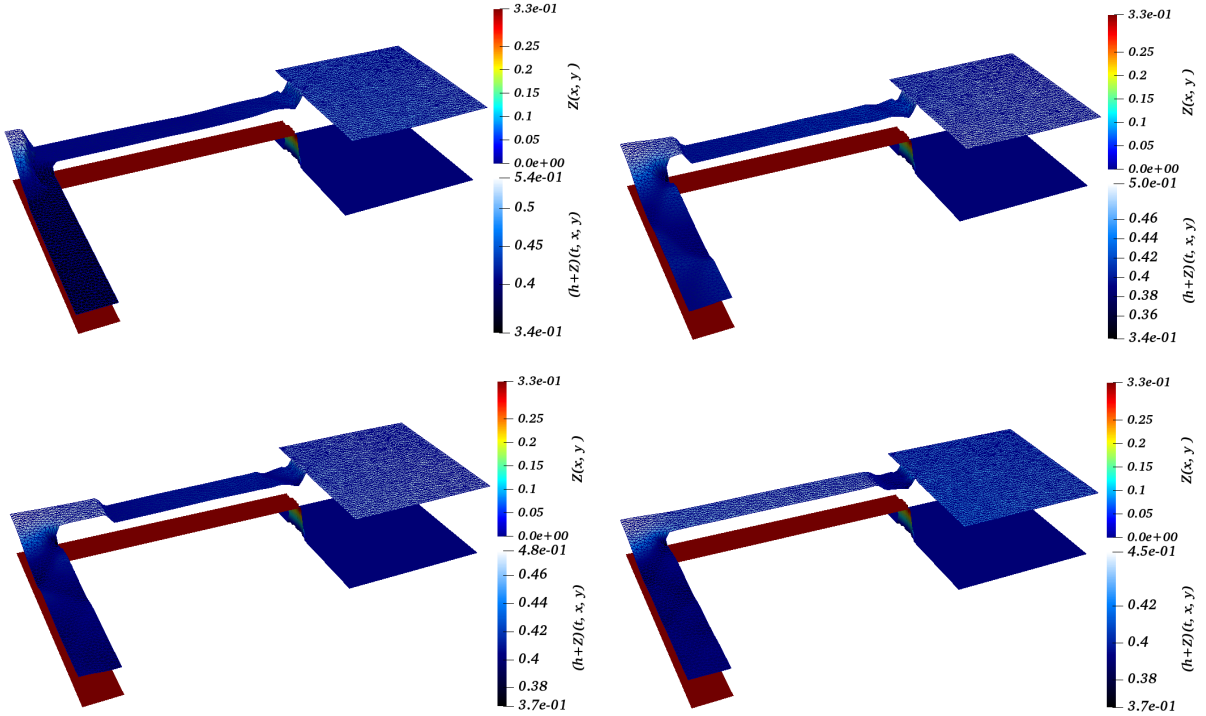

Fig 4.37. 3D view of water surface level $h + Z$ and bed profile Z at various times: $t = 3$ s, $t = 5$ s, $t = 7$ s and $t = 14$ s.

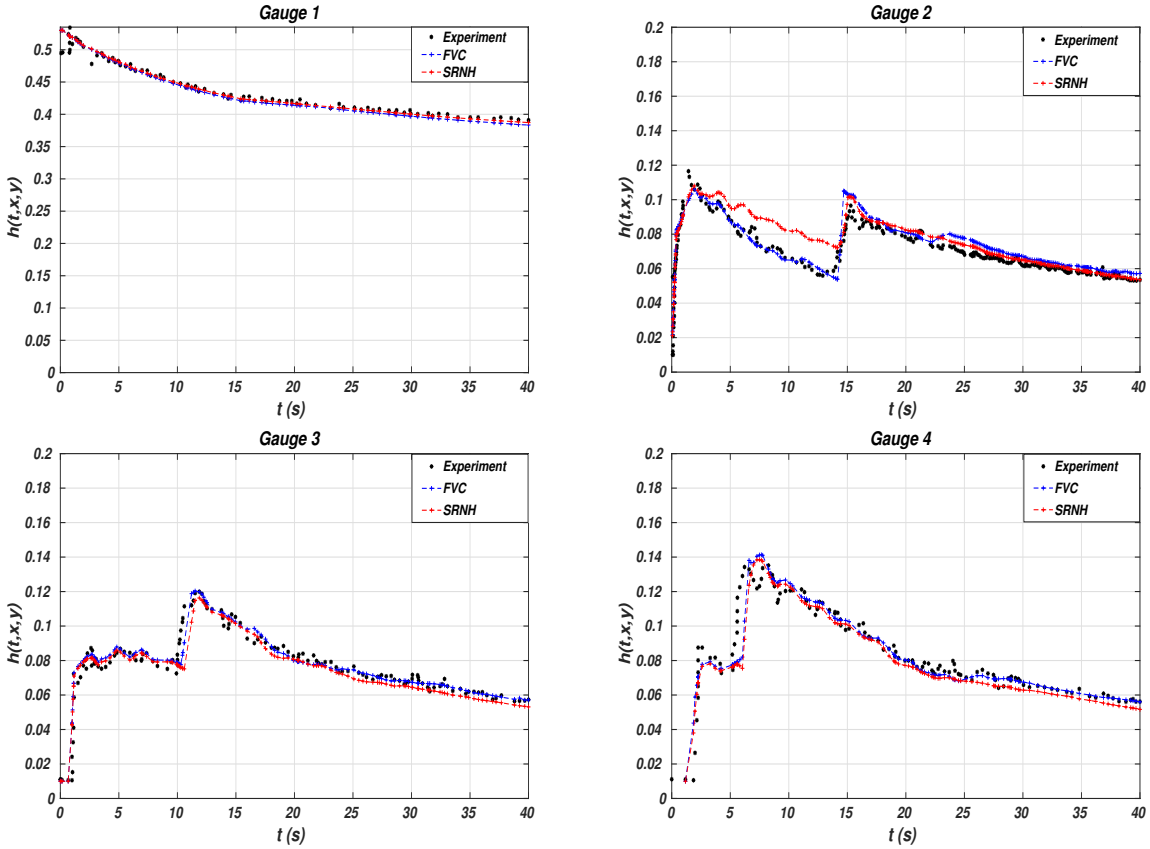

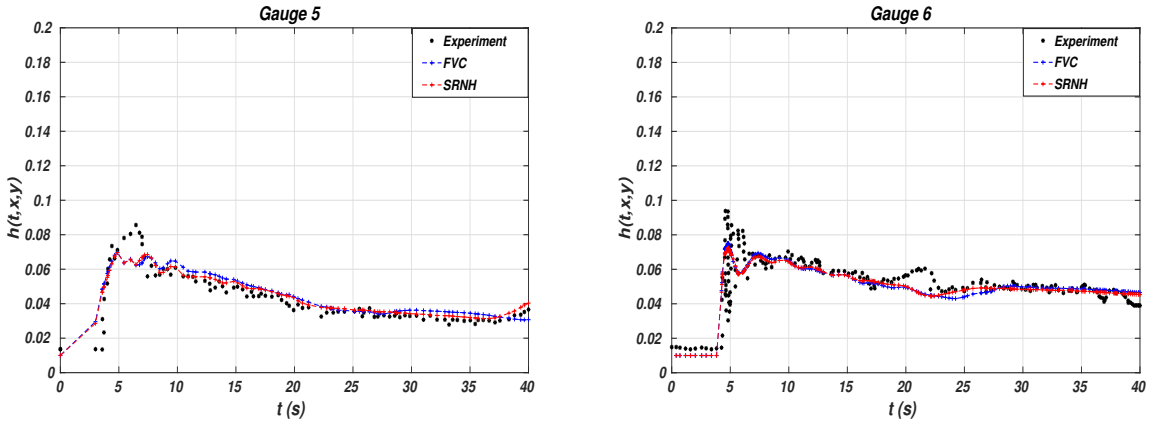

Fig 4.39. Comparisons between numerical and experimental data of water depth h at Gauge 1 to 6.

The variation of water depth with time is compared to the experimental data at different gauge positions, as shown in the figures above for the nearly dry bed case. At most gauge positions, there is good agreement with the experimental data. However, there is a difference at gauge 2 compared to the results presented in the same context by [127]. It can be seen that the numerical solution is of good quality in this area; this accuracy may be due to the consideration of the local head loss caused by the sudden dam failure. This behavior is already noticed in test case 4.4.2.

4.4.9 Pollutant transport in a squared cavity

The objective of this simulation is to reproduce the results presented by Benkhaldoun et al. [7] concerning the transfer of a pollutant in a square cavity with smooth topography. It is a pure advection (i.e., $D_x = D_y = 0$) of pollutant transport within the square cavity as described in references [128] and [129]. The flow domain is a square channel with dimensions of 9000 m $\times$ 9000 m and bottom slopes of $\partial_x Z = \partial_y Z = -0.001$ and the Manning resistance coefficient is fixed at $\eta = 0.025$ s.m$^{-\frac{1}{3}}$. As in the previous work, we impose uniform flow velocities of $u = v = 0.5$ m/s and a uniform flow water depth as the initial condition. To establish the initial distribution of the pollutant concentration, we superimpose two Gaussian pulses centered at $(x_1 = 1400 \text{ m}, y_1 = 1400 \text{ m})$ and $(x_2 = 2400 \text{ m}, y_2 = 2400 \text{ m})$, respectively. The initial concentration is expressed as

$$C(0,x,y) = 10\exp\left(-\frac{(x-x_1)^2+(y-y_1)^2}{264^2}\right) + 6.5\exp\left(-\frac{(x-x_2)^2+(y-y_2)^2}{264^2}\right). \quad (4.51)$$

The initial spatial distribution of concentration is also illustrated in Fig 4.40.

Using the FVC scheme on unstructured meshes proposed in this study, we calculate the concentration after 9600 seconds and compare it with the exact solution. The results are presented graphically in Fig 4.41 which displays a 2D view, and in Fig 4.42, which shows the results along the line $y = x$. To discretize the computational domain, we use 160815 non-uniform triangles (mesh A), with a Courant number of CFL = 0.85. Fig 4.43 displays the outcomes obtained for a refined mesh (mesh B with 372558 cells).

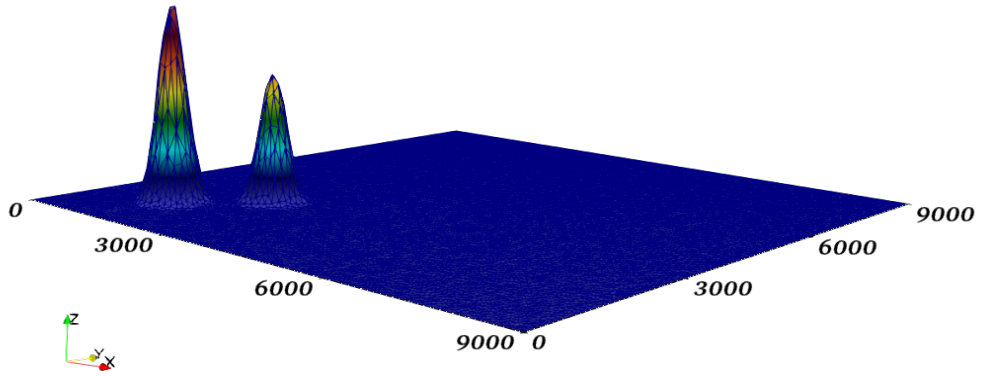

Fig 4.40. Initial data of concentration in a squared cavity.

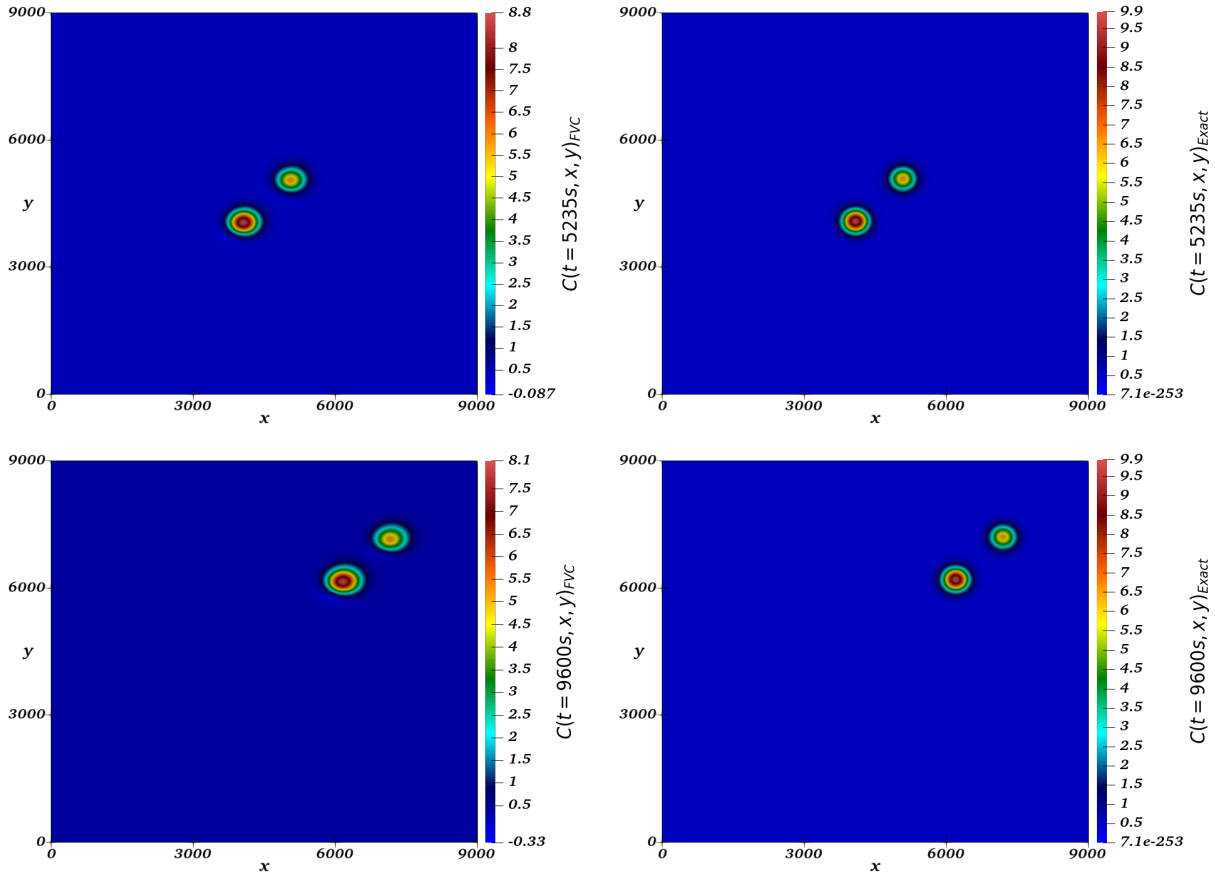

Fig 4.41. Comparative FVC solution (left) and exact solution of pollutant concentration (right) at two simulation times: top to bottom at $t = 5235s$ and $t = 9600s$.

This figure demonstrates that the FVC scheme results that are similar to the exact solution. However, when the Courant number is set to a high value and the mesh is coarse, the FVC scheme used in this study produces oscillations in the calculated concentration at the Gaussian foot level, as demonstrated in the second row on the right side of Fig 4.42 at $t = 9600$ seconds. These oscillations disappear completely when the mesh is refined, as seen in Fig 4.43. Table 4.6 presents the residual, maximum, and minimum values of the pollutant concentration.

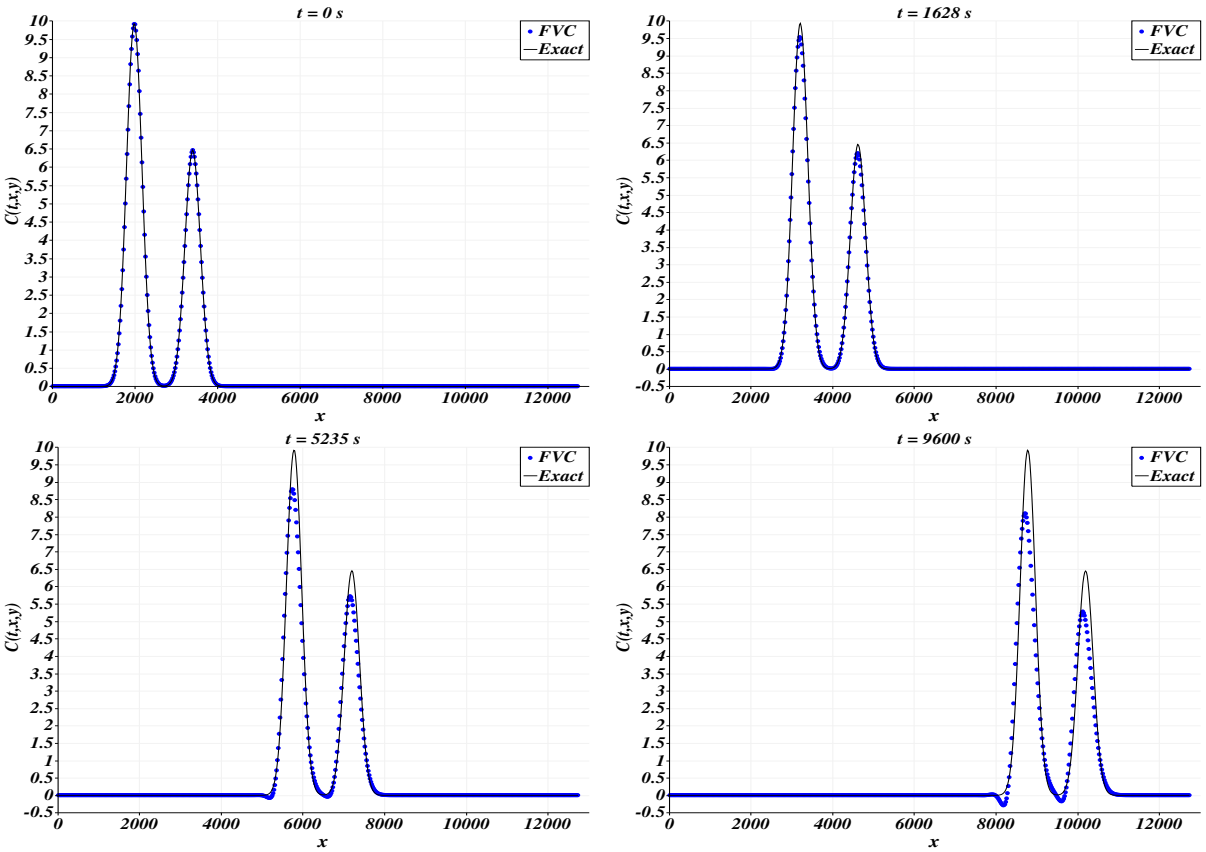

Fig 4.42. Diagonal cross-sections of the pollutant concentration: from top left to bottom right, $t = 0s$, $t = 1628$, $t = 5235$ and $t = 9600$.

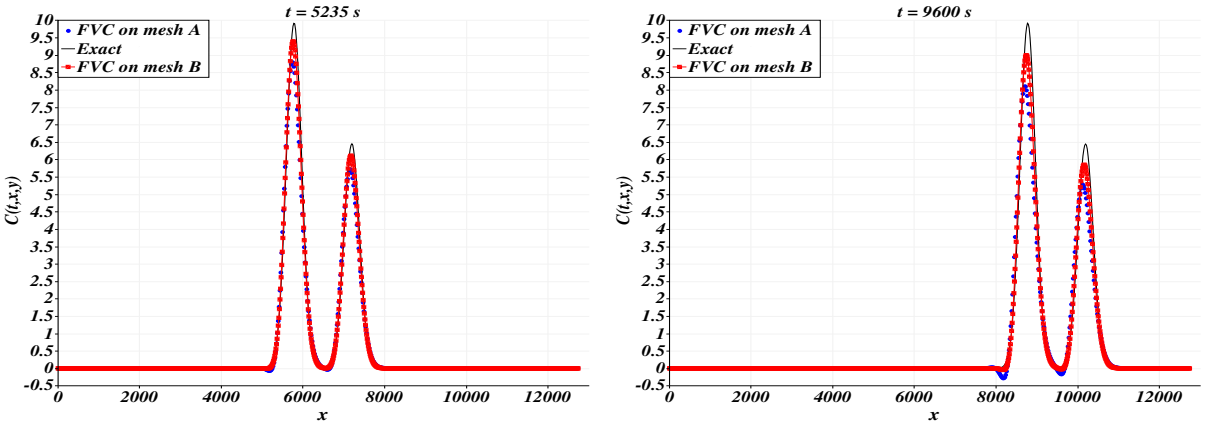

Fig 4.43. The pollutant concentration's diagonal cross-sections were evaluated using exact and FVC schemes on two different meshes, namely mesh A and mesh B, with 160815 and 372558 cells, respectively. The results obtained at time $5235s$ and $9600s$ were compared, and the outcomes are presented on the left and right sides of the figure, respectively.

Table 4.6: The performance evaluation of FVC scheme with two fixed meshes for simulating pollutant transport in a square cavity at time $t = 9600s$.

	Exact	Mesh A	Mesh B
# of cells	-	160815	372558
# of nodes	-	80811	197224
$\min C$	0.0	-0.33	-0.049
$\max C$	10.0	8.1	9.1
Residual in C	-	0.21	0.075

4.4.10 Pollutant transport in the Strait of Gibraltar

The goal of this section is to simulate free-surface flows for the transport of contaminants in real configurations, specifically the hydrodynamics in the Strait of Gibraltar. This aims to examine the effectiveness of the FVC approach in generating solutions in real configurations that have complex geometry and irregular topography.

The Strait of Gibraltar is located between the Iberian Peninsula to the north and the continent of Africa to the south, with the Atlantic Ocean to the west and the Mediterranean Sea to the east. The primary flow in the strait is composed of a chilly top layer of freshwater flowing from the Atlantic and a warm and salty deep current originating from the Mediterranean, as indicated in references [130, 131]. The system spans roughly 60km in length from Spartel and Trafalgar in the west to Ceuta and Gibraltar in the east, as illustrated in Fig 4.44. Its width varies, ranging from around 14km from Tarifa to Punta Cires to a maximum of 44km from Barbate to Tangier. The simulation mesh, depicted in Fig 4.45, consists of 23598 cells and 11648 nodes.

Fig 4.44. Strait of Gibraltar. 35° 58' 18" N, 5° 29' 09" W.

In the simulations, we used the bathymetry shown in Figure 4.46. A similar bathymetry has been used in various numerical studies on predicting the mean flow in the Strait of Gibraltar, as outlined in references [7, 131], particularly in the eastern part between Ceuta and Gibraltar. It should be noted that the strait's bottom is irregular and presents different spatial scales, which

can pose numerical challenges.

This study aims to resolve equation (2.36) while accounting for pollution discharge at the strait's entrance, specifically at the midpoint of the axis between Barbate and Tangier. We assume a wind friction coefficient of $\breve{C}_f = 10^{-5}$ and a Coriolis parameter of $f_c = 8.55 \times 10^{-5}$ s^{-1}.

Identical and fixed diffusion coefficients in both directions, $D_{xx} = D_{yy} = 0.001$ m^2/s. are considered for pollutant transport due to the lack of turbulence effects in the model.

Additionally, we presume that solid boundaries have no pollution concentration, whereas zero pollutant flux applies to other boundaries. Careful attention must be given to this matter due to the highly irregular bathymetry of the strait to avoid severe numerical difficulties. The Manning bottom friction coefficient is established as 0.001 s/m$^{1/3}$, based on González et al [130].

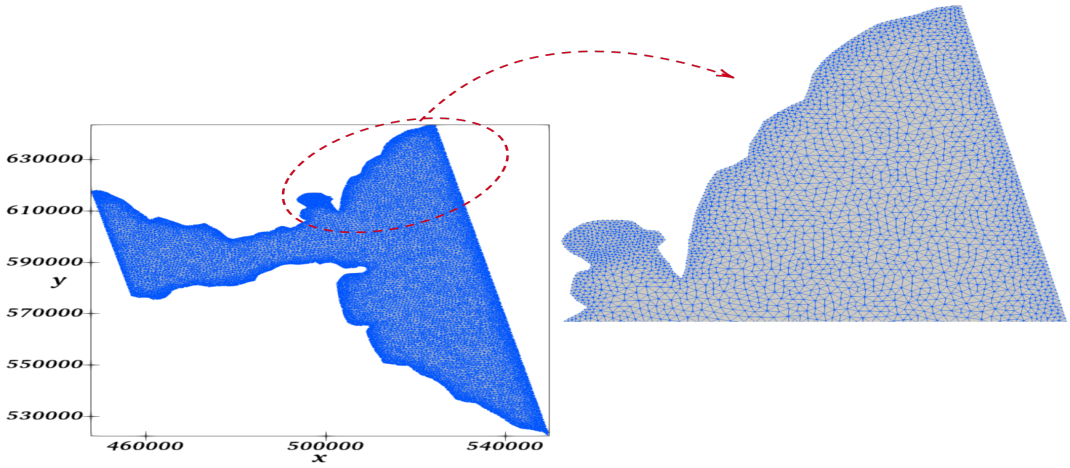

Fig 4.45. Mesh of the computational domain around the Strait of Gibraltar.

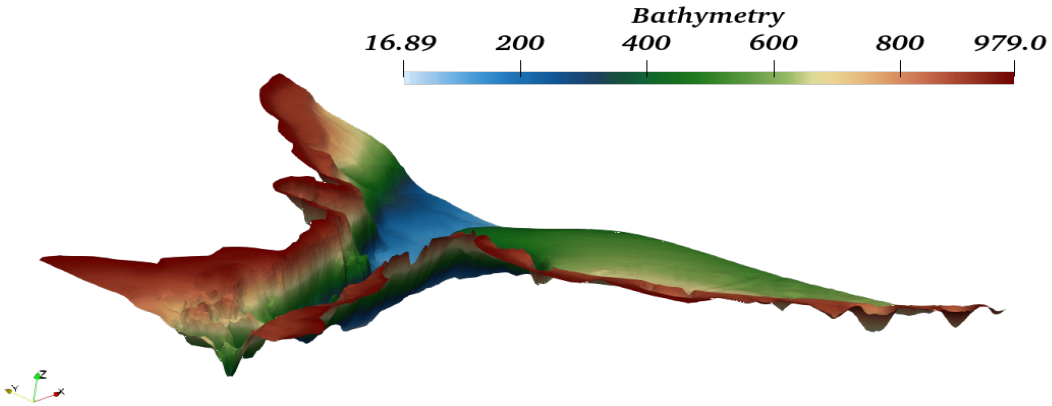

Fig 4.46. 3D view of the Strait of Gibraltar bathymetry.

To drive the problem in the simulations, we utilize the main semi-diurnal tide originating from the Atlantic side, which has an amplitude of 25 cm. The tide data is obtained from the website https://tpxows.azurewebsites.net/. This generates a maximum current of about 1 m/s at the entrance of the strait and represents the average yearly inflow into the Mediterranean

Sea. Therefore, we employ open boundary conditions to simulate the primary component of the tide in the model.

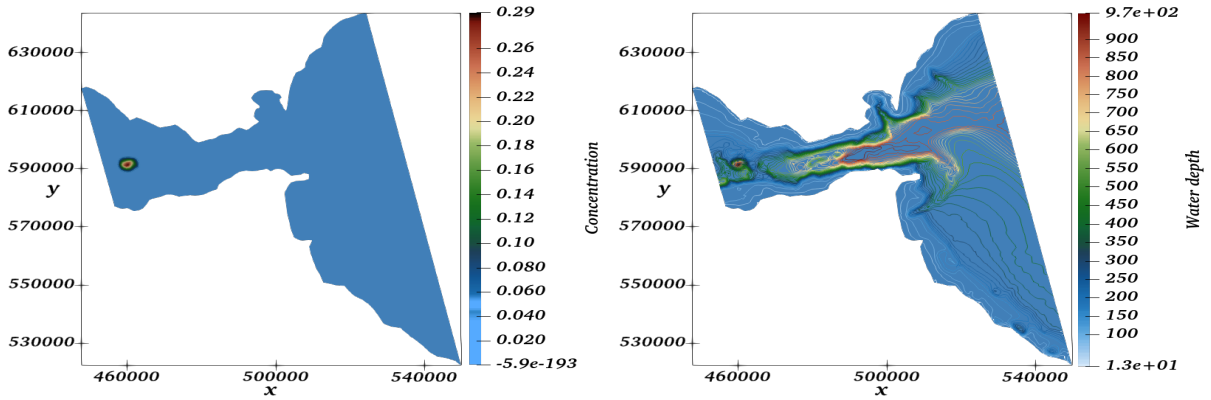

Fig 4.47. Concentration (left) and water depth (right) at the initial state.

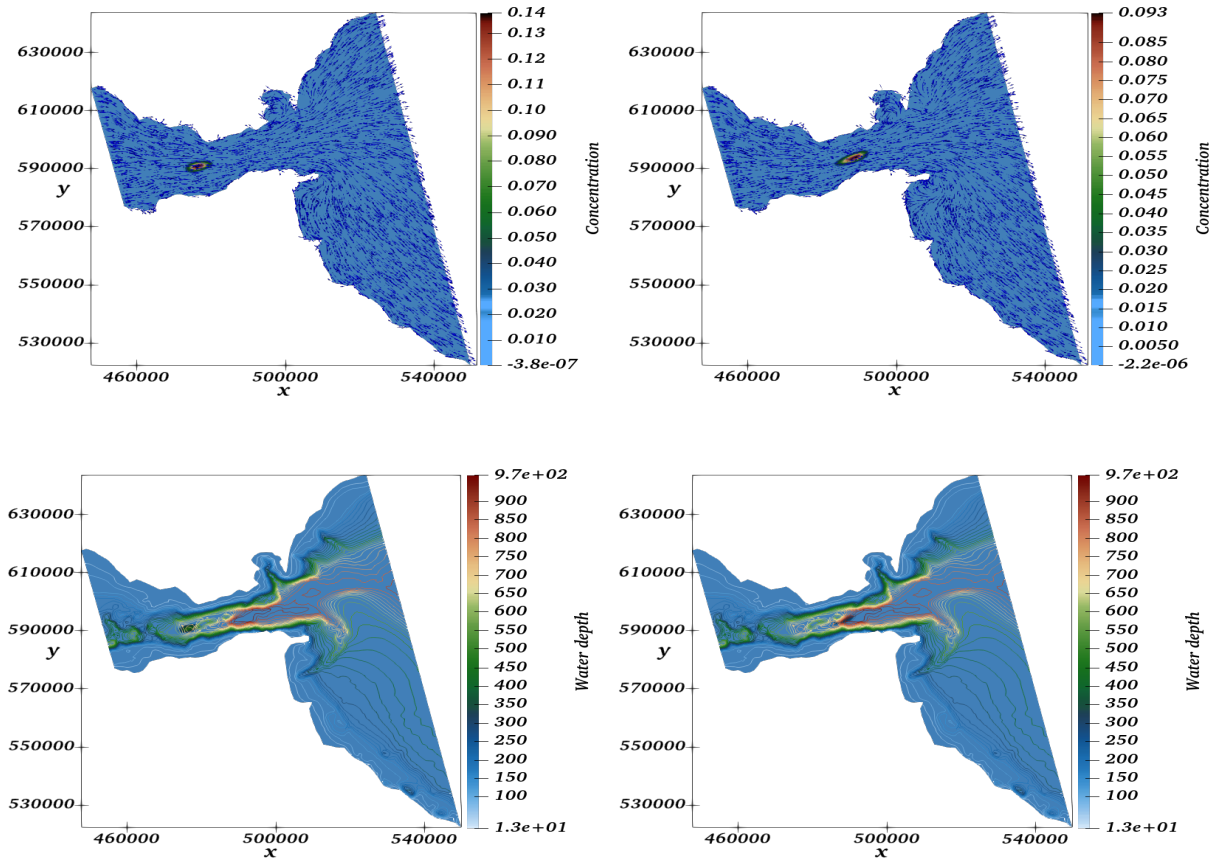

Fig 4.48. The first row illustrates the concentration and velocity fields of the flow, whereas those in the second row illustrate the corresponding water depth variation in the Strait of Gibraltar, with a temporal progression from $t = 1$ hour on the left to $t = 2$ hours on the right.

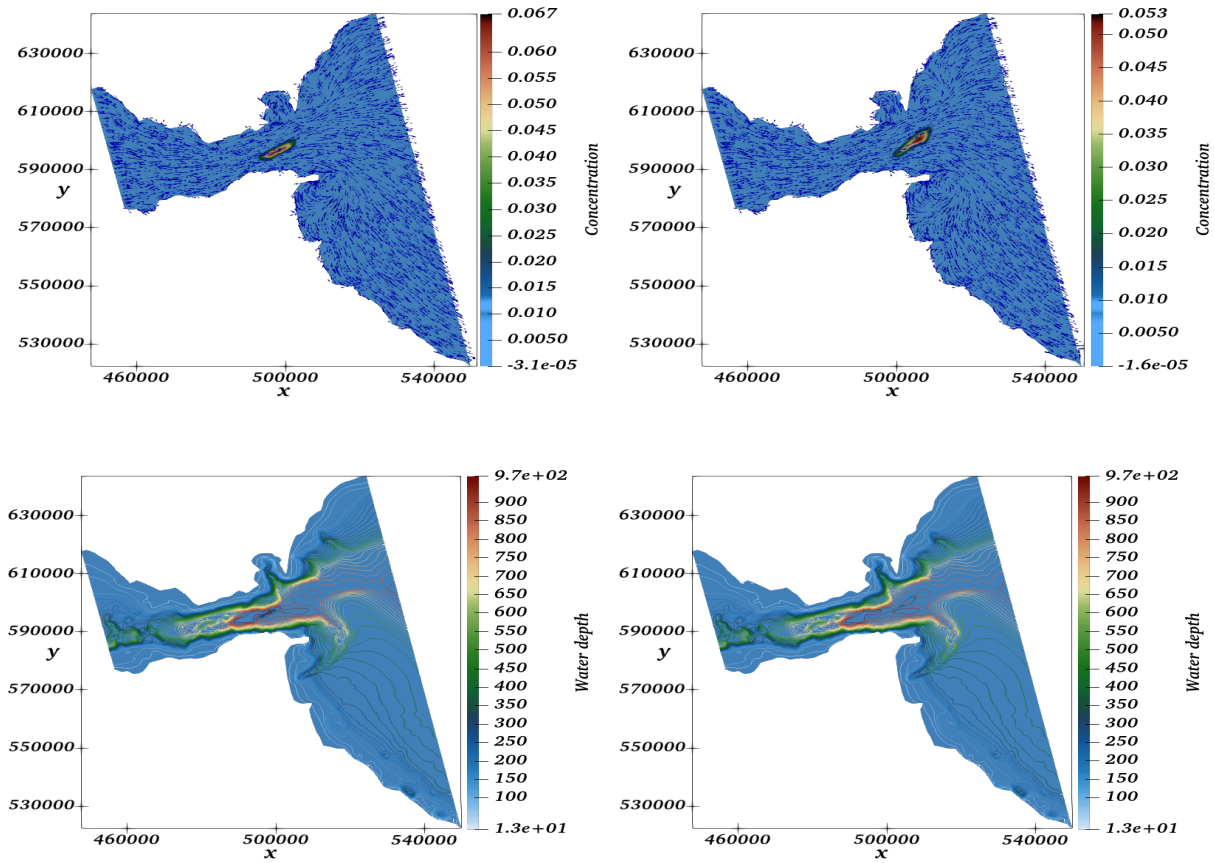

Fig 4.49. The first row presents the concentration and velocity fields of the flow, while the second row displays the concurrent variations in water depth in the Strait of Gibraltar, arranged in temporal sequence from $t = 3$ hours on the left to $t = 4$ hours on the right.

The results of the FVC scheme at six different times (1, 2, 3, 4, 5, and 6 hours) are presented in Fig 4.48, Fig 4.49 and Fig 4.50. The time intervals used in the simulation represent the time it would take for the pollutant to leave the Strait and travel further into the Mediterranean Sea without any wind-induced effects. The concentration profile, velocity fields, and water depth are shown in the figures, with C/C_{max} indicating the ratio of the pollutant concentration to its maximum value at the initial release (as displayed in Fig 4.47). It should be emphasized that no modifications were made to the bathymetry for this particular test case.

The FVC scheme demonstrated a high level of accuracy in capturing the complex features of the flow. The results also revealed its ability to predict complex wave interactions and capture pollutant concentration with sharp resolution. The use of a fine mesh enabled high resolution in regions with steep pollutant concentration gradients, such as the moving fronts. The FVC scheme was found to be a shock-capturing method with very little numerical dissipation, even after long-time simulations. Incorporating physical diffusion into the pollutant transport equation caused the maximum concentration to decrease to around 23% and 15% after 3 and 6 hours, respectively. The FVC scheme, like in the pure advection tests, produced negative concentrations near sharp gradients. These concentrations increased considerably as the pollutant was transported over time. The accumulation of such negative concentrations in the case of non-conservative pollutants could adversely affect the precision of numerical models and lead

to the generation of implausible outcomes. Nonetheless, the FVC scheme provides an accurate resolution to such pollution transport.

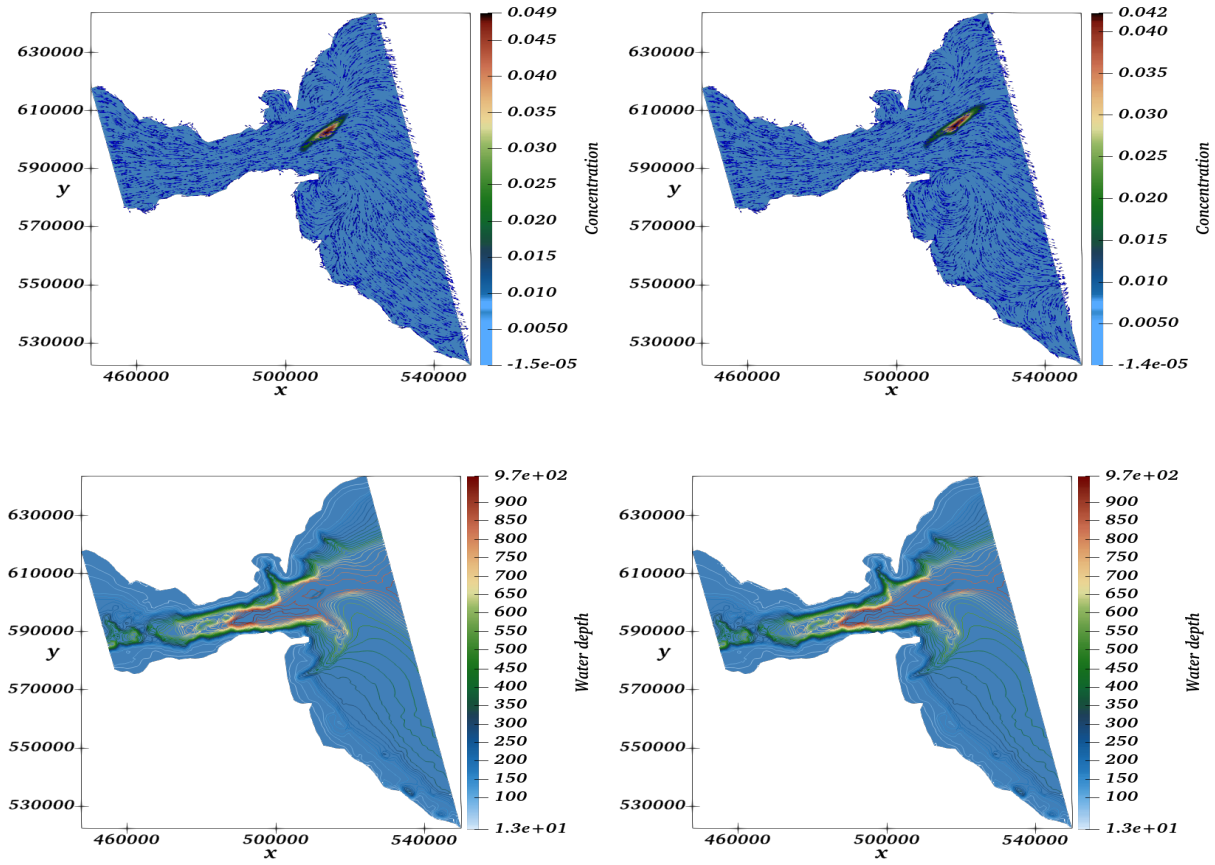

Fig 4.50. The first row illustrates the concentration and velocity fields of the flow, whereas those in the second row illustrate the corresponding water depth variation in the Strait of Gibraltar, with a temporal progression from $t = 5$ hours on the left to $t = 6$ hours on the right.

4.4.11 Two-dimensional multilayer shallow water equations

In this section, we reproduce the same benchmarks studied in [59] using the formulation of the FVC scheme on non-uniform triangular meshes to simulate two-dimensional multilayer shallow water flow. The objective is to demonstrate the accuracy and adaptability of the scheme described above. In the first test case, a simple dam-break problem is posed, and the results are compared to those of three-dimensional Navier-Stokes equations. In the second case, we examine the conservation property of the scheme, using a free surface flow at rest over non-flat topography. We also examine circular dam-break on both flat and non-flat topography. Finally, we simulate a two-dimensional wind-driven flow. For all computations, the initial conditions determine the total water height H, and the water heights of each layer h_θ are defined using equal fractions as follows

$$h_\theta = l_\theta H \quad \text{with} \quad l_\theta = \frac{1}{M}, \quad \theta = 1, \ldots, M.$$

Additionally, in all of our simulations in multilayer swallow water equations, we use $\alpha^n = 1$ and

a constant Courant number CFL $= 0.92$ is utilized, while the time step Δt varies in accordance with the stability criteria

$$\Delta t \leqslant \min \left\{ \frac{|T_i|}{\mathcal{P}_i(|\mathbf{u}_\theta \cdot \mathbf{n}| + \sqrt{gH})_i}, \frac{|T_i|}{\mathcal{P}_i(|\mathbf{u}_\theta \cdot \mathbf{n}| + \sqrt{gH})_i \sqrt{2\alpha^n}} \right\}. \tag{4.52}$$

In order to enforce boundary conditions, similar techniques as those outlined in [59] are employed. For the computational instances analyzed within this section, flux computations at cell boundaries are utilized to impose boundary conditions on the corrector solution. In addition, for the predictor solution, the necessary variables in the boundary cells are set to match the corresponding values of adjacent inner cells.

4.4.11.1 Multilayer dam-break problem

The dam-break problem has traditionally been simulated using single-layer shallow water equations. However, recent research (referenced in [59, 56, 32]) has employed one-dimensional multi-layer shallow water equations to model this problem on a flat bottom. To expand on this, we examine the two-dimensional version of the problem and aim to compare our findings with those of the aforementioned one-dimensional model. The FVC scheme involves solving the multilayer shallow water equations (2.42) in a rectangular channel with a flat bottom of dimensions $100m$ in length and 10 in width. The simulation begins with the following initial conditions.

$$H(0,x,y) = \begin{cases} 2, & \text{if} \quad x \leq 0, \\ 1, & \text{if} \quad x > 0, \end{cases} \qquad u_\theta(0,x,y) = v_\theta(0,x,y) = 0.$$

In this test example, we neglect the wind effects and Coriolis forces, and use the same parameters as in [55, 59, 32] for the one-dimensional case, including the viscosity coefficient $\nu = 0.01$, the gravity $g = 2$, and the friction coefficient $\kappa = 0.1$. The results are presented at time $t = 14s$.

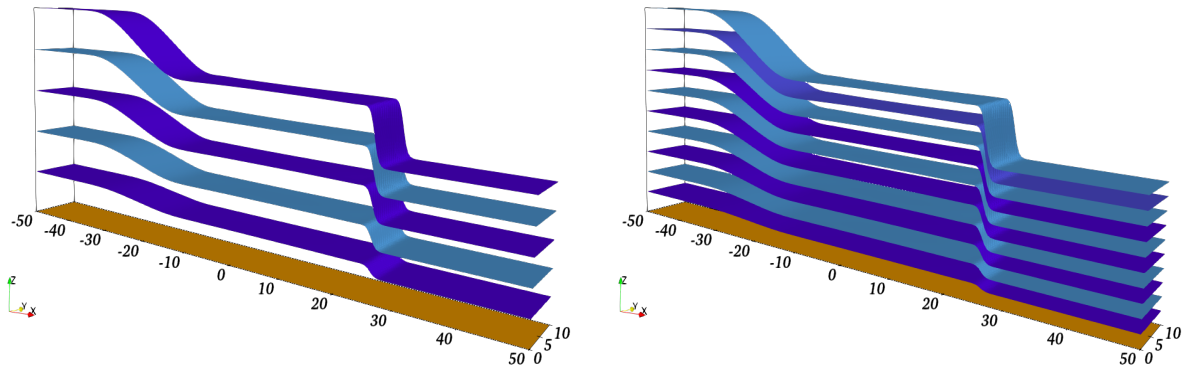

Fig 4.51. The free-surface and interfaces of water in the multilayer dam-break problem over a flat bed at time $t = 14s$ are illustrated using a 5-layer model on the left and a 10 layers model on the right.

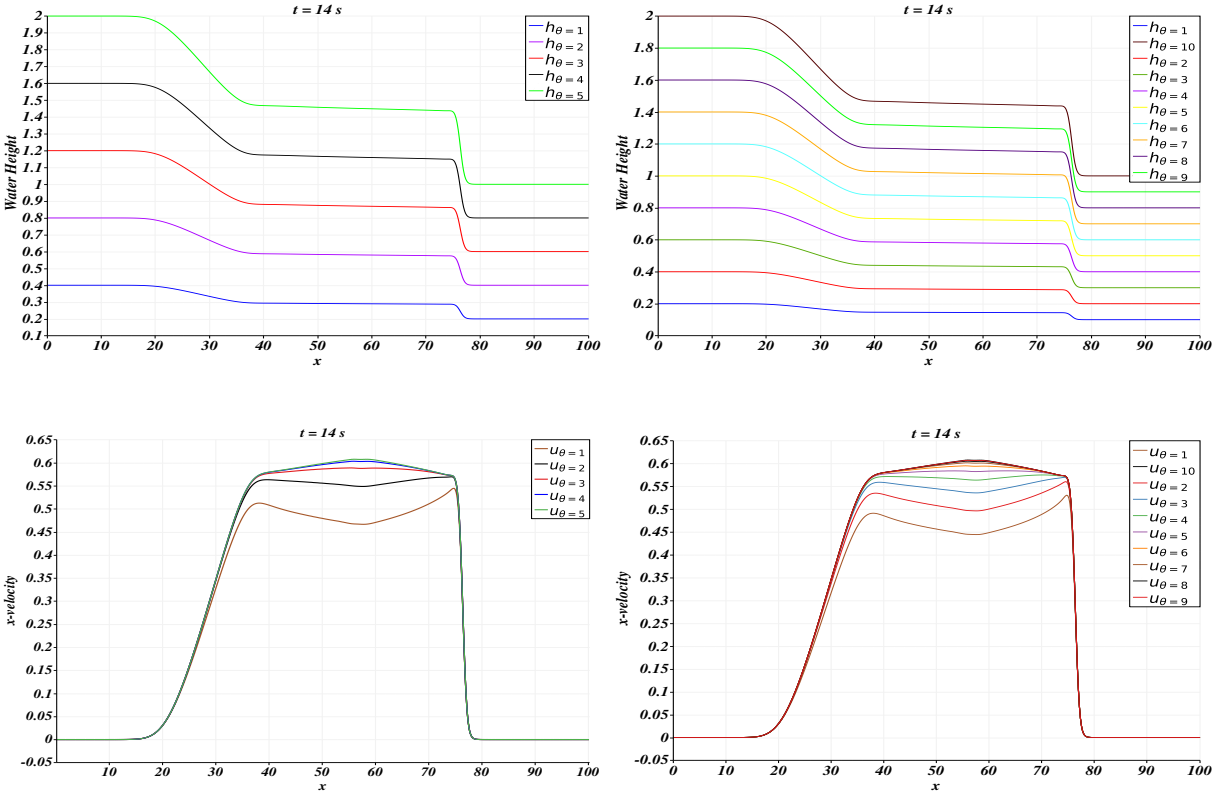

Fig 4.52. Horizontal cross-sectional views of water velocity (bottom) and the water free-surface (top) were examined for the multilayer dam-break problem on a flat bottom at a specific time of $t = 14s$.

Fig 4.51 depicts the water free-surface and interfaces for the 5 layers and 10 layers models at time $t = 14s$, using a mesh with 14546 cells. As is typical in dam-break problems, at $t = 0$, the dam breaks and the flow problem consists of a shock wave propagating downstream and a rarefaction wave propagating upstream. The proposed FVC scheme captures these flow patterns without generating spurious oscillations in the shock area. Under the considered dam-break conditions, it appears that the number of layers in the model has little effect on the flow features, as demonstrated by comparing the water free-surface profiles obtained for the 5-layer and 10-layer models in Fig 4.51. To further highlight these effects, we display horizontal cross-sections of the flow in Fig 4.52.

4.4.11.2 Lake at rest in multilayer flow

The concept of a lake at rest flow was previously proposed [11] to assess the well-balance property of a finite volume method applied to one-dimensional shallow water equations. In this study, we present a similar test case but for two-dimensional shallow water flows. The FVC scheme involves utilizing the Kronecker tensor product of the one-dimensional bed proposed in [11] in both the x- and y-directions. Consequently, we solve the shallow water equations (2.42) by setting the source term associated with the bed, i.e., $f_c = 0$ and $F_\theta = G_\theta = 0$, and defining the bed as

$$Z(x, y) = \frac{1}{10}\mathcal{Z}(x) \otimes \mathcal{Z}(y),$$

where $\mathcal{Z}$ is the bottom profile defined in the appendix section (table of bed elevation $\mathcal{Z}(x)$ and its illustration). The issue is resolved in a squared area measuring 1500 m in length, and the

outcomes are reported at a particular time $t = 10800$ s, as specified in [11, 59].

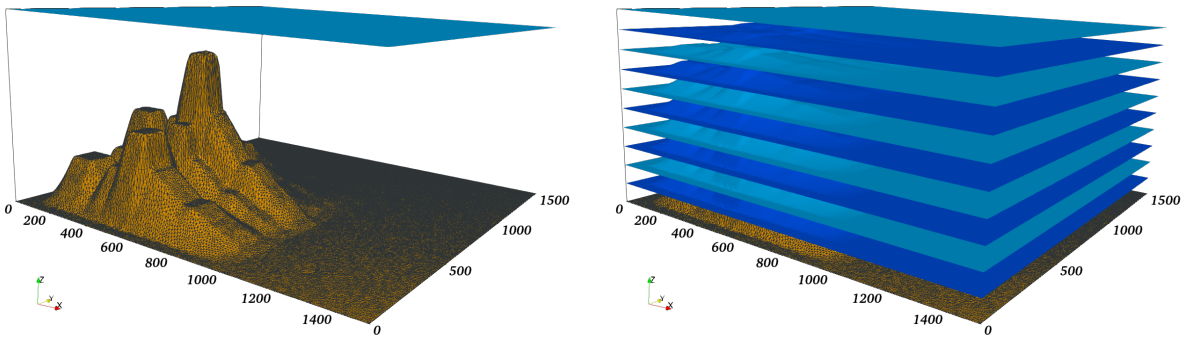

Fig 4.53. Water free-surface and interfaces for the multilayer flow problem at rest at time $t = 10800s$ using single-layer and 10 layers models.

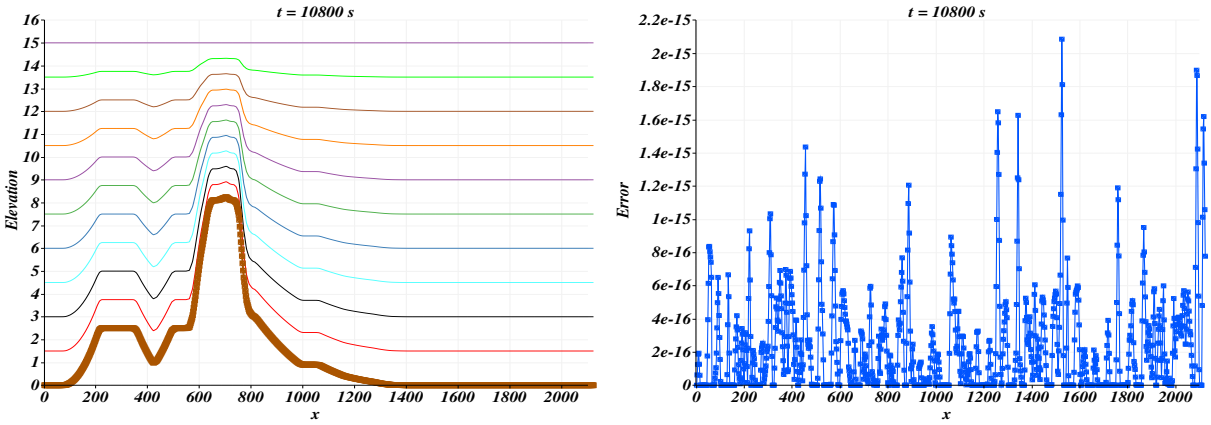

Fig 4.54. Water free-surface and interfaces cross-sectional profile for the 10 layers flow problem under resting conditions at time $t = 10800s$ are presented on the left, while the corresponding water free-surface error is shown on the right.

In real-world scenarios, it is crucial to maintain a constant total water free-surface, and the water velocity must be zero at all times. Nonetheless, several numerical techniques are unsuccessful in sustaining these conditions at the discrete level. Fig 4.53 demonstrates the results obtained for the water free-surface and interfaces using a mesh with 19280 cells and a 10 layers model. As anticipated, the water free-surface remained unchanged during the simulation time, and any disturbances have been detected over the irregular two-dimensional bed. Increasing the number of layers in the model did not negatively affect the water free-surface response of the lake. Fig 4.54 displays the cross-section along the main diagonal ($y = x$) of the 10 layers model's results, and the water-free surface error represented as the difference between the analytical and numerical free-surface solutions. The results in Fig 4.54 demonstrate that the FVC scheme maintains a constant water free-surface with practically zero errors up to machine precision. Similar results were obtained for the 5 layers and 20 layers models, although not reported here. This confirms that the proposed method is well-balanced and accurately resolves two-dimensional multilayer shallow water flows over non-flat bottoms without relying on complex techniques to balance the discretizations of source terms and flux gradients.

4.4.11.3 Wind-driven circulation flow

In this study, we examine a water flow problem driven by wind-induced circulations, which was originally proposed in [61] and commonly used to verify multilayer shallow water models, as described in [132, 55, 32]. We solve the multilayer shallow water equations (2.42) in a square two-dimensional domain that is 2000 m long and contains water with a depth of 6.75 m. The water is subject to a two-dimensional wind force with a speed of $w = 20$ m/s and an angle of 45°. The parameters used in this simulation include $f_c = 0$ for the Coriolis coefficient, $\nu = 0.05$ m^2/s for the viscosity coefficient, $\kappa = 0.00001$ m/s for the friction coefficient, $\sigma = 0.0015$ N/m^2 for the wind stress coefficient, $\rho = 1025$ kg/m^3 for the water density, $\rho_a = 1.2$ kg/m^3 for the air density, and $g = 9.81$ m/s^2 for gravity. We assume a flat bed with no-slip boundary conditions, and we present the results for water heights, streamlines, and velocity fields at time $t = 1800s$ using a mesh with 1106 cells.

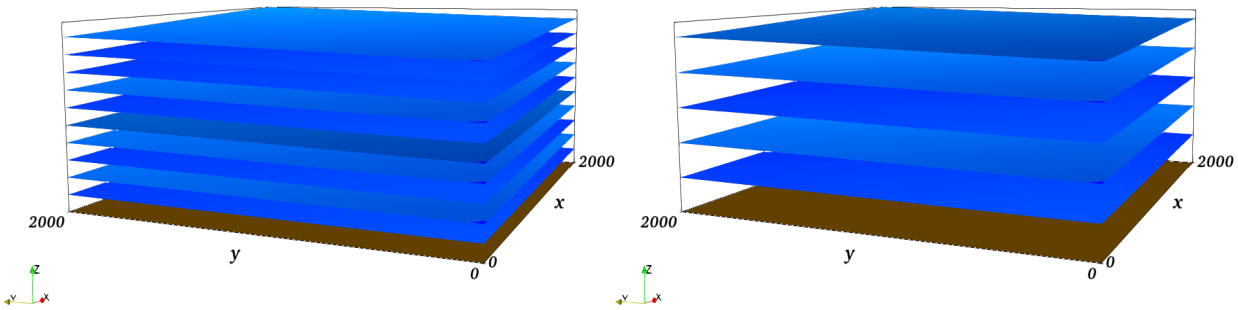

Fig 4.55. Water elevations resulting from the wind-driven circulation at time $t = 1800s$ were determined using both a 5 layers model (on the right) and a 10 layers model (on the left).

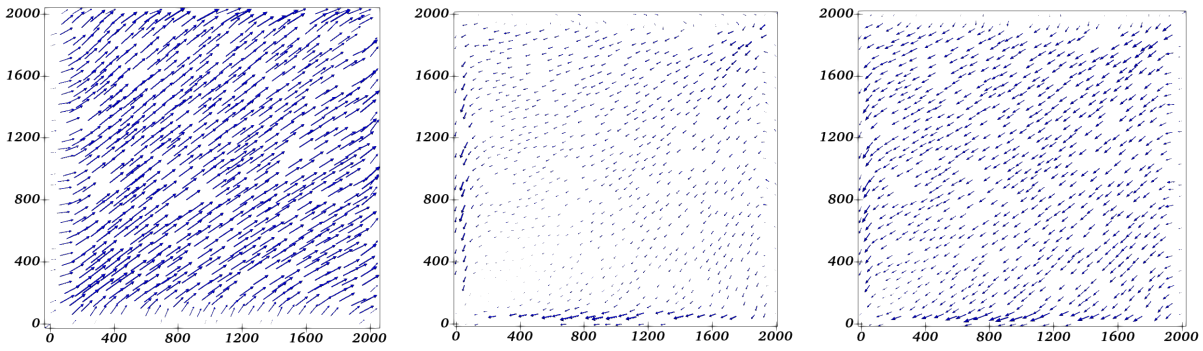

Fig 4.56. Velocity field in the xz-plane for the wind circulation flow using 10 layers: velocity in layer 10, 5 and 1 from left to right respectively.

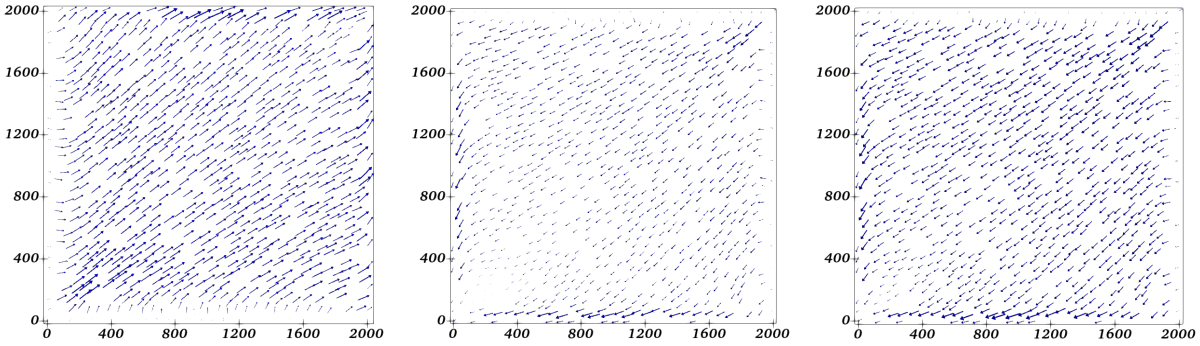

Fig 4.57. Velocity field in the xz-plane for the wind circulation flow using 5 layers: velocity in layer 5, 2 and 1 from left to right respectively.

Fig 4.55 shows the results obtained using 5 layers and 10 layers models. The velocity plots in Fig 4.57 and Fig 4.56 illustrate that the steady cavity flow within closed streamlines consists of a central inviscid core with nearly constant velocity and viscous effects confined to thin shear layers near the walls. These plots also provide an overview of the overall flow pattern and the effect of the number of layers on the structure of the recirculating eddy in the cavity. As anticipated, a re-circulation flow is generated in the computational domain, and the proposed FVC scheme accurately resolves the flow characteristics for this test example without relying on computationally demanding three-dimensional flow models.

4.4.11.4 Multilayer circular dam-break problem

We investigate a circular dam-break problem with multiple layers in a square domain of $[-10, 10] \times [-10, 10]$. The domain is assumed to be flat, with water viscosity $\nu = 0.05$ m^2/s, water density $\rho = 1025$ kg/m^3, gravity $g = 9.81$ m/s^2, Coriolis coefficient $f_c = 1$, and bed friction coefficient $\kappa = 0.001$ m/s. The initial conditions are given by

$$H(0, x, y) = 1 + \frac{1}{2}\left(1 - \tanh\left(\frac{\sqrt{ax^2 + by^2} - 1}{c}\right)\right), \quad u_\theta(0, x, y) = v_\theta(0, x, y) = 0,$$

where $a = \frac{5}{2}$, $b = \frac{5}{2}$, and $c = 0.1$. A similar problem has been previously investigated in [123] and in subsection 4.4.6 for the standard single-layer circular dam-break problem.

In this test, we discretized the computational domain into 21328 cells and obtained water heights and velocity fields for various time steps. Fig 4.58 displays the 3D view of results for water heights using 10 layers at three different time instances, $t = 0.2s$, $0.6s$ and $1s$ and Fig 4.59 presents the horizontal sections at $y = 0$ of these water heights. The results show that as the rarefaction wave progresses outward, the water flows away from the deep central region. The Coriolis effect causes an additional rotational effect on the results, but they remain symmetric and retain a strongly distinguishable wavefront. Fig 4.59 further demonstrates the effects of the Coriolis term on the multilayer circular dam-break problem, showing vertical cross-sections of water heights at $t = 0.2s$ and $t = 1s$. The proposed method accurately captures the Coriolis effects and the vertical velocities, which are critical in understanding the complex flows of these types of dam-break problems. The obtained results indicate that the symmetry is well preserved in the water heights. Note that the velocity profiles are not symmetric due to the inclusion of the Coriolis terms in the multilayer model. The results demonstrate that the considered multilayer models can accurately capture the vertical flow features without relying on the three-dimensional free-surface flow equations.

In the next stage of our study, we investigate multilayer circular dam-break problems on non-flat beds by solving the previous problem over a non-flat bottom

$$Z(x,y) = \frac{1}{2}\mathcal{Z}_x(x) \otimes \mathcal{Z}_y(y),$$

where

$$\mathcal{Z}_x(x) = \begin{cases} \sin\left(\frac{\pi}{4}x\right), & \text{if } -4 \leq x < 4, \\ 0, & \text{elsewhere,} \end{cases} \quad \text{and} \quad \mathcal{Z}_y(y) = \begin{cases} -\cos\left(\frac{\pi}{4}y\right), & \text{if } -2 \leq y < 2, \\ 0, & \text{elsewhere.} \end{cases}$$

In this test scenario, we maintain identical initial conditions and flow parameters as those in previous simulations. Our focus is on evaluating the ability of the proposed FVC scheme to solve multi-layered circular dam-break problems occurring on non-planar surfaces.

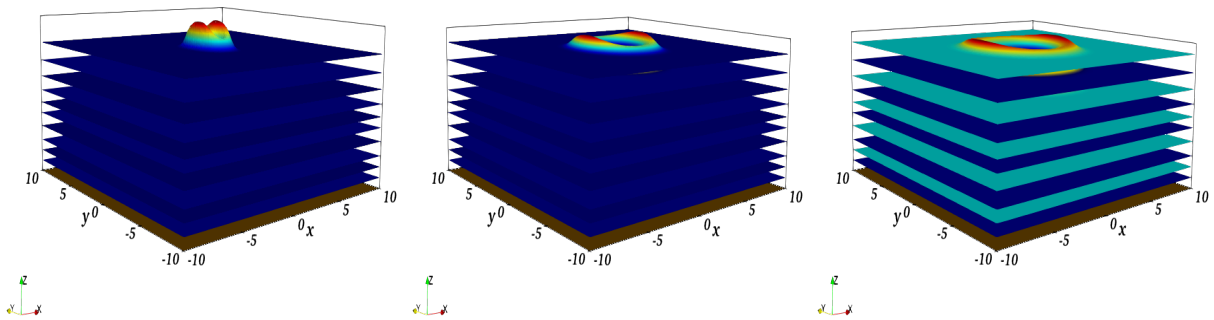

Fig 4.58. 3D view of the water heights obtained for the multilayer circular dam-break on a flat bottom using 10 layers. From left to right $t = 0.2s$, $t = 0.6s$ and $t = 1s$.

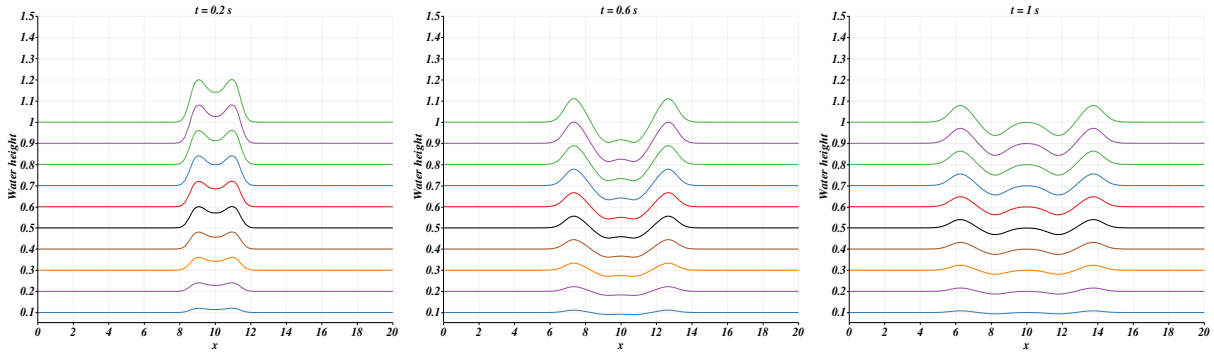

Fig 4.59. Vertical cross-sections at $y = 0$ of water heights from $t = 0.2s$ to $t = 1s$ for the multilayer circular dam-break on a flat bottom using 10 layers.

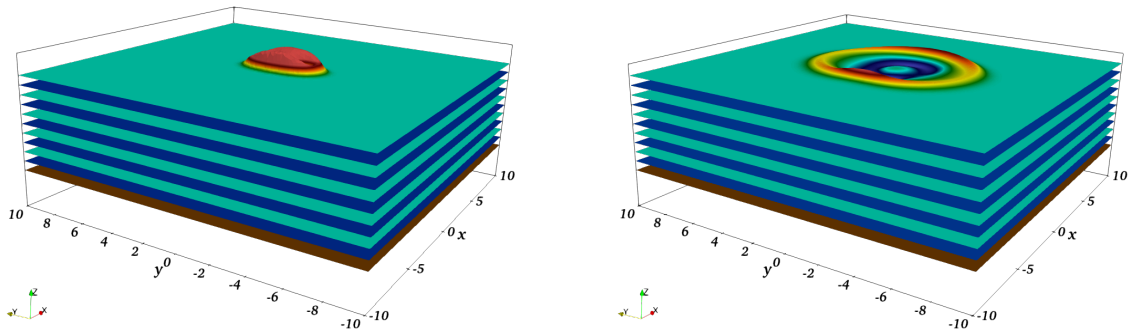

Fig 4.60. 3D view of the water heights obtained for the multilayer circular dam-break on a non-flat bottom using 10 layers. From left to right $t = 0.2s$, and $t = 1s$.

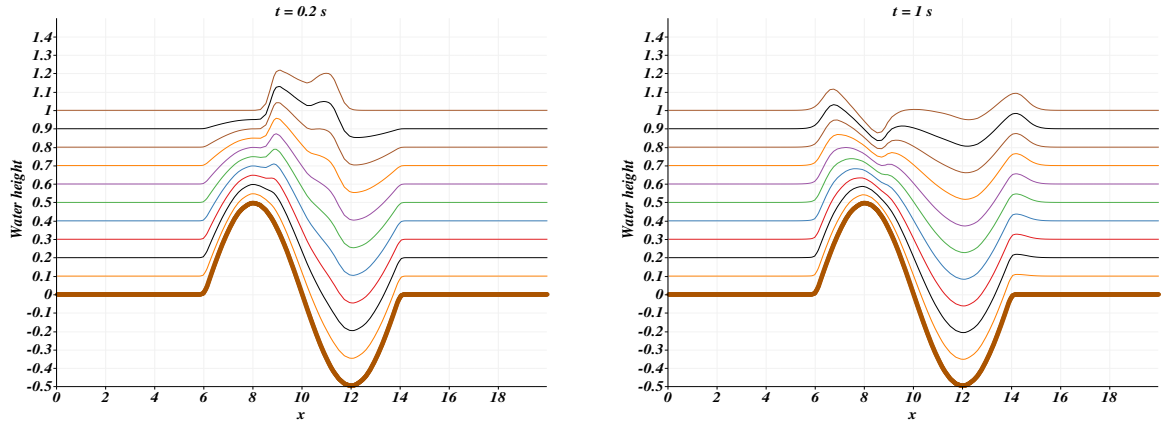

Fig 4.61. Vertical cross-sections at $y = 0$ of water heights at $t = 0.2s$ (left) and at $t = 1s$ (right) for the multilayer circular dam-break on a non-flat bottom using 10 layers.

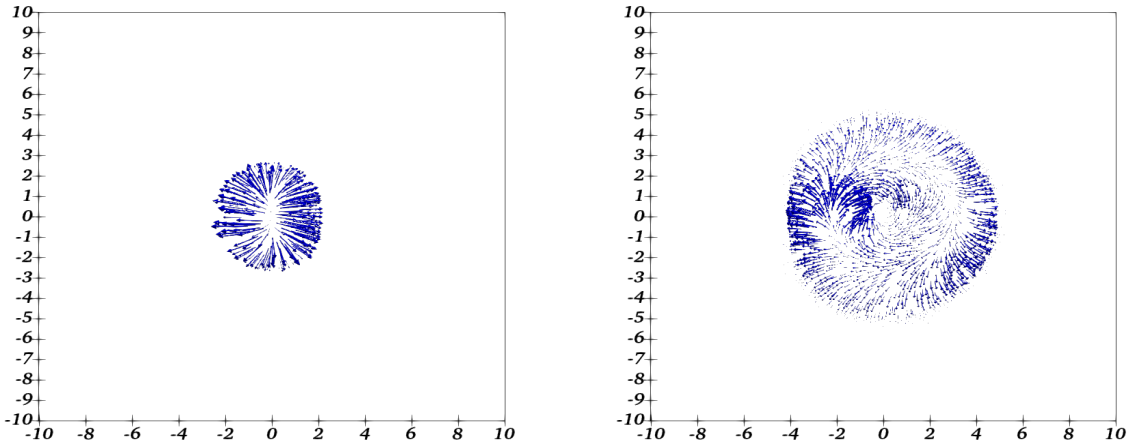

Fig 4.62. Lateral section of the velocity field in the plane xy at layer 10 at $t = 0.2s$ (left) and at $t = 1s$ (right).

Fig 4.60 presents a 3D view of the water heights obtained using 10 layers at time $t = 0.2s$ and $1s$. In Fig 4.62, we depict the velocity fields' lateral and vertical in layer number 10 at $t = 0.2$ and at the final simulation time $t = 1s$. The vertical cross-sections of water heights at $y = 0$ and $t = 0.2s$ then $t = 1s$ are presented in Fig 4.61. The non-flat bathymetry has a direct effect on the flow structure under the actual flow conditions, as evidenced by the results presented. When comparing the results obtained for a flat bottom in Fig 4.59 to those in Fig 4.61, it is clear that the bathymetry has a significant impact on the vertical velocity and the variation in high water level. Additionally. Notably, the rarefaction wave still progresses at the same speed over the non-flat bottom. The multilayer shallow water equations effectively handle this complex flow problem for both flat and non-flat beds and provide new insights into the vertical velocity for shallow water flows. The proposed FVC scheme performs satisfactorily for this flow problem, as it does not diffuse the moving fronts and does not produce spurious oscillations near steep gradients of water heights in the computational domain.

Chapter 5

3D FVC scheme on unstructured meshes: application to compressible Euler equations

Short summary

5.1 Three-dimensional Euler equations

In this section, we present the FVC scheme applied to the 3D Euler equations system (2.53). As we have seen previously, the method comprises two steps and can be interpreted as a predictor-corrector process. In this section, we will make a three-dimensional extension following the same approach as the Chapter 4.

5.1.1 Discretization

We assume a conforming 3D tessellation $\mathcal{T}$ of the computational domain Ω by elements T_i that are called a control volume, they are time independent, see Fig 5.1, such that $\mathcal{T} = \bigcup_i T_i$. Integrating equations (2.58) over a control volume T_i and applying Green's divergence theorem,

the following integral system is obtained.

$$\frac{\partial}{\partial t}\int_{T_i}\mathbf{W}dV+\int_{\partial T_i}\mathbf{F}(\mathbf{W})\cdot\mathbf{n}\;d\sigma=0, \tag{5.1}$$

where ∂T_i is the boundary of the control volume T_i, $\mathbf{n}$ is the normal vector to ∂T_i in the outward direction, dV and $d\sigma$ are respectively the volume element and the surface element. Therefore, the equation (5.1) can be reformulated as

$$\frac{d\mathbf{W}_i}{dt}=-\frac{1}{|T_i|}\sum_{j\in N(i)}|\gamma_{ij}|\Phi(\mathbf{W}_{ij},\mathbf{n}_{ij}), \tag{5.2}$$

where

$$\mathbf{W}_i=\frac{1}{|T_i|}\int_{T_i}\mathbf{W}\;dV, \tag{5.3}$$

is the average quantity on cell T_i stored at the cell center.
$\Phi(\mathbf{W}_{ij},\mathbf{n}_{ij})\simeq\dfrac{1}{|\gamma_{ij}|}\displaystyle\int_{\gamma_{ij}}\mathbf{F}(\mathbf{W})\cdot\mathbf{n}_{ij}d\sigma$, is the numerical flux computed at the interface γ_{ij} between the cells T_i and T_j and $N(i)$ is the set of neighboring cells of the control volume T_i.

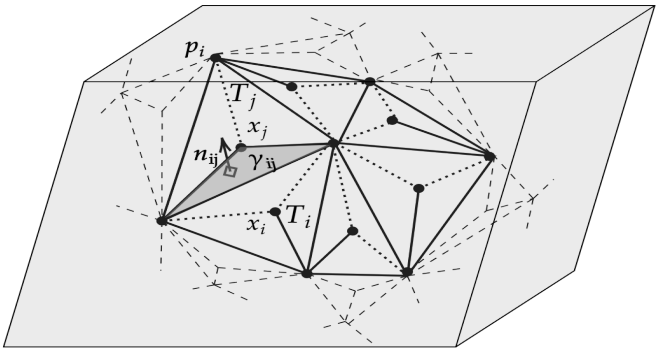

Fig 5.1. Generic control volumes of the computational domain.

Notations:

- p_i, vertex of T_i,
- x_i, centroid of the cell T_i,
- γ_{ij}, boundary face between the cells T_i and T_j,
- $|\gamma_{ij}|$, area of γ_{ij},
- $|T_i|$, volume of the cell T_i,
- ∂T_i, boundary of the cell T_i,
- $\mathcal{P}_i$, the surface area of the cell T_i.
- $\mathbf{n}_{ij}$, unit normal to γ_{ij}, outward to T_i such as, $\mathbf{n}_{ji}=-\mathbf{n}_{ij}$.

We recall that the concept of digital flux approximation is based on the reconstruction of intermediate states $\mathbf{W}_{ij}$ using the method of characteristics. We will employ the same techniques as in the previous chapter, but with a 3D formulation for all functions and computations used in 2D. The intermediate state $\mathbf{W}_{ij}$ will be calculated from a projected velocity model whose velocity components are projected onto the frame $\mathcal{R}=(T_i;\vec{b},\vec{\tau},\vec{\eta})$, where $\vec{\eta}:=(n_x,n_y,n_z)^T$ is the unit outward normal to the surface of the cell T_i, $\vec{\tau}:=(\tau_x,\tau_y,\tau_z)^T$ is the tangential vector at a face of the cell T_i that can be recovered from two points of this surface, and $\vec{b}=(b_x,b_y,b_z)^T$

is a bi-normal vector such as, $\vec{b} := \vec{\tau} \wedge \vec{\eta}$, see Fig 5.2. The projected velocities are defined as $u_\eta := \mathbf{u} \cdot \vec{\eta}$, $u_\tau := \mathbf{u} \cdot \vec{\tau}$ and $u_b := \mathbf{u} \cdot \vec{b}$, i.e.

$$\begin{pmatrix} u_\eta \\ u_\tau \\ u_b \end{pmatrix} = \begin{pmatrix} n_x & n_y & n_z \\ \tau_x & \tau_y & \tau_z \\ b_x & b_y & b_z \end{pmatrix} \cdot \begin{pmatrix} u \\ v \\ w \end{pmatrix}. \tag{5.4}$$

As the rows of the matrix in (5.4) are linearly independent, we write

$$\begin{pmatrix} u \\ v \\ w \end{pmatrix} = \begin{pmatrix} n_x & \tau_x & b_x \\ n_y & \tau_y & b_y \\ n_z & \tau_z & b_z \end{pmatrix} \cdot \begin{pmatrix} u_\eta \\ u_\tau \\ u_b \end{pmatrix}. \tag{5.5}$$

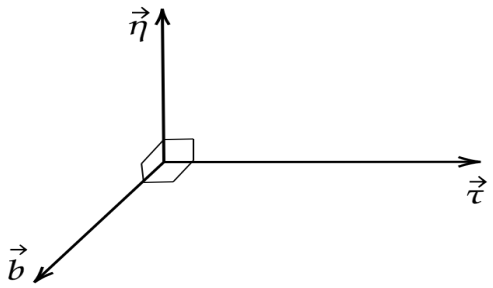

Fig 5.2. The local projection basis.

5.1.2 Construction of the projected speed model

We are proceeding here to the calculation of the projected model associated with the three-dimensional Euler equations. Integrating the equations (2.53) over the cell T_i, the basic equations of the finite volume method obtained using the divergence theorem are given by

$$\frac{\partial}{\partial t}\int_{T_i} \rho \, \mathrm{d}V + \int_{\partial T_i} \rho u_\eta \, \mathrm{d}\sigma = 0, \tag{5.6a}$$

$$\frac{\partial}{\partial t}\int_{T_i} \rho u \, \mathrm{d}V + \int_{\partial T_i} (\rho u u_\eta + p n_x) \, \mathrm{d}\sigma = 0, \tag{5.6b}$$

$$\frac{\partial}{\partial t}\int_{T_i} \rho v \, \mathrm{d}V + \int_{\partial T_i} (\rho v u_\eta + p n_y) \, \mathrm{d}\sigma = 0, \tag{5.6c}$$

$$\frac{\partial}{\partial t}\int_{T_i} \rho w \, \mathrm{d}V + \int_{\partial T_i} (\rho w u_\eta + p n_z) \, \mathrm{d}\sigma = 0, \tag{5.6d}$$

$$\frac{\partial}{\partial t}\int_{T_i} \rho E \, \mathrm{d}V + \int_{\partial T_i} (\rho E u_\eta + p u_\eta) \, \mathrm{d}\sigma = 0, \tag{5.6e}$$

where $\eta = (n_x, n_y, n_z)^T$ the unit outward normal to the surface $|T_i|$ of the cell T_i, τ and b are respectively the tangential and the bi-normal vectors, such that these vectors form an orthonormal basis see Fig 5.3. In order to simplify the system (5.6), we do the following operations $(5.7b) \leftarrow n_x(5.6b) + n_y(5.6c) + n_z(5.6d)$, $(5.7c) \leftarrow t_x(5.6b) + t_y(5.6c) + t_z(5.6d)$ and $(5.7d) \leftarrow b_x(5.6b) + b_y(5.6c) + b_z(5.6d)$. The outcome of these operations is

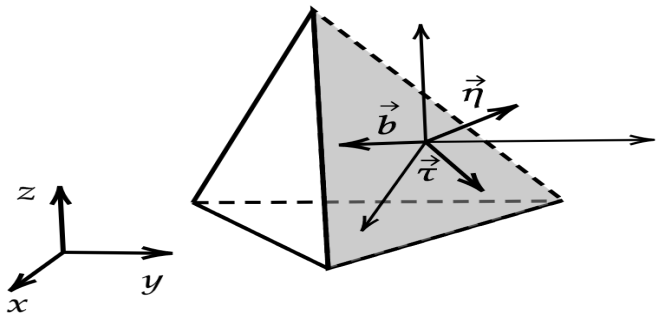

Fig 5.3. The projected velocity on the control volume.

$$\frac{\partial}{\partial t}\int_{T_i}\rho\,\mathrm{d}V+\int_{\partial T_i}\rho u_\eta\,\mathrm{d}\sigma = 0, \tag{5.7a}$$

$$\frac{\partial}{\partial t}\int_{T_i}\rho u_\eta\,\mathrm{d}V+\int_{\partial T_i}\left(hu_\eta^2+p\right)\mathrm{d}\sigma = 0, \tag{5.7b}$$

$$\frac{\partial}{\partial t}\int_{T_i}\rho u_\tau\,\mathrm{d}V+\int_{\partial T_i}\rho u_\tau u_\eta\,\mathrm{d}\sigma = 0, \tag{5.7c}$$

$$\frac{\partial}{\partial t}\int_{T_i}\rho u_b\,\mathrm{d}V+\int_{\partial T_i}\rho u_b u_\eta\,\mathrm{d}\sigma = 0, \tag{5.7d}$$

$$\frac{\partial}{\partial t}\int_{T_i}\rho E\,\mathrm{d}V+\int_{\partial T_i}\left(\rho E u_\eta+p u_\eta\right)\mathrm{d}\sigma = 0, \tag{5.7e}$$

which allows rewriting system (5.7) in a differential form as follows

$$\begin{cases} \dfrac{\partial\rho}{\partial t}+\dfrac{\partial\rho u_\eta}{\partial\eta}=0,\\ \dfrac{\partial\rho u_\eta}{\partial t}+\dfrac{\partial}{\partial\eta}\left(\rho u_\eta^2+p\right)=0,\\ \dfrac{\partial\rho u_\tau}{\partial t}+\dfrac{\partial}{\partial\eta}\left(\rho u_\eta u_\tau\right)=0,\\ \dfrac{\partial\rho u_b}{\partial t}+\dfrac{\partial}{\partial\eta}\left(\rho u_\eta u_b\right)=0,\\ \dfrac{\partial\rho E}{\partial t}+\dfrac{\partial}{\partial\eta}\left(\rho E u_\eta+p u_\eta\right)=0. \end{cases} \tag{5.8}$$

The projected speed model associated with the Euler equations is then reformulated as

$$\frac{\partial\mathbf{U}}{\partial t}(t,X)+u_\eta(t,X)\frac{\partial\mathbf{U}}{\partial\eta}(t,X)=\mathbf{S}(\mathbf{U}), \tag{5.9}$$

$\mathbf{U}$ is the projected conservative unknown, u_η is the normal speed, and $\mathbf{S}(\mathbf{U})$ is the second member that contains other terms of the system.

where

$$\mathbf{U} = \begin{pmatrix} \rho \\ \rho u_\eta \\ \rho u_\tau \\ \rho u_b \\ \rho E \end{pmatrix}, \qquad \mathbf{S}(\mathbf{U}) = \begin{pmatrix} -\rho \partial_\eta(u_\eta) \\ -\rho u_\eta \partial_\eta(u_\eta) - \partial_\eta p \\ -\rho u_\tau \partial_\eta(u_\eta) \\ -\rho u_b \partial_\eta(u_\eta) \\ -\rho E \partial_\eta(u_\eta) - \partial_\eta(p u_\eta) \end{pmatrix}. \tag{5.10}$$

5.1.3 Method of characteristics

This method for hyperbolic systems of conservation laws can be carried out componentwise, provided that the conservative equations can be rewritten in an advective formulation. In general, the advective form of the system under study is built such that conservative variables are transported with the same velocity field. The method avoids the grid distortion difficulties that the conventional Lagrangian schemes have. The characteristic curves associated with (5.9) are the solutions of the following equation.

$$X^c(t_n) = X_\star - \int_{t_n}^{t_n+\alpha^n\Delta t} u_\eta(s, X^c(s))\mathbf{n}\, ds. \tag{5.11}$$

The method of characteristics used traces backwards position at time t_n of particles that will reach the points $X_\star$ of a fixed mesh at time $t_n + \alpha^n \Delta t$, see Fig 5.4.

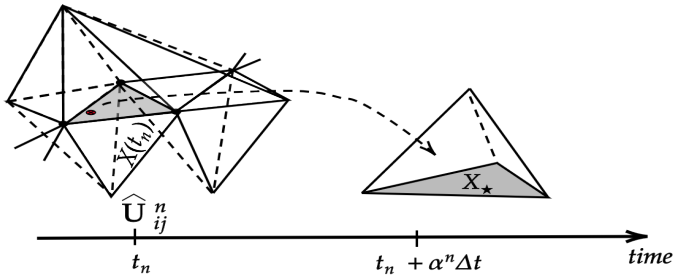

Fig 5.4. Illustration of the time grid for the choice of the starting condition in order to calculate the characteristics of the equation (5.9).

In order to complete the reformulation of the algorithm, the departure points must be calculated once the characteristic curves are known. Therefore, the solution of the advection equation (5.9) is

$$\mathbf{U}(t_n + \alpha^n\Delta t, X_\star) = \mathbf{U}(t_n, X^c(t_n)) + \int_{t_n}^{t_n+\alpha^n\Delta t} \mathbf{S}(\mathbf{U}(s, X^c(t_n)))\, ds. \tag{5.12}$$

In our implementation, a global fixed value for α^n was utilized. However, as mentioned above, a local selection of α^n is also possible. The solution in the characteristic field is calculated by interpolation from the central values of the cells.

$$\mathbf{U}_{ij}^n = \hat{\mathbf{U}}_{ij}^n + \mathbf{I}_\mathbf{F}(\hat{\mathbf{U}}_{ij}^n), \tag{5.13}$$

where $\mathbf{I}_\mathbf{F}$ is the approximation of the integral in (5.12). The solution $\hat{\mathbf{U}}_{ij}^n$ is reconstructed at the interfaces using

$$\hat{\mathbf{U}}_{ij}^n = \mathbf{U}(t_n, X^c(t_n)) = \sum_{k \in V(c)} \beta_k(X^c)\mathbf{U}_k^n, \tag{5.14}$$

with $V(X^c)$ is the set of neighbours by face and vertices to the cell of X^c, see Fig 5.5 and $\beta_k(c)$ is weights coming from the least squares method. It can be written

$$\beta_k(c) = \frac{1 + \lambda \cdot (X^k - X^c)}{\#V(c) + \lambda \cdot R}, \tag{5.15}$$

such as, $\lambda = (\lambda_x, \lambda_y, \lambda_z)$ and $R = (R_x, R_y, R_z)$. The weights parameters are given by formulas

$$R_x = \sum_{k \in V(c)} (x_k - x_c), \quad I_{xx} = \sum_{k \in V(c)} (x_k - x_c)^2, \quad I_{xy} = \sum_{k \in V(c)} (x_k - x_c)(y_k - y_c),$$

and

$$\lambda_x = \frac{(I_{yz}^2 - I_{yy}I_{zz})R_x + (I_{xy}I_{zz} - I_{xz}I_{yz})R_y + (I_{xz}I_{yy} - I_{xy}I_{yz})R_z}{\Delta},$$

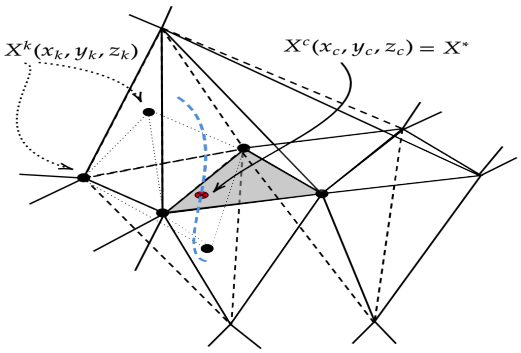

Fig 5.5. Interpolation points illustration.

where

$$\Delta = I_{xx}I_{yy}I_{zz} + 2I_{xy}I_{xz}I_{yz} - I_{xx}I_{yz}^2 - I_{yy}I_{xz}^2 - I_{zz}I_{xy}^2.$$

The same applies to I_{xz}, I_{zz}, I_{yy}, R_y, R_z, λ_y and, λ_z. The aforementioned expressions can be found in the appendix section.

The normal derivative terms in $\mathbf{S}(\mathbf{U})$ are evaluated using the diamond scheme explained in [133, subsection 3.1.1.2] and in the appendix bellow. Once $\mathbf{U}_{ij}^n$ is calculated in the predictor step, the state $\mathbf{W}_{ij}^n$ is recovered from $\mathbf{U}_{ij}^n$ using the projection transformations (5.5). The numerical flux is then given by

$$\Phi(\mathbf{W}_{ij}^n, \mathbf{n}_{ij}) = \mathbf{F}(\mathbf{W}_{ij}^n) \cdot \mathbf{n}_{ij}. \tag{5.16}$$

Regarding the temporal discretization, equation (5.2) can be solved with various explicit temporal numerical schemes; we have chosen in this approach the explicit Euler scheme, which is simple and fast. The time domain is divided into N sub-intervals $[t_n,\ t_{n+1}]$ with time step $\Delta t = t_{n+1} - t_n$ for $n = 0, 1, ..., N-1$. $\mathbf{W}^n$ is the value of a generic function $\mathbf{W}$ at time t_n. The fully-discrete formulation of the equation (5.1) is

$$\mathbf{W}_i^{n+1} = \mathbf{W}_i^n - \frac{\Delta t}{|T_i|} \sum_{j \in N(i)} |\gamma_{ij}| \Phi(\mathbf{W}_{ij}^n, \mathbf{n}_{ij}). \tag{5.17}$$

For the systems of conservation laws, such as the compressible Euler equations, all of the reconstruction procedures are implemented in the characteristic local directions to avoid spurious oscillations.

5.2 Numerical results

In this study, the Courant-Friedrichs-Lewy number for the explicit scheme (5.17) can be written under the following condition

$$\Delta t \leqslant \min\left\{ \frac{|T_i|}{\mathcal{P}_i(|\mathbf{u}\cdot\mathbf{n}|+\sqrt{\gamma P/\rho})_i}, \frac{|T_i|}{\mathcal{P}_i(|\mathbf{u}\cdot\mathbf{n}|+\sqrt{\gamma P/\rho})_i\sqrt{2\alpha^n}} \right\}. \tag{5.18}$$

A fixed $CFL = 0.9$ and $\alpha^n = 1$ in the two-dimensional benchmark and $\alpha^n = 2$ in the three-dimensional case, except in cases where we specify the value of α^n used. is used. All the simulations were performed on an Intel Core i7-8565U CPU @ 1.80GHz × 8, with 15 GB RAM. The CPU times presented in this section include all aspects of computational work including, mesh generation, calculation of characteristic curves, search-locate of departure points, and corrector step.

5.2.1 Shock tube problems

In this section, we present the shock tube problems. Indeed, we consider a tube of length $1m$, separated in the middle by a membrane with on one side a gas at high pressure (p_l, ρ_l) and on the other a gas at low pressure (p_r, ρ_r) see Fig 5.6. Due to the pressure difference, a shock wave propagates in the low-pressure chamber, followed by a contact discontinuity, and an expansion wave propagates in the high-pressure chamber. It is important to mention that the contact discontinuity is solely observable in the density variable. The initial conditions are given by

$$(\rho, p, u, v, w)(0, x, y, z) = \begin{cases} (\rho_l, p_l, u_l, 0, 0) & if\ x \leqslant 0.5, \\ (\rho_r, p_r, u_r, 0, 0) & if\ x > 0.5, \end{cases} \qquad 0 \leqslant y, z \leqslant 0.04,$$

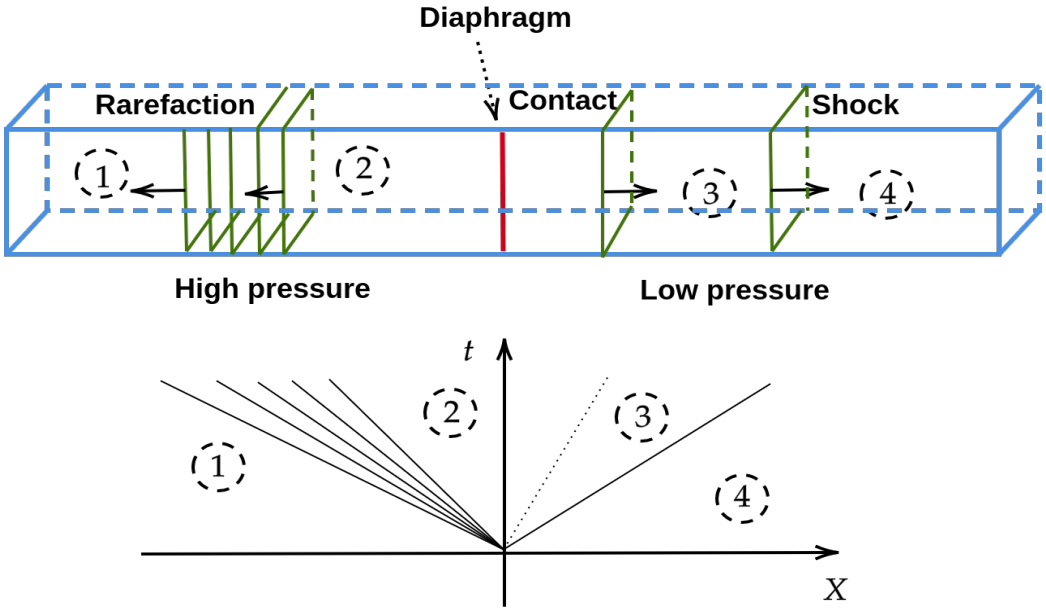

Fig 5.6. Shock tube after the diaphragm broken.

Table 5.1: Initial states left and right and simulation end times for shock tube problem.

Test case	ρ_l	u_l	p_l	ρ_r	u_r	p_r	t_{end}
1	1.0	0.75	1.0	0.125	0.0	0.1	0.2
2	1.0	0.0	10.0	0.125	0.0	1.0	0.06
3	0.445	0.698	3.258	0.5	0.0	0.571	0.14
4	1.0	-2.0	0.4	1.0	2.0	0.4	0.15

For a better comparison, we have also included the exact solution using the open-source code [134] for the shock tube problems. Note that the contact discontinuity and the shock wave are very well captured, and the FVC scheme is highly accurate.

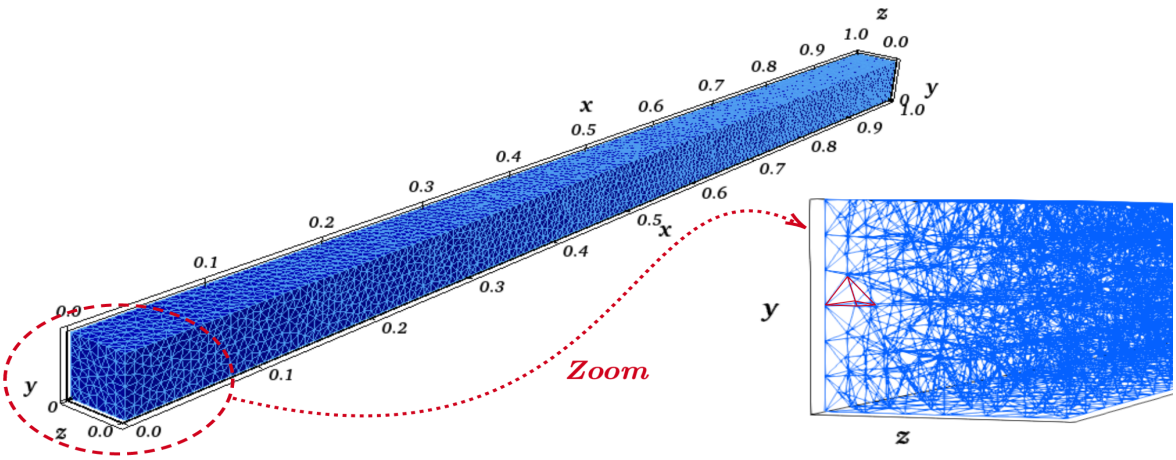

Fig 5.7. Unstructured tetrahedral mesh for the 3D shock tube problems.

The mesh used is a non-uniform tetrahedral grid of 1266261 cells and 258460 nodes with periodic boundary conditions in y and z. The obtained results are shown in Table 5.1 at the time t_{end}.

We present in Fig 5.9 the cross-section at $(y = 0.02m, z = 0.02m)$ of the density and the pressure for each test case of the Table 5.1. All figures show that the numerical solution agrees with the exact solution. We have observed a slight numerical diffusion, which can be corrected by enhancing the order in time and space. In order to quantify the results, we present in Table 5.2 the relative L^1 errors and the accuracy order of ρ and p for simulations on different meshes of a two-dimensional computational domain. As shown in the table below, the numerical and analytical results are in perfect agreement. By comparing these results, we can see that under these conditions, the algorithm can properly predict shock waves without generating oscillations.

Table 5.2: Relative L^1 error and CPU times in s for the tube shock problems using FVC scheme.

# Cells	Maximum of cells height size	Error in ρ	Error in p	Order	CPU time (s)
4141	0.0143	1.878E-04	1.739E-04	-	4.82
11546	0.00812	1.034E-04	1.001E-04	1.311	8.32
23567	0.00645	4.518E-05	3.711E-05	1.356	18.36
43985	0.003679	1.986E-05	1.138E-05	1.409	23.34

In the Fig 5.8, we represent the logarithm of the relative error L^1 calculated in Table 5.2 with respect to the logarithm of the maximum value of the mesh interfaces. These results demonstrate a considerable order of accuracy of the scheme. The errors produced by the FVC scheme with two different values of α^n seem to exhibit varying convergence rates, but we obtain an overall convergence rate of approximately 1.3. However, in order to achieve a similar order of accuracy in the 3D version, it will be necessary to use a three-dimensional mesh with a large number of cells, which will make the simulation computationally expensive.

We observe that the order of accuracy of the method is influenced by the parameter α^n, as illustrated in Fig 5.8. This characteristic has been examined in detail in [31]. In our recent study, we have explored a solution to this problem by introducing a new approach for the choice of α^n, described in [101, 135]. This approach involves modifying the FVC scheme by replacing the constant α^n with a more versatile parameter α_{ij}^n (4.17), thereby providing better control of numerical diffusion. By adopting this new formulation, we have observed a significant improvement in the performance of the FVC scheme, which now exhibits better adaptability and greater robustness.

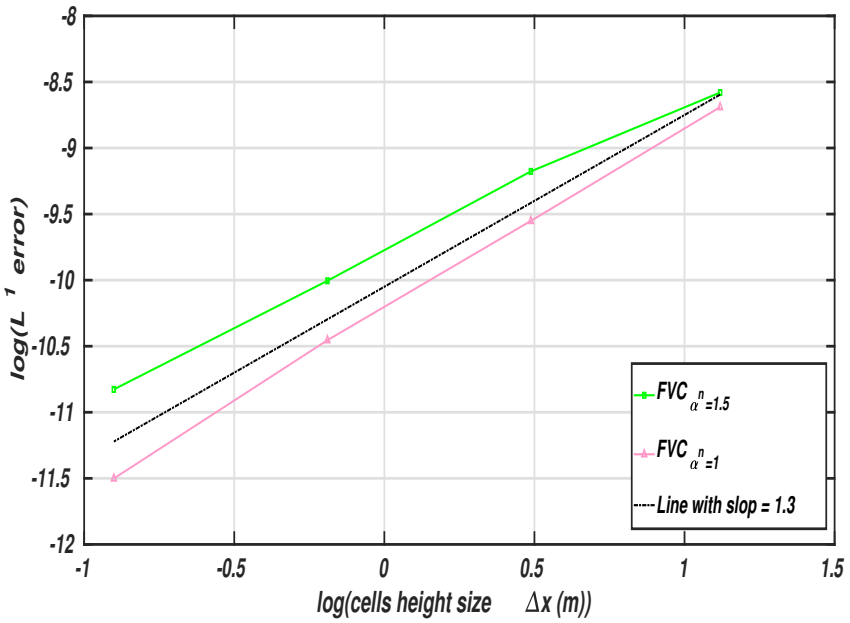

Fig 5.8. Convergence order in L^1 error of the density.

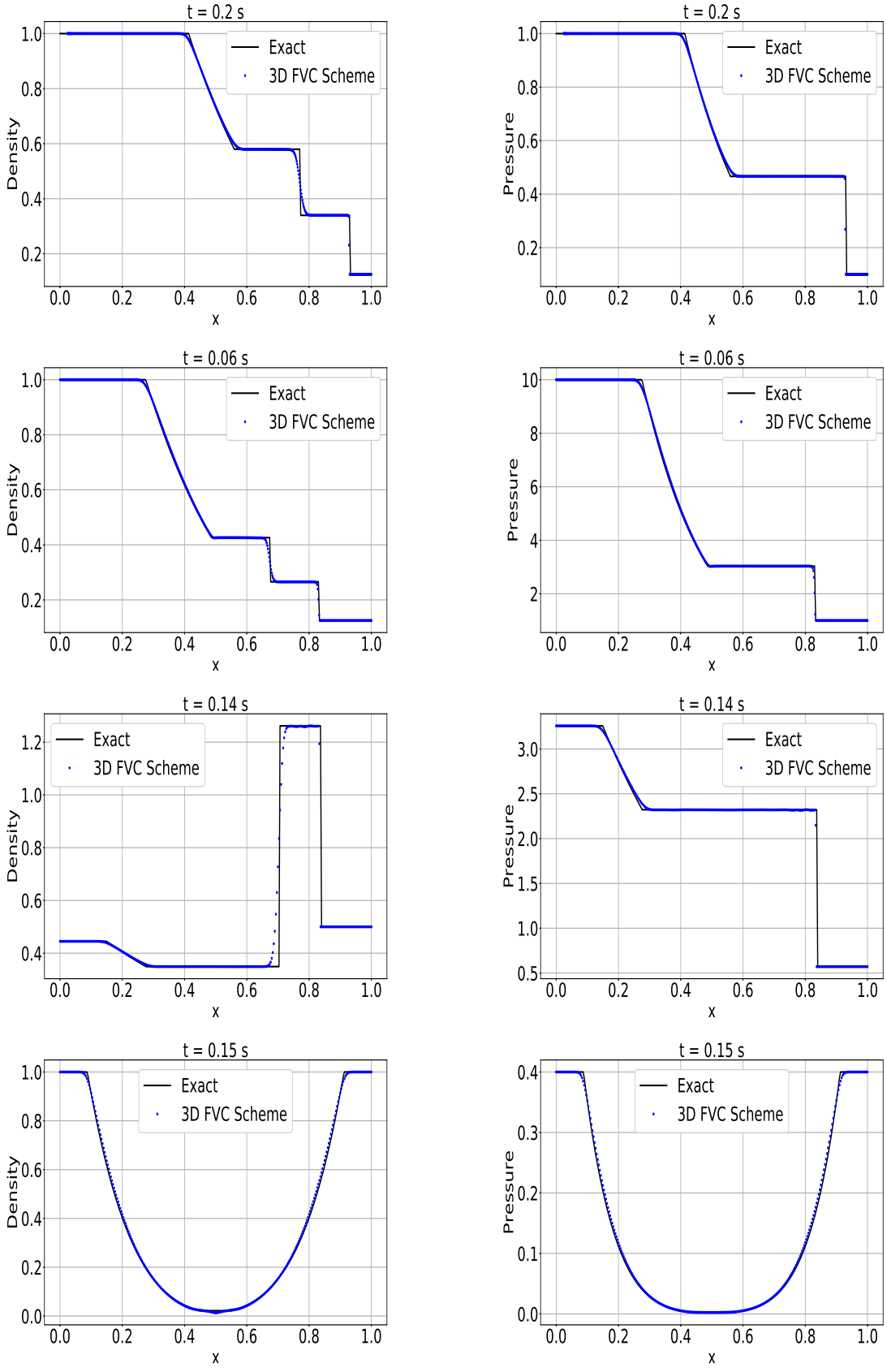

Fig 5.9. A cross-section at $(y = 0.02m, z = 0.02m)$ of the numerical solution of a shock tube problem in comparison with the exact solution.

5.2.2 Radially symmetric Riemann problem

The benchmark proposed in [136] is a two-dimensional problem that exhibits radial symmetry and is analogous to the shock tube problem [136]. Before a sudden disturbance, a hypothetical membrane divides the square domain $\Omega = [-0.5, 0.5]^d$ which corresponds to a square (when d = 2) and a cube (when d = 3), into two subdomains:

$$D_L = \{X \in \Omega \mid ||X|| < 0.13\} \text{ and } D_R = \Omega \setminus D_L.$$

The boundaries of both subdomains are defined as reflective. Initially, the gas is stationary, and the pressure and density inside D_L are higher than those outside. The interior and exterior states of the gas are defined by certain parameters

$$(\rho, p, u, v, w)(0, X) = \begin{cases} (2.0, 15.0, 0.0, 0.0, 0.0) & if\ ||X|| < 0.13, \\ (1.0, 1.0, 0.0, 0.0, 0.0) & if\ ||X|| \geqslant 0.13. \end{cases}$$

At the initial time, when the membrane is abruptly removed, a shock wave initiates radial expansion due to the existing pressure differential. The objective of this benchmark is to accurately capture the moving discontinuities while maintaining the radial symmetry of the solution. Fig 5.10 shows the density and pressure isolines of the solution distribution that have been calculated using the FVC scheme with a triangular mesh composed of 19545 cells in the 2D case. Conversely, in the 3D case, a very coarse mesh consisting of only 985185 tetrahedra was used. In Fig 5.13 we present the density and pressure obtained from the 3D simulation, from which the same conclusions as in the 2D case can be drawn. Fig 5.12 shows the cutlines that indicate the density profiles are symmetric and without oscillation. This demonstrates the effectiveness of the FVC scheme to accurately preserve the radial symmetry of the solution and capture the moving shock wave.

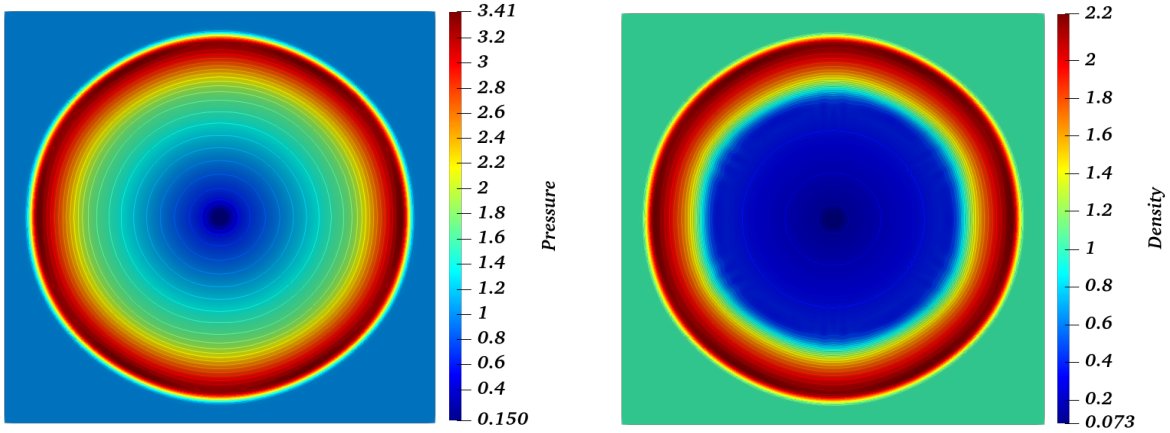

Fig 5.10. The Radially symmetric Riemann problem on a grid of 19545 cells. The initial data for this problem consisted of a symmetric discontinuity in both pressure and density. At time $t = 0.13s$, the pressure and density were recorded and are shown on the left and right sides, respectively.

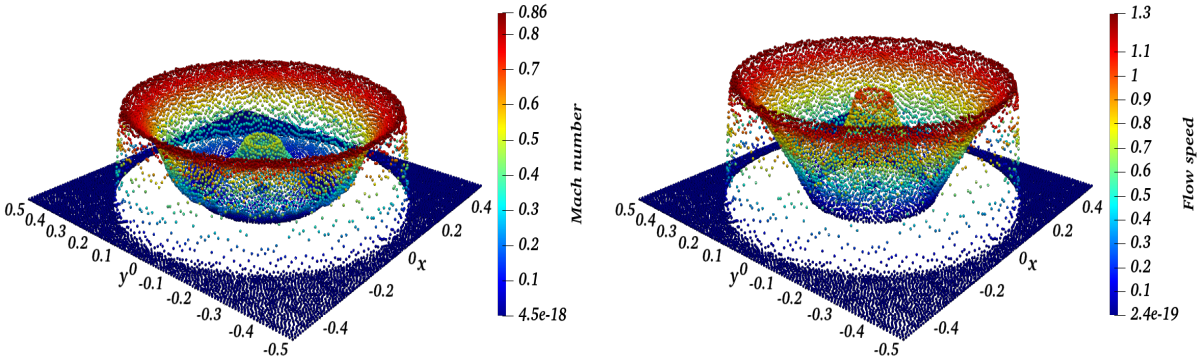

Fig 5.11. 3D view of the mach number (left) and the flow speed (right) of the Radial Riemann Problem on a mesh of 19545 cells at $t = 0.13s$.

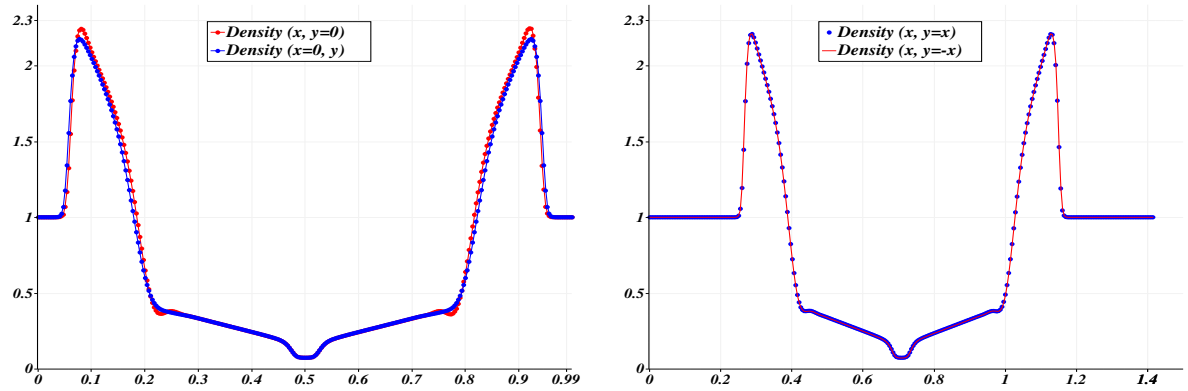

Fig 5.12. The density cutlines for a radially symmetric Riemann problem are illustrated by two cross-sections located at a different points. Left at $y = 0$ and $x = 0$. In the right panel, there are two cross-sections placed at $y = x$ and $y = -x$.

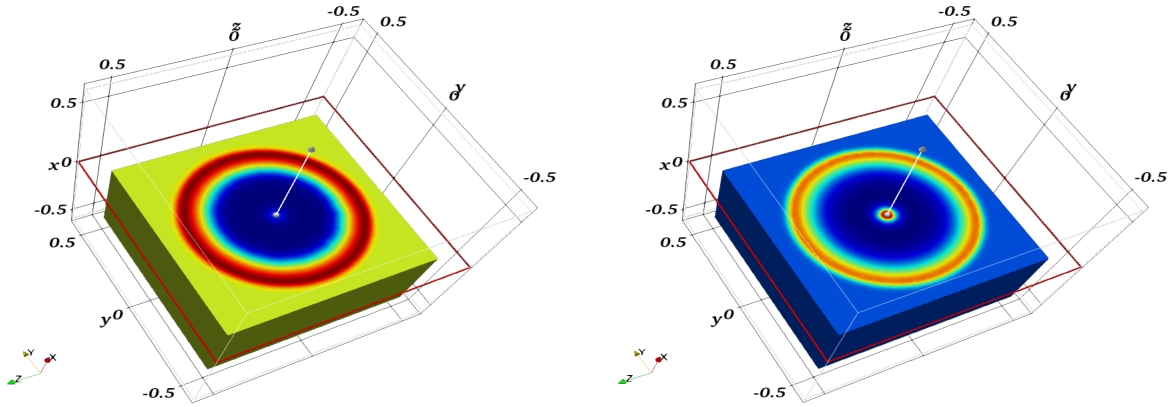

Fig 5.13. A clip plane at $\mathcal{P}(0_{\mathbb{R}^3}; \vec{n} = (1, 0, 0))$ of radially symmetric Riemann problem at time $t = 0.13s$ obtained with an FVC scheme on an unstructured tetrahedral mesh with 985185 tetrahedra. Left: visualization of the density. Right represents the pressure.

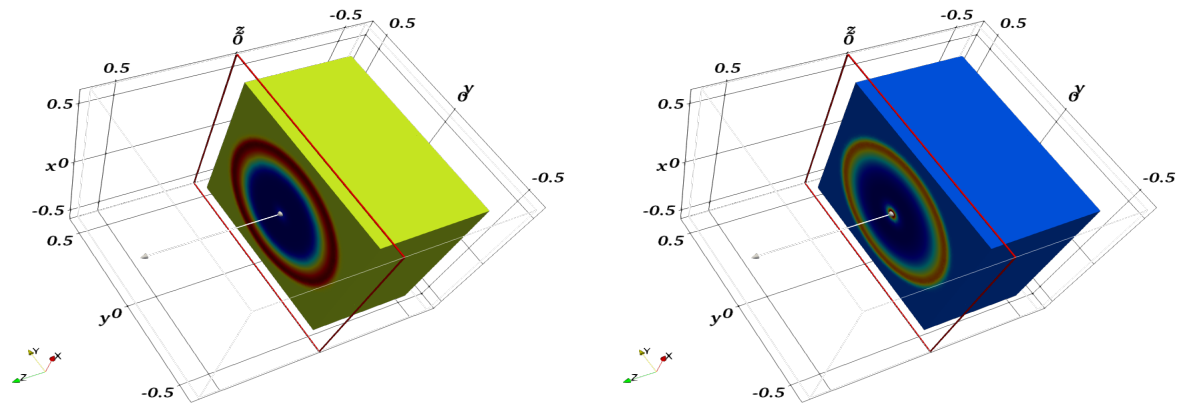

Fig 5.14. A clip plane at $\mathcal{P}(0_{\mathbb{R}^3}; \vec{n} = (0, 0, 1))$ of radially symmetric Riemann problem at time $t = 0.13s$. Left: visualization of the density. Right represents the pressure.

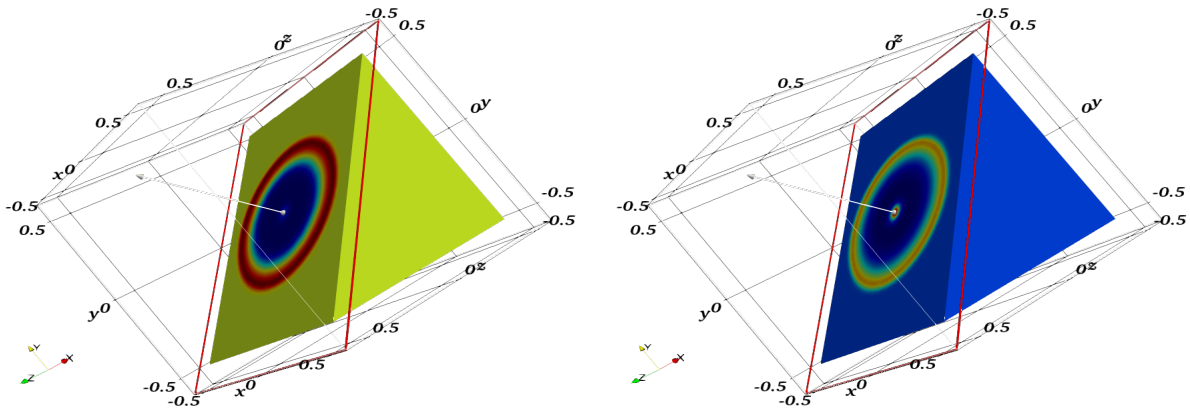

Fig 5.15. A clip plane at $\mathcal{P}(0_{\mathbb{R}^3}; \vec{n} = (0, 1, 1))$ of radially symmetric Riemann problem at time $t = 0.13s$. Left: visualization of the density. Right represents the pressure.

5.2.3 Double Mach reflection problem

In this test, we have reproduced the numerical solution of a challenging physical phenomenon called the double Mach reflection problem. This problem was originally introduced by Woodward and Colella to assess the accuracy of unsteady Euler equations in simulating complex fluid dynamics scenarios. The problem involves a Mach 10 shock wave that collides with an inclined wall of an angle of 60°, see Fig 5.16. The simulation is conducted on a rectangular computational domain, defined as $\Omega = [0.3] \times [0.1]$ consisting of an unstructured mesh of 128116 triangular cells. The pre- and post-shock flow variables are assigned in a specific way for each point (x, y) in the pre-shock region D_L. The primary objective of this study is to examine the behavior of the shock wave generated by the FVC scheme during its interaction with the inclined wall, which can provide valuable insights into the effectiveness of the FVC scheme for simulating such complex fluid dynamics problems.

$$(\rho, p, u, v)(0, x, y) = \begin{cases} \left(8.0, 116.5,\ 8.25\cos(30°), 8.25\sin(30°)\right) & if(x, y) \in D_L, \\ \left(1.4,\ 1.0,\ 0.0,\ 0.0\right) & if(x, y) \in D_R. \end{cases}$$

The shock wave is initially located in $D_L = \left\{(x, y) \mid x < \frac{1}{6} + \frac{y}{\sqrt{3}}\right\}$, while the wall that it reflects off is defined by $1/6 \leq x \leq 3$ and $y = 0$. The top boundary conditions are set to the post-shock conditions for $x < \frac{1}{6} + \frac{1+20t}{\sqrt{3}}$ and pre-shock conditions in $D_R = \Omega \backslash D_L$, accurately capturing the motion of the shock wave. Notably, no boundary conditions are necessary along the line $x = 3$, see Fig 5.16. This problem poses a significant challenge for the unsteady Euler equations.

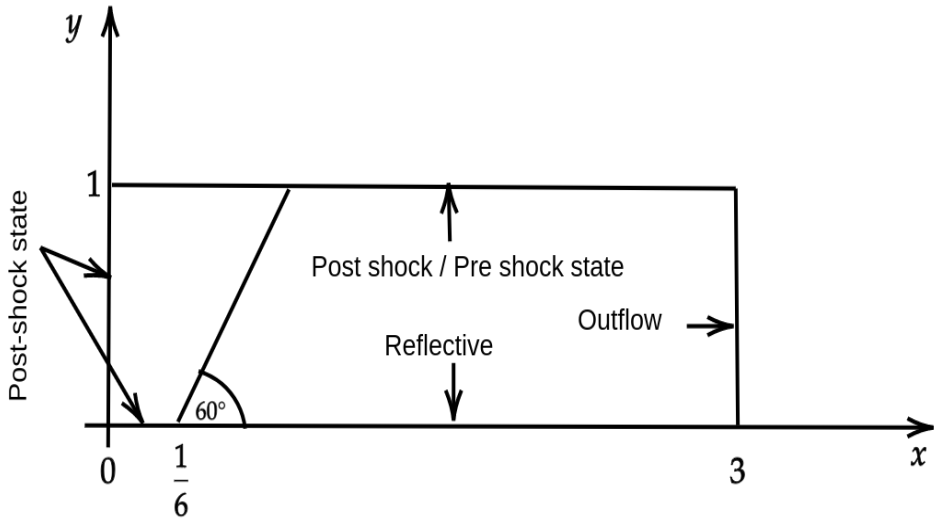

Fig 5.16. The computational domain for the double Mach reflection configuration, along with its corresponding boundary conditions.

We compute solutions up to the final time $t = 0.2s$ on the unstructured triangular mesh of 128116 cells. The density and pressure calculated by the FVC scheme are illustrated in Fig 5.17. As we can see, the profile is captured and in good agreement with the results in [137], albeit with significant numerical diffusion.

Firstly, the wall jet rolls up into a vortex that occurs when the jet reaches the Mach stem. In addition, the shock that connects the contact surface and the transverse wave (making it a Mach double reflection) intensifies, and its triple point, the elbow along the transverse wave, becomes much more distinct. Despite the Kelvin-Helmholtz instabilities along the contact surface, they are not developed due to the order of accuracy, as a higher-order WENO-type scheme would be required to capture them (see [138]). However, it is clear that the FVC scheme captures the solution profile accurately. Furthermore, Fig 5.18 also shows the Mach number with the left contour lines and the flow velocity magnitude with the right contour lines. It is evident that the structure captured by the FVC diagram is also coherent with [137].

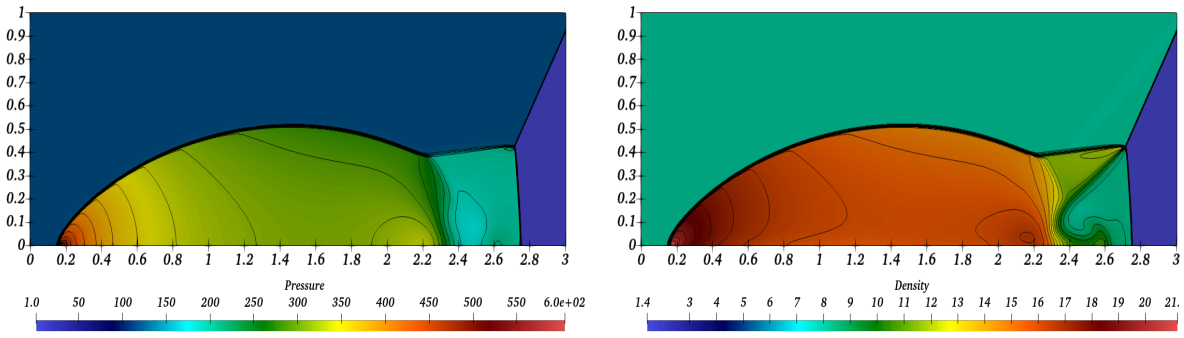

Fig 5.17. On the right side, the FVC scheme's numerical solution is illustrated as density contour lines, while pressure level curves are depicted on the left side. This presentation provides a comprehensive view of the obtained outcomes.

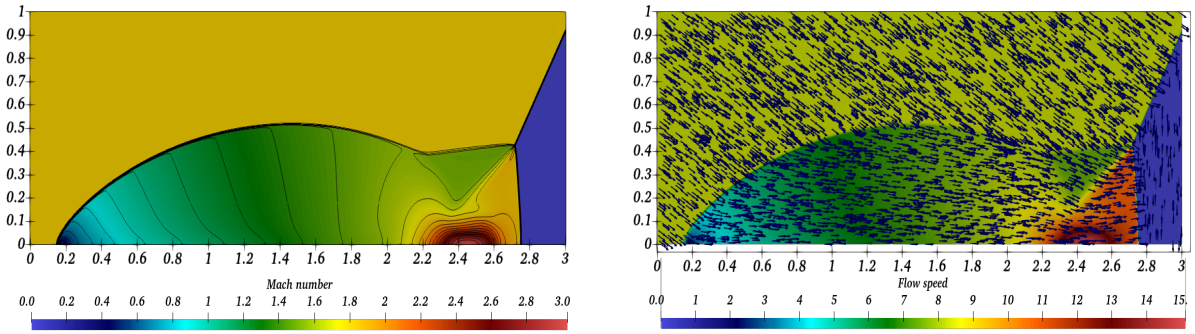

Fig 5.18. At the instant $t = 2s$, the FVC provided a resolution for both the fluid Mach number (on the left) and the flow velocity (on the right) related to the issue of double Mach rarefaction problem.

5.2.4 GAMM channel

This test example was proposed in [139] to study the subsonic and transonic flows described by the Euler equations in a channel with a bump. It was then used by several researchers to validate the ability of their schemes [140, 141, 142]. The flow in the channel is initially uniform, and then the flow tangency condition for the walls and the non-reflective condition for both upstream and downstream the Dirichlet boundaries are applied. The computational domain, which is a rectangle $[-1, 2] \times [0, 1]$ with a circular bump of height 10% on the lower side, is discretized with an unstructured mesh formed by triangular cells. The mesh for the GAMM channel with parameter selection is shown in Fig 5.19. The initial conditions are: $\rho = 1$ in the whole domain and $p = \frac{1}{\gamma}$. As output boundary, we set $p = 0.736952$. The rest of the boundary is an impermeable wall, so a normal velocity component equal to zero is prescribed. The following figures show the numerical results generated by the FVC scheme. The convergence to the steady state is followed by the log L^2 residual, defined as: $Error(\mathbf{W}_i^n) = \frac{1}{N_{ele}} \sqrt{\sum_i \left(\frac{\mathbf{W}_i^{n+1} - \mathbf{W}_i^n}{\Delta t} \right)^2}$, where N_{ele} is a number of all elements in the computational domain.

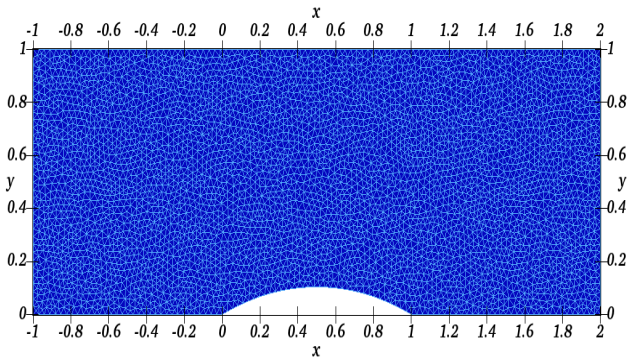

Fig 5.19. Computation mesh with 8755 cells and 4514 nodes for the channel flow with a 10% thick circular arc bump.

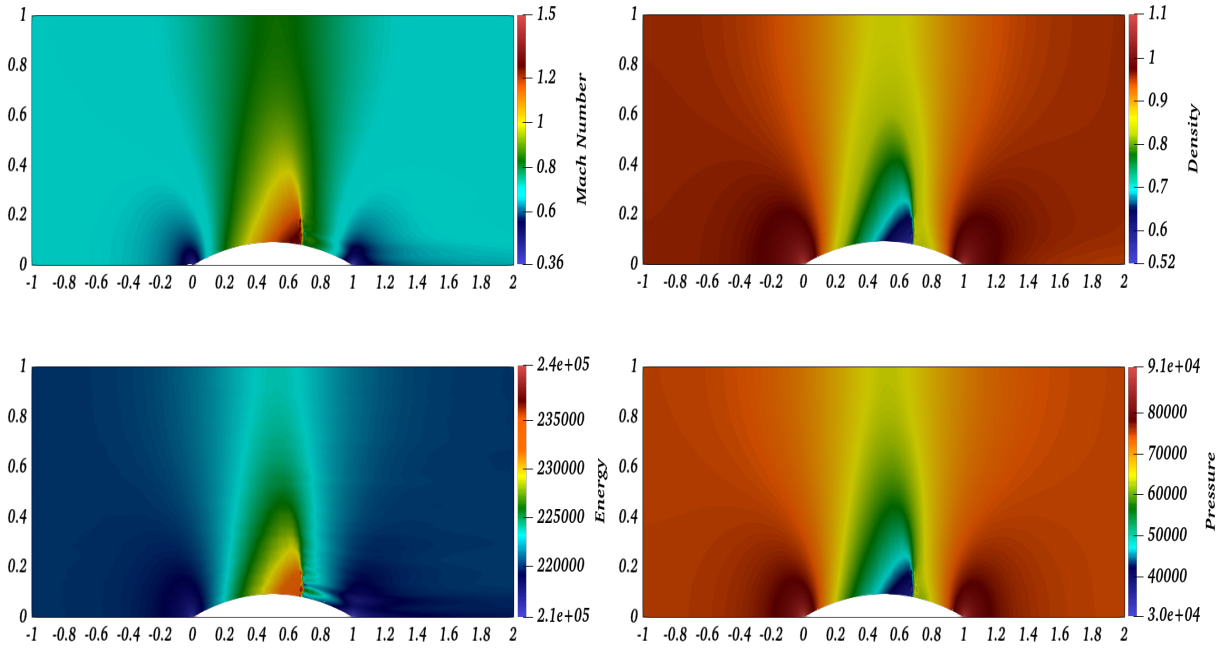

Fig 5.20. Results for the two-dimensional GAMM channel: Mach number (upper-left), Density (upper-right), Energy (lower-left) and Pressure (lower-right) at time t which is assumed to be an equilibrium time.

Fig 5.22 shows the convergence histories of the 2D GAMM channel. This computation is obtained by running the FVC scheme on an unstructured mesh. It is shown that the calculation requires more than $4E + 5$ iterations for the solution to reach the steady state.

Fig 5.20 shows the Mach number distribution, density, energy and pressure of the steady-state solution. As shown in Fig 5.20, the numerical solution is fairly symmetrical concerning the median chord, which is a good indication of the accuracy of the solution for this subsonic application.

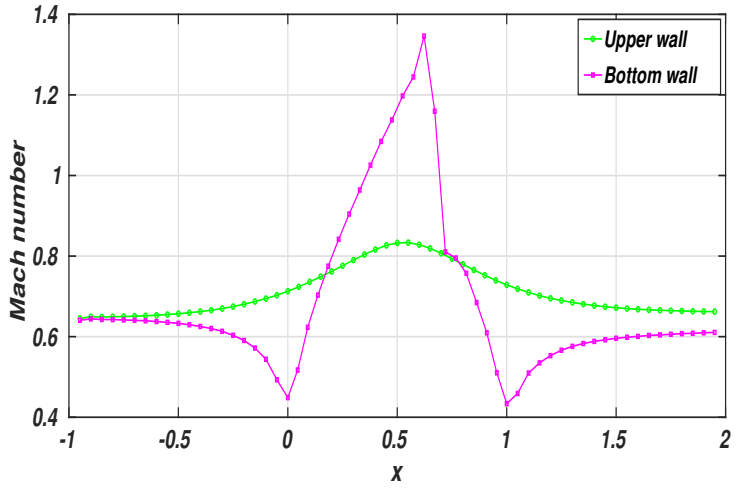

Fig 5.21. Mach number on bottom and upper wall $M_{max} = 1.3891$.

According to the calculation, a supersonic region appears in the solution, which ends with a shock as shown in Fig 5.21 (Inviscid compressible flow in the GAMM channel: Mach number on the bottom and upper walls). The numerical solution calculated by the FVC scheme converges to the stationary state. The obtained results are in excellent agreement with those reported in [143, 144]. The positions of the shock wave are the same, this indicates that the present scheme is accurate, reliable, and fast.

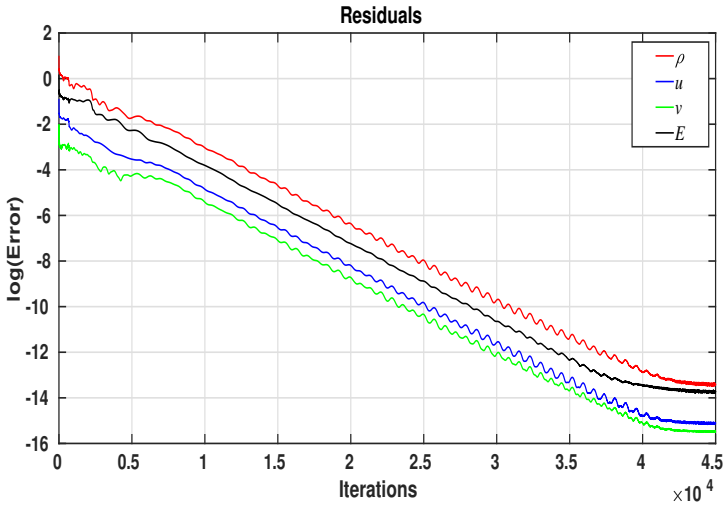

Fig 5.22. Convergence history for 2D GAMM channel.

5.2.5 Forward facing step

This test case, introduced in [145], involves solving the problem of interaction between a Mach 3 supersonic flow and a rising step. The geometry of the mesh used and the boundary conditions for this problem are depicted in Fig 5.23. The area under investigation has a unit height and a length of 3. The step, with a height of 0.2, is located at an abscissa of 0.6. The mesh consists of 38969 cells triangular elements. Region A_1 and boundary B_1 consist of an initially perfect gas with the following characteristics: $\rho = 1.4$, $p = 1$, $u = 3$, and $v = 0$. Reflective wall-

type boundary conditions are imposed on B_1 and B_2. As for B_4, absorbing boundary conditions are employed.

Firstly, walking generates a shock wave that travels to the left. This shock wave then reflects off wall B_3, giving rise to a "Mach" reflection. The reflected Mach wave is subsequently weakened by the rarefaction wave centered on the upper corner of the step. Finally, another reflection appears on wall B_3. Solving this problem is considerably challenging and typically requires the imposition of additional boundary conditions and the introduction of supplementary conditions at the upper corner of the step [145]. Indeed, this singular point produces a separation zone that is purely numerical and slows down the fluid. Typically, the solution involves refining the mesh near the singular point or imposing constant enthalpy and entropy in the neighborhood of this point.

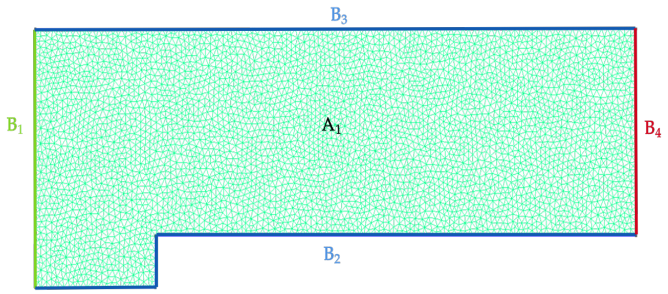

Fig 5.23. Geometry and boundary conditions.

No special treatment was performed in the computation to overcome this issue. All calculations were done using the FVC scheme with a CFL number of 0.85 and are presented for the final time $t_{end} = 4s$. The results obtained with the proposed scheme are shown for pressure, density, and Mach number on the figures Fig 5.25 and Fig 5.24. It can be observed that the figures correctly show the shock waves and the Kelvin-Helmholtz instability vortices [146] are not well-developed along the upper shear wave due to the insufficient order of accuracy to capture this phenomenon, as well as requiring a very fine mesh, see e.g. [138]. Small-scale flow structures are better captured with results obtained from a finer mesh, as expected. Discontinuities (shocks, contacts) seem to be well-captured by the FVC scheme.

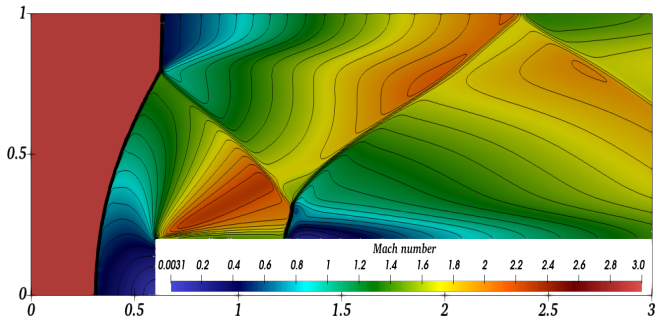

Fig 5.24. Mach number and its contour lines at $t_{end} = 4s$.

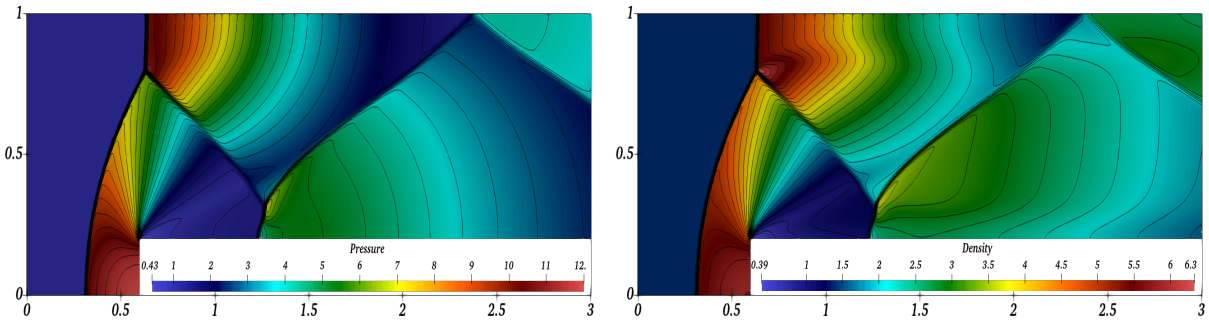

Fig 5.25. Numerical results for forward facing step problem simulated by FVC scheme.

5.2.6 2D Riemann problems

In order to evaluate the accuracy, oscillatory-free, and robustness of the FVC scheme, a series of two-dimensional Riemann problems were simulated. These problems, commonly referred to as configurations 1 to 19, have been extensively investigated in previous scientific studies, such as [147, 148, 149, 150, 151]. The square domain $\Omega = [0, 1]^2$ is divided into four quadrants by the lines $x = 1/2$ and $y = 1/2$, as shown in Fig 5.26. In all simulations, the domain Ω is discretized into 83393 uniform triangles. The initial conditions consist of constant states with dimensions 2×2, which are given by

$$(\rho, p, u, v)(0, x, y) = \begin{cases} (\rho_{TR}, p_{TR}, u_{TR}, v_{TR}), & \text{if } x > 0.5,\ y > 0.5, \\ (\rho_{TL}, p_{TL}, u_{TL}, v_{TL}), & \text{if } x < 0.5,\ y > 0.5, \\ (\rho_{BL}, p_{BL}, u_{BL}, v_{BL}), & \text{if } x < 0.5,\ y < 0.5, \\ (\rho_{BR}, p_{BR}, u_{BR}, v_{BR}), & \text{if } x > 0.5,\ y < 0.5. \end{cases}$$

The values of pressure p, density ρ, components of velocity u, and v for the initial states in the left/right top/bottom quadrants are presented in Fig 5.27. The time at which the results are presented is t_{end}. $\gamma = 1.4$. is used for all simulations, and the density contours in the figures are consistent with the results presented in [147]. All Riemann problems considered in [147] have been designed to ensure that the solutions of the four 1D Riemann problems between quadrants contain exactly one wave, which may be a shock (S), rarefaction (R), or contact discontinuity (J). To maintain consistency with [148], the notations R, S, and J are used in this study.

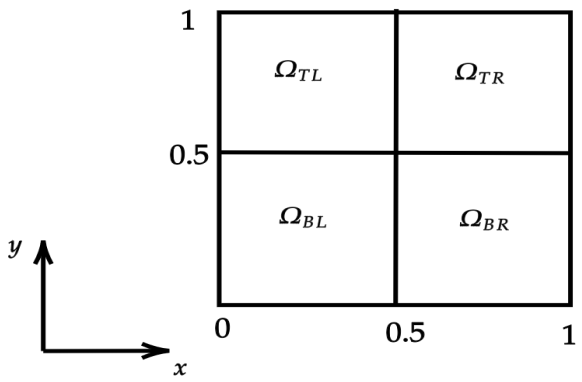

Fig 5.26. The computational domain for 2D Riemann problems.

Configuration Number	Ω_{TL}				Ω_{TR}				Ω_{BL}				Ω_{BR}				
	p_{TL}	ρ_{TL}	u_{TL}	v_{TL}	p_{TR}	ρ_{TR}	u_{TR}	v_{TR}	p_{BL}	ρ_{BL}	u_{BL}	v_{BL}	p_{BR}	ρ_{BR}	u_{BR}	v_{BR}	t_{end}
2	0.4	0.5197	−0.7259	0.0	1.0	1.0	0.0	0.0	1.0	1.0	−0.7259	−0.7259	0.4	0.5197	0.0	−0.7259	0.2
3	0.3	0.5323	1.206	0.0	1.5	1.5	0.0	0.0	0.029	0.138	1.206	1.206	0.3	0.5323	0.0	1.206	0.3
4	0.35	0.5065	0.8939	0.0	1.1	1.1	0.0	0.0	1.1	1.1	0.8939	0.8939	0.35	0.5065	0.0	0.8939	0.25
5	1.0	2.0	−0.75	0.0	1.0	1.0	−0.75	−0.5	1.0	1.0	0.75	0.5	1.0	3.0	0.75	−0.5	0.23
6	1.0	2.0	0.75	0.5	1.0	1.0	0.75	−0.5	1.0	1.0	−0.75	0.5	1.0	3.0	−0.75	−0.5	0.3
7	0.4	0.5197	−0.625	0.1	1.0	1.0	0.1	0.1	0.4	0.8	0.1	0.1	0.4	0.5197	0.1	−0.6259	0.25
8	1.0	1.0	−0.625	0.1	0.4	0.5197	0.1	0.1	1.0	0.8	0.1	0.1	1.0	1.0	0.1	−0.6259	0.25
9	1.0	2.0	0.0	−0.3	1.0	1.0	0.0	0.3	0.4	1.039	0.0	−0.8133	0.4	0.5197	0.0	−0.4259	0.3
10	1.0	0.5	0.0	0.6076	1.0	1.0	0.0	0.4297	0.3333	0.2281	0.0	−0.6076	0.3333	0.4562	0.0	−0.4297	0.15
11	0.4	0.5313	0.8276	0.0	1.0	1.0	0.1	0.0	0.4	0.8	0.1	0.0	0.4	0.5313	0.1	0.7276	0.3
12	1.0	1.0	0.7276	0.0	0.4	0.5313	0.0	0.0	1.0	0.8	0.0	0.0	1.0	1.0	0.0	0.7276	0.25
13	1.0	2.0	0.0	0.3	1.0	1.0	0.0	−0.3	0.4	1.0625	0.0	0.8145	0.4	0.5313	0.0	0.4276	0.3
14	8.0	1.0	0.0	−1.2172	8.0	2.0	0.0	−0.5606	2.6667	0.4736	0.0	1.2172	2.6667	0.9474	0.0	1.1606	0.1
15	0.4	0.5197	−0.6259	−0.3	1.0	1.0	0.1	−0.3	0.4	0.8	0.1	−0.3	0.4	0.5313	0.1	0.4276	0.2
16	1.0	1.0222	−0.6179	0.1	0.4	0.5313	0.1	0.1	1.0	0.8	0.1	0.1	1.0	1.0	0.1	0.8276	0.2
17	1.0	2.0	0.0	−0.3	1.0	1.0	0.0	−0.4	0.4	1.0625	0.0	0.2145	1.0	0.8	0.1	0.1	0.3
18	1.0	2.0	0.0	−0.3	1.0	1.0	0.0	1.0	0.4	1.0625	0.0	0.2145	0.4	0.5197	0.0	0.2741	0.2
19	1.0	2.0	0.0	−0.3	1.0	1.0	0.0	0.3	0.4	1.0625	0.0	0.2145	0.4	0.5197	0.0	−0.4259	0.3

Fig 5.27. Initial states in four top/left (TL), top/right (TR), bottom/left (BL) and bottom/right (BR) quadrants for each configuration. Pressure p, density ρ, x-component of velocity u, y-component of velocity v and the final time t_{end} of the simulations.

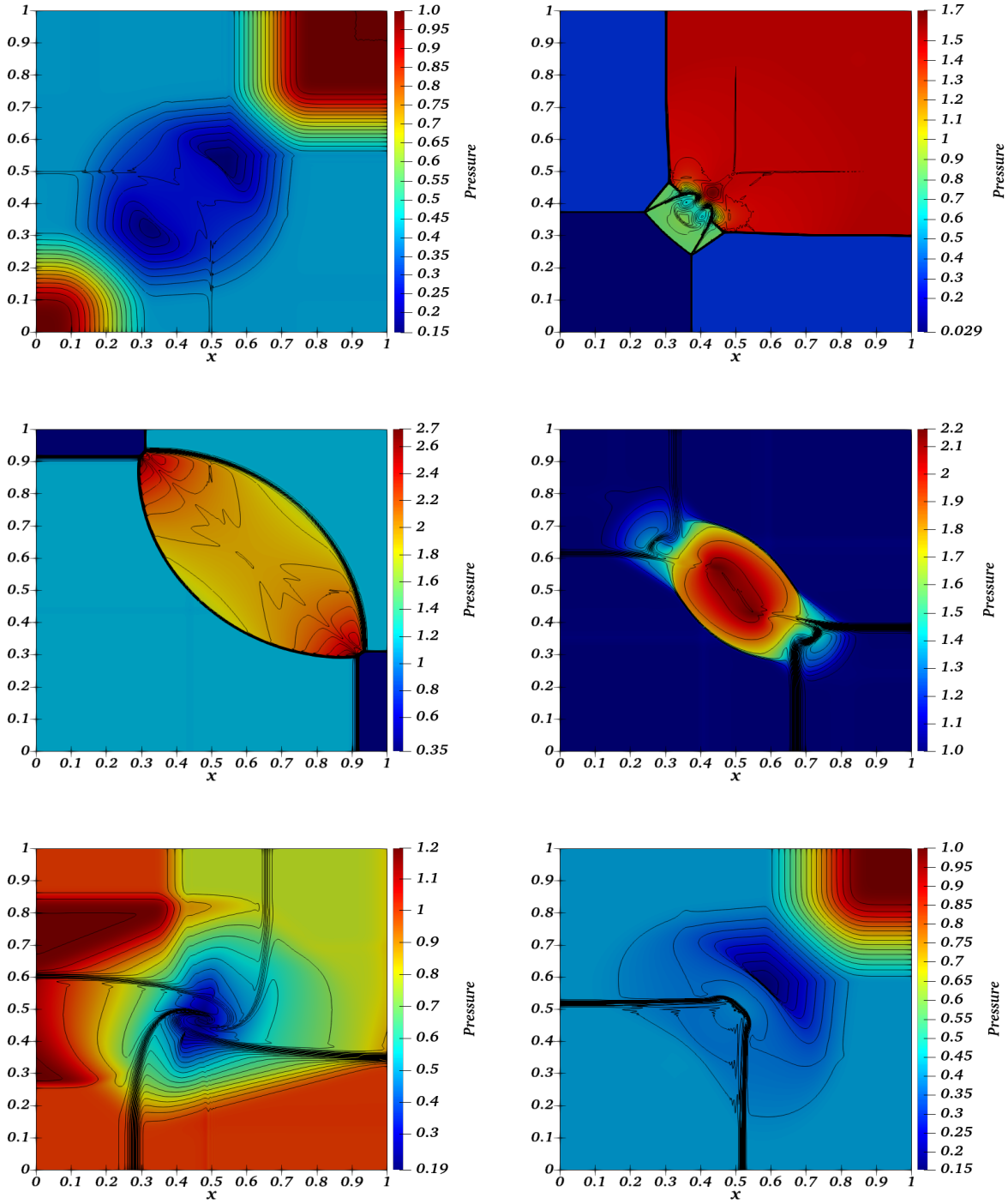

Fig 5.28. The results generated by the FVC scheme for the 2D Riemann problem are presented for configurations 2 through 7. Pressure is represented by color, while 25 contours are used to represent density. The first row corresponds to configurations 2 and 3 from left to right, the middle row corresponds to configurations 4 and 5, and the last row corresponds to configurations 6 and 7. The contour values are (from 0.25 to 1.00), (from 0.2 to 1.71), (from 0.6 to 2.00), (from 0.98 to 3.73), (from 0.33 to 3.11) and (from 0.26 to 0.99), respectively, for configurations 2 to 7.

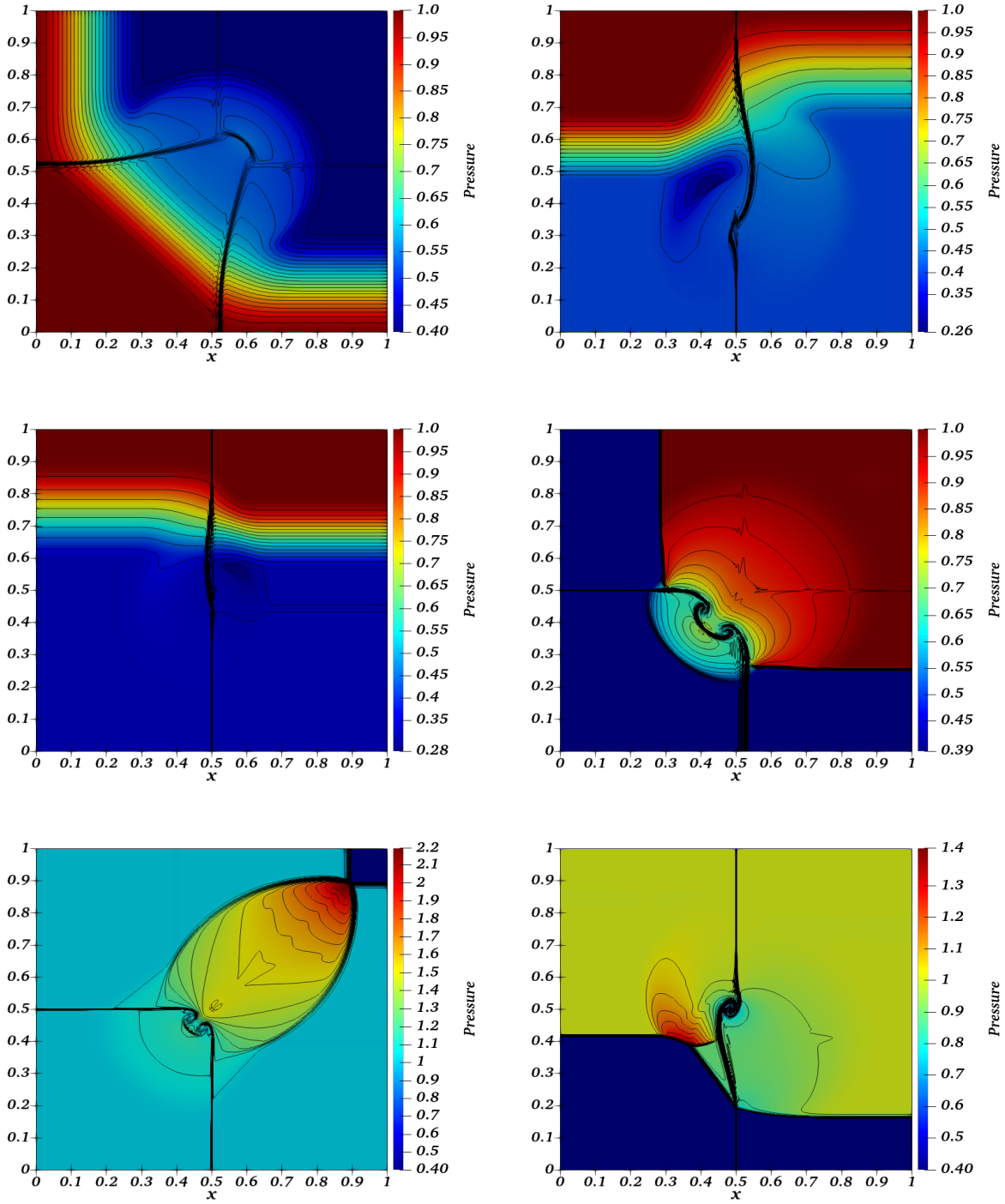

Fig 5.29. The results generated by the FVC scheme for the 2D Riemann problem are presented for configurations 8 through 13. Pressure is represented by color, while 27 contours are used to represent density. The first row corresponds to configurations 8 and 9 from left to right, the middle row corresponds to configurations 10 and 11, and the last row corresponds to configurations 12 and 13. The contour values are (from 0.52 to 0.99), (from 0.42 to 2.00), (from 0.17 to 1.00), (from 0.52 to 1.23), (from 0.53 to 1.61) and (from 0.52 to 2.54), respectively, for configurations 8 to 13.

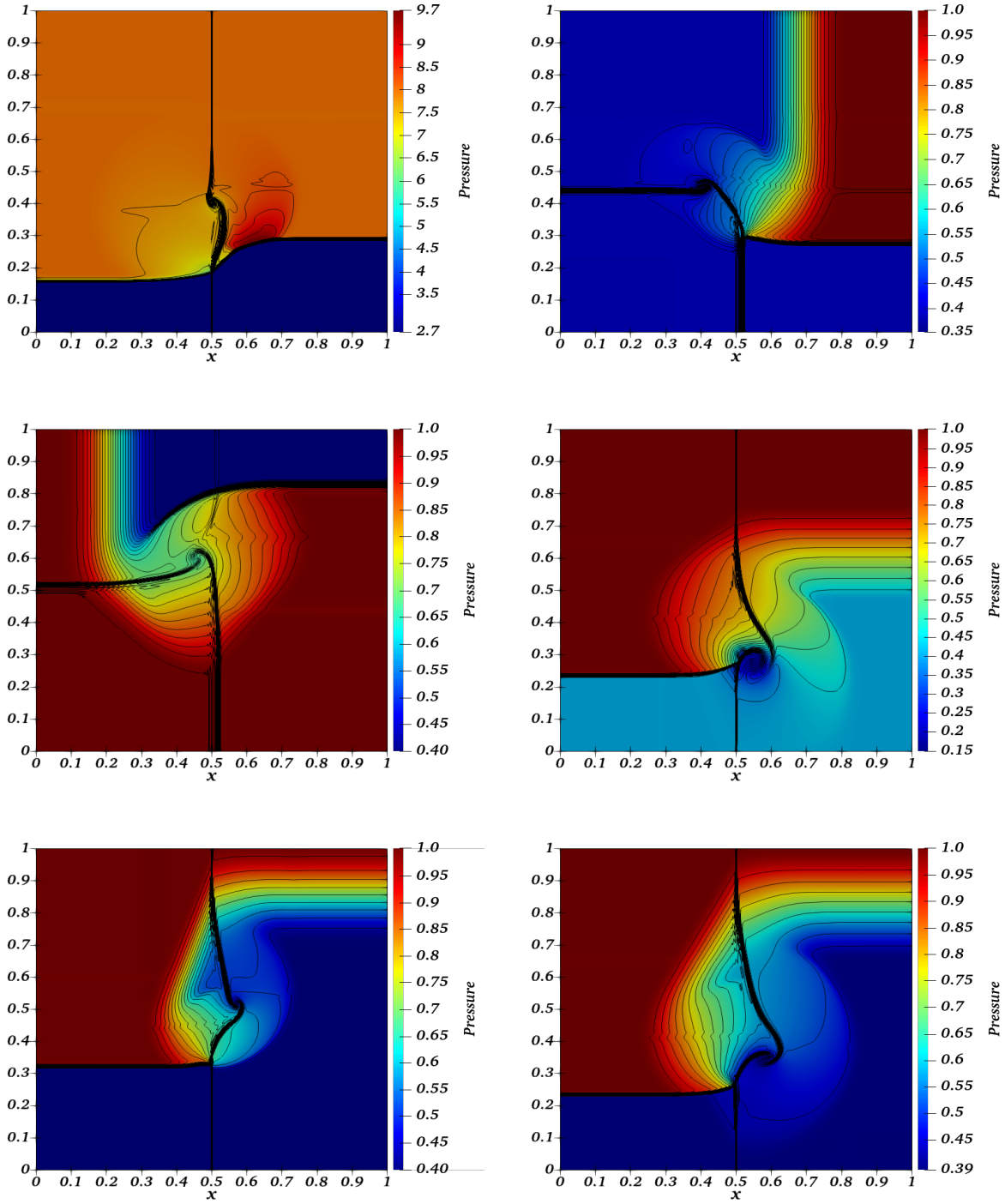

Fig 5.30. The results generated by the FVC scheme for the 2D Riemann problem are presented for configurations 14 through 19. Pressure is represented by color, while 29 contours are used to represent density. The first row corresponds to configurations 14 and 15 from left to right, the middle row corresponds to configurations 16 and 17, and the last row corresponds to configurations 18 and 19. The contour values are (from 0.47 to 2.24), (from 0.43 to 0.99), (from 0.51 to 1.02), (from 0.32 to 2.03), (from 0.49 to 2.04) and (from 0.44 to 2.00), respectively, for configurations 14 to 19.

The numerical solution is compared to the reference solutions of [148] and [149]. The density and pressure results for each configuration are presented in Fig 5.28, Fig 5.29 and Fig 5.30, where the FVC scheme's numerical solution is displayed at the final time with pressure shown in color and density shown in contours. For instance, a reference solution can be found in [148]. In Fig 5.30, Fig 5.28 and Fig 5.30, it can be observed that the computation results with the FVC scheme capture the main flow structures of all proposed configurations comparably. Therefore, the FVC scheme appears to yield good results in capturing shocks without spurious oscillations and in smooth parts of the flow without excessive numerical dissipation. Additionally, the present scheme captures sharper discontinuities.

5.2.7 2D and 3D explosion problems

In this study, we examine a cylindrical and spherical explosion problem in 2D and 3D, respectively. The computational domain is defined as $\Omega = [-1, 1]^d$, which corresponds to a square (when d = 2) and a cube (when d = 3). In the 3D case, only the half-cube with $x < 0$ is considered, and a symmetry boundary condition is imposed at $x = 0$. Meanwhile, the 2D simulation encompasses the entire square. The computational setup represents a cylindrical/spherical extension of the classic Sod problem [152], which has subsequently been utilized in [153, 154], with initial conditions provided by

$$(\rho, p, u, v, w)(0, X) = \begin{cases} (1.0,\ 1.0,\ 0.0,\ 0.0,\ 0.0) & if\ ||X|| < R, \\ (0.125,\ 0.1,\ 0.0,\ 0.0,\ 0.0) & if\ ||X|| \geqslant R, \end{cases}$$

where the initial discontinuity is characterized by a radius, denoted as $R = 0.5$. An adiabatic ideal-gas equation of state is utilized, incorporating an adiabatic index of $\gamma = 1.4$. A reference solution is derived by implementing a two-dimensional Roe scheme on a mesh with 1.235×10^6 cells. Both two-dimensional and three-dimensional FVC schemes are employed. In the 2D scenario, the computational mesh comprises 72532 triangular cells, while the 3D configuration features a coarser mesh with 1732345 tetrahedral cells. In Fig 5.31, the profiles of density and pressure along the x-axis are shown at time $t = 0.2s$ for the two-dimensional situation, in conjunction with the reference solution. Fig 5.31 also includes a graph of the troubled cells, mainly concentrated around the circular shock front. Meanwhile, the intermediate circular contact wave outcomes are boundless at $t = 0.2s$. The cause of this phenomenon is due to the contact wave undergoing constriction during the initial phase of the explosion problem, leading to smearing that enables it to be treated as a smooth characteristic utilizing the FVC method without generating spurious oscillations. Based on the cross-section in the bottom right of Fig 5.31, the shock and contact discontinuity waves are accurately resolved within one element on the primary mesh. Furthermore, the circular structure of the shock wave is well-preserved without any visible imprint of the mesh. We observed a slight oscillation at the foot of the rarefaction wave in Fig 5.31, but not at the contact discontinuity or the shock wave, which questions the hypothesis of oscillations due to the dispersion phenomenon. Additionally, we noticed that this oscillation decreases as the mesh size increases. However, we believe that this oscillation is caused by interpolation, although it has no significant influence on the results. Therefore, this finding demonstrates that the present approach is capable of maintaining cylindrical symmetry and producing robust and non-oscillatory results for shock waves.

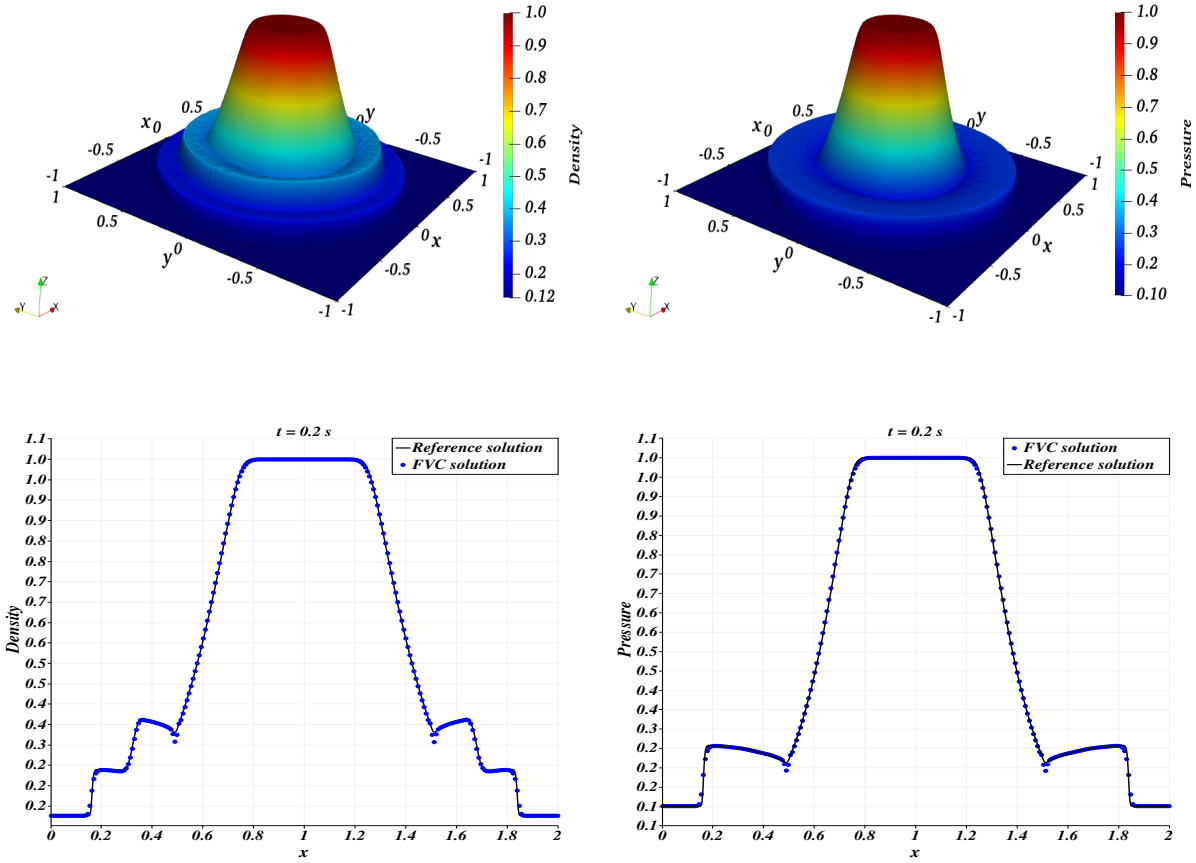

Fig 5.31. Two-dimensional cylindrical explosion problem, the FVC scheme was employed, utilizing a mesh of 72532 cells at a time $t = 0.2s$. The upper row, left side, displays a 3D visualization of the density, while the upper row, right side, depicts the pressure in a similar 3D representation. The shockwave resolution is evidently precise within a singular mesh cell. The lower row demonstrates a unidimensional cross-sectional analysis of the numerical solution for density and pressure, taken along the x-axis with coordinates $(x,\, y = 0)$.

The numerical results for the three-dimensional scenario obtained using a 3D FVC scheme are shown in Fig 5.32, and the same conclusions as in the two-dimensional case can be reached. The parallel version of the manapy[2] code was used to make 3D simulations on the Super Computing Center[3] HPC of the University Mohammed VI Polytechnic, with the aid of 56 CPU cores and a memory capacity of 182, 198 MB.

[2]https://github.com/imadki/manapy
[3]https://crc4.gitlab.io/um6p/operations/um6p-sysops/index.html

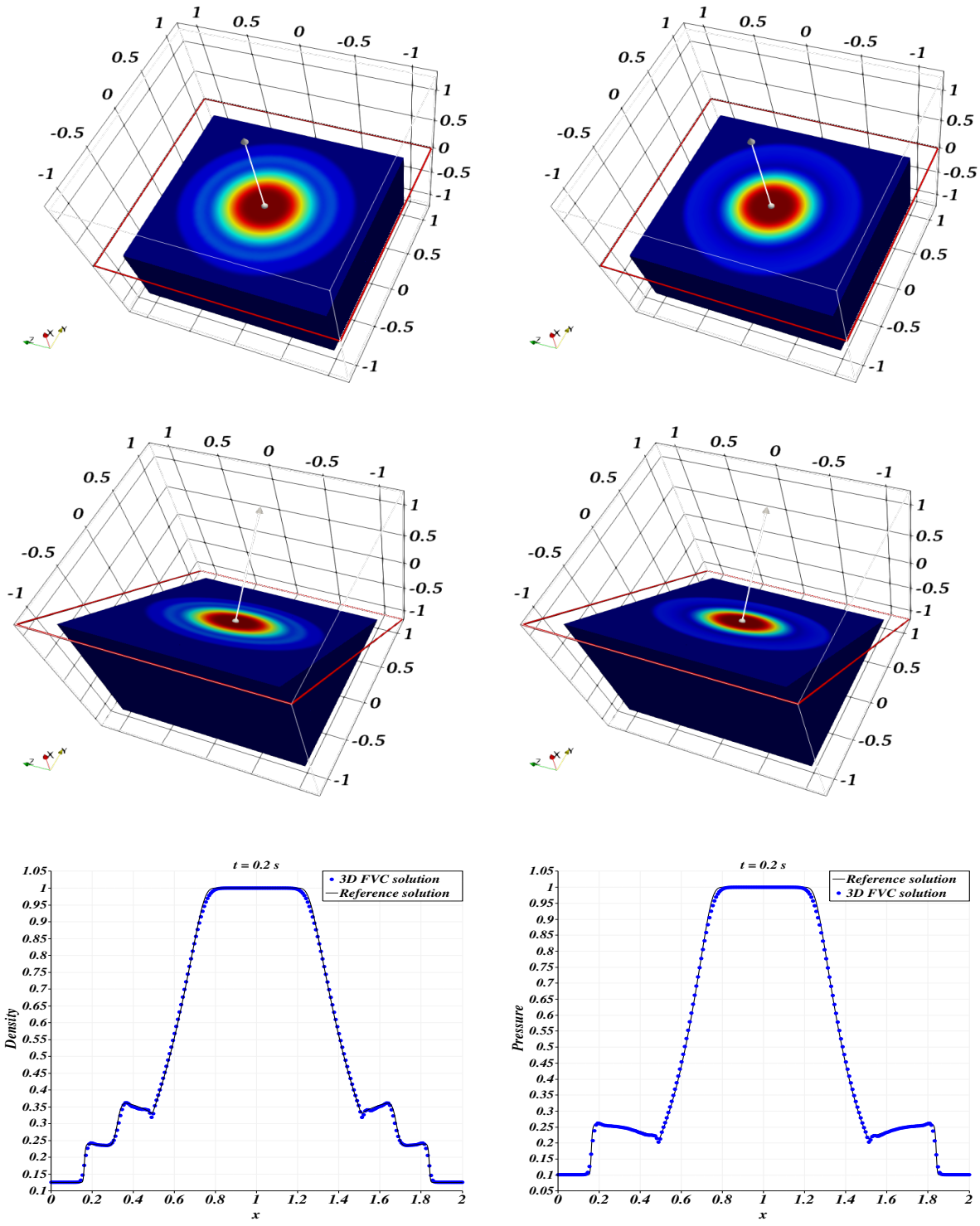

Fig 5.32. Three-dimensional spherical explosion problem at time $t = 0.2s$ using a FVC scheme on an unstructured tetrahedral mesh that consists of 1732345 cells. Top row: includes a visualization of the density and pressure after a plane cut. Bottom row: we illustrate 1D cuts along the x-axis for the density and pressure and compares them with the reference solution.

Fourth Part
Conclusions and Perspectives

Chapter 6

Conclusions and perspectives

This research highlights the effectiveness of the Finite Volume Characteristics (FVC) scheme on unstructured two-dimensional and three-dimensional meshes, particularly in simulating two types of flows: shallow water flow and gas flow. The shallow water flow is modeled using the two-dimensional shallow water equations coupled with the convection-diffusion equation, while the gas flow is modeled using the three-dimensional Euler equations. The FVC scheme demonstrates promising results in solving these complex problems, offering improved accuracy and better representation of the underlying physical phenomena.

To facilitate the solution of these equations, we have developed a computational code[2] based on the FVC scheme applied to unstructured general meshes. In the context of the shallow water model, we have proposed a well-balanced discretization technique for the FVC scheme. This ensures accurate predictions when dealing with problems involving significant source terms, particularly due to rapid variations and strong irregularities in the bottom. This scheme offers several advantages. Firstly, it can solve steady flows over irregular beds without significant numerical errors, thereby demonstrating that the proposed scheme achieves perfect numerical balance of gradient fluxes and source terms. Secondly, it can compute the numerical flux corresponding to the actual state of water flow without relying on Riemann problem solvers. Thirdly, reasonable accuracy can be easily achieved, and no special treatment is required to maintain numerical balance as it is automatically performed in the integrated numerical flux function. Lastly, the proposed approach does not require nonlinear solutions or special front-tracking techniques. Furthermore, it exhibits strong applicability to various conservative numerical schemes, as demonstrated by the numerical results. However, the use of interpolation techniques suitable for unstructured grids is necessary. While the Lagrange polynomial can be used in one-dimensional schemes or Cartesian grid-based schemes, it is not suitable for unstructured grids.

When faced with these challenges, conventional methods that employ Riemann approximation solvers, which are well-suited for purely hyperbolic equations, often encounter numerical instability issues.

Several test cases that were previously proposed in related studies were conducted to evaluate the scheme for both free surface flows and gas flows. These test cases were designed to accurately assess the specific properties of the employed scheme. The numerical results obtained from these various test cases were compared to analytical solutions or experimental data. Through these comparisons, the code demonstrated its proper functionality, accuracy, stability, and robustness. Furthermore, the effectiveness of the implemented boundary condition treatment techniques in the code was confirmed.

For the purpose of comparison, three schemes were introduced into the code: the SRNH

[2]https://github.com/imadki/manapy

scheme (Non-Homogeneous Riemann Solver), the Roe scheme, and the Rusanov scheme. These schemes have demonstrated their accuracy, stability, and robustness in the majority of test cases conducted in this study. The diffusion term is effectively handled using the diamond scheme. The results obtained from the various test cases are satisfactory, instilling confidence in the feasibility of applying the code to large-scale scenarios, such as pollutant transport in the Strait of Gibraltar. Consequently, the findings of this study affirm the reliability of the implemented algorithms and the overall methodology.

The results of this study confirm the reliability of the FVC scheme in an unstructured mesh for solving the shallow water equations, which describe flows of various types: slow, fast, and torrential, over different types of beds: flat or steep, regular or highly irregular. Furthermore, it is capable of generating three-dimensional solutions with acceptable accuracy in handling shocks and contact discontinuities, in the case of Euler equations. This study represents a comprehensive development of the FVC scheme for simulating conservation law models, addressing implementation challenges encountered during the research. The results of this study confirm the significant potential of the developed code in accurately simulating free-surface flows and gas flows described by the Euler equations. The code demonstrates physical consistency and enables the simulation of a wide range of problems and benchmarks. Furthermore, this method is adaptable to various types of meshes on different geometries. Moving forward, future improvements should focus on several key points. First and foremost, it is essential to enhance the interpolation method on arbitrary grids. Additionally, it is crucial to prove positivity for the FVC scheme in its one-dimensional version, which would ensure its validity and promote more widespread usage. Moreover, employing an implicit temporal discretization scheme would be beneficial in achieving improved numerical stability.

Another necessary enhancement pertains to locally managing the parameter α^n using limiter techniques and/or a Ducros Sensor criterion. Furthermore, it would be prudent to implement dynamic mesh refinement sequentially and then in parallel, enabling better adaptation of the mesh to various conditions and constraints.

Furthermore, it is important to incorporate the algorithm for calculating the thickness of the boundary layer into existing models. This would enhance the accuracy of simulations. Finally, it would be interesting to simulate compressible Navier-Stokes equations and subsequently model non-Newtonian fluid behavior.

Appendix

.1 The FVC scheme Algorithm

Considering the system (2.2.1) with the initial condition W_i^0 on the control volume T_i at time t_0. We project (2.2.1) according to the normal η and tangential τ of each edge. This yields the system (4.7) which we will use to construct intermediate states using the method of characteristics.

Algorithm 1 FVC scheme for Shallow Water Equations

$\mathbf{W} = (h, hu, hv)$;
Initialize conditions;
for each time iteration **do**
  Compute the time step Δt;
  Compute $X^c(t_n)$; /*Using formula (4.9)*/
  Compute $\mathbf{U}_{ij}^n$ for all interfaces; /*Using formula (4.10)*/
  Compute $\mathbf{W}_{ij}^n$ for all interfaces; /*Using formula (4.15)*/
  Compute the discretization of source term; /*Using formula (4.30)*/
  Compute the solution $\mathbf{W}^{n+1}$; /*Using formula (4.31)*/
  Update the solution: $\mathbf{W}^{n+1} \leftarrow \mathbf{W}^n$;
  Apply boundary conditions;
end for

.2 Gradient at edge with 2D diamond scheme

The gradient on each edge is approximated by introducing Green's theorem augmented by a first-order Gaussian quadrature formula, for which the values on a node of the mesh are interpolated from those on the cells containing that node. The weak consistency of this scheme has been proved by Coudière et al. [104] for an elliptic equation under certain conditions on the weights of the interpolation.

The partial derivatives on the edge γ_{ij} can be defined as an average of those on the $\mathcal{V}_{SRNL}$ co-volume, centred on the γ_{ij} interface and the two points N and S of γ_{ij}, see Fig 4.5 that is

$$\frac{\partial u_{ij}}{\partial x} := \left.\frac{\partial u}{\partial x}\right|_{\gamma_{ij}} \simeq \frac{1}{\mu\left(\mathcal{V}_{SRNL}\right)} \int_{\mathcal{V}_{SRNL}} \frac{\partial u}{\partial x} du. \tag{1}$$

Applying Green's divergence theorem to the co-volume $\mathcal{V}_{SRNL}$, we obtain the approximation

$$\left.\frac{\partial u}{\partial x}\right|_{\gamma_{ij}} \simeq \frac{1}{\mu\left(\mathcal{V}_{SRNL}\right)} \sum_{\varepsilon \in \partial \mathcal{V}_{SRNL}} u \Big|_{\varepsilon} \int_{\varepsilon} n_{x\varepsilon} d\sigma, \tag{2}$$

where ε represents an edge of the co-volume $\mathcal{V}_{SRNL}$ and $n_{x\varepsilon}$ is the axial component of the unit normal outside ε. If we note $\varepsilon = [N_1, N_2]$, we can also write

$$\left.\frac{\partial u}{\partial x}\right|_{\gamma_{ij}} \simeq \frac{1}{\mu\left(\mathcal{V}_{SRNL}\right)} \sum_{\varepsilon \in \partial \mathcal{V}_{SRNL}} \frac{1}{2}\left(u_{N_1} + u_{N_2}\right) \int_{\varepsilon} n_{x\varepsilon} d\sigma. \tag{3}$$

For a given co-volume see Fig 4.5, the gradient of quantity u is given by

$$\nabla u_{ij} = \frac{1}{2\mu\left(\mathcal{V}_{SRNL}\right)} \left\{ \begin{array}{l} (u_{_S} + u_{_R}) n_{SR} |\gamma_{SR}| + (u_{_R} + u_{_N}) n_{RN} |\gamma_{RN}| + (u_{_N} + u_{_L}) n_{NL} |\gamma_{NL}| \\ \qquad + (u_{_L} + u_{_S}) n_{LS} |\gamma_{LS}| \end{array} \right\},$$

where $u_{_N}$, $u_{_S}$, $u_{_R}$, and $u_{_L}$ represent respectively the values of the quantity u in the point N, S, R and L for more detail, see Fig 4.5. When we modify the expression inside the square braces, we obtain

$$\nabla u_{ij} = \frac{1}{2\mu\left(\mathcal{V}_{SRNL}\right)} \left\{ \begin{array}{l} (n_{_{SR}} |\gamma_{SR}| + n_{_{LS}} |\gamma_{LS}|) u_{_S} + (n_{_{RN}} |\gamma_{RN}| + n_{_{NL}} |\gamma_{NL}|) u_{_N} \\ \qquad + (n_{_{SR}} |\gamma_{SR}| + n_{_{RN}} |\gamma_{RN}|) u_{_R} + (n_{_{NL}} |\gamma_{NL}| + n_{_{LS}} |\gamma_{LS}|) u_{_L} \end{array} \right\},$$

The following equalities are obvious

$$\begin{aligned} n_{_{SR}} |\gamma_{SR}| + n_{_{LS}} |\gamma_{LS}| &= n_{_{SR}} |\gamma_{SR}|, \\ n_{_{RN}} |\gamma_{RN}| + n_{_{NL}} |\gamma_{NL}| &= -n_{_{LR}} |\gamma_{LR}|, \\ n_{_{SR}} |\gamma_{SR}| + n_{_{RN}} |\gamma_{RN}| &= n_{ij} |\gamma_{ij}|, \\ n_{_{NL}} |\gamma_{NL}| + n_{_{LS}} |\gamma_{LS}| &= -n_{ij} |\gamma_{ij}|. \end{aligned}$$

The values of u at the centers R and L are known exactly, while those at the nodes N and S must be determined by an interpolation procedure. For a node p of the mesh, we use a linear approximation of u on the set of cells containing the node p, i.e.,

$$u_p = \sum_{K \in V(p)} \omega_K(p) u_K, \tag{4}$$

where $V(p)$ is the set of triangles surrounding p, u_K is the state at the center of the triangle K and the ω_K are the weights of the interpolation. In order to ensure the weak consistency of the scheme described above, the weights ω_K of the interpolation are computed by a least squares approximation method [104]. The idea is to minimize the quadratic function

$$L_p(\xi) = \sum_{K \in V(p)} \left(u_K - \xi\left(G_K\right)\right)^2, \tag{5}$$

where w is a linear approximation of u over the set of cells containing the node p

$$\xi(x, y) = \beta_1 + \beta_2 x + \beta_3 y.$$

Some simple calculations (see, [104, subsection 3.3]) and noticing that $\xi\left(x_p, y_p\right) = u_p = \beta_1$, leads us to:

$$\omega_K(p) = \frac{1 + \lambda_x\left(x_K - x_p\right) + \lambda_y\left(y_K - y_p\right)}{n_p + \lambda_x R_x + \lambda_y R_y}, \tag{6}$$

where $n_p = \#(V(p))$

$$R_x = \sum_{K \in V(p)} (x_K - x_p), \quad R_y = \sum_{K \in V(p)} (y_K - y_p), \tag{7}$$

$$I_{xx} = \sum_{K \in V(p)} (x_K - x_p)^2, \quad I_{xy} = \sum_{K \in V(p)} (x_K - x_p)(y_K - y_p), \tag{8}$$

$$I_{yy} = \sum_{K \in V(P)} (y_K - y_P)^2, \quad D = I_{xx} I_{yy} - I_{xy}^2, \quad \lambda_x = \frac{I_{xy} R_y - I_{yy} R_x}{D}, \quad \lambda_y = \frac{I_{xy} R_x - I_{xx} R_y}{D}.$$

Hence, using these results, we can prove (4.13). □

.3 Gradient in cell for 2D formulation

For compute $\boldsymbol{\nabla} W_i$, different methods can be used to evaluate this gradient depending on the type of control volumes considered. Here, we have adopted a least squares method, which is a very efficient technique in the case of triangular or quadrangular meshes. The idea is to find the plane passing through W_i and closest to its neighbouring values W_j defined linearly from W_i. For a triangle T_i, consider the expression

$$\Delta(W_i, W_j) = W_i + (x_j - x_i) \frac{\partial W_i}{\partial x} + (y_j - y_i) \frac{\partial W_i}{\partial y} \; - \; W_j, \tag{9}$$

where (x_i, y_i) and (x_j, y_j) are respectively the coordinates of the centres of gravity G_i and G_j of T_i and T_j. The term $\Delta(W_i, W_j)$ represents the difference between the effective value of W at the center of the cell T_j and the value obtained at the center of T_j by the first order Taylor polynomial of the function W defined at the center of T_i. The gradient on the cell T_i is evaluated by minimizing the quadratic function

$$\Psi_i \left(\frac{\partial W_i}{\partial x}, \frac{\partial W_i}{\partial y} \right) = \sum_{j \in \mathbb{T}(i)} |\Delta(W_i, W_j)|^2, \tag{10}$$

where $\mathbb{T}(i)$ is the set of neighbouring triangles of T_i by vertex or by edge see Fig 1. Moreover, $\frac{\partial W_i}{\partial x}$ and $\frac{\partial W_i}{\partial y}$ are then solutions of the following linear system

$$\begin{pmatrix} I_{xx} & I_{xy} \\ I_{xy} & I_{yy} \end{pmatrix} \begin{pmatrix} \frac{\partial W_i}{\partial x} \\ \frac{\partial W_i}{\partial y} \end{pmatrix} = \begin{pmatrix} J_x \\ J_y \end{pmatrix}. \tag{11}$$

A simple compute shows that

$$\begin{aligned} \frac{\partial W_i}{\partial x} &= \frac{J_x I_{yy} - J_y I_{xy}}{D}, \\ \frac{\partial W_i}{\partial y} &= \frac{J_y I_{xx} - J_x I_{yx}}{D}, \end{aligned} \tag{12}$$

where

$$\begin{aligned} &I_{xx} = \sum_{j \in \mathbb{T}(i)} (x_j - x_i)^2, \; I_{yy} = \sum_{j \in \mathbb{T}(i)} (y_j - y_i)^2, \\ &I_{xy} = I_{yx} = \sum_{j \in \mathbb{T}(i)} (x_j - x_i)(y_j - y_i), \; D = I_{xx} I_{yy} - I_{xy}^2, \\ &J_x = \sum_{j \in \mathbb{T}(i)} (x_j - x_i)(W_j - W_i), \; J_y = \sum_{j \in \mathbb{T}(i)} (y_j - y_i)(W_j - W_i). \end{aligned} \tag{13}$$

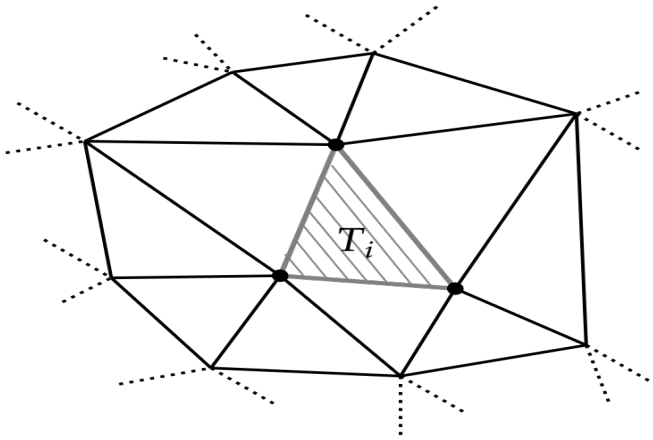

Fig 1. Neighbouring triangles of T_i by vertex or by edge.

.4 Gradient at face with 3D diamond scheme

The construction of the diamond cell $D_{\gamma_{ij}}$ in 3D is constructed by the centers of gravity L, R for cells T_i and T_j that enclose the shared face γ_{ij}. The remaining vertices of the diamond cell correspond to the vertices of the face γ_{ij}, as depicted in Fig 2. An approximation of the gradient ∇u_{ij} is given by the following formula.

$$\begin{aligned}\nabla u_{ij} = \frac{1}{3\mu\left(D_{\gamma_{ij}}\right)} \Big\{ & \left(u_{_A} + u_{_B} + u_{_R}\right) \mathfrak{n}_{ABR} \left|\gamma_{ABR}\right| + \left(u_{_B} + u_{_C} + u_{_R}\right) \mathfrak{n}_{BCR} \left|\gamma_{BCR}\right| \\ & + \left(u_{_C} + u_{_D} + u_{_R}\right) \mathfrak{n}_{CDR} \left|\gamma_{CDR}\right| + \left(u_{_D} + u_{_A} + u_{_R}\right) \mathfrak{n}_{DAR} \left|\gamma_{DAR}\right| \\ & + \left(u_{_A} + u_{_B} + u_{_L}\right) \mathfrak{n}_{BAL} \left|\gamma_{BAL}\right| + \left(u_{_B} + u_{_C} + u_{_L}\right) \mathfrak{n}_{CBL} \left|\gamma_{CBL}\right| \\ & + \left(u_{_C} + u_{_D} + u_{_L}\right) \mathfrak{n}_{DCL} \left|\gamma_{DCL}\right| + \left(u_{_D} + u_{_A} + u_{_L}\right) \mathfrak{n}_{ADL} \left|\gamma_{ADL}\right| \Big\},\end{aligned} \tag{14}$$

where $u_{_A}$, $u_{_B}$, $u_{_C}$, $u_{_D}$, $u_{_R}$ and $u_{_L}$ represent respectively the values of the quantity u in the point A, B, C, D, R and L, $\mathfrak{n}_{ABR}$ (and similarly $\mathfrak{n}_{BCR}$, etc.) represents a unit vector pointing outward from the face denoted by γ_{ABR} (or γ_{BCR}, etc.), and $|\gamma_{ABR}|$ (or $|\gamma_{BCR}|$, etc.) denotes the area of this face. If we factor out one-third from the bracketed expression and make appropriate modifications to the terms inside the bracket, the resulting expression can be obtained.

$$\begin{aligned}\nabla u_{ij} = \frac{1}{3\mu\left(D_{\gamma_{ij}}\right)} \Big\{ & \left(\mathfrak{n}_{ABR} \left|\gamma_{ABR}\right| + \mathfrak{n}_{DAR} \left|\gamma_{DAR}\right| + \mathfrak{n}_{BAL} \left|\gamma_{BAL}\right| + \mathfrak{n}_{ADL} \left|\gamma_{ADL}\right|\right) u_{_A} \\ & + \left(\mathfrak{n}_{ABR} \left|\gamma_{ABR}\right| + \mathfrak{n}_{BCR} \left|\gamma_{BCR}\right| + \mathfrak{n}_{BAL} \left|\gamma_{BAL}\right| + \mathfrak{n}_{CBL} \left|\gamma_{CBL}\right|\right) u_{_B} \\ & + \left(\mathfrak{n}_{BCR} \left|\gamma_{BCR}\right| + \mathfrak{n}_{CDR} \left|\gamma_{CDR}\right| + \mathfrak{n}_{CBL} \left|\gamma_{CBL}\right| + \mathfrak{n}_{DCL} \left|\gamma_{DCL}\right|\right) u_{_C} \\ & + \left(\mathfrak{n}_{CDR} \left|\gamma_{CDR}\right| + \mathfrak{n}_{DAR} \left|\gamma_{DAR}\right| + \mathfrak{n}_{DCL} \left|\gamma_{DCL}\right| + \mathfrak{n}_{ADL} \left|\gamma_{ADL}\right|\right) u_{_D} \\ & + \left(\mathfrak{n}_{ABR} \left|\gamma_{ABR}\right| + \mathfrak{n}_{BCR} \left|\gamma_{BCR}\right| + \mathfrak{n}_{CDR} \left|\gamma_{CDR}\right| + \mathfrak{n}_{DAR} \left|\gamma_{DAR}\right|\right) u_{_R} \\ & + \left(\mathfrak{n}_{BAL} \left|\gamma_{BAL}\right| + \mathfrak{n}_{CBL} \left|\gamma_{CBL}\right| + \mathfrak{n}_{DCL} \left|\gamma_{DCL}\right| + \mathfrak{n}_{ADL} \left|\gamma_{ADL}\right|\right) u_{_L} \Big\}.\end{aligned} \tag{15}$$

APPENDIX

The vector equilibrium implies

$$\begin{aligned}
&\mathfrak{n}_{ABR}\,|\gamma_{ABR}| + \mathfrak{n}_{DAR}\,|\gamma_{DAR}| + \mathfrak{n}_{BAL}\,|\gamma_{BAL}| + \mathfrak{n}_{ADL}\,|\sigma_{ADL}| = \mathfrak{n}_{BRDL}\,|\gamma_{BRDL}|\,,\\
&\mathfrak{n}_{ABR}\,|\gamma_{ABR}| + \mathfrak{n}_{BCR}\,|\gamma_{BCR}| + \mathfrak{n}_{BAL}\,|\gamma_{BAL}| + \mathfrak{n}_{CBL}\,|\sigma_{CBL}| = \mathfrak{n}_{ALCR}\,|\gamma_{ALCR}|\,,\\
&\mathfrak{n}_{BCR}\,|\gamma_{BCR}| + \mathfrak{n}_{CDR}\,|\gamma_{CDR}| + \mathfrak{n}_{CBL}\,|\gamma_{CBL}| + \mathfrak{n}_{DCL}\,|\gamma_{DCL}| = -\mathfrak{n}_{RBDL}\,|\gamma_{RBDL}|\,,\\
&\mathfrak{n}_{CDR}\,|\gamma_{CDR}| + \mathfrak{n}_{DAR}\,|\gamma_{DAR}| + \mathfrak{n}_{DCL}\,|\gamma_{DCL}| + \mathfrak{n}_{ADL}\,|\gamma_{ADL}| = -\mathfrak{n}_{ALCR}\,|\gamma_{ALCR}|\,,\\
&\mathfrak{n}_{ABR}\,|\gamma_{ABR}| + \mathfrak{n}_{BCR}\,|\gamma_{BCR}| + \mathfrak{n}_{CDR}\,|\gamma_{CDR}| + \mathfrak{n}_{DAR}\,|\gamma_{DAR}| = \mathfrak{n}_{ij}\,|\gamma_{ij}|\,,\\
&\mathfrak{n}_{BAL}\,|\gamma_{BAL}| + \mathfrak{n}_{CBL}\,|\gamma_{CBL}| + \mathfrak{n}_{DCL}\,|\gamma_{DCL}| + \mathfrak{n}_{ADL}\,|\gamma_{ADL}| = -\mathfrak{n}_{ij}\,|\gamma_{ij}|\,.
\end{aligned} \tag{16}$$

When we use the vector equilibrium, we can write for the gradient ∇u_{ij}

$$\begin{aligned}
\nabla u_{ij} = \frac{1}{3\mu\left(D_{\gamma_{ij}}\right)}\Big\{\ &(u_{_A} - u_{_C})\,\mathfrak{n}_{BRDL}\,|\gamma_{BRDL}| + \\
&+ (u_{_B} - u_{_D})\,\mathfrak{n}_{ALCR}\,|\gamma_{ALCR}| + (u_{_R} - u_{_L})\,\mathfrak{n}_{ij}\,|\gamma_{ij}|\ \Big\}.
\end{aligned} \tag{17}$$

The values $u_{_A}$, $u_{_B}$, $u_{_C}$ and $u_{_D}$ are computed by the least square method

$$\begin{aligned}
u_{_A} &= \sum_{p=1}^{N(A)} w_k(p) u_{_p}, \quad u_{_B} = \sum_{p=1}^{N(B)} w_k(p) u_{_p},\\
u_{_C} &= \sum_{p=1}^{N(C)} w_k(p) u_{_p}, \quad u_{_D} = \sum_{p=1}^{N(D)} w_k(p) u_{_p}.
\end{aligned} \tag{18}$$

The weights $w_k(p)$ is given by

$$w_k(p) = \frac{1 + \lambda_x\,(x_p - x_A) + \lambda_y\,(y_p - y_A) + \lambda_z\,(z_p - z_A)}{\Delta}, \tag{19}$$

where

$$\begin{aligned}
&I_{xx} = \sum_{p=1}^{N(A)} (x_p - x_A)^2\,, \quad I_{xy} = \sum_{p=1}^{N(A)} (x_p - x_A)\,(y_p - y_A)\,, \quad R_x = \sum_{p=1}^{N(A)} (x_p - x_A)\,,\\
&I_{yy} = \sum_{p=1}^{N(A)} (y_p - y_A)^2\,, \quad I_{xz} = \sum_{p=1}^{N(A)} (x_p - x_A)\,(z_p - z_A)\,, \quad R_y = \sum_{p=1}^{N(A)} (y_p - y_A)\,,\\
&I_{zz} = \sum_{p=1}^{N(A)} (z_p - z_A)^2\,, \quad I_{yz} = \sum_{p=1}^{N(A)} (y_p - y_A)\,(z_j - z_v)\,, \quad R_z = \sum_{p=1}^{N(A)} (z_p - z_A)\,,
\end{aligned} \tag{20}$$

and

$$\Delta = I_{xx} I_{yy} I_{zz} + 2 I_{xy} I_{xz} I_{yz} - I_{xx} I_{yz}^2 - I_{yy} I_{xz}^2 - I_{zz} I_{xy}^2,$$

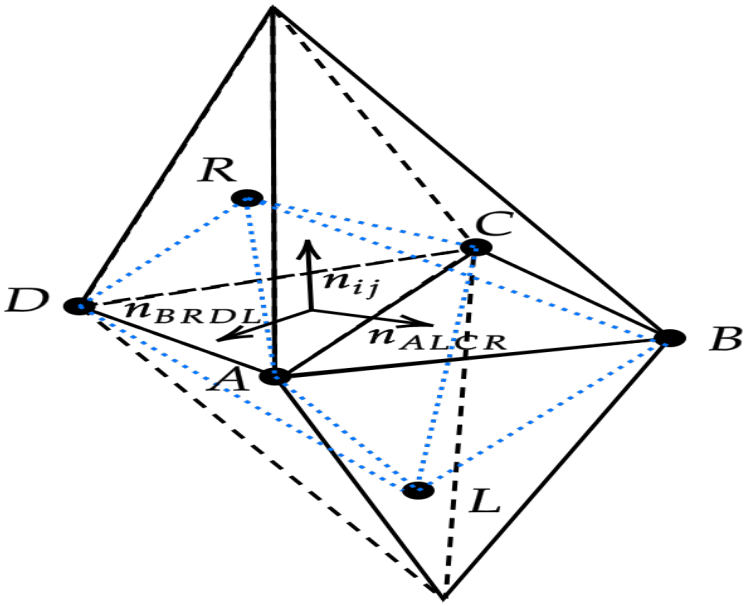

Fig 2. Diamond cell for 3D formulation.

and

$$\lambda_x = \frac{\left(I_{yz}^2 - I_{yy}I_{zz}\right) R_x + \left(I_{xy}I_{zz} - I_{xz}I_{yz}\right) R_y + \left(I_{xz}I_{yy} - I_{xy}I_{yz}\right) R_z}{\Delta},$$

$$\lambda_y = \frac{\left(I_{xy}I_{zz} - I_{xz}I_{yz}\right) R_x + \left(I_{xz}^2 - I_{xx}I_{zz}\right) R_y + \left(I_{yz}I_{xx} - I_{xz}I_{xy}\right) R_z}{\Delta}, \tag{21}$$

$$\lambda_z = \frac{\left(I_{xz}I_{yy} - I_{xy}I_{yz}\right) R_x + \left(I_{yz}I_{xx} - I_{xz}I_{xy}\right) R_y + \left(I_{xy}^2 - I_{xx}I_{yy}\right) R_z}{\Delta}.$$

.5 Roe scheme for 3D Euler equations

This scheme was first proposed by Roe [69]. It is a scheme based on solving local Riemann problems at each cell interface, except that the Riemann problem is linearized around an averaged state, which is called the Roe averages. The Roe numerical flux is given by

$$\Phi^{Roe}\left(\mathbf{W}_i, \mathbf{W}_j\right) = \frac{1}{2}\left(F\left(\mathbf{W}_i\right) + F\left(\mathbf{W}_j\right) - \left|\tilde{A}\left(\mathbf{W}_i, \mathbf{W}_j\right)\right| \cdot \left(\mathbf{W}_j - \mathbf{W}_i\right)\right), \tag{22}$$

where $\tilde{A}\left(\mathbf{W}_i, \mathbf{W}_j\right)$ is the Roe matrix associated with the problem. In the case of the Euler equations (2.58), this matrix is given by

$$\tilde{A} = \mathbf{P}\mathbf{\Lambda}\mathbf{P}^{-1}, \tag{23}$$

where

$$\mathbf{\Lambda} = \begin{pmatrix} \tilde{u}_\eta - \tilde{c} & 0 & 0 & 0 & 0 \\ 0 & \tilde{u}_\eta & 0 & 0 & 0 \\ 0 & 0 & \tilde{u}_\eta + \tilde{c} & 0 & 0 \\ 0 & 0 & 0 & \tilde{u}_\eta & 0 \\ 0 & 0 & 0 & 0 & \tilde{u}_\eta \end{pmatrix}, \quad \mathbf{P_n} = \begin{pmatrix} 1 & 1 & 1 & 0 & 0 \\ \tilde{u} - \tilde{c}n_x & u & \tilde{u} + \tilde{c}n_x & b_x & \tau_x \\ \tilde{v} - \tilde{c}n_y & \tilde{v} & \tilde{v} + \tilde{c}n_y & b_y & \tau_y \\ \tilde{w} - \tilde{c}n_z & w & \tilde{w} + \tilde{c}n_z & b_z & \tau_z \\ \tilde{H} - \tilde{u}_\eta\tilde{c} & |\tilde{\mathbf{u}}|^2/2 & \tilde{H} + \tilde{u}_\eta\tilde{c} & \tilde{u}_b & \tilde{u}_\tau \end{pmatrix},$$

and the Roe averages are expressed as

$$\begin{aligned}
\tilde{\rho} &= \sqrt{\rho_i \rho_j}, \\
\tilde{u} &= \frac{\sqrt{\rho_i} u_i + \sqrt{\rho_j} u_j}{\sqrt{\rho_i} + \sqrt{\rho_j}}, \\
\tilde{v} &= \frac{\sqrt{\rho_L} v_i + \sqrt{\rho_j} v_j}{\sqrt{\rho_i} + \sqrt{\rho_j}}, \\
\tilde{w} &= \frac{\sqrt{\rho_L} w_i + \sqrt{\rho_j} w_j}{\sqrt{\rho_i} + \sqrt{\rho_j}}, \\
\tilde{H} &= \frac{\sqrt{\rho_L} H_i + \sqrt{\rho_i} H_j}{\sqrt{\rho_i} + \sqrt{\rho_j}}, \\
\tilde{c} &= \left((\gamma - 1) \left(\tilde{H} - \frac{1}{2} |\tilde{\mathbf{u}}|^2 \right) \right)^{\frac{1}{2}}.
\end{aligned}$$

We recall that

$$\begin{aligned}
E &= \frac{1}{\gamma} H + \frac{\gamma - 1}{2\gamma} |\mathbf{u}|^2, \\
u_\eta &= u n_x + v n_y + w n_z, \\
u_b &= u b_x + v b_y + w b_z,
\end{aligned}$$

and

$$u_\tau = u \tau_x + v \tau_y + w \tau_z.$$

cf. Fig 5.2.

.6 SRNH scheme for shallow water equations

For a simplified presentation of the SRNH scheme [73, 7], we write the projected system of (2.22) in vector form

$$\frac{\partial U}{\partial t} + \frac{\partial F_\eta(U)}{\partial \eta} = S_\eta(U) \tag{24}$$

The predictor stage of the SRNH scheme involves using the projected system to compute the mean states U_{ij}^n on each edge. It is formulated using a staggered approach as follows

$$U_{ij}^n = \frac{1}{2} \left(U_i^n + U_j^n \right) - \frac{1}{2} \operatorname{sgn} \left[\nabla F_\eta(\bar{U}) \right] \left(U_j^n - U_i^n \right) + \frac{1}{2} \left| \nabla F_\eta(\bar{U})^{-1} \right| S_{\eta ij}^n, \tag{25}$$

where

$$U = \begin{pmatrix} h \\ h u_\eta \\ h u_\tau \end{pmatrix}, \quad F_\eta(U) = \begin{pmatrix} h u_\eta \\ h u_\eta^2 + \frac{1}{2} g h^2 \\ h u_\eta u_\tau \end{pmatrix}, \quad S_{\eta ij}^n = -g \frac{h_i + h_j}{2} \left(Z_j - Z_i \right) \begin{pmatrix} 0 \\ 1 \\ 0 \end{pmatrix}. \tag{26}$$

In (25), $\bar{U}$ represents the Roe average, is given by

$$\bar{U} = \frac{1}{2} \left(h_i + h_j \right) \begin{pmatrix} 1 \\ \frac{u_i \sqrt{h_i} + u_j \sqrt{h_j}}{\sqrt{h_i} + \sqrt{h_j}} n_x + \frac{v_i \sqrt{h_i} + v_j \sqrt{h_j}}{\sqrt{h_i} + \sqrt{h_j}} n_y \\ - \frac{u_i \sqrt{h_i} + u_j \sqrt{h_j}}{\sqrt{h_i} + \sqrt{h_j}} n_y + \frac{v_i \sqrt{h_i} + v_j \sqrt{h_j}}{\sqrt{h_i} + \sqrt{h_j}} n_x \end{pmatrix}. \tag{27}$$

The sign and inverse matrices of the Jacobian of system (24) are defined by

$$\operatorname{sgn}\left[\nabla F_\eta(\bar{U})\right] = \mathcal{R}(\bar{U})\operatorname{sgn}[\Lambda(\bar{U})]\mathcal{R}^{-1}(\bar{U}) \text{ and } \quad \left|\nabla F_\eta(\bar{U})^{-1}\right| = \mathcal{R}(\bar{U})\left|\Lambda(\bar{U})^{-1}\right|\mathcal{R}^{-1}(\bar{U}) \quad (28)$$

where $\Lambda(\bar{U})$ and $\mathcal{R}(\bar{U})$ are, respectively, the matrix of eigenvalues and the matrix of eigenvectors. An explicit calculation of these matrices yields

$$\Lambda = \begin{pmatrix} \bar{u}_\eta - \bar{c} & 0 & 0 \\ 0 & \bar{u}_\eta & 0 \\ 0 & 0 & \bar{u}_\eta + \bar{c} \end{pmatrix},\ \mathcal{R} = \begin{pmatrix} 1 & 0 & 1 \\ \bar{u}_\eta - \bar{c} & 0 & \bar{u}_\eta + \bar{c} \\ \bar{u}_\tau & 1 & \bar{u}_\tau \end{pmatrix} \text{ and } \mathcal{R}^{-1} = \begin{pmatrix} \frac{\bar{u}_\eta + \bar{c}}{2\bar{c}} & -\frac{1}{2\bar{c}} & 0 \\ -\bar{u}_\tau & 0 & 1 \\ -\frac{\bar{u}_\eta - \bar{c}}{2\bar{c}} & \frac{1}{2\bar{c}} & 0 \end{pmatrix}.$$

Here, $\bar{c} = \sqrt{g\bar{h}}$ is the velocity calculated at the interface γ_{ij} of the control volume. It is also easy to verify that the sign matrix in (25) is given as follows

$$\operatorname{sgn}\left[\nabla F_\eta(\bar{U})\right] = \begin{pmatrix} \frac{\operatorname{sgn}(\bar{\lambda}_1)\bar{\lambda}_3 - \operatorname{sgn}(\bar{\lambda}_3)\bar{\lambda}_1}{2\bar{c}} & \frac{\operatorname{sgn}(\bar{\lambda}_3) - \operatorname{sgn}(\bar{\lambda}_1)}{2\bar{c}} & 0 \\ \frac{|\bar{\lambda}_1|\bar{\lambda}_3 - |\bar{\lambda}_3|\bar{\lambda}_1}{2\bar{c}} & \frac{|\bar{\lambda}_3| - |\bar{\lambda}_1|}{2\bar{c}} & 0 \\ \bar{u}_\tau\left(\frac{\operatorname{sgn}(\bar{\lambda}_1)\bar{\lambda}_3 - \operatorname{sgn}(\bar{\lambda}_3)\bar{\lambda}_1}{2\bar{c}} - \operatorname{sgn}(\bar{u}_\eta)\right) & \bar{u}_\tau\frac{\operatorname{sgn}(\bar{\lambda}_3) - \operatorname{sgn}(\bar{\lambda}_1)}{2\bar{c}} & \operatorname{sgn}(\bar{\lambda}_2) \end{pmatrix}, \quad (29)$$

where $\bar{\lambda}_1 = \bar{u}_\eta - \bar{c}, \bar{\lambda}_2 = \bar{u}_\eta$ and $\bar{\lambda}_3 = \bar{u}_\eta + \bar{c}$. Using the matrices above, the projected state U_{ij}^n on each edge γ_{ij} can be easily obtained from the predictor step (25). The conservative state W_{ij}^n is then evaluated using the transformations $u = u_\eta n_x - u_\tau n_y$ and $v = u_\eta n_y + u_\tau n_x$.

Finally, applied to the system (2.22), the SRNH scheme consists of a predictor step and a corrector step, and can be formulated as follows.

$$\begin{cases} U_{ij}^n = \frac{1}{2}\left(U_i^n + U_j^n\right) - \frac{1}{2}\operatorname{sgn}\left[\nabla F_\eta(\bar{U})\right]\left(U_j^n - U_i^n\right) + \frac{1}{2}\left|\nabla F_\eta(\bar{U})^{-1}\right| S_{\eta ij}^n, \\ W_i^{n+1} = W_i^n - \frac{\Delta t}{|T_i|}\sum_{j\in N(i)}\mathbb{F}\left(W_{ij}^n; n_{ij}\right)|\gamma_{ij}| + \Delta t S_i^n. \end{cases} \quad (30)$$

.7 Exact solution of ideal dam break problem

For each time $t \geqslant 0$, the analytical solution of ideal dam break without friction is given by

$$h(t,x) = \begin{cases} h_l \\ \frac{1}{9g}\left(2\sqrt{gh_l} - \frac{x - x_m}{t}\right) \\ h_m \\ h_r \end{cases}, \ u(t,x) = \begin{cases} 0 & if \quad x \leqslant x_m - t\sqrt{gh_l}, \\ \frac{2}{3}\left(\sqrt{gh_l} + \frac{x - x_m}{t}\right) & if \quad x_m - t\sqrt{gh_l} \leqslant x < t(u_m - c_m), \\ u_m & if \quad t(u_m - c_m) \leqslant x < x_m + tv_c, \\ 0 & if \quad x \geqslant x_m + tv_c. \end{cases}$$

where $v_c = \dfrac{2c_m^2(\sqrt{gh_l} - c_m)}{c_m^2 - gh_r}$ is the speed of the shock and $c_m = \sqrt{gh_m}$ the solution of

$8c_m^2c_l^2(c_l - c_m)^2 - (c_m^2 - c_r^2)(c_m^2 + c_r^2) = 0.$

.8 Elevation of the bed is employed in specific cases as described in Chapter 4.

x	0	50	100	150	250	300	350
$Z(x)$	0	0	2.5	5	5	3	5
x	400	425	435	450	475	500	505
$Z(x)$	5	7.5	8	9	9	9.1	9
x	530	550	565	575	600	650	700
$Z(x)$	9	6	5.5	5.5	5	4	3
x	750	800	820	900	950	1000	1500
$Z(x)$	3	2.3	2	1.2	0.4	0	0

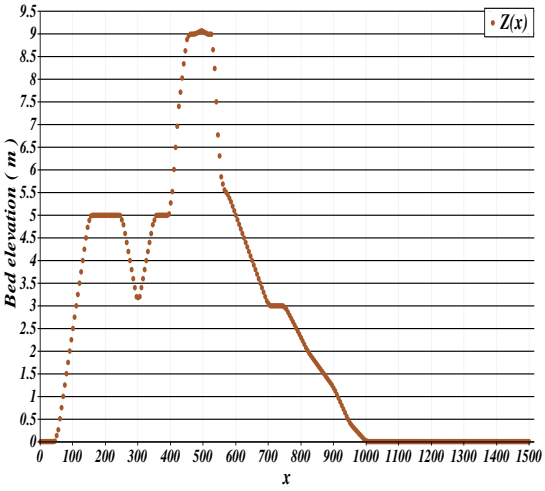

List of Figures

List of Tables

Fifth Part
Bibliographical References

Bibliography

[1] R. Boukharfane, *Contribution à la simulation numérique d'écoulements turbulents compressibles canoniques*. PhD thesis, ISAE-ENSMA Ecole Nationale Supérieure de Mécanique et d'Aérotechique-Poitiers, 2018.

[2] J. Dubois, *Modélisation, approximation numérique et couplage du transfert radiatif avec l'hydrodynamique*. PhD thesis, Bordeaux 1, 2009.

[3] G. Faccanoni, *Étude d'un modèle fin de changement de phase liquide-vapeur. Contribution à l'étude de la crise d'ébullition.* PhD thesis, Ecole Polytechnique X, 2008.

[4] C. Sanchez-Linares, M. de la Asunción, M. J. Castro, S. Mishra, and J. Šukys, "Multi-level monte carlo finite volume method for shallow water equations with uncertain parameters applied to landslides-generated tsunamis," *Applied Mathematical Modelling*, vol. 39, no. 23-24, pp. 7211–7226, 2015.

[5] S. Avgerinos, M. Castro, E. Macca, and G. Russo, "A semi-implicit finite volume method for the exner model of sediment transport," *arXiv preprint arXiv:2303.03801*, 2023.

[6] M. Castro, J. González-Vida, J. Macias, and C. Parés, "Realistic applications of a tidal 2d two-layer shallow water model to the strait of gibraltar," in *AIP Conference Proceedings*, vol. 1168, pp. 1429–1432, American Institute of Physics, 2009.

[7] F. Benkhaldoun, I. Elmahi, M. Seaıd, *et al.*, "Well-balanced finite volume schemes for pollutant transport by shallow water equations on unstructured meshes," *Journal of Computational Physics*, vol. 226, no. 1, pp. 180–203, 2007.

[8] F. Benkhaldoun and M. Seaïd, "Combined characteristics and finite volume methods for sediment transport and bed morphology in surface water flows," *Mathematics and Computers in Simulation*, vol. 81, no. 10, pp. 2073–2086, 2011.

[9] F. Benkhaldoun, I. Elmahi, and M. Seaïd, "Application of mesh-adaptation for pollutant transport by water flow," *Mathematics and Computers in Simulation*, vol. 79, no. 12, pp. 3415–3423, 2009.

[10] F. Benkhaldoun, I. Elmahi, and M. Seaïd, "A new finite volume method for flux-gradient and source-term balancing in shallow water equations," *Computer Methods in Applied Mechanics and Engineering*, vol. 199, no. 49-52, pp. 3324–3335, 2010.

[11] A. Bermudez and M. E. Vazquez, "Upwind methods for hyperbolic conservation laws with source terms," *Computers & Fluids*, vol. 23, no. 8, pp. 1049–1071, 1994.

[12] Y. Cheng, A. Chertock, M. Herty, A. Kurganov, and T. Wu, "A new approach for designing moving-water equilibria preserving schemes for the shallow water equations," *Journal of Scientific Computing*, vol. 80, no. 1, pp. 538–554, 2019.

[13] D. H. Cuong and M. D. Thanh, "A well-balanced van leer-type numerical scheme for shallow water equations with variable topography," *Advances in Computational Mathematics*, vol. 43, no. 5, pp. 1197–1225, 2017.

[14] I. Kissami, M. Seaid, and F. Benkhaldoun, "Numerical assessment of criteria for mesh adaptation in the finite volume solution of shallow water equations," *Advances in Applied Mathematics and Mechanics*, vol. 12, pp. 503–526, 2020.

[15] J. Li, G. Li, S. Qian, and J. Gao, "High-order well-balanced finite volume weno schemes with conservative variables decomposition for shallow water equations," *Advances in Applied Mathematics and Mechanics*, vol. 13, no. 4, pp. 827–849, 2021.

[16] M. E. Vázquez-Cendón, "Improved treatment of source terms in upwind schemes for the shallow water equations in channels with irregular geometry," *Journal of Computational Physics*, vol. 148, no. 2, pp. 497–526, 1999.

[17] C. Berthon, M. M'Baye, M. H. Le, and D. Seck, "A well-defined moving steady states capturing godunov-type scheme for shallow-water model," *International Journal on Finite Volumes*, vol. 15, 2020.

[18] M. J. Castro, T. M. de Luna, and C. Parés, "Well-balanced schemes and path-conservative numerical methods," in *Handbook of numerical analysis*, vol. 18, pp. 131–175, Elsevier, 2017.

[19] S. Bulteau, M. Badsi, C. Berthon, and M. Bessemoulin-Chatard, "A fully well-balanced and asymptotic preserving scheme for the shallow-water equations with a generalized manning friction source term," *Calcolo*, vol. 58, no. 4, p. 41, 2021.

[20] A. Chertock, M. Dudzinski, A. Kurganov, and M. Lukáčová-Medvid'ová, "Well-balanced schemes for the shallow water equations with coriolis forces," *Numerische Mathematik*, vol. 138, no. 4, pp. 939–973, 2018.

[21] V. Michel-Dansac, C. Berthon, S. Clain, and F. Foucher, "A well-balanced scheme for the shallow-water equations with topography or manning friction," *Journal of Computational Physics*, vol. 335, pp. 115–154, 2017.

[22] F. Bouchut, *Nonlinear stability of finite Volume Methods for hyperbolic conservation laws: And Well-Balanced schemes for sources*. Springer Science & Business Media, 2004.

[23] L. Gosse, *Computing qualitatively correct approximations of balance laws*, vol. 2. Springer, 2013.

[24] R. Abgrall and C.-W. Shu, *Handbook of numerical methods for hyperbolic problems: applied and modern issues*, vol. 18. Elsevier, 2017.

[25] R. Manning, "On the£ ow of water in open channels and pipes. inst," *Civil Eng. Ireland*, vol. 20, pp. 161–207, 1891.

[26] D. Olbers, J. Willebrand, and C. Eden, *Ocean dynamics*. Springer Science & Business Media, 2012.

[27] J. Zhu and J. Qiu, "A new type of finite volume weno schemes for hyperbolic conservation laws," *Journal of Scientific Computing*, vol. 73, no. 2, pp. 1338–1359, 2017.

[28] B. Perthame and C. Simeoni, "A kinetic scheme for the saint-venant system with a source term," *Calcolo*, vol. 38, no. 4, pp. 201–231, 2001.

[29] F. Benkhaldoun, S. Sari, and M. Seaïd, "A family of finite volume eulerian–lagrangian methods for two-dimensional conservation laws," *Journal of Computational and Applied Mathematics*, vol. 285, pp. 181–202, 2015.

[30] F. Benkhaldoun, S. Sari, and M. Seaid, "Projection finite volume method for shallow water flows," *Mathematics and Computers in Simulation*, vol. 118, pp. 87–101, 2015.

[31] F. Benkhaldoun and M. Seaïd, "A simple finite volume method for the shallow water equations," *Journal of Computational and Applied Mathematics*, vol. 234, no. 1, pp. 58–72, 2010.

[32] E. Audusse, F. Benkhaldoun, S. Sari, M. Seaid, and P. Tassi, "A fast finite volume solver for multi-layered shallow water flows with mass exchange," *Journal of Computational Physics*, vol. 272, pp. 23–45, 2014.

[33] E. Godlewski and P.-A. Raviart, *Numerical approximation of hyperbolic systems of conservation laws*, vol. 118. Springer Science & Business Media, 2013.

[34] R. J. LeVeque and R. J. Leveque, *Numerical methods for conservation laws*, vol. 214. Springer, 1992.

[35] B. Després, *Numerical methods for Eulerian and Lagrangian conservation laws*. Birkhäuser, 2017.

[36] B. Després and F. Dubois, *Systèmes hyperboliques de lois de conservation: Application à la dynamique des gaz*. Editions Ecole Polytechnique, 2005.

[37] R. J. DiPerna, "Convergence of approximate solutions to conservation laws," in *Transonic, Shock, and Multidimensional Flows*, pp. 313–328, Elsevier, 1982.

[38] S. Krushkov, "First order quasilinear equations with several space variables," *Math. USSR. Sb*, vol. 10, pp. 217–243, 1970.

[39] A. d. Saint-Venant, "Theorie du mouvement non permanent des eaux, avec application aux crues des rivieres et a l'introduction de marees dans leurs lits," *Comptes rendus des seances de l'Academie des Sciences*, vol. 36, pp. 174–154, 1871.

[40] Y.-E. Shi, *Résolution numérique des équations de Saint-Venant par la technique de projection en utilisant une méthode des volumes finis dans un maillage non structuré*. PhD thesis, Université de Caen, 2006.

[41] J.-F. Gerbeau and B. Perthame, "Derivation of viscous saint-venant system for laminar shallow water; numerical validation," 2000.

[42] O. Delestre, *Simulation du ruissellement d'eau de pluie sur des surfaces agricoles*. PhD thesis, Université d'Orléans; Université d'Orléans, 2010.

[43] J.-M. Hervouet, *Hydrodynamics of free surface flows: modelling with the finite element method*, vol. 360. Wiley Online Library, 2007.

[44] E. F. Toro, *Shock-capturing methods for free-surface shallow flows*. Wiley-Blackwell, 2001.

[45] G. J. Gassner, A. R. Winters, and D. A. Kopriva, "A well balanced and entropy conservative discontinuous galerkin spectral element method for the shallow water equations," *Applied Mathematics and Computation*, vol. 272, pp. 291–308, 2016.

[46] P.-L. Lions, B. Perthame, and P. E. Souganidis, "Existence and stability of entropy solutions for the hyperbolic systems of isentropic gas dynamics in eulerian and lagrangian coordinates," *Communications on Pure and Applied Mathematics*, vol. 49, no. 6, pp. 599–638, 1996.

[47] U. S. Fjordholm, S. Mishra, and E. Tadmor, "Well-balanced and energy stable schemes for the shallow water equations with discontinuous topography," *Journal of Computational Physics*, vol. 230, no. 14, pp. 5587–5609, 2011.

[48] S. Rekolainen, J. Kämäri, M. Hiltunen, and T. M. Saloranta, "A conceptual framework for identifying the need and role of models in the implementation of the water framework directive," *International Journal of River Basin Management*, vol. 1, no. 4, pp. 347–352, 2003.

[49] I. Guymer, C. Wilson, and J. Boxall, "Modelling solute transport processes in free surface flow cfd schemes," *Computational Fluid Dynamics: Applications in Environmental Hydraulics*, pp. 51–69, 2005.

[50] D. Vanzo, A. Siviglia, and E. F. Toro, "Pollutant transport by shallow water equations on unstructured meshes: Hyperbolization of the model and numerical solution via a novel flux splitting scheme," *Journal of Computational Physics*, vol. 321, pp. 1–20, 2016.

[51] V. Caleffi and A. Valiani, "A 2d local discontinuous galerkin method for contaminant transport in channel bends," *Computers & Fluids*, vol. 88, pp. 629–642, 2013.

[52] A. Siviglia and E. F. Toro, "Waf method and splitting procedure for simulating hydro-and thermal-peaking waves in open-channel flows," *Journal of Hydraulic Engineering*, vol. 135, no. 8, pp. 651–662, 2009.

[53] D. Liang, X. Wang, R. A. Falconer, and B. N. Bockelmann-Evans, "Solving the depth-integrated solute transport equation with a tvd-maccormack scheme," *Environmental Modelling & Software*, vol. 25, no. 12, pp. 1619–1629, 2010.

[54] A. Rambaud, "A dynamic multilayer shallow water model," 2012.

[55] E. Audusse, M.-O. Bristeau, B. Perthame, and J. Sainte-Marie, "A multilayer saint-venant system with mass exchanges for shallow water flows. derivation and numerical validation," *ESAIM: Mathematical Modelling and Numerical Analysis*, vol. 45, no. 1, pp. 169–200, 2011.

[56] E. Audusse, "A multilayer saint-venant model: derivation and numerical validation," *Discrete and Continuous Dynamical Systems-B*, vol. 5, no. 2, pp. 189–214, 2005.

[57] F. Bouchut and T. M. De Luna, "A subsonic-well-balanced reconstruction scheme for shallow water flows," *SIAM Journal on Numerical Analysis*, vol. 48, no. 5, pp. 1733–1758, 2010.

[58] M. J. Castro, J. A. Garcıa-Rodrıguez, J. M. González-Vida, J. Macıas, C. Parés, and M. E. Vázquez-Cendón, "Numerical simulation of two-layer shallow water flows through channels with irregular geometry," *Journal of Computational Physics*, vol. 195, no. 1, pp. 202–235, 2004.

[59] S. Sari, T. Rowan, M. Seaid, and F. Benkhaldoun, "Simulation of three-dimensional free-surface flows using two-dimensional multilayer shallow water equations," *Communications in Computational Physics*, vol. 27, no. 5, pp. 1413–1442, 2020.

[60] E. D. Fernández-Nieto, E. H. Koné, and T. Chacón Rebollo, "A multilayer method for the hydrostatic navier-stokes equations: a particular weak solution," *Journal of Scientific Computing*, vol. 60, pp. 408–437, 2014.

[61] N. J. Shankar, H. F. Cheong, and S. Sankaranarayanan, "Multilevel finite-difference model for three-dimensional hydrodynamic circulation," *Ocean Engineering*, vol. 24, no. 9, pp. 785–816, 1997.

[62] Z. Wang, T. Hopfes, M. Giglmaier, and N. A. Adams, "Effect of mach number on droplet aerobreakup in shear stripping regime," *Experiments in Fluids*, vol. 61, no. 9, pp. 1–17, 2020.

[63] E. F. Toro, *Riemann solvers and numerical methods for fluid dynamics: a practical introduction*. 2013.

[64] F. Pascal, "Sur des méthodes d'approximation effectives et d'analyse numérique pour les équations de la mécanique de fluides," *Mémoire d'habilitation à diriger des recherches, Université d'Orsay*, 2002.

[65] R. Eymard, T. Gallouët, and R. Herbin, "Finite volume methods: handbook of numerical analysis," *PG Ciarlet and JL Lions (Eds)*, 2000.

[66] R. Courant, E. Isaacson, and M. Rees, "On the solution of nonlinear hyperbolic differential equations by finite differences," *Communications on Pure and Applied Mathematics*, vol. 5, no. 3, pp. 243–255, 1952.

[67] S. K. Godunov and I. Bohachevsky, "Finite difference method for numerical computation of discontinuous solutions of the equations of fluid dynamics," *Matematičeskij sbornik*, vol. 47, no. 3, pp. 271–306, 1959.

[68] V. V. Rusanov, "The calculation of the interaction of non-stationary shock waves with barriers," *Zhurnal Vychislitel'noi Matematiki i Matematicheskoi Fiziki*, vol. 1, no. 2, pp. 267–279, 1961.

[69] P. L. Roe, "Approximate riemann solvers, parameter vectors, and difference schemes," *Journal of Computational Physics*, vol. 43, no. 2, pp. 357–372, 1981.

[70] E. Audusse, F. Bouchut, M.-O. Bristeau, R. Klein, and B. Perthame, "A fast and stable well-balanced scheme with hydrostatic reconstruction for shallow water flows," *SIAM Journal on Scientific Computing*, vol. 25, no. 6, pp. 2050–2065, 2004.

[71] M. Dumbser, A. Hidalgo, M. Castro, C. Parés, and E. F. Toro, "Force schemes on unstructured meshes ii: Non-conservative hyperbolic systems," *Computer Methods in Applied Mechanics and Engineering*, vol. 199, no. 9-12, pp. 625–647, 2010.

[72] R. Radespiel and N. Kroll, "Accurate flux vector splitting for shocks and shear layers," *Journal of Computational Physics*, vol. 121, no. 1, pp. 66–78, 1995.

[73] F. Benkhaldoun and L. Quivy, "A non homogeneous riemann solver for shallow water and two phase flows," *Flow, Turbulence and Combustion*, vol. 76, no. 4, pp. 391–402, 2006.

[74] A. Kurganov and D. Levy, "Central-upwind schemes for the saint-venant system," *ESAIM: Mathematical Modelling and Numerical Analysis*, vol. 36, no. 3, pp. 397–425, 2002.

[75] A. Harten, J. M. Hyman, P. D. Lax, and B. Keyfitz, "On finite-difference approximations and entropy conditions for shocks," *Communications on Pure and Applied Mathematics*, vol. 29, no. 3, pp. 297–322, 1976.

[76] B. Van Leer, "Towards the ultimate conservative difference scheme. v. a second-order sequel to godunov's method," *Journal of Computational Physics*, vol. 32, no. 1, pp. 101–136, 1979.

[77] P. Colella and P. R. Woodward, "The piecewise parabolic method (ppm) for gas-dynamical simulations," *Journal of Computational Physics*, vol. 54, no. 1, pp. 174–201, 1984.

[78] A. Harten, B. Engquist, S. Osher, and S. R. Chakravarthy, "Uniformly high order accurate essentially non-oscillatory schemes, iii," *Journal of Computational Physics*, vol. 131, no. 1, pp. 3–47, 1997.

[79] I. El Mahi, *Schémas volumes finis pour la simulation numérique de problèmes à fronts raides en maillages non structurés adaptatifs*. PhD thesis, Rouen, 1999.

[80] P. K. Sweby, "High resolution schemes using flux limiters for hyperbolic conservation laws," *SIAM Journal on Numerical Analysis*, vol. 21, no. 5, pp. 995–1011, 1984.

[81] P. Roe, "Generalized formulation of tvd lax-wendroff schemes," tech. rep., 1984.

[82] T. Barth and D. Jespersen, "The design and application of upwind schemes on unstructured meshes," in *27th Aerospace sciences meeting*, p. 366, 1989.

[83] P. Galon and J. Nunziati, "Méthode des volumes finis dans europlexus–extension du schéma à l'ordre deux en espace et en temps," tech. rep., Tech. rep. DEN/DM2S/SEMT/DYN/RT/08-001/B, CEA, 2008.

[84] G. D. Van Albada, B. Van Leer, and W. Roberts Jr, "A comparative study of computational methods in cosmic gas dynamics," *Astronomy and Astrophysics, vol. 108, no. 1, Apr. 1982, p. 76-84.*, vol. 108, pp. 76–84, 1982.

[85] C. Tai, D. Chiang, and Y. Su, "Explicit time marching methods for the time-dependent euler computations," *Journal of Computational Physics*, vol. 130, no. 2, pp. 191–202, 1997.

[86] R. B. Lowrie, P. L. Roe, and B. Van Leer, "Space-time methods for hyperbolic conservation laws," *ICASE LARC INTERDISCIPLINARY SERIES IN SCIENCE AND ENGINEERING*, vol. 6, pp. 79–98, 1998.

[87] S. K. Godunov, "A difference method for numerical calculation of discontinuous equations of hydrodynamics," *Math. Sb*, vol. 47, p. 217, 1959.

[88] R. Courant, K. Friedrichs, and H. Lewy, "Über die partiellen differenzengleichungen der mathematischen physik," *Mathematische Annalen*, vol. 100, no. 1, pp. 32–74, 1928.

[89] A. Harten, P. D. Lax, and B. v. Leer, "On upstream differencing and godunov-type schemes for hyperbolic conservation laws," *SIAM review*, vol. 25, no. 1, pp. 35–61, 1983.

[90] J.-M. Hervouet, *Hydrodynamique des écoulements à surface libre: Modélisation numérique avec la méthode des éléments finis*. Presses de l'école nationale des Ponts et Chaussées, 2003.

[91] J. Hervouet, "Hydrodynamique des écoulementsa surface libre, apport de la méthode des éléments finis," 2001.

[92] I. Orlanski, "A simple boundary condition for unbounded hyperbolic flows," *Journal of Computational Physics*, vol. 21, no. 3, pp. 251–269, 1976.

[93] A. F. Blumberg and L. H. Kantha, "Open boundary condition for circulation models," *Journal of Hydraulic Engineering*, vol. 111, no. 2, pp. 237–255, 1985.

[94] L. Simon, "Contribution to the modelling of surface water flow and transport," *Th. D. Paris, France, Ecole Nationale des Ponts et Chaussées*, vol. 16, 1994.

[95] R. Flather, "A tidal model of the northwest european continental shelf," *Mem. Soc. Roy. Sci. Liege*, vol. 10, pp. 141–164, 1976.

[96] E. D. Palma and R. P. Matano, "On the implementation of open boundary conditions for a general circulation model: The three-dimensional case," *Journal of Geophysical Research: Oceans*, vol. 105, no. C4, pp. 8605–8627, 2000.

[97] R. Vacondio, B. Rogers, P. Stansby, and P. Mignosa, "Sph modeling of shallow flow with open boundaries for practical flood simulation," *Journal of Hydraulic Engineering*, vol. 138, no. 6, pp. 530–541, 2012.

[98] F. Bethuel, "Une introduction aux équations aux dérivées partielles," *https://www.ljll.math.upmc.fr/MathModel/enseignement/polycopies/M2-Base-EDP-18-09-26.pdf*.

[99] E. Godlewski and P.-A. Raviart, *Hyperbolic systems of conservation laws*. No. 3-4, Ellipses, 1991.

[100] S. Sahmim, F. Benkhaldoun, and F. Alcrudo, "A sign matrix based scheme for non-homogeneous pde's with an analysis of the convergence stagnation phenomenon," *Journal of Computational Physics*, vol. 226, no. 2, pp. 1753–1783, 2007.

[101] W. Aboussi, M. Ziggaf, I. Kissami, and M. Boubekeur, "A highly efficient finite volume method with a diffusion control parameter for hyperbolic problems," *J. Mathematics and Computers in Simulation (submitted after a first revision).*

[102] G. A. Sod, *Numerical methods in fluid dynamics: initial and initial boundary-value problems*, vol. 1. Cambridge University Press, 1985.

[103] M. Ziggaf, M. Boubekeur, F. Benkhaldoun, I. El Mahi, and I. Kissami, "The FVC scheme on unstructured meshes for the two-dimensional shallow water equations," in *International Conference on Finite Volumes for Complex Applications*, pp. 455–465, Springer, 2020.

[104] Y. Coudière, J.-P. Vila, and P. Villedieu, "Convergence rate of a finite volume scheme for a two dimensional convection-diffusion problem," *ESAIM: Mathematical Modelling and Numerical Analysis*, vol. 33, no. 3, pp. 493–516, 1999.

[105] K. Mohamed, *Simulation numérique en volume finis, de problèmes d'écoulements multidimensionnels raides, par un schéma de flux à deux pas*. PhD thesis, Université Paris-Nord-Paris XIII, 2005.

[106] K. Mohamed, "A finite volume method for numerical simulation of shallow water models with porosity," *Computers & Fluids*, vol. 104, pp. 9–19, 2014.

[107] L. Monthe, F. Benkhaldoun, and I. Elmahi, "Positivity preserving finite volume roe: schemes for transport-diffusion equations," *Computer Methods in Applied Mechanics and Engineering*, vol. 178, no. 3-4, pp. 215–232, 1999.

[108] B. Da Veiga, J. Droniou, and G. Manzini, "A unified approach for handling convection terms in finite volumes and mimetic discretization methods for elliptic problems," *IMA Journal of Numerical Analysis*, vol. 31, no. 4, pp. 1357–1401, 2011.

[109] C. Chainais-Hillairet and J. Droniou, "Finite-volume schemes for noncoercive elliptic problems with neumann boundary conditions," *IMA Journal of Numerical Analysis*, vol. 31, no. 1, pp. 61–85, 2011.

[110] T. Gallouët, R. Herbin, and M. H. Vignal, "Error estimates on the approximate finite volume solution of convection diffusion equations with general boundary conditions," *SIAM Journal on Numerical Analysis*, vol. 37, no. 6, pp. 1935–1972, 2000.

[111] D. L. Ropp and J. N. Shadid, "Stability of operator splitting methods for systems with indefinite operators: Advection–diffusion–reaction systems," *Journal of Computational Physics*, vol. 228, no. 9, pp. 3508–3516, 2009.

[112] S. Zhao, J. Ovadia, X. Liu, Y.-T. Zhang, and Q. Nie, "Operator splitting implicit integration factor methods for stiff reaction–diffusion–advection systems," *Journal of Computational Physics*, vol. 230, no. 15, pp. 5996–6009, 2011.

[113] S. Gottlieb and C.-W. Shu, "Total variation diminishing runge-kutta schemes," *Mathematics of computation*, vol. 67, no. 221, pp. 73–85, 1998.

[114] V. Desveaux, *Contribution à l'approximation numérique des systèmes hyperboliques*. PhD thesis, Université de Nantes, 2013.

[115] U. S. Fjordholm and S. Mishra, "Vorticity preserving finite volume schemes for the shallow water equations," *SIAM Journal on Scientific Computing*, vol. 33, no. 2, pp. 588–611, 2011.

[116] J. J. Stoker, *Water waves: The mathematical theory with applications*, vol. 36. John Wiley & Sons, 2011.

[117] F. Henderson, "Open channel flow. macmillan series in civil engineering," *New York*, 1966.

[118] R. J. Fennema and M. Hanif Chaudhry, "Implicit methods for two-dimensional unsteady free-surface flows," *Journal of Hydraulic Research*, vol. 27, no. 3, pp. 321–332, 1989.

[119] E. Audusse, M.-O. Bristeau, and B. Perthame, *Kinetic schemes for Saint-Venant equations with source terms on unstructured grids*. PhD thesis, INRIA, 2000.

[120] R. J. Fennema and M. H. Chaudhry, "Explicit methods for 2-d transient free surface flows," *Journal of Hydraulic Engineering*, vol. 116, no. 8, pp. 1013–1034, 1990.

[121] R. J. LeVeque, "Balancing source terms and flux gradients in high-resolution godunov methods: the quasi-steady wave-propagation algorithm," *Journal of Computational Physics*, vol. 146, no. 1, pp. 346–365, 1998.

[122] Z. Wang, J. Zhu, and N. Zhao, "A new fifth-order finite difference well-balanced multi-resolution weno scheme for solving shallow water equations," *Computers & Mathematics with Applications*, vol. 80, no. 5, pp. 1387–1404, 2020.

[123] A. C. Kuo and L. M. Polvani, "Nonlinear geostrophic adjustment, cyclone/anticyclone asymmetry, and potential vorticity rearrangement," *Physics of Fluids*, vol. 12, no. 5, pp. 1087–1100, 2000.

[124] F. Alcrudo and P. Garcia-Navarro, "A high-resolution godunov-type scheme in finite volumes for the 2d shallow-water equations," *International Journal for Numerical Methods in Fluids*, vol. 16, no. 6, pp. 489–505, 1993.

[125] S. S. Frazão and Y. Zech, "Dam break in channels with 90 bend," *Journal of Hydraulic Engineering*, vol. 128, no. 11, pp. 956–968, 2002.

[126] M. Guan, N. Wright, and P. Sleigh, "A robust 2d shallow water model for solving flow over complex topography using homogenous flux method," *International Journal for Numerical Methods in Fluids*, vol. 73, no. 3, pp. 225–249, 2013.

[127] J. G. Zhou, D. M. Causon, D. M. Ingram, and C. G. Mingham, "Numerical solutions of the shallow water equations with discontinuous bed topography," *International Journal for Numerical Methods in Fluids*, vol. 38, no. 8, pp. 769–788, 2002.

[128] Z. Ahmad and U. Kothyari, "Time-line cubic spline interpolation scheme for solution of advection equation," *Computers & fluids*, vol. 30, no. 6, pp. 737–752, 2001.

[129] T. Komatsu, K. Ohgushi, and K. Asai, "Refined numerical scheme for advective transport in diffusion simulation," *Journal of Hydraulic Engineering*, vol. 123, no. 1, pp. 41–50, 1997.

[130] M. A. García, M. González, M. Espino Infantes, and A. Sánchez-Arcilla Conejo, "Un modelo numérico en elementos finitos para la corriente inducida por la marea. aplicaciones al estrecho de gibraltar," 1995.

[131] J. Almazan, H. Bryden, T. Kinder, and G. Parrilla, "Seminario sobre la oceanografia fisica del estrecho de gibraltar, 24-28 october 1988, madrid," *Sociedad Espa˜ aola de Estudios para la Comunicacirn fija a traves del Estrecho de Gibraltar (SECEG), Madrid*, 1989.

[132] G. Strang, "On the construction and comparison of difference schemes," *SIAM Journal on Numerical Analysis*, vol. 5, no. 3, pp. 506–517, 1968.

[133] J. Karel, *Numerical simulation of streamer propagation on unstructured dynamically adapted grids*. PhD thesis, Université Paris-Nord-Paris XIII, 2014.

[134] bhqasx, "1d_euler_exact.zip," *(https://www.mathworks.com/matlabcentral/fileexchange/46383-1d_euler_exact-zip). MATLAB Central File Exchange.*, 2022.

[135] W. Aboussi, M. Ziggaf, I. Kissami, and M. Boubekeur, "A finite volume scheme with a diffusion control parameter on unstructured hybrid mesh: application to two-dimensional euler equations," *Submitted to the FVCA 10 conference .*

[136] R. J. LeVeque, "Simplified multi-dimensional flux limiting methods," *Numerical Methods for Fluid Dynamics IV*, vol. 175, p. 190, 1993.

[137] D. Kuzmin, "Hierarchical slope limiting in explicit and implicit discontinuous galerkin methods," *Journal of Computational Physics*, vol. 257, pp. 1140–1162, 2014.

[138] M. Dumbser and R. Loubère, "A simple robust and accurate a posteriori sub-cell finite volume limiter for the discontinuous galerkin method on unstructured meshes," *Journal of Computational Physics*, vol. 319, pp. 163–199, 2016.

[139] G. Moretti, "Experiments on initial and boundary conditions," tech. rep., 1980.

[140] J. Fürst, M. Janda, and K. Kozel, "Finite volume solution of 2d and 3d euler and navier-stokes equations," *Mathematical Fluid Mechanics*, pp. 173–194, 2001.

[141] J. Halama and F. Benkhaldoun, "Finite volume characteristic flux scheme for transonic flow problems," 2006.

[142] M. Slouka and K. Kozel, "Numerical calculations of 2d transonic flow in gamm channel and over the profile," in *EPJ Web of Conferences*, vol. 143, p. 02109, EDP Sciences, 2017.

[143] P. Kryštufek and K. Kozel, "Numerical solution of compressible steady flows in a 2d gamm channel and dca 18% profile," in *EPJ Web of Conferences*, vol. 25, p. 01043, EDP Sciences, 2012.

[144] J. FÜRST, "Numerical solution of inviscid and viscous flows using weighted least square scheme and quadrilateral or triangular mesh," in *Czech-Japanese Seminar in Applied Mathematics*, p. 8, 2004.

[145] P. Woodward and P. Colella, "The numerical simulation of two-dimensional fluid flow with strong shocks," *Journal of Computational Physics*, vol. 54, no. 1, pp. 115–173, 1984.

[146] M. Rabaud and F. Moisy, "The kelvin–helmholtz instability, a useful model for wind-wave generation?," *Comptes Rendus. Mécanique*, vol. 348, no. 6-7, pp. 489–500, 2020.

[147] C. W. Schulz-Rinne, J. P. Collins, and H. M. Glaz, "Numerical solution of the riemann problem for two-dimensional gas dynamics," *SIAM Journal on Scientific Computing*, vol. 14, no. 6, pp. 1394–1414, 1993.

[148] P. D. Lax and X.-D. Liu, "Solution of two-dimensional riemann problems of gas dynamics by positive schemes," *SIAM Journal on Scientific Computing*, vol. 19, no. 2, pp. 319–340, 1998.

[149] R. Liska and B. Wendroff, "Comparison of several difference schemes on 1d and 2d test problems for the euler equations," *SIAM Journal on Scientific Computing*, vol. 25, no. 3, pp. 995–1017, 2003.

[150] M. Bohm, S. Schermeng, A. R. Winters, G. J. Gassner, and G. B. Jacobs, "Multi-element siac filter for shock capturing applied to high-order discontinuous galerkin spectral element methods," *Journal of Scientific Computing*, vol. 81, pp. 820–844, 2019.

[151] A. Kurganov and E. Tadmor, "Solution of two-dimensional riemann problems for gas dynamics without riemann problem solvers," *Numerical Methods for Partial Differential Equations: An International Journal*, vol. 18, no. 5, pp. 584–608, 2002.

[152] G. A. Sod, "A survey of several finite difference methods for systems of nonlinear hyperbolic conservation laws," *Journal of Computational Physics*, vol. 27, no. 1, pp. 1–31, 1978.

[153] O. Zanotti, F. Fambri, M. Dumbser, and A. Hidalgo, "Space–time adaptive ader discontinuous galerkin finite element schemes with a posteriori sub-cell finite volume limiting," *Computers & Fluids*, vol. 118, pp. 204–224, 2015.

[154] V. A. Titarev and E. F. Toro, "Ader schemes for three-dimensional non-linear hyperbolic systems," *Journal of Computational Physics*, vol. 204, no. 2, pp. 715–736, 2005.

List of publications

1. Ziggaf M., Boubekeur M., kissami I., Benkhaldoun F. A well-balanced FVC scheme for 2d shallow water fows on unstructured triangular meshes. (Advances in applied mathematics and mechanics. Adv. Appl. Math. Mech., doi:10.4208/aamm.OA-2022-0113)

2. Aboussi, W., Ziggaf, M., Kissami, I., & Boubekeur, M. (2023). A highly efficient finite volume method with a diffusion control parameter for hyperbolic problems. Mathematics and Computers in Simulation.

3. Aboussi W., Ziggaf M., kissami I., Boubekeur M. A finite volume scheme with a diffusion control parameter on unstructured hybrid mesh: application to two-dimensional Euler equations. (Accepted for publication in the FVCA10 book of proceedings).

4. Ziggaf M., Kissami, I,. Elmahi I., Benkhaldoun F. A new finite volume predictor-corrector scheme for solving the perfect gas dynamics model in multiple spatial dimensions on unstructured meshes. (Accepted for publication in a special volume of the SEMA-SIMAI Springer Series).

5. Z. Moussa and K. Imad, "MPI-Based Simulation of the Shallow Water Model using the Finite Volume Characteristics Scheme," 2022 6th International Conference on Computer, Software and Modeling (ICCSM), 2022, pp. 52-57, doi: 10.1109/ICCSM57214.2022.00016.

6. M. Ziggaf, I. Kissami, M. Boubekeur, F. Benkhaldoun and I. Elmahi, A three-dimensional FVC scheme on non-uniform tetrahedron meshes: application to the 3D Euler equation, in: eccomas2022. URL https://www.scipedia.com/public/Ziggaf-et-al-2022a

7. Ziggaf, Moussa, Boubekeur, Mohamed, Benkhaldoun, Fayssal, et al. The FVC scheme on unstructured meshes for the two-dimensional Shallow Water Equations. In : International Conference on Finite Volumes for Complex Applications. Springer, Cham, 2020. p. 455-465.

8. Bradji, A., Ziggaf, M. (2021). A Convergence Result of a Linear SUSHI Scheme Using Characteristics Method for a Semi-linear Parabolic Equation. In: Dimov, I., Fidanova, S. (eds) Advances in High Performance Computing. HPC 2019. Studies in Computational Intelligence, vol 902. Springer, Cham. https://doi.org/10.1007/978-3-030-55347-0-38.

Study and implementation of an Eulerian-Lagrangian method on 2D/3D unstructured meshes for the numerical simulation of fluid flow models

Abstract

This thesis presents a study on the development and effectiveness of the Characteristic Finite Volume (FVC) scheme on unstructured 2D and 3D meshes for simulating two types of flows: shallow water flows described by the Saint-Venant equations (also known as shallow water equations) with single-layer and multilayer configurations, and gas flows modeled by the Euler equations. The FVC scheme shows promise by offering first-order accuracy and improved representation of physical phenomena. A computational code based on this scheme was developed to solve the corresponding equations, and a well-balanced discretization of the FVC scheme was proposed for the shallow water model, allowing for the prediction of the code's application to problems with significant source terms and irregular bottom topography.

Various test cases were conducted to evaluate the numerical simulation of free-surface flows and gas flows. These evaluations involved comparisons between numerical results and analytical solutions or experimental data. The performed comparisons confirm the reliability, accuracy, stability, and robustness of the proposed code and scheme, as well as the effectiveness of the techniques used to handle boundary conditions. The results obtained from the various test cases are satisfactory, providing confidence in the large-scale application of the scheme, particularly in domains such as pollutant transport in the Strait of Gibraltar.

In summary, this study demonstrates the reliability of the FVC scheme on unstructured meshes for solving conservation equations, such as the Euler equations and shallow water equations. This scheme offers a robust and accurate solution for a wide range of flows and bottom topography configurations.

Keywords Shallow water model; Method of characteristics; 2D FVC scheme; Finite volume method; Multilayer shallow water equations; Well-balanced scheme; Euler equations, 3D FVC scheme; Diamond scheme; unstructured meshes; Conversations laws; Riemann problem.

Étude et mise en œuvre d'une méthode Eulérienne-Lagrangienne sur des maillages non structurés 2D/3D pour la simulation numérique de modèles d'écoulements fluides

Résumé

Cette thèse présente une étude portant sur le développement et l'efficacité du schéma des Volumes Finis Caractéristiques (FVC) sur des maillages non structurés en 2D et 3D, pour la simulation de deux types d'écoulements : les écoulements d'eau peu profonde, décrits par les équations de Saint-Venant (également connues sous le nom d'équations de l'eau peu profonde), avec des configurations monocouche et multicouches, ainsi que les écoulements de gaz, modélisés par les équations d'Euler. Le schéma FVC se révèle prometteur en offrant une précision accrue au premier ordre et une meilleure représentation des phénomènes physiques. Un code de calcul basé sur ce schéma a été développé pour résoudre les équations correspondantes, et une discrétisation bien équilibrée du schéma FVC a été proposée pour le modèle d'eau peu profonde, permettant de prédire l'application du code à des problèmes avec des termes sources importants et une irrégularité du fond.

Différents cas test ont été exécutés pour évaluer la simulation numérique des écoulements à surface libre ainsi que les écoulements de gaz. Ces évaluations ont consisté en des comparaisons entre les résultats numériques et des solutions analytiques ou des données expérimentales. Les comparaisons effectuées confirment la fiabilité, la précision, la stabilité et la robustesse du code et du schéma proposés, ainsi que l'efficacité des techniques utilisées pour traiter les conditions aux limites. Les résultats obtenus lors des différents cas test sont satisfaisants, ce qui permet d'envisager avec confiance l'application à grande échelle, notamment dans des domaines tels que le transport de polluants dans le détroit de Gibraltar.

En résumé, cette étude démontre la fiabilité du schéma FVC sur des maillages non structurés pour la résolution des équations de conservation, telles que les équations d'Euler et les équations d'eau peu profonde. Ce schéma offre une solution robuste et précise pour une large gamme d'écoulements et de configurations de fond.

Mots clés Équations de Saint-Venant; Méthode des caractéristiques; Schéma FVC bidimensionnelle; Méthode des volumes finis; Équations multicouches d'eau peu profonde; Schéma bien équilibré; Équations d'Euler; Schéma FVC en 3D; Schéma diamond; Maillages non structurés; Lois de conservation; Problème de Riemann.